



University of Constantine 3 Salah Boubnider

Faculty of process Engineering

Department of Chemical engineering

**Modeling of Trickle Bed Catalytic
Reactors and Industrial Applications to
GTL Process**

THESIS

Submitted for the Award of the Degree of Doctor of Science in

Process Engineering.

Option: Chemical Engineering

By

Maher LAKKAICHI

Academic Year

2025-2026



University of Constantine 3 Salah Boubnider

Faculty of process Engineering

Department of Chemical engineering

N° de Série :

N° d'ordre :

Modeling of Trickle Bed Catalytic Reactors and Industrial Applications to GTL Process

THESIS

Submitted for the Award of the Degree of Doctor of Science in
Process Engineering.

Option: Chemical Engineering

By

Maher LAKKAICHI

Before the jury composed of:

Ouassila LARKECHE	President	Lecturer	University of Constantine 3
Nawel OUTILI	Supervisor	Professor	University of Constantine 3
Mehdi LOUAER	Examiner	Lecturer	University of Constantine 3
Mahfoud KADJA	Examiner	Professor	University of Constantine 1
Mohamed SI-AMEUR	Examiner	Professor	University of Batna 2
Azeddine KABOUCHE	Examiner	Professor	University of Oum El Bouaghi
Abdesslam-Hassen MENIAI	Guest	Professor	University of Constantine 3

Academic Year

2025-2026

ACKNOWLEDGEMENTS

This thesis work would not have been possible without the support of many people. Many thanks to my supervisor, Nawel OUTILI, who has accompanied and guided me since the beginning of this project of thesis. Also, who knew how to find the right words to direct me to the right lines of research, and knew how to find the words of encouragement. Pr. Nawel OUTILI read my numerous revisions and helped make some sense of the confusion. I have benefited greatly from your wealth of knowledge and meticulous editing.

Also, many thanks to Dr. Ouassila LARKECHE who accepted to chair the jury committee. Also, I would like to express my heartfelt gratitude to my thesis jury members; Dr. Mehdi LOUAER; Pr. Mahfoud KADJA; Pr. Mohamed SI-AMEUR and Pr. Azeddine KABOUCHE, for accepting to judge my work. The honorable committee members who spent their precious time and intellectual efforts in reading and examining the thesis manuscripts. Your detailed feedback and constructive criticism will be an incentive for me to complete the deficiencies and enrich this research work.

Thanks also to Pr. Abdesslam Hassen Meniai, who so generously took time out of his schedules to participate in my research and provided me precious pieces of advice.

Also, I would like to thank Pr. BOUSBA Salim who helped me by providing me with interesting techniques to accomplish my bibliographic research.

Thanks to the University of Constantine 3 Salah Boubnider, mainly Faculty of Process Engineering, for awarding me a thesis Completion Fellowship, providing me with the required supports to complete this project.

Thanks also to SONATRACH that provided me with the technical support Aspen HYSYS V12 to accomplish some part of this project.

Finally, I will never regret being grateful to Pr. Saci NACEF who left us last year, may God have mercy on him. I had the honor that, he supervised me for the project of 'Magistère'. That work was the basis of my current doctoral research.

DEDICATION

This thesis is dedicated to the memory of my father. Although he was my inspiration to pursue my doctoral degree, he was unable to attend this moment of success.

This is for him; for the great man who planted in me the love of physics and mathematics.

I dedicate my thesis work to my mother; the woman who raised me to love studying and for the love of science.

I dedicate this work to my small family; to my wife who has always been my support, who was able to discuss with me about some relevant topics to this thesis, who gave me tenderness acting as a potential energy to go ahead. To my daughters Lina and Jouana, who I see will have a brilliant future.

Further, yet importantly, I dedicated this project to my dear sisters Meriem and Ibtissem and my dear brothers Hamza and Ahmed, who I share with them memories engraved inside my heart.

Last but not the least, I would also like to thank every person who respects my scientific ideas.

TABLE OF CONTENTS

LIST OF FIGURES.....	vi
LIST OF TABLES.....	viii
LIST OF ABBREVIATIONS	ix
GENERAL INRODUCTION	1
CHAPTER I.....	5
LITERATURE REVIEW	5
1.1 Introduction.....	5
1.2 Trickle Bed Reactors (TBRs).....	6
1.3 PBR types.....	7
1.4 Characterization of packed bed reactors (PBRs)	9
1.4.1 Equivalent particle diameter.....	10
1.4.2 Solid particle sphericity (or shape factor)	10
1.4.3 Porosity.....	11
1.4.4 Investigations on the structure of packed beds.....	13
1.5 Hydrodynamic of TBRs.....	14
1.5.1 Single-phase flow in PBRs.....	15
1.5.2 Two-phase flow in PBRs.....	18
1.5.3 Modeling and simulation of TBRs using CFD	28
1.5.4 Some recent studies on TBRs.....	29
1.6 GTL Process background: from genesis to modern applications	31
1.7 Some recent works on GTL process.....	35
1.8 Fischer-Tropsch Synthesis (FTS)	37
1.8.1 FTS mechanisms	38
1.8.2 Catalysts of FTS	39
1.8.3 Support materials for FTS catalyst.....	41
1.8.4 Kinetics of FTS	41
1.8.5 FTS products selectivity.....	43
1.8.6 Factors impacting CO conversion and products selectivity	45
1.9 Modeling and simulation of FTPBR	49
1.10 Conclusion	54
CHAPTER II	55
MODELING AND SIMULATION OF FISCHER-TROPSCH PACKED BED	
REACTOR	55
2.1 Introduction.....	55
2.2 Simulation methodology on COMSOL Multiphysics 5.6.....	55
2.3 Hydrodynamic simulation: Pressure drop analysis in a slender packed bed	
reactor using CFD.....	56
2.3.1 Generation of geometries	57
2.3.2 Meshing	61
2.3.3 CFD modeling	61
2.3.4 Numerical setup.....	66
2.4 Case study of Fischer-Tropsch Synthesis in packed bed reactors.....	68
2.4.1 The Fischer-Tropsch MultiTubular Packed Bed Reactor (FT-MTPBR)	68
2.4.2 Simplifying assumptions	69
2.4.3 Geometry generation	70
2.4.4 Mesh generation	71
2.4.5 Governing equations	71
2.4.6 Boundary conditions	77
2.4.7 Numerical simulations.....	78

2.5	Conclusion	80
CHAPTER III.....		80
RESULTS AND DISCUSSION.....		80
3.1	Introduction.....	80
3.2	Hydrodynamic study	81
3.2.1	Validation of the Three Dimension Resolved Particle Model (3D-RPM)	81
3.2.2	Comparison of pressure drop simulated results	84
3.3	Results of the case study: modeling and simulation of Fischer-Tropsch	
	Packed Bed Reactor.....	89
3.3.1	Kinetics of the FT reaction: Effect of the temperature on the CO consumption rate	89
3.3.2	Mesh independence study	92
3.3.3	Comparison between the current model and models from literature	95
3.3.4	Effects of the bed aspect ratio (AR)	104
3.3.5	Limit temperature of thermally viable PBRs of large-scale FT reactors: Cases 1 and 2	106
3.3.6	Performance comparison of packed beds with different aspect ratios for large-scale FT reactors: Cases 1 and 2	108
3.3.7	Limit temperature of thermally viable PBRs of small-scale FT reactors: Cases 3 and 4	114
3.3.8	Performance comparison of packed beds with different aspect ratios for small scale FT reactors: Cases 3 and 4	116
3.4	Conclusion	123
GENERAL CONCLUSION AND PERSPECTIVES		125
REFERENCES		128
APPENDICES.....		141
	Appendix A: Deriving the circle diameter of the hypothetical 2D geometry	141
	Appendix B: The GCI methodology.....	141
	Appendix C: Design of the FTBPR (Computing the tubes number)	143
	Appendix D: Aspen HYSYS program: Simplified syngas production unit, using natural gas as feedstock.....	144
	Appendix E: List of Publications.....	145

LIST OF FIGURES

Figure 1.1 : Typical Packed Bed Reactor (PBR) crossed by gas-liquid flow downwards, called Trickle-Bed reactor (TBR)	5
Figure 1.2: PBR types : (a) Tubular PBR, (b) Structured PBR, (c) Micro PBR and (d) Multitubular PBR (MTPBR) : A. Azarpour et al. [1] and V. V. Ranade [2]	9
Figure 1.3: Porosities at different scales: S. Sabet [49].....	11
Figure 1.4: Radial and axial porosity distribution within a PBR: P. R. Gunjal [57].....	12
Figure 1.5: Flow regimes of concurrent two-phase flow downward in PBR V. V. Ranade and R. P. Utikar [86]	19
Figure 1.6: Effect of Hysteresis phenomena on two-phase pressure drop (a) from V. V. Ranade et al. [2] and (b) from A. K. Saroha and I. Nandi [90].....	20
Figure 1.7: Slit approach: (a) Single slit M. H. Al-Dahhan et al [102], (b) Double slit I. Iliuta et al [103] and I. Iliuta and F. Larachi [104]	23
Figure 1.8: Interaction forces at the particle scale according to Attou et al. [106]	23
Figure 1.9: Liquid holdup hysteresis at different gas and liquid flow rates : Z. Cheng et al [114]: (a) low gas flow rate, (b) high gas flow rate.....	27
Figure 1.10: Wetting of particles: V. V. Ranade [2]	27
Figure 1.11: Main steps of conventional GTL process : F. T. Alsudani et al. [134].....	32
Figure 1.12: FTS products distribution: products weight fractions versus chain growth probability: D. Weber et al [168]	44
Figure 1.13: Type of conventional FTS reactors: a) Slurry Bubble Column Reactor (SBCR), (b) Multi-Tubular Packed Bed Reactor (MTPBR), (c) Fluidized Bed Reactor (FBR) and (d) Circulating Fluidized Bed Reactor (CFBR) : F. T. Alsudani et al [134]..	46
Figure 1.14: Types of reactors used in small scale GTL : D. Braide [9].....	48
Figure 2.1: Geometries used in different modeling approaches: (a) Real geometry: Three-Dimensional Resolved-Particle Model (3D-RPM); (b) Conceptual geometry: Two-dimensional Resolved-Particle Model (2D-RPM); (c) Two-Dimensional axisymmetric: Pseudo-homogeneous Model (2D-PHM).....	59
Figure 2.2: Flow chart of the hydrodynamic simulations	67
Figure 2.3: MTPBR and single tube demonstration for FTS: reproduced from Jess et al. [186].....	68
Figure 2.4: Generated geometry for the FTPBR model: J. W. Pratt [159]	70
Figure 2.5: Flow chart of the FTPBR reactor simulation.....	79
Figure 3.1: Comparison between the 3D-RPM and Robbins' CFD models, with respect to MRI data in term of axial Reynolds particle number as a function of normalized radial distance for different inlet Re_p values: (a) line graph position, (b) $Re_{p_in}=27$, (b) $Re_{p_in}=55$ and (c) $Re_{p_in}=111$	82
Figure 3.2: Comparison of frictional pressure drop simulated results as a function of normalized axial distance, for all cases at different inlet Re_p values: (a) 27, (b) 55 and (c) 111.	85
Figure 3.3: Comparison of frictional pressure drop simulated results as a function of Double-Unit-Cell number for all cases at different inlet Re_p values: (a) 27, (b) 55 and (c) 111.	87
Figure 3.4: Mean Relative Deviation (MRD) of the simulated pressure drop results in Cases (II, III, IV and V) in reference to Case I at different inlet Re_p values.....	88
Figure 3.5: Predicted CO consumption rate versus time, under isothermal conditions: Effect of reaction temperature ($H_2/CO=2$).....	90

Figure 3.6: Evolution of adiabatic temperature over time, for different initial temperature values ($H_2/CO=2$).....	91
Figure 3.7: Effect of grid size on results (a) axial reactor temperature profile and (b) CO conversion rate profile at the bed exit: $U=0.55$ m/s, $H_2/CO=1.5$ and $T=214$ °C	93
Figure 3.8: Mesh independence tests for (a) maximum reactor temperature and (b) CO conversion rate	94
Figure 3.9: Comparison between the current model (continuous curves), Lee and Cheng (marked curves: o) and Jess and Kern (marked curves: +): Effect of inlet/cooling temperature on the axial temperature profiles ($U=0.55$ m/s and $H_2/CO=2$)	96
Figure 3.10: Comparison between the current model and model of literature: Effect of inlet/cooling temperature on CO conversion rates ($U=0.55$ m/s and $H_2/CO=2$)	97
Figure 3.11: Logarithmic values of normalized hydrocarbon product weight fraction versus carbon number: Comparison between the current and Lee and Cheng models	98
Figure 3.12: Mass fraction profiles in the gaseous phase, along the bed axis, for the baseline case conditions: Comparison between the current model (Continuous curves) and the model of Lee and Cheng (marked curves) (a) C1, C2 and C6 (b) H_2 , CO and H_2O	99
Figure 3.13: Normalized pressure profile: Comparison of the current model against that of Lee and Cheng for the baseline case conditions	100
Figure 3.14: Comparison between the current model (Continuous curves) and that by Lee and Cheng (marked curves) at $T=214$ °C and $U=0.55$ m/s: Effect of H_2 to CO ratio on the axial temperature	101
Figure 3.15: Comparison between the current model (continuous curves) and that of Lee and Cheng (marked curves) at $T=214$ °C and $H_2/CO=2$: Effect of feed velocity on the axial temperature	103
Figure 3.16: Limit temperature for thermally viable reactors of Case 1 (a) $AR=2$, (b) $AR=4$, (c) $AR=8$ and (d) $AR=15.33$	107
Figure 3.17: Limit temperature for thermally viable reactors of Case 2 (a) $AR=2$, (b) $AR=4$ and (c) $AR=8$	108
Figure 3.18: Simulated results of Case 1 in terms of (a) axial temperature and (b) CO conversion rates, (c) C_{5+} radial exit flux and (d) axial normalized pressure drop: Comparison between packed beds with different aspect ratios	109
Figure 3.19: Simulated results of Case 2 in terms of (a) axial temperature and (b) CO conversion rates, (c) C_{5+} mass flux and (d) axial normalized pressure drop: Comparison between packed beds with different aspect ratios	110
Figure 3.20: Limit temperatures of Case 3 (a) $AR=2$, (b) $AR=4$, (c) $AR=8$ and (d) $AR=15.33$	115
Figure 3.21: Limit temperatures of Case 4 (a) $AR=2$, (b) $AR=4$, (c) $AR=8$ and (d) $AR=15.33$	116
Figure 3.22: Inlet/cooling temperature versus bed aspect ratio: Comparison between Cases 3 and 4.....	118
Figure 3.23: Pressure drop versus bed aspect ratio: Comparison between Cases 3 and 4	118
Figure 3.24 : CO conversion rate of different PBRs: Comparison between Cases 3 and 4... ..	119
Figure 3.25: Simulation results of the productivity of C_{5+} , LPG and C_{3+} , with respect to the productivity of PBR2: Comparison between packed beds with different aspect ratios (Case 3)	121
Figure 3.26: Simulation results of the productivity of C_{5+} , LPG and C_{3+} , with respect to the productivity of PBR2: Comparison between packed beds with different aspect ratios of Case 4.....	121

LIST OF TABLES

Table 1.1 : Some advantages and disadvantages of TBRs	6
Table 1.2: Sphericities of some materials with different shapes [47].....	10
Table 1.3: Some significant empirical correlations for bulk porosity calculation.....	12
Table 1.4: Some known axially averaged porosity correlations.....	13
Table 1.5: Some known friction factor correlations in infinite PBRs	17
Table 1.6: Some common friction factor correlations of single-phase flow in slender PBRs.....	18
Table 1.7: Relative Permeabilities correlations	22
Table 1.8: Some recent models of dynamic liquid holdup	26
Table 1.9: Some specific characteristics of the main FTS catalysts.....	39
Table 1.10: Comparison between iron and cobalt catalysts [158].....	40
Table 1.11: Kinetics of FTS over Cobalt catalyst.....	42
Table 1.12: Main FTS products [158]	43
Table 1.13: Some advantage and disadvantages of conventional FTS reactors	47
Table 1.14: Comparison between MTPBR and CFB, in term of products selectivity [156]	48
Table 1.15: Some significant recent modeling works about Fischer-Tropsch synthesis in packed bed reactor.....	53
Table 2.1: Simulated hydrodynamic cases	63
Table 2.2: Drag force sub-models	65
Table 2.3: Characteristics of the baseline case FT-MTPBR and the operating conditions [108], [174]	69
Table 2.4: Stoichiometric coefficients of the FT reaction	75
Table 2.5: Operating conditions of FT reactors simulations	78
Table 3.1: Mean Relative Deviation of the predicted axial Rep: Comparison between the current 3D model and Robbin's CFD model, with respect to MRI data.....	83
Table 3.2: Mesh independence study: Error estimates in 3D simulations, in term of pressure drop, at different inlet Rep values.....	84
Table 3.3: Data used for the GCI methodology.....	93
Table 3.4: Mesh independence study: Asymptotic values of maximum reactor temperature and CO conversion rate with their associated GCIs.....	94
Table 3.5: Simulated results of CO conversion rates: Comparison between our model and that of Lee and Cheng	101
Table 3.6: Characteristics of PBRs: Effect of aspect ratio	104
Table 3.7: Specifications of the studied cases	105
Table 3.8: Simulated results of the large-scale FT reactors (Cases 1 and 2): Comparison between packed beds with different aspect ratios	111
Table 3.9: Comparison between the tubes number with unconverted gas recycling and without recycling, for all scenarios of large-scale reactors.....	113
Table 3.10: Simulated results of the small-scale FT reactors (Cases 3, 4): Comparison between packed beds with different aspect ratios	117
Table 3.11: Economical comparison between the three scenarios of small-scale FTS	123

LIST OF ABBREVIATIONS

- AR : Aspect Ratio
- ARGE : *ARbeitsGEmeinschaft*
- ASF : Anderson-Schulz-Flory
- ATR : Auto-Thermal Reactor
- CAPEX : Capital Expenditures
- CBA : CarboxyBenzAldehyde
- CFB : Circulating Fluidized Bed
- CFD : Computational Fluid Dynamics
- CSTR : Continuous Stirred Tank Reactor
- CT : Computer Tomography
- CTL : Coal To Liquid
- C₃₊ : The hydrocarbons with a number of carbon atom higher or equal to 3
- C₅₊ : The hydrocarbons with a number of carbon atom higher or equal to 5
- DAC : Direct Air Capture
- DEM : Discrete Element Method
- DNS : Direct Numerical Simulation
- DUC : Double Unit cell
- DZD : Algerian Dinar
- ER : Eley-Rideal
- ES : Eisfeld and Schnitzlein
- FDI : Fault Detection and Isolation
- FEA : Finite Element Analysis
- FEM : Finite Element Method
- FFB : Fixed Fluidized Bed
- FT : Fischer-Tropsch
- FTPBR : Fischer-Tropsch Packed Bed Reactor
- FTR : Fischer-Tropsch Reactor
- FTS : Fischer-Tropsch Synthesis
- FVM : Finite Volume Method
- HIR : High Interaction Regime
- HTFT : High Temperature Fischer-Tropsch
- HTSFTP : High Temperature Slurry Fischer-Tropsch Process
- GCI : Grid Convergence Index
- GTL : Gas To Liquid
- IBM : Immersed Boundary Method
- IRR : Internal Rate of Return
- PBR : Packed Bed Reactor
- LBM : Lattice Boltzmann Method
- LCOP : Levelized Cost of Production
- LHHW : Langmuir-Hinshelwood-Hougen-Watson
- LIR : Low Interaction Regime
- LPG : Liquefied Petroleum Gas
- LTFT : Low Temperature Fischer-Tropsch
- MLPANN : Multilayer Perceptron Artificial Neural Network
- MMCFD : Million Cubic Foot a Day
- MR : Membrane Reactor
- MRD : Mean Relative Deviation

- MRI : Magnetic Resonance Imaging
- MTPBR : Multitubular Packed Bed reactor
- MTFT : Medium Temperature Fischer-Tropsch
- MWCNTs : MultiWalled Carbon Nano Tubes
- NG : Natural Gas
- NPV : Net Present Value
- OPEX : Operating Expenditures
- PCS : Pseudo Continuous Simulation
- PIC : Proportional Integral Controller
- PHM : Pseudo-homogeneous Method
- POT : Pay Out Time
- PR : Peng-Robinson
- PRS : Particle Resolved Simulation
- PRDNS : Particle Resolved Direct numerical Simulation
- PTA : Purified Terephalic Acid
- REV : Representative Elementary Volume
- RPM : Resolved-Particle Model/Method
- SAS : Sasol Advanced Synthol
- SBS : Slurry Bubble Column
- SHT : Synthol High Temperature
- SMDS : Shell Middle Distillates Synthesis
- SOEL : Solid Oxide Electrolysis
- STDCM : Standard Cubic Meter
- USD : United States Dollar
- TBR : Trickle Bed Reactor
- WGS : Water Gas Shift

ABSTRACT

Trickle-Bed Reactors (TBRs) are widely utilized in industrial applications. One of the main industrial applications of TBRs is transforming a gaseous mixture of hydrogen and carbon monoxide, called syngas, to environment-friendly synthetic liquid fuels, via Fischer-Tropsch Synthesis (FTS), which is a strongly exothermic reaction.

The aim of this work is to develop a pseudo-homogeneous two-dimensional (2D) Fischer-Tropsch Packed Bed Reactor (FTPBR) model in order to investigate the use of slender packed bed reactors for FTS. This will facilitate the excess heat removal from the bed as well as enhance the performance. To accomplish this objective; two main studies have been conducted, which are (i) hydrodynamic study and (ii) then using its results to develop a FTPBR model. The modeling was carried out using the Finite Element Analysis (FEA) software known as COMSOL Multiphysics 5.6.

Firstly, it was confirmed that the Einfeld and Schnitzlein drag force model should be applied in the momentum balance equation of a two-dimensional pseudo-homogeneous model for low aspect-ratio packed beds. Moreover, a novel 2D modeling approach was proposed for packed bed reactors with an aspect ratio of 2, under laminar flow conditions, mainly of particle Reynolds number lesser than 111.

Secondly, based on the Eulerian mixture approach, a mathematical 2D pseudo-homogeneous model of the FTPBR was developed and validated by confronting its simulated results against those of models of literature as well as by conducting a consistent error discretization uncertainty study. Then it was exploited for the optimization of large-scale FT reactor as well as to optimize and design a small-scale FT reactor. For each scale, two cases were investigated. While the feedstock of the large-scale cases was natural gas, the small-scale cases used biomass as feedstock. For each case, four PBRs with different aspect ratios ranges from 2 to 15.33 were simulated.

It has been found that, the large PBR is the optimized reactor for the large scale, which can be used in a GTL plant to process 170000 m³ of natural gas - at standard conditions - for producing more than 626 tons of C₅₊ per day. Otherwise, the slender PBR with aspect ratio of 4 is the most efficient for the small scale. This reactor is 2 m long and 1916 mm in diameter, which is composed of 6698 tubes arranged in triangular pattern. Besides, it was designed to be fitted into a mobile micro-refinery to process 6 tons of wood chips or 6.6 tons of municipal solid waste per day, to daily produce 4827.16 kg/d and 281.55 kg/d of C₅₊ and LPG, respectively.

Keywords: Packed bed reactor, Pressure drop, Gas-To-Liquid, Fischer-Tropsch, Thermal runaway, Aspect ratio, modeling and simulation, COMSOL Multiphysics.

RESUME

Les réacteurs catalytiques à lit fixe arrosé (RCLFA), traversé par co-courant gaz-liquide de haut vers le bas, sont largement utilisés dans les applications industrielles. L'une des principales applications industrielles des RCLFA est la transformation d'un mélange gazeux d'hydrogène et de monoxyde de carbone, appelé gaz de synthèse, en carburants liquides synthétiques propres, via la synthèse Fischer-Tropsch (SFT), qui est une réaction fortement exothermique.

L'objectif de ce travail est de développer un modèle pseudo-homogène bidimensionnel (2D) d'un réacteur à lit fixe pour la synthèse Fischer-Tropsch (FTPBR), afin d'étudier l'utilisation de réacteurs à lit fixe mince pour la SFT. Cela facilitera l'évacuation de l'excès de chaleur du lit et améliorera les performances. Pour atteindre cet objectif ; deux études principales ont été menées, qui sont (i) l'étude hydrodynamique et (ii) l'utilisation de ses résultats pour développer un modèle du réacteur FTPBR. La modélisation a été réalisée à l'aide du logiciel d'analyse par éléments finis (AEF) connu sous le nom de COMSOL Multiphysics 5.6.

Tout d'abord, il a été confirmé que le modèle de force de traînée d'Eisfeld et Schnitzlein devrait être appliqué dans l'équation de conservation de quantité de mouvement du modèle pseudo-homogène bidimensionnel, pour les lits fixes à faible rapport de diamètre du réacteur au diamètre des particules (rapport d'aspect). De plus, une nouvelle approche de modélisation 2D a été proposée pour les réacteurs à lit fixe avec un rapport d'aspect de 2, dans des conditions d'écoulement laminaire, principalement de nombre de Reynolds de particule inférieur à 111.

Deuxièmement, sur la base de l'approche du mélange Eulérienne, un modèle mathématique 2D pseudo-homogène du FTPBR a été développé et validé en confrontant ses résultats simulés à ceux des modèles de la littérature ainsi qu'en menant une étude d'incertitude de discrétisation d'erreur cohérente. Ensuite, il a été exploité pour l'optimisation d'un réacteur Fischer-Tropsch (FT) à grande échelle ainsi que pour l'optimisation et la conception d'un réacteur FT à petite échelle. Pour chaque échelle, deux cas ont été étudiés. Alors que la matière première des scénarios à grande échelle était le gaz naturel, les scénarios à petite échelle utilisaient la biomasse comme matière première. Pour chaque cas, quatre RCLFA avec des rapports d'aspect différents allant de 2 à 15,33 ont été simulés.

Il a été constaté que le large RCLFA est le réacteur optimisé pour la grande échelle, qui peut être utilisé dans une usine GTL pour traiter 170000 m³ de gaz naturel - sous les conditions standards - pour produire plus de 626 tonnes de C₅₊ par jour. Sinon, le RCLFA mince avec un rapport d'aspect de 4 est le plus efficace pour la petite échelle. Ce réacteur de 2 m de long et 1916 mm de diamètre, est composé de 6698 tubes disposés en triangle. En outre, il a été conçu pour être placé dans une micro-raffinerie mobile afin de traiter 6 tonnes de copeaux de bois ou 6,6 tonnes de déchets solides municipaux par jour, afin de produire quotidiennement 4827,16 kg/j et 281,55 kg/j de C₅₊ et de GPL, respectivement.

Mots clés : Réacteur à lit fixe, Chute de pression, Gaz au liquide, Fischer-Tropsch, Emballlement thermique, rapport d'aspect, Modélisation et simulation, COMSOL Multiphysics.

ملخص

تستخدم المفاعلات ذات المحفز الثابت التي يعبرها التيار المشترك للغاز والسائل من أعلى إلى أسفل، على نطاق واسع في التطبيقات الصناعية. أحد التطبيقات الصناعية الرئيسية هو تحويل خليط غازي من الهيدروجين وأول أكسيد الكربون، يسمى الغاز التخليقي، إلى وقود سائل اصطناعي نظيف، عن طريق تفاعل فيشر و تروبش، وهو تفاعل طارد للحرارة للغاية.

الهدف من هذا العمل هو تطوير نموذج شبه متجانس ثنائي الأبعاد لمفاعل فيشر-تروبش ذو محفز ثابت (FTPBR) من أجل دراسة استخدام هذه المفاعلات ذات قطر المفاعل إلى الجسيمات (Aspect Ratio (AR)) منخفض لتسهيل عملية التخلص من الحرارة الفائضة بالإضافة إلى تحسين الأداء. لتحقيق هذا الهدف، تم إجراء دراستين رئيسيتين، وهما (1) الدراسة الهيدروديناميكية و (2) ثم استخدام نتائجها لتطوير نموذج مفاعل (FTPBR). تم إجراء النمذجة باستخدام برنامج تحليل العناصر المحدودة المعروف باسم « COMSOL Multiphysics 5.6 ». أولاً، تم التأكيد على أنه يجب تطبيق نموذج قوة السحب « Einfeld and Schnitzlein » في معادلة توازن الزخم للنموذج شبه المتجانس ثنائي الأبعاد للمفاعلات ذات قطر المفاعل إلى الجسيمات منخفض. علاوة على ذلك، تم اقتراح نهج جديد للنمذجة ثنائية الأبعاد لمفاعلات ذات المحفز الثابت ذات قيمة قطر المفاعل إلى الجسيمات تبلغ 2، في ظل ظروف التدفق الصفحي، بشكل أساسي لعدد رينولدز الجسيمي الأقل من 111.

ثانياً، بناء على نهج خليط أويلر (Euler) ، تم تطوير نموذج رياضي شبه متجانس ثنائي الأبعاد لمفاعل فيشر-تروبش ذو محفز ثابت (FTPBR) والتحقق من صحته من خلال مواجهة نتائج المحاكاة مقابل نتائج نماذج مرجعية وكذلك من خلال إجراء دراسة متسقة لعدم اليقين في تمييز الخطأ. تم استغلاله لتحسين مفاعل FT لمصنع GTL ذا مقياس كبير وكذلك لتحسين وتصميم مفاعل لمصنع GTL ذا مقياس صغير. لكل مقياس، تم التحقيق في حالتين. في حين أن المادة الخام للمقياس كبير هي الغاز الطبيعي، فإن المقياس صغير يستخدم الكتلة الحيوية كمادة خام. لكل حالة، تمت محاكاة أربع مفاعلات ذات قيمة قطر المفاعل إلى الجسيمات مختلفة تتراوح من 2 إلى 15.33.

لقد وجد أن المفاعل الأوسع هو المفاعل الأمثل للاستعمالات ذات النطاق الواسع، والذي يمكن استخدامه في مصنع GTL لمعالجة 170000 متر مكعب من الغاز الطبيعي – تحت الشروط القياسية – لإنتاج أكثر من 626 طناً من C_5+ يوميا. خلاف ذلك، فإن المفاعل الضيق ذات قيمة AR تبلغ 4 هو الأكثر كفاءة للاستعمالات ذات النطاق الصغير. يبلغ طول هذا المفاعل 2 متر وقطره 1916 مم، ويتكون من 6698 أنبوباً مرتبة في نمط مثلثي. إلى جانب ذلك، تم تصميمه ليتم تركيبه في مصفاة صغيرة متنقلة لمعالجة 6 طن من رقائق الخشب أو 6.6 طن من النفايات الصلبة البلدية يوميا، لإنتاج 4827.16 كجم/يوم و 281.55 كجم/يوم من C_5+ وغاز البترول المسيل، على التوالي.

الكلمات المفتاحية: مفاعل ذو محفز ثابت، هبوط الضغط، غاز الى سائل، فيشر-تروبش، الهروب الحراري، قطر المفاعل إلى الجسيمات، النمذجة الرياضية، برنامج المحاكاة « COMSOL Multiphysics 5.6 ».

GENERAL INRODUCTION

Trickle-bed reactors (TBRs) represent the predominant type of reactor employed in industrial three-phase reaction systems. Their applications span a variety of sectors, including chemical, petrochemical, petroleum, waste treatment, electrochemical, and biochemical processes. The global production capacity of products processed through TBRs is estimated to be approximately 1.6 billion tons per year, with an associated economic value of around USD 300 billion annually [1].

A TBR, which is a Packed Bed Reactor (PBR) with a fixed catalytic bed penetrated by a concurrent gas-liquid down-ward flow, is our research area in this thesis. Due to its unique advantage in handling catalysts on large scale and operation at high pressure, it is widely used in chemical and petroleum processes [1]. Some applications of trickle bed reactors (TBRs) are summarized in [2].

One of the important chemical reactions, which can take place in TBRs, is the transformation of a mixture of some elementary gaseous to liquid hydrocarbons. Here, we are talking about Fischer-Tropsch Synthesis (FTS), which transforms syngas, which is a mixture of Hydrogen (H_2) and carbon monoxide (CO), into sulfur-free and aromatic-free synthetic liquid fuels. The whole process is called Gas-To-Liquid technology (GTL). Basically, the term GTL describes a technology that converts natural gas (NG) into high-quality liquid fuels, including jet fuel, diesel, and gasoline.

The global GTL market revenues was valued at USD 60.56 billion in 2024 and is expected to reach USD 118.91 billion by 2032, exhibiting an annual growth rate of 8.7% during the forecast period (2024-2032). The market growth is mainly driven by increasing demand for cleaner and more efficient fuels, strict government regulations on emissions and growing environmental concerns [3].

The GTL process consists of three main units, which are (i) syngas production, (ii) Fischer-Tropsch synthesis and (iii) upgrading unit [4], [5], [6].

The Fischer-Tropsch reactor is the heart of this process. Actually, there have been existed three main routes to obtain the syngas mixture with a well specified ratio; via natural gas, coal or biomass [7], [8]. Generally, natural gas and coal feedstock are used for large scale GTL process which has been shown to have a significant economic robustness. However, the risk associated with investment is directly related to the scale, which adversely influences the decision-making process regarding the development and investment in new large-scale GTL plants. The third feedstock, which is biomass, can be

used as feedstock for small scale GTL plants. Small-scale GTL plants present several logistical and environmental benefits over large-scale applications, in addition to requiring a lower overall capital investment. Their flexibility allows them to utilize a broader array of carbon-containing resources as feedstock, including municipal waste and wood chips. During the last decade many research on small scale GTL process has been done [4], [9], [10], [11], [12], [13], [14], [15].

The objective of this thesis is the modeling and simulation of Fischer-Tropsch Packed Bed Reactor (FTPBR) crossed by concurrent gas-liquid down-ward flow. The simulations will be carried out by developing two calculation codes, using COMSOL Multiphysics 5.6 software. Via the first code the hydrodynamics of a low aspect ratio packed bed reactor crossed by single incompressible laminar flow will be investigated. The second code will use the results of the hydrodynamic model to simulate the whole FTS phenomena involved in the FTPBR reactor. Finally, the effect of bed-to-catalyst particle diameter, called also Aspect Ratio (AR), on the FTPBR reactor will be investigated for large and small scale applications. The heat transfer between the catalyst bed and the surrounding coolant is significantly influenced by the aspect ratio of the packed bed, which subsequently affects the kinetics of the FT reaction. Hot spot formation is the major drawback of packed bed reactors, mainly for highly exothermic reactions (such as the FT reaction), which may also cause reactor runaway, catalyst deactivation as well as limit the reactor performance. Recent studies reported that, using slender packed beds with low aspect ratio enhances the heat transfer in packed bed reactors, which facilitates the elimination of the excess heat out of the bed, through the reactor wall [10], [16], while keeping the pressure drop at a reasonable level [17]. This insures a safe, stable and economic operation of packed bed reactors with low aspect ratio.

The large scale FTS plant may be applied, in Algeria, to transform natural gas into high-value liquid hydrocarbons. This is an attractive option since two-thirds of the Algerian territory remains underdeveloped or unexplored, with an estimated 100 undeveloped discoveries [18]. Apart from the economic benefits, environment will be preserved by avoiding gas flaring.

Similarly, the small scale FTS may be used, in Algeria, to transform organic biomass into environment-friendly liquid fuels. This is an ambition trend as Algeria produces nearly 34 million tons of waste annually, with a value of around DZD 40 billion, however the recycling rate remains tiny [19]. In this case also, the environment will be conserved by minimizing the waste incineration or depositing on landfills.

To accomplish this study, the work is structured into three chapters, which are organized as follows:

Chapter I:

The first chapter is composed of two main sections, which are:

- (i) General definitions of the main characteristics of packed bed reactor, for single and two phase flow-based processes applications and a general overview about some recent studies on packed bed reactor crossed by a concurrent gas-liquid downward flow, and
- (ii) Background about GTL technology, general overview about recent works on GTL technology, a background about the Fischer-Tropsch synthesis and a general summary of recent studies about modeling and simulation of FTPBR.

Chapter II:

In this chapter the calculation codes using COMSOL Multiphysics 5.6 of both the hydrodynamic model as well as the FTPBR model will be developed. Regarding the hydrodynamic study, the mass and momentum conservation equations in free and porous mediums will be developed. The resulting models are three-dimensional (3D) and two-dimensional (2D) models with a new 2D modeling approach will be proposed. The boundary conditions will be developed and set out. Concerning the FTPBR modeling, a 2D pseudo-homogeneous model, using the Eulerian mixture approach, will be developed. It consists of mass conservation, momentum transfer, heat transfer and concentrated species transport equations in porous media. Next, the boundary conditions and constitutive relationships for the averaged physical properties will be developed and set out. Moreover, the kinetic model of the Fischer-Tropsch reaction will be presented. Finally, for each of the studies a Flow chart of the simulation methodology will be illustrated.

Chapter III:

In this chapter, the obtained results will be presented and discussed. First of all, we will present the results of the hydrodynamic models, which are the 3D resolved particle model, the proposed conceptual 2D resolved particle model and the 2D pseudohomogenous models. Once the 3D model is validated by confronting its simulated results against those of models of literature as well as by a consistent error discretization uncertainty study, it will be used to validate the 2D models. Second of all, the results of the hydrodynamic study will be used to develop the FTPBR model. Once the FTPBR model validated against benchmark models of literature as well as by a consistent error discretization uncertainty study, it will be exploited to simulate two scale-based

multitubular Fischer-Tropsch packed bed reactors; large and small scales. Third of all, a parametric study will be carried out, regarding the bed aspect ratio, to optimize the FT reactor for large scale applications, as well as to optimize and design an FT reactor for small scale mobile FTS plant.

We end the thesis with a general conclusion that summarizes the main results obtained and some prospects of this present work.

CHAPTER I

LITERATURE REVIEW

1.1 Introduction

A typical packed bed reactor (PBR) consists of a cylindrical container that is filled with solid catalyst particles stacked between two parallel fixed sieves. It finds applications in many industrial field areas. While single-phase applications of PBRs are encountered when the reactants and products form one phase, such as synthesis gas production, the two-phase flow applications of PBR come upon if the reactants or products exist in two-phases, such as Low Temperature Fischer-Tropsch Synthesis (LTFTS). The catalytic fixed bed reactors crossed by gas-liquid flow downwards, as depicted in Figure (1.1) are the most utilized in industry [20].

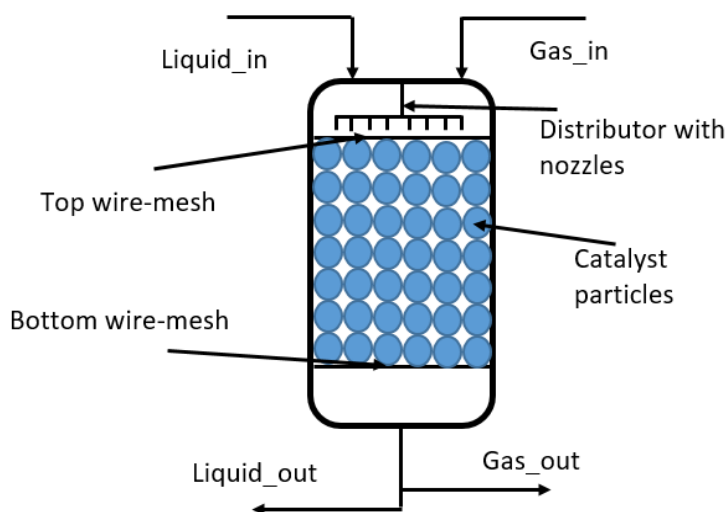


Figure 1.1 : Typical Packed Bed Reactor (PBR) crossed by gas-liquid flow downwards, called Trickle-Bed reactor (TBR)

In fact, TBRs find applications in many domains such as petroleum refining, petro-chemistry, biochemical and environmental engineering, electro-chemistry, fine chemical and pharmaceutical industry [21], [22]. About 1.6 billion tons/year of products processed in TBRs, with a value of 300 billion \$/year [1].

TBRs are more favorable than fluidized or slurry reactors for its advantage in terms of established plug flow regime [1], flexibility and efficiency [23]. Meanwhile, TBRs are inappropriate for reactions with fast catalyst deactivation as well as when liquid

maldistribution conditions are full filled, leading to hot spots formation [1], [24]. Some advantages and disadvantages of TBRs are illustrated in Table (1.1) [25], [26].

Table 1.1 : Some advantages and disadvantages of TBRs

Advantages	Disadvantages
<ul style="list-style-type: none"> • Plug flow behavior 	<ul style="list-style-type: none"> • Large catalyst particles: Low effectiveness
<ul style="list-style-type: none"> • High catalyst to liquid ratio 	<ul style="list-style-type: none"> • Poor heat and mass transfer
<ul style="list-style-type: none"> • Wide output range 	<ul style="list-style-type: none"> • Long catalyst life desired
<ul style="list-style-type: none"> • Low power dissipation 	<ul style="list-style-type: none"> • Inability to handle slurry
<ul style="list-style-type: none"> • Ease of separation catalyst and liquid 	<ul style="list-style-type: none"> • Potential for liquid maldistribution
<ul style="list-style-type: none"> • Flexibility of operation mode 	<ul style="list-style-type: none"> • Potential thermal runaway
<ul style="list-style-type: none"> • Lower capital and operating cost 	

Generally, the reactions implemented in TBRs are exothermic, thus a huge amount of heat is generated leading to the formation of hot spots, if the excess heat will not be carefully managed [27]. Hot spots may cause serious problems such as particles sintering, increasing coke formation, which affects the catalyst activity and its external surface area. This decreases catalyst life time as well as leads to reactor temperature runaway [27]. Using a slender packed bed reactor, with external cooling, is an effective option to facilitate the transfer of reaction heat out of the reactor [28], [29].

Investigations into the hydrodynamic properties of slender packed bed reactors are still required for their optimal design, especially for the pressure drop and flow resistance [30], [31], [32].

One of the most applications of TBRs is the production of synthetic fuels via Fischer-Tropsch reaction that is considered as the main reaction of Gas To Liquid process (GTL).

Fischer-Tropsch is a highly exothermic reaction and implementing this process in slender packed bed reactors will be studied in this thesis.

1.2 Trickle Bed Reactors (TBRs)

The internal structure of the catalyst bed, as well as, the contacting between different phases has significant impact on TBRs hydrodynamics. Pressure drop, liquid

holdup and flow regimes are the main important hydrodynamic parameters. Packing characteristics also affects the residence time distribution, heat and mass transfer rates. Solid catalyst density in TBRs is much higher than in other types of tri-phase reactors. The solid particles are typically porous, with various shapes spanning from spherical to extrudates, cylindrical, tribole and multibole [1], [2]. Evacuation the excess energy liberated by the exothermic reactions occurring in TBRs is a crucial task when designing an optimal process. Catalyst solid Particle equivalent diameter and bed porosity are among the most critical parameters influencing the TBRs performance, since these two parameters substantially affect the hydrodynamics and hence impacting catalyst wetting and heat and mass transfer in the bed [33]. Recent advances in experimental and computational techniques allow us to deeper understand complex phenomenon occurring within TBRs. By way of illustration, magnetic resonance imaging (MRI) and computed tomography (CT) can provide precise information on gas, liquid and solid distribution inside the packed bed. Furthermore, using advanced software, Computational Fluid Dynamics (CFD) is an effective tool to simulate gas-liquid flow through the porous medium under real operating conditions [1], [2].

1.3 PBR types

Four configurations for PBRs, exit as follows [1], [2]:

- i. Conventional PBR: it forms the most common type for conventional chemical reactor engineering technology. It can operate well in low fluid velocity regimes and provides a large surface-to-volume ratio for chemical reactions. Generally, a conventional PBR has a height of about 10 to 30 m, consisting of one section or more; each section is considered as a fixed bed of catalyst particles [1], [26]. It consists of randomly packed catalyst particles, which are supported on an inert material providing a mechanical resistance to crumbling. Moreover, to prevent thermal shocks of particles, their outer layer is impregnated with an active catalytic material. The particles are loaded in between two fixed wire mesh sieve plates. Fluids enter the bed using nozzles to establish uniform flow distribution at the bed inlet. An external jacket can be used to cool down the bed for exothermic reactions (See Figure (1.2a)). The significant drawback of this type is the poor heat transfer.
- ii. Semi-structured PBR: Figure (1.2b) presents this configuration, where the solid particles are loaded non-randomly or catalyst coated on structured packing [like

- SULZER KATA-PACK]. Monolith reactors consisting of large number of interconnected small channels [34]. Monoliths are advantageous geometries for catalyst hosting via immobilization in the form of catalyst particles randomly packed in the channels. This arrangement enhances the heat transfer properties of conventional PBRs [35].
- iii. Micro-PBR: It consists of a number of micro-channels packed with solid particles. This configuration is shown in Figure (1.2c). Its function is similar to conventional PBR, but with a smaller bed and particle sizes. The advantage of this configuration with respect to the first configuration is the enhanced heat and mass transfer coefficient due to the higher surface area-to-volume ratio, as well as the efficient elimination of side reactions [36]. For this reason, it is widely used for highly exothermic reactions such as hydrogenation and oxidation reactions [37]. However, some drawbacks are encountered, namely cleaning, clogging and higher initial investment costs compared to conventional PBRs. Besides, Microchannel flow is primarily laminar, resulting in diffusion-dominated mass transfer from bulk to catalyst surface. Furthermore, it exhibits a low energy efficiency when it uses for photo-catalysis such as water purification or pharmaceutical compounds manufacturing [34]. In this case, the micro-PBR should be replaced by a semi-structured PBR.
- iv. Multitubular Packed Bed Reactor (MTPBR) (Figure (1.2d)): this configuration is usually utilized for PBRs with important heat transfer effects using low aspect-ratio tubes (<10), named slender tubes, filled with solid catalyst particles [38], [39]. Generally, a cooling pressurized boiling water is used to limit the temperature in the multitubular packed bed reactors, and thus to avoid the production of more unwanted methane [40]. Note that, for single tube fixed bed reactor, the cooling medium could be oil. In this case, Flow maldistribution is more remarkable because of the amplifying wall effects. Therefore, a deeper studying of hydrodynamics in this type of PBRs is essential for their design. MTPBRs of bundle of slender tubes are favored for lowering pressure drop and facilitating heat transfer in/out the bed across the tubes wall [41].

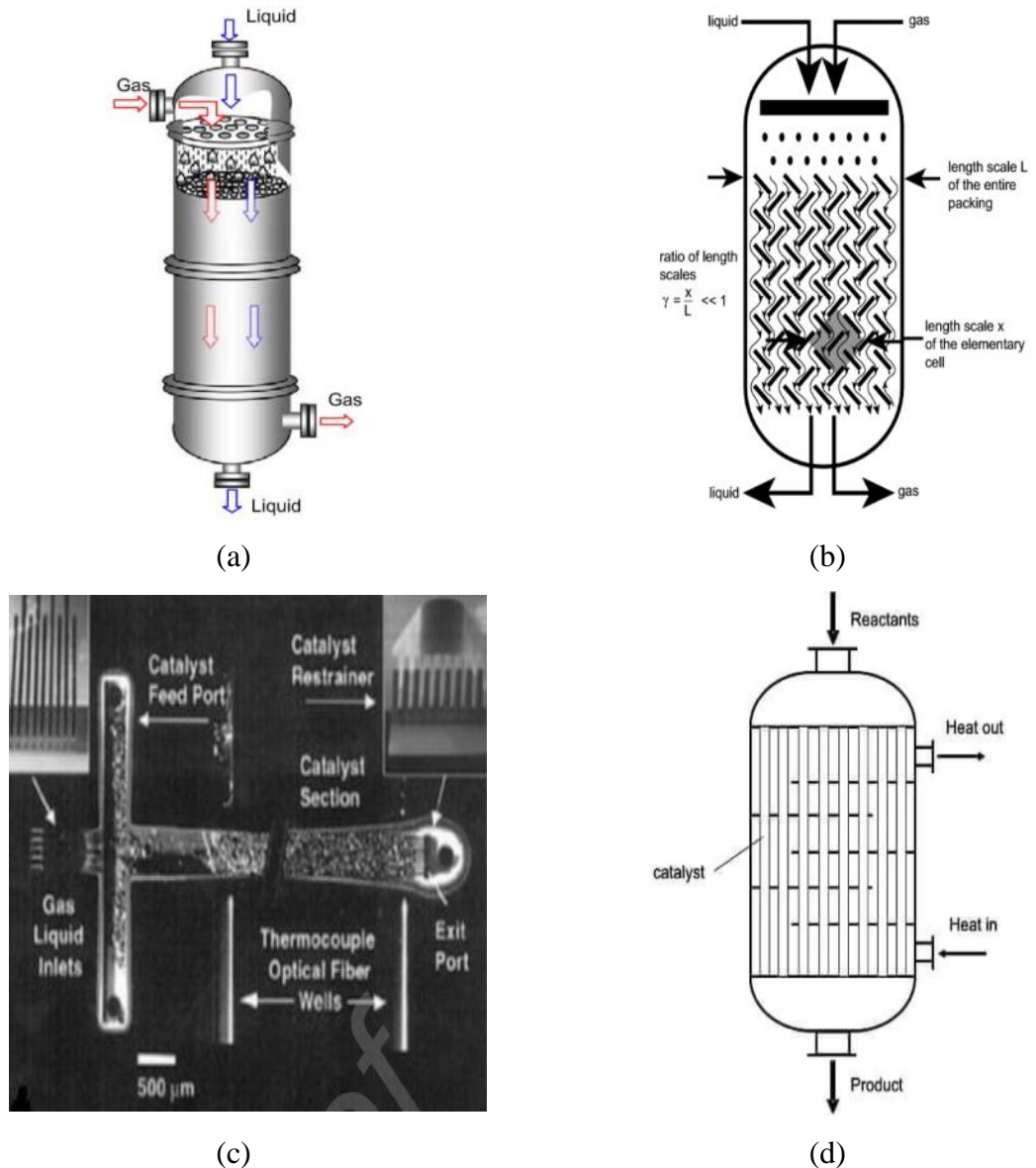


Figure 1.2: PBR types : (a) Tubular PBR, (b) Structured PBR, (c) Micro PBR and (d) Multitubular PBR (MTPBR) : A. Azarpour et al. [1] and V. V. Ranade [2]

1.4 Characterization of packed bed reactors (PBRs)

Before studying the phenomena occurring in a trickle bed reactor, the structural characteristics of packed beds should be known [42]. These are the key geometrical parameters of a PBR that may affect considerably the mass, heat and momentum transfer phenomena and hence the yield [42], [43], [44].

1.4.1 Equivalent particle diameter

The equivalent diameter particle, having a symbol 'd_p', is a length characteristics of a solid catalyst particle. It represents the diameter of an equal-specific surface hypothetical-sphere, that is [45]:

$$d_p = 6 \frac{V_p}{S_p} \quad (1.1)$$

Where S_p and V_p are the area and the volume of the solid catalyst particles. Here, the actual particle is matched with an imaginary sphere having the same specific area ($\frac{S_p}{V_p}$). The equivalent particle diameter is an important parameter for studying hydrodynamics, heat and mass transfer phenomenon in packed beds [46]

1.4.2 Solid particle sphericity (or shape factor)

It is an important geometrical characteristic of solid particles used in a packed bed and it measures how spherical a solid particle is [43], [47]. It is defined as the ratio of the surface area of an equal-volume hypothetical sphere, with a diameter (d_{sph}), to the surface area of the actual catalyst particle, that is

$$\phi_s = \frac{d_p}{d_{sph}} = \frac{6}{\frac{d_{sph}}{S_p}} \quad (1.2)$$

$$d_{sph} = \left(\frac{6V_p}{\pi} \right)^{\frac{1}{3}} \quad (1.3)$$

Sphericities of some known specific materials are presented in Table (1.2).

Table 1.2: Sphericities of some materials with different shapes [47].

Material	ϕ_s
Crushed coal	0.75
Crushed sandstone	0.8-0.9
Round sand	0.92-0.98
Crushed glass	0.65
Mica flakes	0.28
Sillimanite	0.75
Common salt	0.84

1.4.3 Porosity

The porosity describes the fraction of vacant space in a material domain, which can include any fluid such as air or water [47]. It represents the most pertinent property of the porous structure of the PBR [48]. It was distinguished between two independent porosities, in the literature, depending on the considered scale; at a single particle scale or at the bed scale as shown in Figure (1.3) [49].

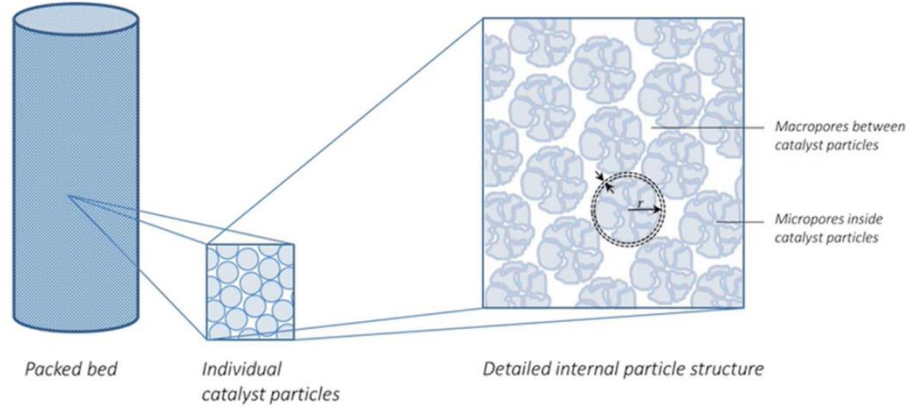


Figure 1.3: Porosities at different scales: S. Sabet [49]

In a packed bed reactor, the particles do not fill the bed volume, so that, the fraction of volume that is not occupied by solid particles is called the mean void volume fraction and is depicted as:

$$\varepsilon = \frac{V_B - V_S}{V_B} \quad (1.4)$$

Here, ε is the average bed porosity or the interparticle porosity, V_B is the total bed volume and V_S is the solid catalyst volume.

Now let us zoom in on one particle and it can be seen that, the particle is full of pores. The ratio of porous volume to a specified particle volume is called the particle porosity, the pore porosity or the intraparticle porosity and it written as:

$$\varepsilon_P = \frac{V_P}{V_S} \quad (1.5)$$

Here, V_P is the total pore volume within a porous particle filled with a stagnant mobile phase.

The sum of these two independent porosities defined in equations (1.4) and (1.5), give a rise to the total porosity within the bed, given as [25]:

$$\varepsilon_{TOT} = \frac{V_P + V_B - V_S}{V_B} = \varepsilon + \varepsilon_P(1 - \varepsilon) \quad (1.6)$$

The mean bed porosity can be determined experimentally [50] or predicted using empirical correlations or analytical equations [51]. Three experimental techniques have been applied to determine the bed porosity, which are [48], [52]:

- Direct measurements that use a destructive approach;
- Direct measurements, which employ a non-destructive approach;
- Imaging techniques, such as X-ray radiography, X-ray computed tomography, gamma ray computed tomography and magnetic resonance imaging (MRI) for beds packed with metallic particles [53].

Some correlations for predicting the bulk or overall porosity of randomly packed beds are presented in Table (1.3).

Table 1.3: Some significant empirical correlations for bulk porosity calculation

Model by	Equation	Ref.
Benyahia and O'Neill (2005)	$\varepsilon_b = 0.1504 + \frac{0.2024}{\phi_s} + \frac{1.0184}{\left[\frac{D}{(d_p+0.1226)}\right]^2}$	[43]
De Klerk (2003)	$\varepsilon_b = \varepsilon_\infty + 0.35e^{-0.39\left(\frac{D}{d}\right)}, \quad \varepsilon_\infty = 0.375 - 0.391$	[54], [55]
Mueller (2019)	$\varepsilon_b = \varepsilon_\infty + 0.225\left(\frac{d}{D}\right), \quad \varepsilon_\infty = 0.369$	[55]

In fact the bed porosity varies in the axial and the radial directions [48], [52], [56] as presented by Figure (1.5). Generally, the radial porosity profiles are considered for the hydrodynamic studies of PBRs [52], [56]

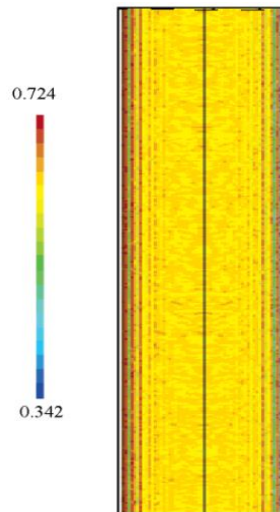


Figure 1.4: Radial and axial porosity distribution within a PBR: P. R. Gunjal [57]

Several correlations of axially averaged radial porosity profile exist in the literature. Common correlations are summarized in Table (1.4).

Table 1.4: Some known axially averaged porosity correlations

Model by	Equation	Bed to particle diameter ratio $\frac{D}{d_p}$	Ref.
Martin (1978)	$\varepsilon(x) = \varepsilon_{\min} + (1 + \varepsilon_{\min})x^2, -1 \leq x \leq 0$ $\varepsilon(x) = \varepsilon_{\infty} + (\varepsilon_{\min} - \varepsilon_{\infty})e^{-\frac{x}{4}}\cos\left(\frac{\pi x}{y}\right), x > 0$ $x = 2\frac{R-r}{d} - 1, \varepsilon_{\min} = 0.23, \varepsilon_{\infty} = 0.39$	$y=0.816, \frac{D}{d_p} = 20.3$	[54], [55]
Cohen and Metzner (1981)	$\frac{1-\varepsilon(z)}{1-\varepsilon_{\infty}} = 4.5\left(z - \frac{7}{9}z^2\right), z \leq 0.25$ $\frac{\varepsilon(z)-\varepsilon_{\infty}}{1-\varepsilon_{\infty}} = a_1 e^{a_2 z} \cos(a_3 z - a_4)\pi, 0.25 \leq z \leq 8$ $\varepsilon(z) = \varepsilon_{\infty}, 8 \leq z \leq \infty$ $z = \frac{R-r}{d}, a_1 = 0.3436, a_2 = 0.4273, a_3 = 2.4509, a_4 = 2.2011$	$\frac{D}{d_p} = \infty$	[54], [55]
De Klerk (2003)	$\varepsilon(z) = 2.14z^2 - 2.53z + 1, z \leq 0.637$ $\varepsilon(z) = \varepsilon_{\infty} + 0.29e^{-0.6z} \cos(2.3\pi(z - 0.16)) + 0.15e^{-0.9z}, z > 0.637$ $z = \frac{R-r}{d}$	$\frac{D}{d_p} > 2$	[54], [55]
Mueller (2019)	$\varepsilon(r) = \varepsilon_b + (1 - \varepsilon_b)J_0(ar^*)e^{-br^*},$ $a = 7.45 - \frac{3.15}{\frac{D}{d}}, 2.02 \leq D/d \leq 13.0,$ $a = 7.45 - \frac{11.25}{\frac{D}{d}}, 13.0 \leq D/d,$ $b = 0.315 - \frac{0.735}{\frac{D}{d}}, r^* = \frac{r}{d} \left[1.3 \frac{r}{d} + \left(1.6 + \left(\frac{2.6}{\frac{D}{d}} \right)^{-1} \right) \right] \text{ if}$ $\frac{r}{d} < \frac{1}{1.3} \left[1 - \left(1.6 + \frac{2.6}{\frac{D}{d}} \right)^{-1} \right], \text{ else } r^* = \frac{r}{d},$ $\varepsilon_b = \varepsilon_{\infty} + \frac{0.225}{\frac{D}{d}}, \varepsilon_{\infty} = 0.369$	$2.02 \leq D/d$	[55]

1.4.4 Investigations on the structure of packed beds

Typically, there are two ways to study and to rebuild the 3D pore structure which are (i) experimental techniques (i.e., magnetic resonance imaging and X-ray computational tomography imaging) and (ii) numerical methods [31]. While, the former is quite complex and costly, the latter can provide a deeper insight on the bed's structure as well as provide a random distribution of the particles [42]. In recent years, several numerical approaches

have come on stream, to reproduce the packed bed textual structure such as the rigid body (in the open-source software Blender) [58], [59], Monte Carlo, optimization, packing algorithms and the Discrete Element Methods (DEM) [48], [60]. DEM method, by applying fluid mechanics laws on a single particle in motion, is the most promising, in terms of attaining high accuracy level and low numerical cost. EDEM 2.5.1 [61], STAR-CCM+ [59], which represent some commercial softwares, and icoUncoupledKinematicParcelFoam [62], representing an open source CFD software, have been used to rebuilt the packed bed internal structure based on the DEM. The porosity of the DEM generated packed bed can be achieved via three methods as follows [48]:

1. The gradually injected random packing method: the hypothetical spherical-particles are injected from the bed's top, at a well-defined rate. Under the effect of gravity, the particles fall and pile-up to form the bed.
2. The force fitted method: the imaginary spheres are generated at the bed's bottom and then the following spheres are forced upwards to form the bed.
3. The bulk drop method: a cluster of conceptual particles is formed on the top of the bed and then the particles drop simultaneously producing the bed.

1.5 Hydrodynamic of TBRs

Hydrodynamics, transfer phenomena and reaction kinetics are strongly coupled which complicates the design and the study of TBRs performance [1], [63]. Hydrodynamics play a crucial role in the design, operation and scale-up of TBRs. Special attention has been dedicated to the hydrodynamics of TBRs [27], [64], [65], [66], [67]. According to several experimental and theoretical studies, it has been identified that, not only the bed textual characteristics, such as bed porosity, affect the TBR behavior. But also pressure drop, liquid holdup and distribution, wetting efficiency and flow regime transition have a considerable influence on the TBR performance and they represent the key hydrodynamic parameters for TBRs design [1], [25], [63], [68]. These hydrodynamic parameters are often determined from cold flow experimental studies on laboratory-scale TBRs using air-water systems. In this section, we are addressing some comprehensive information about available models for the estimation of these parameters required for the design of TBRs. However, a prior step is to provide an insight about single-phase flow in packed bed reactors (PBRs). Hydrodynamics in PBRs crossed with single-phase flow, is

not only needed for single-phase flow applications, but also serves as the foundation for analyzing two-phase flow in PBRs [1], [69], [70].

1.5.1 Single-phase flow in PBRs

It is important to understand the fundamental of single-phase flow in packed beds before discussing two-phase flow. Packed bed reactor crossed by a single phase flow are widely used in various industries, such as distillation, adsorption, catalytic reactions (like steam and dry reforming of methane [28]) and scrubbing [28], [71]. Single-phase flow in a PBR involves a complex pattern of flowing fluid phase in the vacant space of the bed, through channels or pores of various sizes and shapes. Forces acting on a packed bed are fluid drag, gravitational and buoyancy forces, so that, each solid catalyst particle tends to remain at its position inside the packed bed. The resultant of all these forces causes mechanical energy dissipation along the packed bed, leading to pressure drop of the fluid phase within the bed.

Pressure drop is the most important hydrodynamic parameter for the design a packed bed system. Pressure drop across a packed bed can be determined via three ways. Firstly, it can be determined experimentally on the real system, which is too costly task regarding time and money. Secondly, using some correlations from the literature, which were developed mechanistically such as the porosity-permeability-based expression of Kozeny-Carman [72], [73], or empirically such as the well know Ergun equation [74]. The third approach is numerical, such as the particle resolved or the pseudo-homogenous simulations [30], [42]. Flow regimes in packed bed reactors crossed by a single-phase flow differ from free flows, because of the existence of packed solids obstacle. In this case the modified Reynolds number (or the particle Reynolds number) will be used, which is defined as [75]

$$\text{Re}_p = \frac{\rho d_p U}{\mu \epsilon} \quad (1.7)$$

Here, ρ [$\text{kg} \cdot \text{m}^{-3}$], μ [$\text{Pa} \cdot \text{s}$] and U [$\text{m} \cdot \text{s}^{-1}$] are the fluid density, dynamic viscosity and superficial velocity. It is noteworthy that, the modified Reynolds number differs from the free flow (or the original) Reynolds number. The original Reynolds number is the most important dimensionless number in CFD, defined as the ration between convective and diffusion transport, written as:

$$\text{Re} = \frac{\rho d_p U}{\mu} \quad (1.8)$$

Four distinct flow regimes regions appear in packed beds, according the modified particle Reynolds number value [33], [76]. These flow regimes span from creeping flow ($Re_p < 1$), to steady laminar ($1 - 10 < Re_p < 150$), unsteady laminar ($150 < Re_p < 300$) and turbulent ($Re_p > 300$). Nevertheless, other studies stated that, the turbulent flow regime appears at $Re_p > 900$ [33], [69].

❖ Single-phase flow pressure drop in infinite diameter packed bed

Pressure is an intensive physical quantity, on which gas and liquid physiochemical properties depends. Therefore, it considerably influences the heat and mass transfer rates within the packed bed. Furthermore, pressure variation strongly affects fluids density, thermal conductivity, dynamic viscosity, heat capacity, surface tension and Henry's constant [1], [54], which impacts the gas solubility in the liquid phase [1], [77]. Mechanical energy dissipation, due to one or two-phase flow crossing an array of fixed solid particles causes pressure to decrease (or to drop) along the bed [1], [70], [78], [79], and from this the term pressure drop was derived. An appropriate pressure drop model is crucial for accurate design of a PBR. Several correlations for single pressure drop prediction in packed beds with a high tube to particle diameter ratio (> 10) exist in literature [80] (see Table 1.5). The Ergun equation, obtained from substantial experimental data, shows the pressure drop along the bed as a function of numerous factors [74]. It is considered a benchmark, as proved by the following equation [80], [81]:

$$\frac{\Delta P}{L} = E_1 \mu \frac{(1 - \varepsilon)^2 U}{\varepsilon^3 d_p} + E_2 \rho \frac{(1 - \varepsilon) U^2}{\varepsilon^3 d_p} \quad (1.9)$$

Here, $\frac{\Delta P}{L}$ [Pa. m⁻¹] is the pressure drop per unit length of the bed and the parameters E_1 [-] and E_2 [-] are the Ergun's constants which their values are 150 and 1.75, respectively [74]. The general form of Ergun equation can be transformed into dimensionless form, as shown in Equation (1.10), by introducing the concept of the modified friction factor, which is expressed as a set of parameters as depicted by Equation (1.11) [31], [81].

$$f^* = \frac{150}{Re_p} + 1.75 \quad (1.10)$$

$$f^* = \frac{\Delta P}{L} \frac{d_p \varepsilon^3}{\rho U^2 (1 - \varepsilon)} \quad (1.11)$$

Table (1.5) summarizes some known friction factor correlations in infinite PBRs.

Table 1.5: Some known friction factor correlations in infinite PBRs

Model by	Correlation	Range	Ref.
Ergun (1952)	$f^* = \frac{150}{Re_p} + 1.75$	$1 \leq Re_p \leq 10^4$	[41], [76], [80], [81]
K. Allen (2013)	$f^* = \frac{129}{\left(\frac{2}{3}\right)Re_p} + \frac{3.27}{\left(\left(\frac{2}{3}\right)Re_p\right)^{0.12}}$	-	[81]
Reger (2023)	$f^* = \frac{160}{Re_p} + \frac{3f(\varepsilon)}{Re_p^{0.1}}$ $f(\varepsilon) = 253.9\varepsilon^4 - 499.3\varepsilon^3 + 264.7\varepsilon^2 - 115.6\varepsilon + 14.21$	$625 < Re_p < 10^4$	[81], [82]

Analyzing these correlations, it can be drawn that, particle equivalent diameter, superficial velocity, operating fluid properties and bed porosity considerably impact pressure drop in PBRs. For instance, Ergun equation (1.1) is the most widely used correlation for infinite beds (high aspect ratio PBR). It is worthy to note that, the above correlations constitute a sample of single-phase pressure drop models that are required to model two-phase flow and to predict two-phase flow pressure drop through packed bed reactors.

❖ Single-phase flow pressure drop in slender packed bed: Effect of reactor diameter

Actually, pressure drop across a packed bed not only depends on the above motioned parameters, but also on the bed diameter which appears to have a significant impact for slender cylindrical beds having a low aspect ratio (tube to particle diameter lesser than 10) [41]. Highly exothermic or endothermic reactions should be carried within slender PBRs, to facilitate the heat transfer in/out the bed across the wall. Besides, Rapid heat removal through coolant requires higher fluid velocity, which might increase the power needed for circulating the coolant fluid and may cause mechanical damage for the TBR internals along with the accelerated erosion phenomena [41], [83]. Table (1.6) summarizes some common friction factor correlations of single-phase flow in slender PBRs.

Table 1.6: Some common friction factor correlations of single-phase flow in slender PBRs

Model by	Correlation	Ranges	Ref.
Foumeny et al. (1993)	$f^* = \frac{130}{Re_P} + \frac{1}{0.335 + 2.28\left(\frac{d_P}{D}\right)}$	$5 \leq Re_P \leq 8.5 \times 10^3$ $3 < \frac{D}{d_P} < 25$	[41]
Eisfeld and Schnitzlein (2001)	$f^* = \frac{154A_w^2}{Re_P} + \frac{A_w}{B_w}$ $A_w = 1 + \frac{4d_P}{6(1-\varepsilon)D}$ $B_w = \left(1.15\left(\frac{d_P}{D}\right)^2 + 0.87\right)^2$	$0.02 < Re_P < 7 \times 10^4$ $\frac{D}{d_P} < 55$	[41], [76]
Cheng (2011)	$f^* = \frac{A_w}{Re_P} + B_w$ $A_w = 185 + 17\frac{\varepsilon}{1-\varepsilon}\left(\frac{D}{D-d_P}\right)^2$ $B_w = 1.3\left(\frac{\varepsilon}{1-\varepsilon}\right)^{\frac{1}{3}} + 0.03\left(\frac{D}{D-d_P}\right)^2$	$1.1 < \frac{D}{d_P} < 50.5$	[41]

1.5.2 Two-phase flow in PBRs

The interfacial interaction between the gas and the liquid phases makes the hydrodynamics of TBRs quite complex, resulting in highly non-linear mathematical model [27], [84]. The key hydrodynamic parameters of two-phase flow across a PBR are discussed hereinafter.

❖ Flow regimes

Flow regimes in a TBR influence considerably other hydrodynamic phenomenon such as pressure drop and liquid holdup. Therefore, determining what flow regime a TBR is operating in, is the first hydrodynamic task to be solved before finding out other hydrodynamic parameters [1].

Several works exist in literature concerning the characterization of the flow regimes in TBRs. Initially, it was explored, experimentally, by MCILvried (1956) and Larkins (1959) [1], [85]. Regarding the interaction intensity, the flow regimes are classified into two categories; the Low Interaction Regime (LIR), represented by the trickle flow and the High Interaction Regimes (HIR), manifested in bubble, pulse, spray and dispersed flows, as depicted in Figure (1.5).

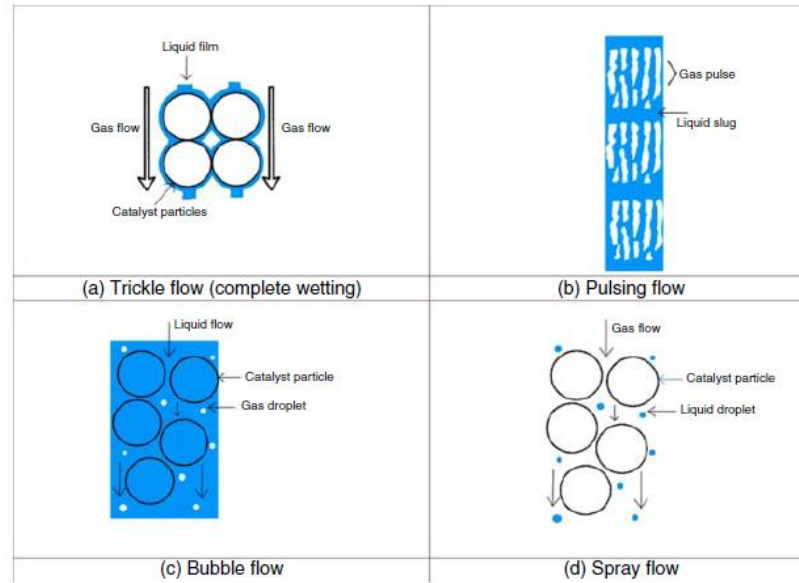


Figure 1.5: Flow regimes of concurrent two-phase flow downward in PBR V. V. Ranade and R. P. Utikar [86]

For low flow rates of the fluids, the LIR is appeared, while for the higher flow rates the HIR is achieved. The LIR is characterized by a sharp interfacial area between the gas and the liquid phases. The HIR is occurred because of the high gas-liquid shear stress, which leads to formation of several flow regimes as shown in Figure 1.5. Bubble flow regime is formed at high liquid flow rates and low gas flow rates; the continuous liquid phase contains small bubbles. Increasing the gas velocity leads to the coalescence of the gas bubbles resulting in the dispersed bubble flow. Again, rising up simultaneously the gas and liquid velocities, the pulsing regime occurs which is characterized by an alternating flow of continuous gas plugs and continuous liquid slugs. Maintaining lower liquid flow rates and increasing gas flow rates results in the spray flow regime. Overall, the trickling and pulsing them are the most encountered at the industrial scale [1], [63]. To cite an instance, hydrogenation reactor operates under trickling flow regime conditions and hydrotreating TBRs prefer pulsing flow regime for which heat and mass transfer phenomenon are highly heightened. At this circumstance, cyclical crossing of rich-liquid waves occurs, promoting uniform liquid distribution [63]. Furthermore, trickling-to-pulsing flow transition is of great interest in industry since operating near this limit, the gas-liquid mass transfer rate will be enhanced [2], [86].

❖ Two-phase flow pressure drop

Pressure drop is an important hydrodynamic parameter when designing a TBR. It is not only needed for calculating energy consumption for gas compression and liquid pumping, but it is also related to other parameters such as liquid holdup and interfacial mass transfer phenomenon [25], [87]. Additionally, the reliability of the applied pressure drop correlation determines the validity of pseudo-homogeneous models for complex flows in TBRs as well as the accurate prediction of the average behavior of the entire bed [1], [33], [69], [88]. Two-phase pressure drop has a strong link to single phase pressure drop, which in turn depends on operating conditions, fluid properties and bed characteristics. For instance, it increases with the decrease in particles diameter. It may be also affected by bed diameter for low aspect ratio packed bed for which the ratio column to particle diameter is lower than a certain limit value. In the literature, different limit values were reported. For example, Winterberg [89] concluded in his work that, above tube to particle diameter ratio of 10, the column wall does not affect pressure drop. Others mentioned that, this value is twofold [25], [68]. Other important parameters may affect considerably two-phase pressure drop are flow regimes, liquid holdup and distribution and bed wettability. This is due the additional resistance to flow caused by the existence of the second fluid and interfacial interaction between the gas, the liquid and the solid phases. Furthermore, it has been recognized that, hysteresis phenomena, which is attributed to the pre-wetting history of the bed, plays a crucial role in determining two-phase pressure drop [90], [91] (See Figure (1.6)).

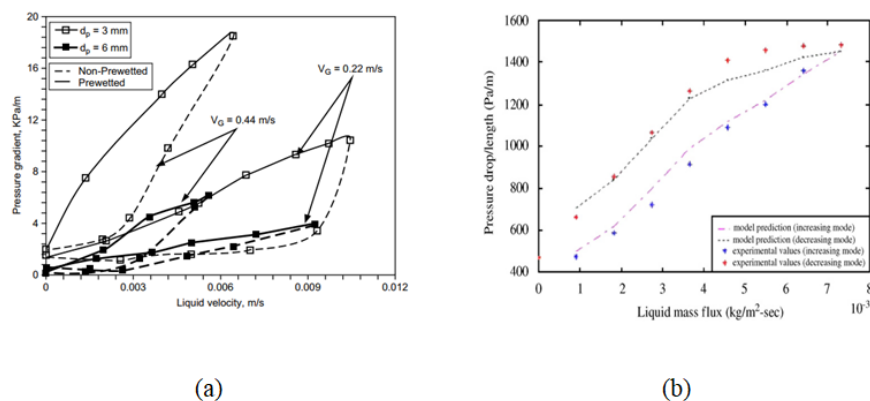


Figure 1.6: Effect of Hysteresis phenomena on two-phase pressure drop (a) from V. V. Ranade et al. [2] and (b) from A. K. Saroha and I. Nandi [90]

This effect can be eliminated by prewetting the bed totally before starting operation on TBR. However, reaching a well determined operating point is required; otherwise even

when working with a prewetted bed, pressure drop can have multiple values at identical operating conditions [92]. Studies reported that, operating pressure should be greater than 0.1 atm/m [25]. Working under higher pressure drop values minimizes liquid maldistribution and homogenizes the catalyst wetting. Therefore, one should carefully choose the range of operating velocities for both the gas and the liquid phases.

As it was said in the prior section, single-phase pressure drop models are the starting point in two-phase pressure drop evaluation. The most often used model is the Ergun equation (Equation (1.9)). Several models exist in the literature for estimating two-phase pressure drop. One interesting model is that, the two-phase pressure drop correlation using the Lockhart-Martinelli number defined as [25], [93], [94]:

$$X_L = \frac{1}{X_G} = \frac{U_L}{U_G} \sqrt{\frac{\rho_L}{\rho_G}} \quad (1.12)$$

Many authors used this number jointly with other dimensionless numbers such as the Reynolds and Weber numbers. For instance, the Equation (1.13) was proposed by [95]:

$$\frac{\Delta P}{L} = \frac{2\rho_G U_G^2 [A(X_G \xi_1)^j + A(X_G \xi_1)^k]}{d_p} \quad (1.13)$$

Where ξ_1 , A, B, j and k are the model parameters which depend on the flow regimes under consideration.

Phenomenological models represent an interesting method for predicting two-phase pressure drop. As far as I have known during this research, three basic phenomenological approaches have been existed in the literature. These include (i) the relative permeability, (ii) the slit and (iii) the two-fluid interaction models. All of these models, which are based on the Ergun equation [66], will be described in the following sections.

(i) Relative permeability models

In this approach the original Ergun equation is modified to Equation (1.14), by introducing a term called phase relative permeability which accounts for the presence of the second phase [96].

$$\frac{\Delta P_\alpha}{L} = \frac{1}{K_\alpha} \left[E_1 \mu \frac{(1-\varepsilon)^2}{\varepsilon^3} \frac{U_\alpha}{d_p} + E_2 \rho \frac{(1-\varepsilon)}{\varepsilon^3} \frac{U_\alpha^2}{d_p} \right] \quad \alpha = g, l \quad (1.14)$$

While the relative permeability of the gas phase is a function of gas saturation, the relative permeability of the liquid phase is a function of the reduced liquid saturation, as shown in Table (1.7) [25], [96].

Table 1.7: Relative Permeabilities correlations

Gas phase relative permeability	Liquid phase relative permeability	Ref.
$S_g^{4.8}$	$\delta_1^{2.43}$	[85]
$S_g^{\chi+0.0478\text{Re}_G^{0.774}}$, The constant χ depends on the particle shape	$\delta_1^{2.49}$, $\delta_1 \geq 0.3$ $0.4\delta_1^{2.1}$, $\delta_1 < 0.3$	[97]
$0.4S_g^{3.5}$, $S_g < 0.64$ $0.4S_g^{5.8}$, $S_g \geq 0.64$	$\delta_1^{2.29}$, Film flow δ_1^2 , Rivulet flow	[98]

The phase saturation and reduced liquid saturation will be defined in the subsequent sections.

(ii) Slit models

The original silt model, which is a phenomenological model, was first proposed by Holub [99], [100] based on modifying the Ergun equation to Equation (1.15), using a conceptual geometrical representation, as shown in Figure (1.7a).

$$\frac{\Delta P_\alpha}{L} = \left(\frac{\varepsilon}{\varepsilon_\alpha}\right)^3 \left[E_1 \mu \frac{(1-\varepsilon)^2 U}{\varepsilon^3 d_p} + E_2 \rho \frac{(1-\varepsilon) U^2}{\varepsilon^3 d_p} \right] \rho_\alpha g \quad (1.15)$$

The slit approach approximates the actual bed geometry at the pore level by a single flat-walled slit with the characteristics lengths as shown in Figure (1.7a). In the figure the symbol ‘**T**’ is the tortuosity factor, which is the ratio of the effective length to the bed height defined as [72]:

$$\mathbf{T} = \frac{L_{\text{eff}}}{L} \quad (1.16)$$

The drawback of this original silt model is that, it is just applicable in trickle flow regime for low operating pressure and no interaction between the flowing phases as well as for a complete wetting of the solid particles. Few years later, the Holub’s model was extended by considering the gas-liquid interfacial velocity and shear slip factors, which account for the gas-liquid interfacial interactions under high-pressure operating conditions [101], [102].

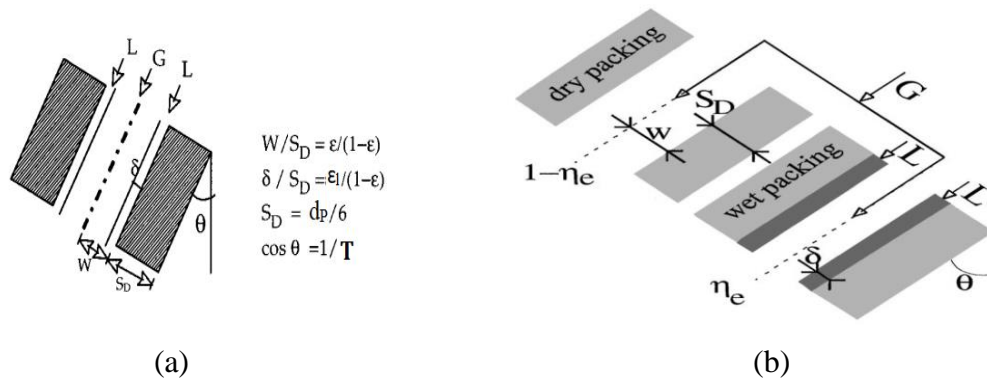


Figure 1.7: Slit approach: (a) Single slit M. H. Al-Dahhan et al [102], (b) Double slit I. Iliuta et al [103] and I. Iliuta and F. Larachi [104]

To take into consideration the partial wetting of the bed, a generalized double-slit model, as depicted in Figure (1.7b), was proposed by Iliuta et al. [103], [104], [105] which also takes into account the gas-liquid interfacial shear.

(iii) Two-fluid interaction models

The two-fluid interaction modeling approach was first introduced by Attou et al. [106]. The idea was based on applying a force balance at the particle scale, as shown in Figure (1.8).

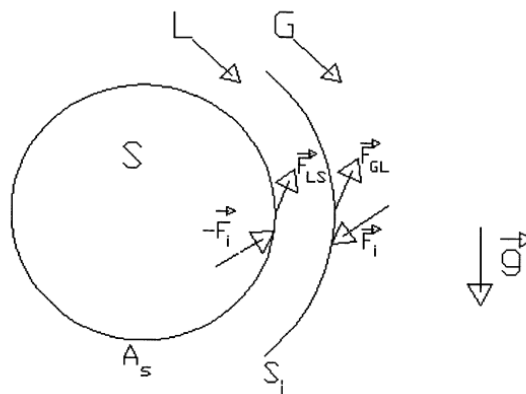


Figure 1.8: Interaction forces at the particle scale according to Attou et al. [106]

This led to deduce the force resultant applied on each phase by the other phases. Then, the Ergun equation was modified by introducing an effective particle diameter, an effective porosity and a two-phase flow tortuosity factor to account for the presence of one flowing phase with respect to the second flowing phase.

The final pressure drop model can be represented by the following equations set:

$$\text{Liquid phase pressure drop} \quad \frac{\Delta P_l}{L} = f_{gl} - f_{ls} \quad (1.17)$$

$$\text{Gas phase pressure drop} \quad \frac{\Delta P_g}{L} = -(f_{gl} + f_i) \quad (1.18)$$

$$\text{Liquid-solid drag force} \quad f_{ls} = S_l (A_{ls} \mu_l U_l + B_{ls} \rho_l U_l^2) \theta_1(S_l) \quad (1.19)$$

$$\text{Gas-liquid drag force} \quad f_{gl} = (1 - S_l) (A_{gl} \mu_g U_r + B_{gl} \rho_g U_r^2) \quad (1.20)$$

$$\text{Relative velocity} \quad U_r = U_g - \left(\frac{1-S_l}{S_l} \right) U_g \quad (1.21)$$

$$\text{The gas-solid drag force} \quad f_i = (1 - S_l) (A_{gl} \mu_g U_g + B_{gl} \rho_g U_g^2) \quad (1.22)$$

Here, $\theta_1(S_l)$ is the two-phase flow tortuosity factor, which was supposed to be inversely proportional to the liquid phase saturation, given as:

$$\theta_1(S_l) = \frac{1}{S_l} \quad (1.23)$$

The momentum transfer coefficients are given as follows:

$$A_{ls} = 180 \frac{(1-\varepsilon)^2}{S_l^3 \varepsilon^3 d_p^2} \quad (1.24)$$

$$B_{ls} = 1.8 \frac{1-\varepsilon}{S_l^3 \varepsilon^3 d_p} \quad (1.25)$$

$$A_{gl} = 180 \frac{(1-(1-S_l)\varepsilon)^2}{S_l^3 \varepsilon^3 d_p^2} \left(\frac{1-\varepsilon}{1-(1-S_l)\varepsilon} \right)^{\frac{2}{3}} \quad (1.26)$$

$$B_{gl} = 1.8 \frac{(1-(1-S_l)\varepsilon)}{S_l^3 \varepsilon^3 d_p} \left(\frac{1-\varepsilon}{1-(1-S_l)\varepsilon} \right)^{\frac{1}{3}} \quad (1.27)$$

In 2007, a modification was introduced by Boyer et al. [107] on the original model of Attou et al. by considering a new formulation of the two-phase flow tortuosity factor which was as follows:

$$\theta_1(S_l) = \frac{1}{S_l^n} \quad (1.28)$$

The exponent n takes the value of -0.54 for aqueous fluids and -0.02 for organic fluids.

The above equations can also serve as closures of the momentum balance equations when modeling multiphase flows in packed bed reactors, using the pseudo-homogeneous approach. In some cases, the assumption of zeroth drift velocity between the gas and the liquid can be hold, mainly for extremely dispersed flows [86]. In this case, the gas and the liquid phases are supposed to flow at the same velocities. Therefore, one can apply the mixture Eulerian model, which is one of the Euler-Euler modeling approach, by using the

mixture properties in terms of density and dynamic viscosity as well as mass-averaged velocity [108].

❖ **Liquid saturation or holdup**

A key hydrodynamic parameter is the fraction of the void (or the bed) volume occupied by the liquid phase. It is called liquid saturation if the reference volume is the void volume and the liquid holdup if the reference volume is the bed volume [109]. They are linked together using the bed porosity as follows:

$$S_l = \frac{\varepsilon_l}{\varepsilon} \quad (1.29)$$

The liquid holdup is the sum of the external and the internal liquid holdups, written as:

$$\varepsilon_l = \varepsilon_l^{\text{ext}} + \varepsilon_l^{\text{int}} \quad (1.30)$$

In turn, the external liquid holdup is divided into static and dynamic liquid holdups. It represents the amount of the liquid drained from the bed by gravity after stopping the gas and the liquid inflows. While the dynamic liquid holdup is the moving or the flowing fraction of the liquid phase within the bed, the static liquid holdup represents the ratio of the stagnant liquid volume between the solid particles to the total volume of liquid recovered after the full draining of the bed. It is given by the well know formula of Carbonell [85] given as:

$$\text{Static liquid holdup} \quad \varepsilon_l^0 = \frac{1}{20 + 0.9Eo} \quad (1.31)$$

$$\text{Eötvos number} \quad Eo = \frac{\rho_l g d_p^2 \varepsilon^2}{\sigma(1 - \varepsilon)^2} \quad (1.32)$$

The Eötvos number is a measure of the importance of gravitational forces compared to surface tension forces. The static liquid holdup is a function of liquid physical properties, particle shape, size, and wettability [25].

The knowledge of liquid saturation or holdup is important in assessing [25]:

- The two-phase pressure drop,
- The liquid residence time,
- The external wetting efficiency,
- Average liquid film thickness and
- Mass transfer rates

Under the LIR, the liquid holdup is related to the inlet velocity and the physical properties of the liquid phase, packing bed characteristics and wettability. Under the HIR, the gas velocity, density and the operating pressure also affect the liquid holdup. Without forgetting the effect of the liquid surface tension, which appears to be dominant in the case of particle with a diameter below 1 mm, because the capillary forces become stronger. Regarding the bed aspect ratio, for a given particle size, the liquid holdup increases with the increase in the bed diameter [25].

The dynamic liquid holdup models are divided into two types; empirical and phenomenological models [110]. Some recent correlations of the liquid holdup are summarized in Table (1.8)

Table 1.8: Some recent models of dynamic liquid holdup

Model	Ref.
$\varepsilon_l = 0.002 \left(\frac{D}{d_p}\right)^{1.28} Re_l^{0.38}$	[111]
$\varepsilon_l = 0.1367 Re_{p,l}^{0.27946} Re_g^{-0.03643} \left(1 + \frac{\Delta P/L}{\rho_l g}\right)^{-0.44184} We_l^{0.25458}$ $We_l = \frac{\rho_l d_p U^2}{\sigma_l}$	[63]
$\varepsilon_l = 0.07 + (HB)^{0.17} \exp(HB)$ $HB = \frac{(We)^{0.5}}{X_L} \left(\frac{\varepsilon^3}{1-\varepsilon}\right)^{3.5} \left(\frac{Re_l}{Re_g}\right)^2$ $X_L = \frac{U_l \rho_l^{0.5}}{U_g \rho_g^{0.5}}, \text{ Ratio of liquid to gas inertial forces.}$	[112]

The correlations of liquid holdup are generally expressed in terms of dimensionless numbers such as the Reynolds number and the Weber number, which represents the ratio of the liquid inertial to the liquid surface tension forces [25].

Recently Qi et al. [113] developed a hybrid pressure drop and liquid holdup phenomenological model to predict simultaneously, with high quality, the liquid holdup and pressure drop within TBRs.

Liquid holdup, like pressure drop, exhibits hysteresis as the gas and liquid flow rates vary, as shown in Figure (1.9). The magnitude of hysteresis is determined by the extent to which the bed has been pre-wetted. The greatest extent of hysteresis occurs when the bed is completely dry [25]. It has been outlined that, the increase in the gas flow rate can reduce the hysteresis trend [114].

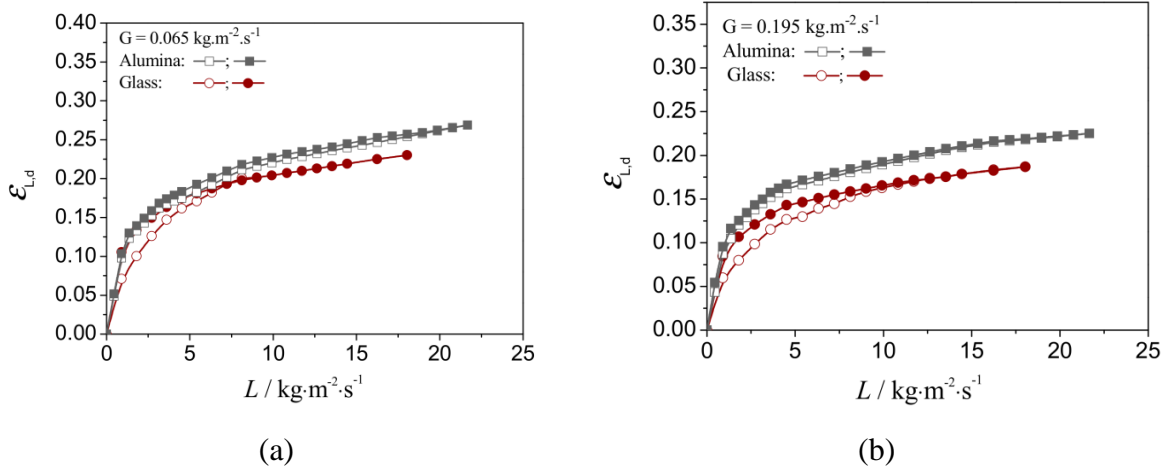


Figure 1.9: Liquid holdup hysteresis at different gas and liquid flow rates : Z. Cheng et al [114]: (a) low gas flow rate, (b) high gas flow rate

❖ Wetting efficiency

Sometimes industrial-scale trickle bed processes operate at lower liquid superficial velocities ($<0.5 \text{ cm/s}$) [2], where the catalyst particles are not fully wetted (See Figure (1.10)).

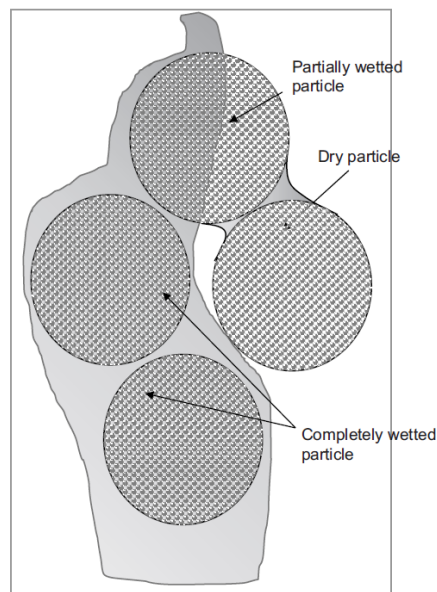


Figure 1.10: Wetting of particles: V. V. Ranade [2]

Thus, the topic of incomplete wetting has garnered a lot of attention, and several research have been conducted to look into how wetting affects the overall rate, conversion/selectivity and heat transfer in trickling bed reactors. Actually, there exist two types of wetting when using porous catalytic particles [70]:

- a) Internal wetting at the pore scale: This is caused by the liquid filling the porous particles. Generally, the internal wetting is complete ($f_{in}=1$). In some cases, under conditions of liquid maldistribution at the bed inlet or in case of liquid flow channeling, as well as, for liquid volatile and extremely exothermic reactions, the internal wetting efficiency is lesser than unity [1], [2], [115].
- b) External wetting at the particle scale: this phenomenon is more important in TBRs. It represents the fraction of the external catalyst surface covered by the flowing liquid [2], [109]. Incomplete external wetting is attributed to the stagnant liquid pockets because of lower liquid flow rates and it has a considerable impact on the overall performance of the reactor. A well-known equation for the estimation of the external wetting efficiency was proposed by Lappalainen et al. [29], written as:

$$f_w = 0.355 \left(\frac{\rho_l d_p \varepsilon_1 u_{l,z}}{\mu_l (1-\varepsilon)} \right)^{0.185} \left(\frac{\rho_l g d_p^2 \varepsilon^2}{\sigma_l (1-\varepsilon)^2} \right)^{-0.188} \left(\frac{\rho_l^2 g d_p^3 \varepsilon^3}{\mu_l^2 (1-\varepsilon)^3} \right)^{0.27} \left(1 + \frac{\varepsilon_g u_{g,z}}{(\rho_l d_p)^{0.5}} \right)^{-0.014} \quad (1.33)$$

1.5.3 Modeling and simulation of TBRs using CFD

As the spectrum of applications of TBRs is enormous, it is no surprise that, intensive study has been performed for a dozen or so years to better our understanding of the events occurring in the trickle-bed reactors [64]. Trickle bed reactors have certain unique features and complexities that require thorough consideration of hydrodynamics, mass transfer, and reaction kinetics to construct predictive models for their performance and comprehend the recommendations for their design and scale-up [2].

In recent years, numerical simulations of chemical processes and multiphase flow, using CFD, in packed bed reactors have gained popularity due to the enhanced capabilities of computers [116]. In the existing literature, two distinct categories of simulations have been used to address the transport phenomena in PBRs: Particle Resolved Simulation (PRS) and the Pseudo Continuous Simulation (PCS). The PRS, which is combination of CFD and DEM, coupled with heat and mass transfer phenomena, is applied for modeling multiphase flows across a PBR. It consists on discretizing the packed bed domain and then, based on some numerical methods, the microscopic Navier-Stokes equations or the Reynolds Averaged Navier-Stokes equations will be solved. In the literature, there have been existed three numerical methods, being (i) the Finite Element Method (FEM), (ii) the Finite Volume method (FVM) and (iii) the Lattice Boltzmann Method (LBM). The outputs are: (i) local bed porosity, (ii) local velocity field and (iii) local pressure. Besides, other

transport parameters including thermal and mass transfer rates, as well as drag force coefficient will be provided, and could be communicated to the PCS.

In the PCS, each phase is treated as an interpenetrating continuum. The conservation equations of mass, momentum and energy will be solved for each flowing phase using the Eulerian-Eulerian methods [117]. Besides, the solid phase is considered implicitly, via the bed porosity. In fact, PCS require particles size distribution, porosity and specific area, as well as closure relationships of complex interfacial interactions, such as drag forces acting on each flowing phase. These complementing models should be found experimentally or obtained via PRS. Furthermore, Eulerian-Eulerian approaches do not resolve precise transport processes at the particle scale, which is critical for understanding trickling bed reactors [117]. These were the main drawbacks of PCS.

On the other hand, in the DEM-based models the number of particles is a limiting constraint. Thus, for a large packed bed domain size, more powerful computers are required. This may represent a real challenge [30], [42]. Nevertheless, it should be kept in mind that, the DEM-based models enable the prediction of local hydrodynamic behavior (local velocity field) and allow to assess the presence of undesirable phenomena, such as back-mixing, channeling and hot spots formation [118].

1.5.4 Some recent studies on TBRs

Since 2018, several studies on TBRs have been done. In 2018, a study was done by [29] about the application of an oscillating TBR in offshore fields for Fischer-Tropsch synthesis over cobalt-based catalyst. The set of partial differential equations of unsteady state mass, momentum and energy balances, closed with appropriate closure relationships were integrated from the reactor inlet to its outlet. The model was validated by confronting the predicted results, in terms of carbon monoxide conversion rate, with the experimental results of Satterfield et al. (1985) for vertical packed bed reactor. Furthermore, it was found that, operating under floating conditions outperform the fixed configuration because of reduced wetting efficiency in the highest zone caused by the reverse secondary flow and lower liquid holdup. This enhancement reaches its maximum when operating in between the vertical and the inclined position.

In the same year, a three-phase model was developed by [119], without considering any deactivation model. The goal was to enhance the MethylAcetylene and PropaDiene (MAPD) hydrogenation process by identifying key operating parameters that influence the

reactor performance. It was found that, increasing the diluent flow rate increased the Propylene concentration, whereas the increase in temperature decreased its production rate.

One year later, a study was done by [120], to model and evaluate the hydrodesulfurization and deactivation rates of partially wetted trilobe catalyst. By using the finite element method, 2D steady state simulations were carried out, at the bed as well as the particle scales. The temporal variation of the effective diffusivity was investigated by the micro-scale simulations. It was concluded that, the sulfur mass fraction did not change a lot with a fresh catalyst particle. Besides, the catalyst deactivation was attributed to demetallization and coking.

By 2020, a dynamic mathematical modeling was carried out by [121], to control the quality of Purified Terephthalic Acid (PTA) product, by monitoring the concentration of 4-CarboxyBenzAldehyde (4-CBA), which is the main impurity in the hydropurification process. The study's findings were: (i) the reactor feed impurities can be efficiently controlled by a sophisticated control approach and (ii) the hydrogen solubility has a significant effect on the product quality. Furthermore, it was suggested that, the dynamic model could be further completed by considering the radial coordinate.

In 2021, a modeling and simulation study was accomplished by [122]. It concerned a hybrid system of trickle bed reactor and multistage reverse osmosis process for the removal of phenol from wastewater. This process is crucial because phenol is among the most toxic pollutants in industrial wastewater. The simulations investigated the effect of operating parameters on the performance of different multistage reverse osmosis configurations combined with a trickle bed reactor. According to the study, flow rate and concentration had little effect on operation, unless both are increased at the same time. Additionally, four performance metrics were applied for comparison, which were permeate concentration, rejection, recovery, and specific energy. It was concluded that, the four-performance metrics employed were interconnected and affected the quality and quantity of the final freshwater product.

In the same year, a research work, by [123], whose goal was to demonstrate how syngas could be methanated and upgraded to bio-methane in a TBR using either manure or sludge-based inoculum as microbial basis. It was demonstrated that, it is possible to construct a reactor platform that can methanate syngas while concurrently upgrading it to biomethane.

By 2022, the effect of increasing gas pressure on biomethanation in TBRs was investigated by [124]. It was shown that, operating under higher pressure led to successful

biomethanation above 90%, at a gas retention time of 21 minutes. This was attributed to the enhanced transfer rates of H₂ and CO₂ under higher operating pressure.

Two years ago, a general dynamic model of TBR was established by [125]. The model could be applied for any reacting system, since it takes into consideration all the key design parameters. Arabinose oxidation was considered as a case study. It was proved that, using small catalyst particles led to rapid conversion, but it requires longer TBR. Furthermore, it was confirmed that, using larger particles slow down the reactants conversion. This was ascribed to mass transfer limitations in the case of larger particles.

In the same year, 2023, a pilot-scale TBR was constructed and installed, by [126], in a wastewater unit to upgrade raw biogas from the local digester. It was revealed that, appropriate ammonia and sulfur supply increased methanation performance, resulting in a consistent methane production with a synthetic methane quality more than 98%. Furthermore, the reactor operation which lasted for 450 days with only two shutdowns, marked an essential step towards full-scale integration.

Finally, yet importantly, in 2023, a critical review study was carried out by [127] about a bio-methanation reaction of hydrogen and carbon dioxide in TBRs. The authors made a comparison study between several relevant works, in the literature. It was revealed that, higher methanation performance is envisaged by enhancing the methanogens' interaction with the feed gases and enriching hydrogenotrophic methanogens. Furthermore, it has been proven that, TBRs have shown potential on a semi-industrial scale with reaction volumes of up to 1 m³. However, the scale-up to the industrial level needs to be investigated.

1.6 GTL Process background: from genesis to modern applications

Gas To Liquids, GTL, is a process that can provide an alternative for the conventional petrochemical transportation fuels, by substitution with synthetic fuels derived from the Fischer-Tropsch process [128], [129]. In 1923, two German scientists, Franz Fischer and Hans Tropsch, discovered the catalytic conversion of carbon monoxide and hydrogen (synthesis gas) into synthetic hydrocarbons, giving rise to the Gas-to-Liquid (GTL) technology [6], [128], [130]. GTL is a technology that can provide an alternative to conventional petrochemical transportation fuels by substituting synthetic fuels obtained via the Fischer-Tropsch process. Liquid transportation fuels derived from the FTS process are appealing, clean and sustainable energy source [131]. This technology is based on four

main steps, which are (1) Pre-treatment of natural gas, (2) syngas (H_2 and CO) production, (3) Fischer-Tropsch reactions and (4) product upgrading [9], [132]. Some articles considers, only the last three steps [6], [133] (See Figure (1.11)).

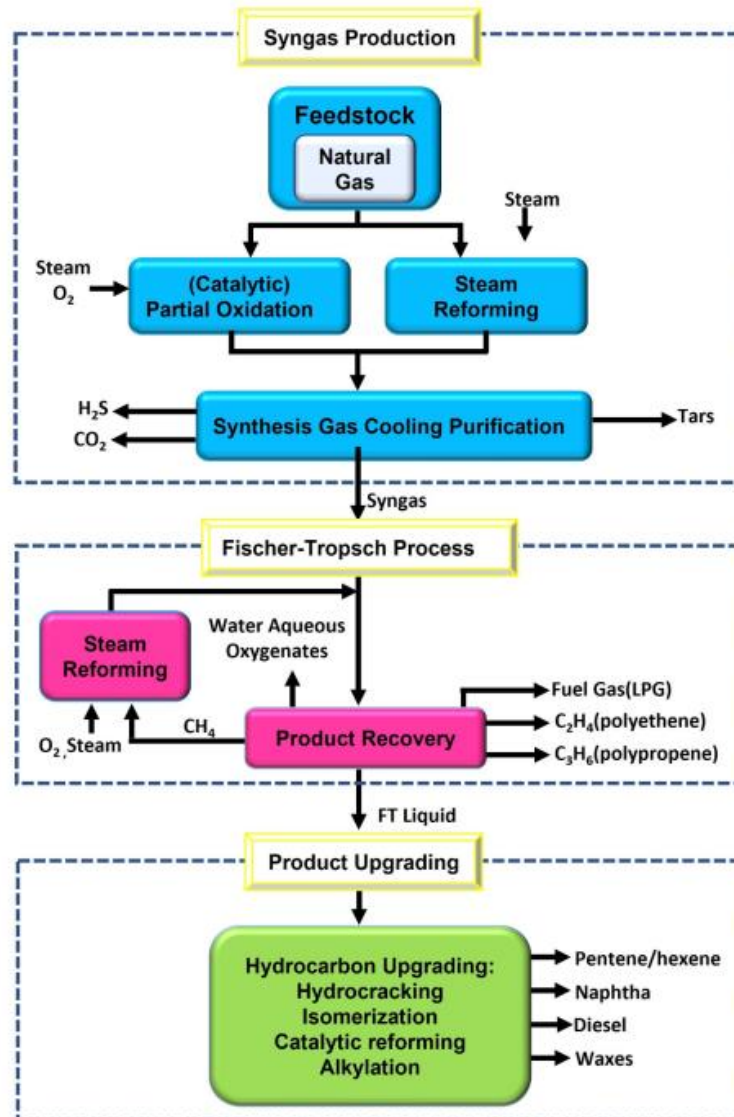


Figure 1.11: Main steps of conventional GTL process : F. T. Alsudani et al. [134]

Initial works were focusing on the catalyst aspect of the FTS [135]. Because of the limited supply of cobalt, original investigations employed nickel catalyst, but the large production rates of methane over nickel switched the focus toward cobalt. Since 1937, studies about the use of iron as catalyst have begun. It was noted that, using alkali-iron catalysts, at medium pressures between 5 and 30 bars, could improve the product yields and showed longer catalyst life time. Again, by 1938, research on the use of ruthenium-based catalysts was reported. It was observed that, high boiling waxes could be produced over ruthenium-based catalysts.

At the industrial scale, the first application of FTS was in Germany by 1936 [136]. It consisted of nine plants [135] with a production rate between 25000 and 30000 tons/year of gasoline and diesel oil (primary oils) and paraffinic wax [136]. However, it came to end after the World War II [135].

After the War, the Fischer-Tropsch technology was exported outside Germany. By 1954, a Coal-To-Liquid (CTL) plant based on Fischer-Tropsch process, but using Coal as feedstock, started to produce in Novochoerkassk (Russia). The process used a tubular reactor packed with cobalt-thorium (Co-Th) catalyst [137]. The products were not just gasoline and diesel, but also special reagents, solvents, soap and other products representing a total annual production rate of 50000 tons [137]. The facility ceased to operate in 1992, due to economic constraints [137].

The second era of the FTS started by the mid-1950s. In 1955, a continuous operation commercial plant was built and began to operate, in South Africa, by the South Africa Coal Oil and Gas Cooperation (Sasol) Company [135], [136]. The process became more efficient and cleaner [137]. It used Circulating Fluidized Bed (CFB) and fused iron-based catalyst. Coal was fed to the reactor, under pressure between 2 and 2.5 MPa and temperature of 340 °C. Using this High Temperature Fischer-Tropsch (HTFT) process, the plant produced 180000 tons/year of hydrocarbons. Besides, it was possible to produce a diversity of hydrocarbons including gasoline, olefins and oxygenates [137].

In the same year, Sasol carried out Low Temperature Fischer-Tropsch (LTFT) reactions, at 200 to 250 °C, in Mutlitubular Packed Bed Reactor (MTPBR), to produce waxes, over precipitated iron-based catalyst [136].

In 1993, a slurry reactor was used by Sasol, adopting the same conditions as those used when operating in the MTPBR [136]. The feedstock was, initially, coal as for the CFB reactor, and after that, shifted to natural gas [136].

By the beginning of the 1980s, Sasol constructed two much larger FT plants, using CFB reactor, over fused Fe/K catalyst [135], [136]. The process was HTFT and the feedstock was coal and then natural gas. By 1995, the CFB reactors were replaced by Sasol Advanced Synthol (SAS) reactors [136].

The outset of the modern GTL plants based on the FTS started by the early 1990s, with the discovery of stranded natural gas reserves. In 1993, Shell and petroSA Companies, using Cobalt and iron catalysts, built and operated two plants producing 10000 bbl/d and 25000 bbl/d of liquid hydrocarbons in Bintulu (Malaysia) and Mossel Bay (South Africa), respectively [135]. The feedstock was natural gas. While Shell's company

used a MTPBR (based on the LTFT process), PetroSA used a CFB reactor (based on the HTFT process). Concerning the Shell's plant, the process' name is the Shell Middle Distillates Synthesis (SMDS), for which the heavy paraffinic products are converted to middle distillates via hydroprocessing. Regarding the PetroSA plant, gasoline is the main product [136]. The Oryx GTL plant; a commercial venture of Sasol with Qatar petroleum at Ras Laffan in Qatar, was built in 2003 and started to produce, in 2007 with a capacity of 34000 bbl/d [138]. This plant reached its nominal capacity (1500000 tons/year) in 2009 [137].

The high-temperature slurry FT process (HTSFTP) was constructed in China, in 2009. This process uses an iron-based catalyst in a slurry-bed reactor at 270 °C, making it a medium-temperature FT process (MTFT, 270-300 °C) [135], [136].

By 2011, the GTL plant (Qatar Petroleum, Pearl GTL development) was built at Las Raffan, Qatar, being the largest in the history of the pearl GTL plant having a production capacity of 6 million tons of hydrocarbons per year [135], [136], [137]. It uses the Shell Middle Distillate Synthesis process over CoTiO₂ catalyst. In addition, it is based on the LTFT technology; in a multitubular fixed-bed reactor. The process uses natural gas as feedstock (Shell's pearl GTL) [136].

Chevron-Sasol established an FT facility in Escravos, Nigeria, in 2013. The plant applies LTFT technology, using a slurry phase reactor, natural gas as feed stock and a cobalt-based catalyst (Co/Al₂O₃).

Several countries, including China, Indonesia, and Iran, are interesting to construct plants to transform syngas to FT liquid fuels. In 2016, Synfuels China developed the medium-temperature slurry-bed FT process (MTSFTP) technology for producing high-quality clean liquid fuels, mainly gasoline and gasoil. This facility uses iron-based FT synthesis catalysts and slurry-bed FT reactor. Furthermore, it includes product upgrading unit, being the largest unique coal-to-liquids plant in the world [136], [139].

Currently, Cerilon expects to build a GTL plant, to convert the stranded gas of North Dakota into high quality synthetic products, having a capacity of 24000 bbl/d. Actually, the project is in the phase of engineering, and the start-up is scheduled for 2028 [140].

Taking everything in consideration, today, five commercial-scale GTL plants are operating, with a total capacity of 259000 bbl/d. Shell's pear GTL plant in Qatar, at 140000 bbl/day, represent more than a half of the world's total commercial synthetic fuels production [141].

1.7 Some recent works on GTL process

Since 2009, several works have existed, in literature to deeply investigate and to optimize the GTL process. For instance, Aspen HYSY process software was used by Kim et al. (2009) [142] to simulate the GTL process and looking for the optimum operating conditions. By applying the thermodynamic model (state equation) Soave-Redlich-Kwong (SRK) and varying the operating conditions, it was found that, using an H₂ to CO ratio of 2 and an operating temperature of 255°C gave the optimum yields.

In 2010, Bao [143] provided a techno-economic study of this process and showed that, to keep the process commercial, the minimum production rate should be 68000 bbl/d.

After that, By the mean of MATLAB and Aspen HYSYS, Lee (2011) [144] carried out an optimizing study to maximize the production of gasoline and diesel. They studied the benefits of recycling of unconverted gaseous over an iron catalyst in order to minimize capital (CAPEX) and operating (OPEX) expenditures. MATABL was utilized to estimate the kinetic parameters by fitting some parameters such as particles and reactor sizes to experimental data. Aspen HYSYS flow-sheets applied these kinetic models to simulate nine (09) different FT plants. The results demonstrated that, the plants that employs recycling and co-feeding produced larger volumes of gasoline and diesel.

Later on, by 2013, a GTL plant was optimized and its performance was investigated, by Knutsen, cited in [130], using Honeywell's Unisim software and Peng-Robinson (PR) equation of state, but excluding the upgrading unit. Cobalt catalyst was used in the auto-thermal reformer and the multi-tubular trickle bed reactor to react syngas aiming to produce 17000 bbl/d. This value was optimized by running simulations to be 19000 bbl/d. The resulting carbon and thermal efficiencies were 82.41% and 65.93%, respectively, without economics consideration. Considering economics, these efficiencies were lower; 77.25% and 61.77% with a yield of 18620 bbl/d.

In 2015, Otaraku and Vincent [145] used Aspen HYSYS with Peng-Robinson state equation to optimize an FT plant, considering just the syngas and the Fischer-Tropsch units. The air separation, desulphurization and the product upgrading units were excluded. The results of the baseline case, of carbon and thermal efficiencies were 82.41% and 65.93%, respectively, and the production rate was 19940 bbl/d.

by 2016, to implement the FT reactions, a slurry bubble column was simulated as a continuous stirred tank reactor (CSTR) by Rafiee and Panahi [146]. The reactor capacity was 2000 m³ that is the same as the one used in the Sasol Oryx plant. It has been concluded

that, using a three-stage FT reactor gave a wax production rate of 79.2 tons/h, being higher than the rates when using single and two-stage FT reactor, whose their production rates were 77.7 and 78.9 tons/h, respectively.

In 2019, Chinedu et al. [147], using Honeywell's Unisim design and basing on Peng-Robinson as thermodynamic model, conducted a simulation study of the GTL plant. In their study, two cases were considered, where they used oxygen (O₂) and carbon dioxide (CO₂) as reactant in the feedstock for the production of syngas. It was found that, when using CO₂, the H₂ to CO ratio was 2.17 compared to 2.21 when using O₂. Concerning the carbon efficiency, it was found that, the baseline case gave a lower efficiency of 77.68 % as compared to with the proposed method, which gave an efficiency of 92.17%, being the efficient method. Additionally, using the proposed CO₂ method yielded 5730 bbl/d, representing an increase of 5.5% with respect to the baseline case.

Another work in the same year by Greyling et al. [148], was about applying Fault Detection and Isolation (FDI) within the GTL process. The authors developed a model of a GTL process in Aspen HYSYS, and its performance was validated. It was demonstrated for the first time that, the FDI technique can fruitfully be applied in the GTL process with recycle streams.

In 2021, Khezri et al. [149] applied surrogate models, instead of process simulators, to investigate the replacement of costly simulations of process optimization in the self-optimizing control procedure. It was concluded that, the Multilayer Perceptron Artificial Neural Network (MLPANN) could effectively replace the detailed GTL process flow-sheet simulator.

By 2022, Teimouri et al. [128] analyzed the capability of CFD simulation in evaluating the FTS performance in many types of reactors and addressed some present challenges that facing this process, such as the hot spots formation issue of PBRs.

In 2023, Atayaet al. [150] simulated an advanced reformer-based GTL plant based on the CARGEN process. The CAGREN process replaces the Auto-thermal reactor (ATR) with two-reactor system for methane reforming. This new configuration co-produced MultiWalled Carbon NanoTubes (MWCNTs) and syngas. Furthermore, the CO₂ emissions decreased by 73%, with respect to the ATR-based GTL plant having a liquids production rate of 50000 bbl/day.

In 2024, Eyberg et al. [131] used Aspen Plus to simulate two different routes of transforming carbon dioxide and hydrogen to jet fuels. The two routes were Fischer-Tropsch and Methanol to Jet. The carbon dioxide obtained from Direct Air Capture (DAC)

and hydrogen from Solid Oxide Electrolysis (SOEL). Prior to GTL process the educts mixture (CO_2 and H_2) is transformed into syngas (CO and H_2). The carbon efficiencies via the Fischer-Tropsch and Methanol routes were 91.1% and 83.3%, respectively. The selectivity toward Jet fuel was 32%. Energy efficiencies were 41.2% and 40.8% and energy yields were 72.9% and 73.4% for FT and Methanol optimal configurations, respectively. For both the FT and the methanol routes, the resulting Levelized Cost of Production (LCOP) was about 0.23 Euro/kWh_{syn}, which was three times higher and the 2022's price of fossil-based jet fuel. The projects will be only profitable if the imposed tax on CO_2 is about 500 Euro/ton of CO_2 .

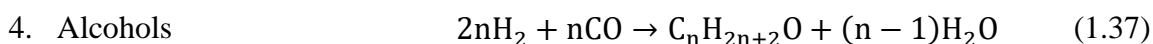
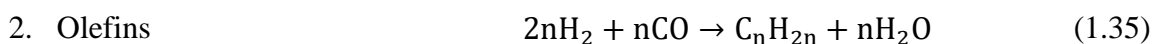
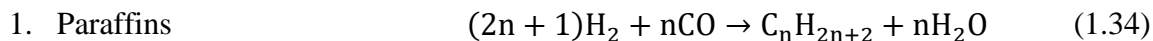
In the current year also, a research work was carried out, by Jafari et al. [151]; was about techno-economic evaluation of flare-gas valorization targeting net-zero strategy. The GTL technology could be integrated with energy-intensive refineries to valorize flare gas into high-value products such as gasoline, diesel, and kerosene. The authors compared between conventional and membrane-based GTL processes. Their findings were remarkable in terms of carbon dioxide emissions and total capital cost reductions when using the innovative membrane-based GTL technique. The former was reduced by 23.3% and the latter was lowered by 13%.

To sum up, in order to increase GTL's competitiveness, the process must be as close to ideal as feasible in terms of efficiencies and economics. This is strongly tied to operating conditions, but also to the choice of primary processing steps in the process, such as reformer technology, reactor type, and catalyst, as they result in slightly varied products and process performance. Furthermore, the GTL technology will have promising future by introducing new techniques in parallel with the conventional GTL process, such as using hydrogen selective Membrane Reactor (MR) for synthesis gas generation, followed by conversion into liquid fuels via Fischer-Tropsch Reactor (FTR). Studies revealed that, with 356.5 MMSCFD of flare gases, this integrated MR-GTL technology demonstrated the highest Internal Rate of Return (IRR), with a net profit of USD 1.155 billion per year [151].

1.8 Fischer-Tropsch Synthesis (FTS)

Fischer-Tropsch reaction is the most crucial application of syngas [152]. Via this catalytic reaction, a mixture of carbon monoxide and hydrogen can be transformed into hydrocarbons spanning from methane to waxes [131], [153]. Generally, ruthenium, nickel,

iron and cobalt are used as catalysts [135]. At the industrial level, cobalt and iron catalysts are the most used. The operating conditions of temperature and pressure range from 200 to 350 °C and 10 to 60 bars, respectively [135]. Cobalt is preferred for producing long chain hydrocarbons, since it has a high activity for LTFT process [154]. In general, the chemical catalytic reactions occurring in an FT reactor are as follows:



The ability to favor particular reactions depends on the utilized catalyst, even though the operating conditions may considerably affect the reactions route. Nickel promotes methane formation under specific conditions of temperature (180-270 °C) and hydrogen to carbon monoxide ratio ($\text{H}_2/\text{CO}=1-2$). Whereas, cobalt, iron and ruthenium favorite paraffins and olefins productions. Equations (1.34), (1.35) and (1.37) represent the formation of hydrocarbons. Equation (1.38) represents the carbide cobalt formation. Water Gas Shift reaction (Equation (1.36)) is catalyzed on iron catalyst under particular conditions, which is enabling operating at lower hydrogen to carbon monoxide ratio [135].

1.8.1 FTS mechanisms

Adsorption of CO on the catalyst surface initiates the FT process. After that, chain propagation can occur through many routes. Depending on the nature of the monomer formed on the catalyst surface and the manner of the chain growth, there exist several mechanisms [155]. Three different mechanisms have been proposed: the carbide mechanism, hydroxyl-carbene mechanism and CO insertion [155], [156], [157].

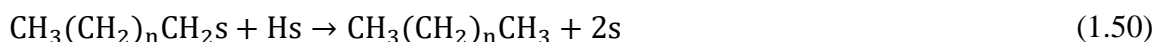
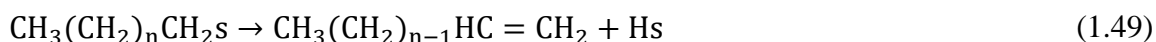
In the first mechanism, called the carbide (or carbene) mechanism, was proposed for the first time by Fischer and Tropsch, the adsorbed CO is dissociated to form carbide (C) and oxygen (O) surface atoms. Then the C atoms are partially hydrogenated to forms CH_x intermediates serving as the chain growth monomer. Termination happens by desorption of unsaturated intermediates to produce olefins, or by adding methyl group ($-\text{CH}_3$) or H_2 to form paraffin [156].

The second mechanism, named the hydroxyl-carbene mechanism involves partial hydrogenation of adsorbed CO to enol group ($-\text{CHOH}$) which is then condensed with

another enol species with H₂O elimination to form a surface species of –COH-CH₃ and ends up to an alkene and water [135].

Thirdly, the carbonyl insertion mechanism consists of the insertion of an adsorbed CO into the metal-alkyl bond leading to the formation of aldehydes [135].

Because the formation of hydrocarbons is weak via the 2nd and the 3rd mechanisms, most of the studies have focused on the carbide mechanism. A series of elementary steps correspond to the carbide mechanism are presented here below [135], [158]:



1.8.2 Catalysts of FTS

Under FT process conditions, FT reaction catalysts are often active in the hydrogenation and metal carbonyl production reactions [157]. Iron, nickel, cobalt and ruthenium are the only metals that can provide the activity needed for the FTS [135]. An overview of the main characteristics of these catalysts is outlined in Table (1.9).

Table 1.9: Some specific characteristics of the main FTS catalysts

Active metal	Price	FT activity	WGS activity	Hydrogenation activity
Ni	Expensive	Low	Low	Very high
Co	Expensive	High	Low	High
Fe	Cheap	Low	Very high	Low
Ru	Very expensive	Very high	Low	High

The drawbacks of Ni and Ru catalysts are [135]:

- Ni prefer methane formation under the specific FTS conditions
- Ru is very expensive, even though it favorites the formation of C5+ cuts.

A comparison between iron and cobalt catalysts is illustrated in Table (1.10).

Table 1.10: Comparison between iron and cobalt catalysts [158]

Advantages of cobalt catalyst	Advantages of iron catalyst
<ul style="list-style-type: none"> • Shows high selectivity to long chain HC 	<ul style="list-style-type: none"> • Heavy paraffins (waxes) are the main product
<ul style="list-style-type: none"> • Gives satisfactory stability of n-paraffins and n-olefins 	<ul style="list-style-type: none"> • Provides moderate stability towards alkanes, alkenes
<ul style="list-style-type: none"> • Shows low selectivity towards oxygenates 	<ul style="list-style-type: none"> • Shows moderate selectivity towards oxygenates
<ul style="list-style-type: none"> • Exhibits low activity towards the water gas shift reaction 	<ul style="list-style-type: none"> • Exhibits high activity towards the water gas shift reaction
<ul style="list-style-type: none"> • Assures higher production rates and longer life time compared to iron 	<ul style="list-style-type: none"> • Lesser yields and life time
<ul style="list-style-type: none"> • Not inhibited by water leading to higher yields in comparison with iron 	<ul style="list-style-type: none"> • Inhibited by water consumed through WGS reaction
<ul style="list-style-type: none"> • More expensive 	<ul style="list-style-type: none"> • Cheaper
<ul style="list-style-type: none"> • Temperature up to 260 °C 	<ul style="list-style-type: none"> • Temperature up to 350 °C
<ul style="list-style-type: none"> • Larger catalyst particles 	<ul style="list-style-type: none"> • Smaller catalyst particles

The most significant drawbacks of cobalt catalyst are: (1) its price is higher compared to iron, and (2) its poor performance due to excessive methane production, which can occur when the correct support and promoter are not employed [158].

Concerning Fe catalyst, some disadvantages exist, which are as follows [158]:

- Hydrothermal sintering and oxidation can occur due to the increase of water partial pressure, resulting through the WGS reaction;
- In packed bed reactors, the iron catalyst deactivated progressively toward the reactor exit due to production of water and carbon dioxide by WGS reaction;
- Ability to produce undesired aromatics when operating at elevated temperatures.

Finally, we have to note that, adding promoters may influence considerably the FTS activity and selectivity, mainly for cobalt, for which promoters have a detrimental effects on its activity [157].

1.8.3 Support materials for FTS catalyst

The purpose of support application in the FTS process can be summarized in three goals [158]:

- Providing a high surface area for dispersion of the catalyst's active sites;
- Stabilizing the active phase under reaction conditions;
- Providing adequate mechanical strength as well as facilitating mass and heat transfer throughout the reactor.

Metal oxides including Al_2O_3 , SiO_2 , TiO_2 , ZrO_2 , and carbon materials are the most commonly used supports in FTS [157].

1.8.4 Kinetics of FTS

The kinetics of the FT reaction is unknown and still debated in the literature [159]. It is an important step when designing, optimization and simulation of FT reactors. In the literature, there exist several models of iron and cobalt catalysts. Because of the variety of mechanisms and the high number of species present in the reaction medium, the developing of an accurate kinetic model is challenging. Kinetic studies on the FT synthesis are divided into two areas. While the first category focuses solely on the rate of syngas disappearance, the second gives information about the product compositions [157], [160]. For both categories, the reaction rate expressions can be determined empirically, by using power-law rate equation, mechanistically or semi-empirically, such as the Langmuir-Hinshelwood-Hougen-Watson (LHHW) or Eley-Rideal (ER) rate expressions. It was demonstrated that, the power-law model was able to represent the kinetics for a tight range of operating conditions, in contrary with LHHW model, which was able to explain the kinetics on a large interval of operating conditions. These models depend strongly on the catalyst nature and the operation conditions, so that, no single kinetic expression could be applicable to account for CO consumption or products spectrum distribution [158], [160].

There have existed several FTS kinetic models for Co and Fe based catalysts as well as many kinetic models for the water gas shift reaction. During the FTS, water is not adsorbed on the iron catalyst active sites making the difference in kinetics in compared with cobalt catalyst, which has a low activity towards the water gas shift reaction [158]. A

summary of iron and cobalt-based rate equations are presented by [157]. In the following chapter we will deal with cobalt catalyst, so that, some cobalt-based kinetic models of CO consumption, from literature, are summarized in Table (1.11).

Table 1.11: Kinetics of FTS over Cobalt catalyst

Catalyst	Operating conditions			Kinetic expression	Ref.
	P (PMa)	T (°C)	H ₂ /CO (mol/mol)		
Co/TiO ₂	2	180-238	1.0-4.0	Model 1: $r_{ft} = aP_{CO}^{-0.24}P_{H_2}^{0.74}$ $a=0.004$ Model 2: $r_{ft} = b \frac{P_{CO}P_{H_2}^{0.74}}{(1+cP_{CO})^2}$ $b=0.0011$ and $c=0.04$	[161]
Co-Ru/Al ₂ O ₃	4.5-6.5	235-250	1.7-2.3	$r_{ft} = A \frac{P_{H_2}^{0.5}P_{CO}^{0.5}}{(1+aP_{H_2}^{0.5}+bP_{CO}^{0.5}+cP_{CO})^2}$ (in supercritical phase) A, a, b and c are constant values.	[162]
Co/Al ₂ O ₃	0.8-2.5	210-235	1.8-2.7	$r_{ft} = \Phi \frac{P_{H_2}^n P_{CO}^m}{(1+K_{CO}P_{CO})^2}$ Φ : is a function of the rate constant of the determining elementary steps and the adsorption equilibrium constants of species. The value of parameters n and m depend on the determining elementary step and K_{CO} is the CO adsorption equilibrium constant.	[163]
Co-Ce/SiO ₂	1.013	200-300	1.0-1.5	$r_{ft} = k_1 \frac{P_{CO}}{(1+\Phi P_{CO}^{0.5}+K_{H_2}^{0.5}P_{H_2}^{0.5})^2}$ k_1 : is the forward rate constant for CO dissociative adsorption, K_{H_2} is the equilibrium constant of the H ₂ adsorption step Φ is a function of the rate constant of elementary steps and the equilibrium constant of the CO adsorption step.	[164]
Co/Al ₂ O ₃	1.0-2.5	185-220	1.5-3.0	$r_{ft} = k_{m,CO} \frac{C_{CO,g}C_{H_2,g}}{(1+K_{CO}C_{CO,g})^2}$ $k_{m,CO}$: is the rate constant for the Langmuir-Hinshelwood equation for FT on Co per unit mass of catalyst, K_{CO} is the adsorption coefficient of CO and $C_{CO,g}$ and $C_{H_2,g}$ are the concentrations of CO and H ₂ in the gas phase.	[165]

An important step in kinetic analysis is ensuring that, the intrinsic reaction rate is not limited by internal and external mass transfer rates. To this purpose, the impacts of interphase and intraparticle mass transport resistances should be investigated using Weisz-Prater and Mears criteria for internal and exterior mass transfer restrictions, respectively [166], [167]. While increasing fluid superficial velocity increases the exterior diffusion rate, reducing the catalyst pellet size improves internal mass transfer.

1.8.5 FTS products selectivity

FTS generates a wide range of products with varied chain lengths and functionalities. The actual product distribution of an FT process depends on numerous reaction parameters, such as reaction conditions (temperature and partial pressures of the reactants and feed composition), the reactor system employed, the catalyst composition and its physical properties. While n-olefins and n-paraffins are the main products of the primary reactions, oxygenates (carboxylic acids, aldehydes, 1-alcohols, ketones) and branched compounds are the main product of side reactions [135]. Some main product cuts are illustrated in Table (1.12).

Table 1.12: Main FTS products [158]

Name	Carbon number range
Fuel gas	C ₁ -C ₂
Liquid petroleum gas (LPG)	C ₃ -C ₄
Gasoline	C ₅ -C ₁₂
Naphta	C ₈ -C ₁₂
Kerosene/jet fuel	C ₁₁ -C ₁₃
Diesel	C ₁₃ -C ₁₇
Middle distillates	C ₁₀ -C ₂₀
Soft wax	C ₁₉ -C ₂₃
Medium wax	C ₂₄ -C ₃₅
Hard wax	C ₃₅ +

FTS product distribution can be described using the Anderson-Schulz-Flory distribution model (ASF) [40], [129], [131], which is illustrated on Figure (1.12), and follows the following equation:

$$\log\left(\frac{W_n}{n}\right) = n \log \alpha + \log\left(\frac{(1-\alpha)^2}{\alpha}\right) \quad (1.51)$$

In this, W_n [-] is the mass fraction of specific product, n [-] is the product carbon number and α [-] is the chain growth probability [40], [129].

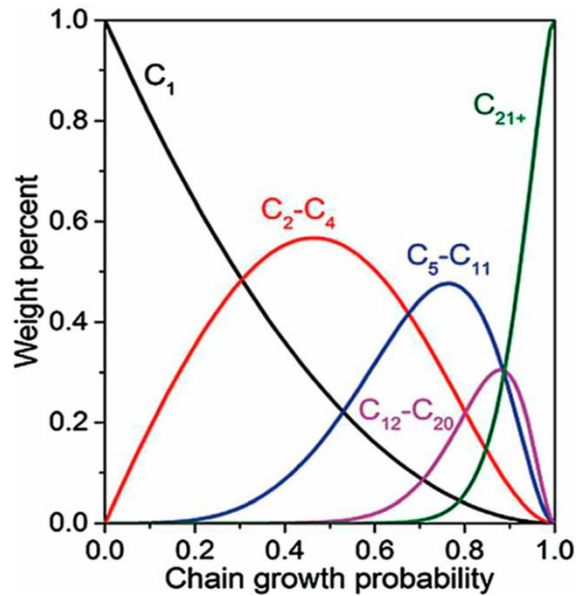


Figure 1.12: FTS products distribution: products weight fractions versus chain growth probability: D. Weber et al [168]

In another way of speaking, the total molar flow rate of products with a well-determined carbon number declines exponentially using the following expression:

$$X_n = n(1 - \alpha)^2 \alpha^{n-1} \quad (1.52)$$

Here, X_n [–] is the molar fraction of hydrocarbon compound composed of n atoms of carbon.

However, it is worthy of note that, the idealized ASF model deviates from the precise description of the hydrocarbon spectrum formed by the FTS process. The selectivity of carbon number in FTS products does not entirely align with the traditional ASF model due to three sorts of deviations: higher methane production than expected, a production of ethene lower than expected and greater selectivity towards heavier hydrocarbons, which is attributed to the increase of the chain growth probability with the carbon number [158]. These deviations were, occasionally, attributed to non-steady state operation of the reactor system [135]. In general, the nature of the active metal, support, promoters, reactors design and operating conditions all affect the products distribution [158].

1.8.6 Factors impacting CO conversion and products selectivity

❖ Effects of the Nature of Active Components, Support, and the Promoters

In term of active phase of Fe and Co metals, iron carbide and metallic Co have been proven to be the active phases for chain polymerization during the FT reaction. While the metallic cobalt species are responsible for enhancing the product selectivity of the FT reaction towards C_{5+} , the mechanism of iron carbide species for the iron catalyst is unclear. Actually, during the iron-based FT reaction, a combination of phases comprising Fe_3O_4 , metallic Fe, and Fe carbides exist, which is the outcome of the catalyst's reconstruction under syngas reacting system. The type of support is another important factor in determining the selectivity of FT products. The metal-support interaction and the support physicochemical parameters have a considerable impact on FTS products selectivity. The promoter is, also, another component that determines the selectivity of FT products. These materials are added to the catalyst in very small concentrations (~1-2% wt) to improve its catalytic, structural, electronic, and textural features. They can also act as stabilizers and poison-resistant agents. While the support has a physical effect, the promoter has greater chemical effects on the catalyst [157].

❖ Effects of Process Conditions

The selectivity of FT products is highly dependent on the process conditions. Temperature is a key process parameter that can influence the selectivity of FT products. It has been revealed that, by increasing the temperature, the products of FTS shift towards lower carbon number species, for both iron-based and cobalt-based FTS [158]. The impact of process parameters on the selectivity of an industrial cobalt-based FTS was examined by Niu et al. [169]. It was concluded that, decreasing temperature and increasing pressure conduct to lowering methane yields and climbing the production rate of C_{5+} . Another important operation condition is the total pressure, for which it was found that, increasing the total pressure shifts the selectivity towards long chain hydrocarbons and oxygenates. Additionally, boosting the total pressure up to 6 MPa may improve positively the CO conversion and C_{5+} yields on Co- Al_2O_3/SiO_2 catalyst [170]. It was also found that, operating under high pressure up to 6 MPa, the catalyst is more likely to deactivate than when operating at a lower pressure of 2 MPa. It is worthy of note that, by raising the H_2/CO ratio, lighter hydrocarbons are preferred [158].

❖ Effects of reactor type

The choice of the appropriate reactor is crucial to control the FTS yields and temperature. Since FT reaction is highly exothermic, managing the temperature is a big challenge when designing an FT reactor. Neglecting the thermal effects on the yield of the catalytic reactor leads to undesirable effects, such as high methane production rate, deposit of carbon on the catalyst surface and accelerated catalyst deactivation process. Four basic reactor types have proven its efficacy toward FTS [134], [171], as illustrated in Figure (1.13)):

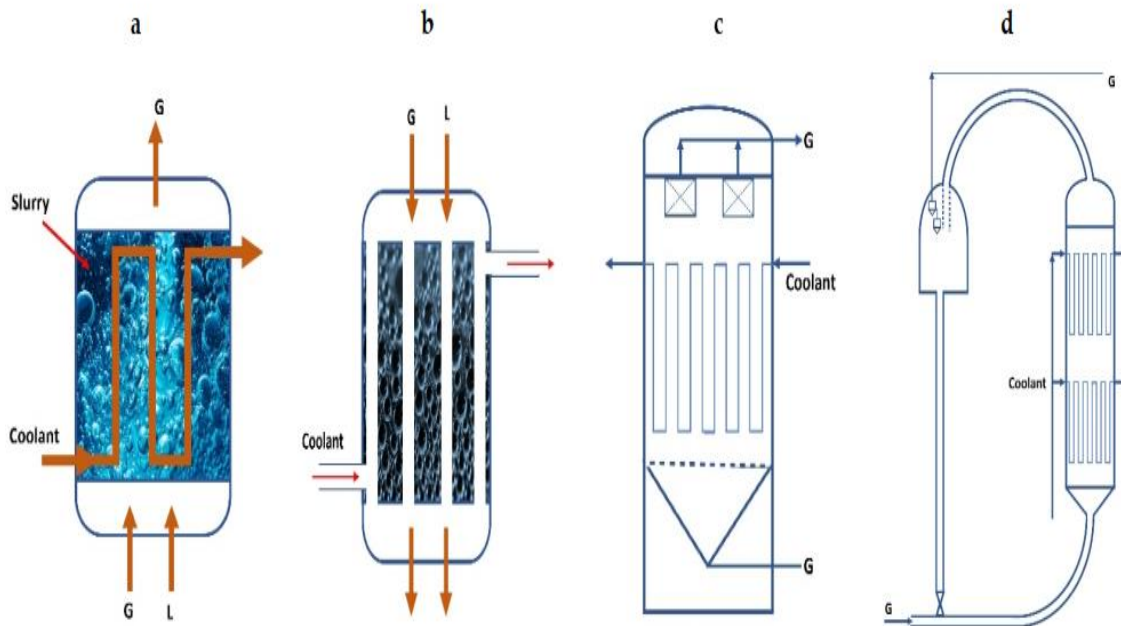


Figure 1.13: Type of conventional FTS reactors: a) Slurry Bubble Column Reactor (SBCR), (b) Multi-Tubular Packed Bed Reactor (MTPBR), (c) Fluidized Bed Reactor (FBR) and (d) Circulating Fluidized Bed Reactor (CFBR) : F. T. Alsudani et al [134]

Some advantage and disadvantages of these reactor types are summarized in Table (1.13)

Table 1.13: Some advantage and disadvantages of conventional FTS reactors

Reactor type	Advantages	Disadvantages
Slurry Bubble Column (SBC)	Efficient heat and mass transfer. Ease of operation and low cost [172]. Favorites middle distillates cut [136].	Back missing of the gas phase. Recovery of the catalyst particles. Scale-up issues [136].
Packed Bed Reactor (PBR)	High catalyst loading/reactor volume leading to higher productivity/reactor volume. Easy to scale-up from a single tube to pilot plant [173].	Diffusion related issues with the catalyst particle. Inconvenient heat transfer [157].
Circulating Fluidized Bed (CFB)	Simplicity of catalyst loading and replacement during the reaction [136].	Energy requirement, in terms of higher temperature to achieve higher conversion and for circulating the catalyst, led to replacement with fixed fluidized bed [157].
Fixed Fluidized Bed (FFB)	Replaced CFB to minimize energy requirements devoted for circulation, pressure drop and reducing operation temperature [157].	

Generally, it is useful to use PBR for FTS instead of other reactors types because [135]:

- (i) Operating near plug flow conditions leading to higher conversions,
- (ii) Low sensibility to poisons, so that, the catalyst yields for longer time and
- (iii) Better operating flexibility.

However, there exist some limitations, which are as follows

- (i) Lower heat transfer performance and shorter safety distance to deactivation temperature (260 °C for Co and for a safe distance of 10 °C, the maximum temperature should not exceed 250 °C) [9],
- (ii) Limited averaging working temperature causing a limited conversion rate (maximum averaged temperature around 225 °C),
- (iii) Higher capital expenditures (higher CAPEX),
- (iv) Elevated pressure drop leading to higher operating expenditures (higher OPEX) and
- (v) Difficulties and constraints to change catalyst, such as production interruption

A typical packed bed reactor, such as Sasol ARbeitsGEmeinschaft (ARGE), operates as a tube-shell heat exchanger. It has a cylindrical shape of diameter of 3 m containing 2050 tubes, each 56 mm in diameter and has a length of 12 m, packed with

catalyst particles. The excessive heat is extracted by using pressurized steam. Averaged temperature within the reactor is between 210 and 225 °C for cobalt catalyst and a little higher from 230 to 245 °C for iron case. CO conversions do not exceed 50% to avoid reaction run away [135]. A comparison between ARGE process and Synthol High Temperature (SHT) using circulating Fluid Bed (CFB) in term of selectivity is presented in Table (1.14).

Table 1.14: Comparison between MTPBR and CFB, in term of products selectivity [156]

Cut	Synthol High Temperature (CFB)	ARGE low temperature (MTPBR)
C ₁ - C ₂	16.0	5.4
C ₃ - C ₆ (paraffins)	5.0	8.4
C ₃ - C ₆ (olefins)	33.5	7.6
C ₇ - 160 °C	17.2	8.0
160 – 350 °C	14.0	19.5
350+ °C	7.8	48.1
Water soluble oxygenates	6.8	3.0

Lately, new FTS reactors technology has been applied, within the framework of small-scale FTS intensification. This includes monolith, micro-channel and milli-fixed bed reactors, as shown in Figure (1.14).

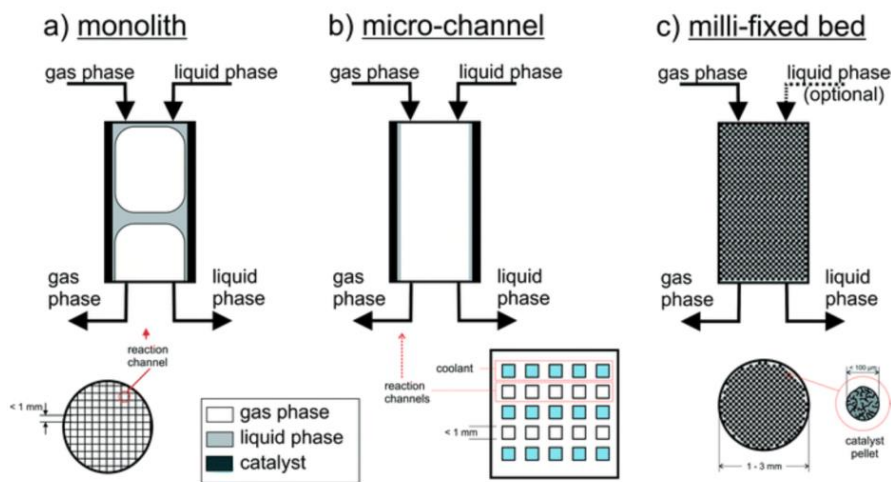


Figure 1.14: Types of reactors used in small scale GTL : D. Braide [9]

Small-scale GTL uses smaller-size reactors for syngas and FT steps. These types of reactors consist of compacted modular packed bed designs, having tight channels. Because

heat transfer is more efficient for tight channels of the bed, the whole GTL process will be intensified [11], [12]. Small-scale GTL has many application areas, such as in offshore environment [11] and flare gas recovering and transforming into synthetic fuels [13], [151].

The main limitation of the small-scale GTL is the limited capacity spanning from 50 to 5000 bbl per day [13]. For this reason, the conventional reactors cannot be dispensed.

Recently, there is a trend in utilizing multi-tubular packed beds with slender tubes or micro-channel reactors to increase conversion, due to their high capacities to handle the excessive heat generated during the FTS reaction and consequently can operate at optimal temperatures [117].

1.9 Modeling and simulation of FTPBR

Although numerous academics researches have addressed the design of fixed bed reactors, only a few substantial modeling studies on FT fixed bed reactors have been published in the open literature [135]. The fixed bed mode of operation is characterized by the compacted packing of the solid catalytic particles and the heat extraction procedure through the reactor wall. While packing with small particles results in greater pressure gradients over the bed length, packing with bigger particles are looser and exhibits lower pressure drop, with reservations about pore diffusion limitation as demonstrated by [16]. The fundamental aspect when designing a PBR for FTS is to balance between the packing characteristics and the income of hydrocarbons with high carbon number. This might be performed by modifying the PBR key design elements including particle size and shape, bed to particle diameter ratio (aspect ratio) or by altering the operating conditions namely the reactant inlet temperature and feed composition as well as the cooling medium temperature. One further important area, is the inclusion of precise kinetic data of the FT reaction, taking place in the catalyst and the specification of the product spectrum, consisting of hydrocarbons with the number of carbon atoms up to 150 [16].

Mathematical modeling of FTPBRs offers a comprehensive picture of the process in order to optimize catalyst and reactor design [159]. Preliminary tentative of modeling FT packed bed reactor were quite simple models and did not meet the complexity of the FTS process [16]. Recently, deeper studies have rightfully concentrated on mass transfer within the catalyst particles. In this, pore diffusion has a significant influence on the

reactants consumption and products selectivity [16]. Some important recent modeling studies in the literature will be presented, hereinafter.

In 2009, Jess and Kern [174] used the effectiveness factor method, considering internal mass transfer to simulate a 2D pseudo-homogeneous FT reactor, packed with iron or cobalt catalysts, using boiling water as cooling medium. No product distribution model was considered, as illustrated in Table (1.14). The effective rate associated with cobalt is marginally greater than that of iron. Consequently, a temperature setting for cobalt can be set at a level that is 20°C lower than that required for iron. The conversion rates and product selectivities are nearly identical, allowing for the safe operation of the reactor, without the risk of a temperature runaway. The findings of the simulations align with existing literature and indicate that, there remains potential for the optimization of fixed bed Fischer-Tropsch reactors, particularly through improved heat transfer phenomenon.

Later, in 2012, a similar model was developed by Lee and Chung [108], however the model considered two-phase gas-liquid flow in the packed bed and used the Ergun correlation for the momentum balance equation. The feedstock was syngas derived from biomass gasification. The distribution model of the product is founded on an innovative concept of chain growth that is dependent on carbon number, as well as the stoichiometric relationship between the synthesis gas and the produced hydrocarbons. The temperature profiles within the reactor have received major attention by the authors, as appropriate thermal control is critical for the FT exothermic catalytic reaction. The model has the potential to find the optimal operating parameters required to get the largest yield of the desired products, namely liquid hydrocarbon fuels, while limiting thermal deactivation of the catalyst.

With recent increases in computational power, computational fluid dynamics (CFD) has become a viable method to analyze complex flows coupled with kinetics and transfer phenomena to simulate packed bed reactor for Fischer-Tropsch synthesis. Applying CFD codes on an FTPBR has three main purposes: (i) establishing conservation equations for mass, momentum and energy, coupled with kinetics, (ii) maximizing the product selectivity and yields by optimizing the operating conditions and (iii) supporting the reactor design and engineering [128].

Few years ago, the performance of Fischer-Tropsch synthesis, on cobalt supported catalyst, in trickle-bed reactors for offshore floating applications was studied using a complex three-directional time-dependent multiphase model by [175]. The model included volume-averaged mass, momentum, and species balance equations in liquid and gas

phases, as well as diffusion and chemical reactions within the catalyst particles. It was found that, using symmetric oscillating trickle-bed reactors enhances the Fischer-Tropsch synthesis performance, compared to the fixed vertical configuration.

One year later; in 2019, a dynamic 1D pseudo-homogeneous model of Fischer-Tropsch synthesis in packed bed reactors was developed by [176]. The outcome of the study is that, operating under specific conditions would allow high CO conversion, high C_{5+} selectivity, low yields of methane and preventing hot spots formation. These optimum operation conditions, in terms of temperature, pressure and gas space velocity, were corresponding to temperature range from 230 °C to 245 °C, 10 bars and 15 bars and 1800 NmL/g_{cata}/h.

Later on; in 2020, a 1D pseudo-homogeneous model with a dynamics control of the cooling jacket temperature was proposed by [173], to study a Fischer-Tropsch synthesis in a fixed bed reactor. A Proportional Integral Controller (PIC) was used to grantee a good thermal management and optimizing the reactor performance. It was verified that, controlling the reactor temperature, via implementing a control scheme in the cooling medium is of great importance to prevent the reactor runaway and enhancing its performance.

In 2021, Chandra et al [16] applied direct numerical simulation (DNS) to simulate Fischer-Tropsch synthesis in a slender packed bed reactor with a tube to particle diameter ratio of 4. The external and internal transport limitations were entirely considered, in a fully resolved manner with the velocity field and without using any empirical closure relationships. The boundary problem conditions are solved using the Immersed Boundary Method (IBM). Next, The DNS model's results are compared to a 1-D heterogeneous reactor model that considered intra-particle reaction and diffusion, as well as fluid phase transport, via external mass and heat transfer coefficients. Both models used the same kinetic model. The plug flow assumption was considered by the 1D model. It has been concluded that, Direct Numerical Simulation enables for precise estimates of the conversion, yield, selectivity, and temperature profiles. This is notably different from the 1D model, which requires closure relationships, such as wall-to-bed heat transfer coefficients, interfacial transfer coefficients, and dispersion coefficients. DNS is free of any empirical closures. Finally, the discrete element method was used to simulate the entire bed which consists of 220 particles, considering six scenarios by varying the wall temperature and the feed composition in order to investigate the influence of temperature and H_2 to CO ratio. The findings of the complete bed simulations show that, managing the

reactor temperature is of fundamental relevance in determining the yield and selectivity of hydrocarbon products. The authors suggested that, future research should be focusing on finding the optimal operating temperature for maximum selectivity in a non-isothermal non-adiabatic system.

In 2022, Shen et al. [10] simulated an FT multitubular packed bed reactor for a micro-refinery, which can be fitted into mobile container. ANSYS Fluent software was used to run the simulations. The MTPBR was fed by syngas derived from biomass and used Co-based catalyst. The effect of the tubes diameter on the carbon monoxide conversion rate and productivity was studied. Four packed bed models, using four different tubes diameters, were simulated. For each tube diameter model, the catalyst activity varied to limit the maximum temperature within the backed tubes. Simulations were carried out under maximum temperature constraint to avoid the thermal runaway of the reactor. In other way, the inlet operating temperature for each case was set to have the maximum possible value without exceeding a certain limit value, to avoid temperature runaway and for ensuring safe operation as well as to extend the lifetime of the designed reactor. The optimal inlet temperature value varied with tubes diameter. As the tube diameter increases, the optimum temperature increases, so that, the CO conversion and the products yields increase. The simulation results indicated that, a C_{3+} productivity of 15.3 kg/h can be achieved when using tube diameter of 19.05 mm, space velocity of 300/h and catalyst activity 6,95 times that of the baseline case. The designed MTPBR was a bundle of 2857 tubes arranged in triangular pattern. This reactor was designed for small scale Fischer-Tropsch synthesis which can process 2 or 2.2 tons/d of wood chips or municipal solid waste.

Table 1.15: Some significant recent modeling works about Fischer-Tropsch synthesis in packed bed reactor

Model	Model Type	Time-dependency	PBR Reactor type	External cooling/ Isothermal conditions	Internal mass transfer	Product distribution model
Jess and Kern [174]	2D pseudo-homogeneous	Steady-state	MTPBR	External cooling	Yes	No
Lee and Cheng [108]	2D heterogeneous	Steady-state	MTPBR (two-phase flow)	External cooling	Yes	Non-ASF
Iliuta and Larachi [29]	3D pseudo-homogeneous	Unsteady-state	Oscillating TBR	Isothermal conditions	Yes	No
Méndez and Ancheyta [176]	1D pseudo-homogeneous	Unsteady-state	PBR	External cooling	No	Non-ASF
Méndez and Ancheyta [173]	1D pseudo-homogeneous	Unsteady-state	PBR	External cooling	No	Non-ASF
Chandra et al. [16]	3D resolved particle model 1D heterogeneous model	Unsteady-state	Slender PBR	External cooling	Yes	ASF
Shen et al. [10]	2D pseudo-homogeneous	Steady-state	MTPBR (slender and large tubes)	External cooling	No	Non-ASF

The table above summarizes some significant work about the modeling of Fischer-Tropsch packed bed reactors, during the last fifteen years, which span from simple one-dimensional to computationally-costly three-dimensional resolved particle models, such as that developed by Chandra et al., in 2021. Besides, it is clearly observed that, the Anderson-Schulz-Flory (ASF) distribution model was considered by Chandra et al., whereas non-ASF products distribution models were used by others. Jess and Kern as well as Iliuta and Larachi did not consider the products distribution in their models, so that, their models outputs were only CO conversion and reactor temperature profile within the bed. Moreover, some authors considered the temporal time derivatives, while others considered the steady state operations. Only the model of Iliuta and Larachi considered isothermal conditions. Furthermore, the models of Lee and Cheng as well as Iliuta and Larachi considered two-phase flow in their reactor models to account for the heavier hydrocarbons formation along the packed bed. Moreover, the last two models simulated slender packed bed reactors for Fischer-Tropsch synthesis. It is worthy to note that, recently Shen et al. used syngas derived from biomass to model a multitubular packed bed reactor composed of slender tubes.

1.10 Conclusion

Hydrodynamics affects considerably the mass and heat transfer phenomena as well as the effective kinetic rate in complex reacting systems. Trickle bed reactor is one of the most sophisticated reacting mediums. Therefore, understanding its hydrodynamics is crucial. With recent development in CFD, two approaches have existed to study the TBR hydrodynamics. While the DEM-based approach is numerically costly, the pseudohomogeneous approach provides the averaged quantities, over a control volume. One of the important hydrodynamic parameters is pressure drop. An appropriate correlation for drag force to account for pressure drop, used by a pseudo-homogeneous model, is essential to obtain accurate results.

The FT reaction is very exothermic and the selectivity for long chain hydrocarbons is, significantly temperature dependent. Effective heat management is critical for constructing a FT reactor, as high temperature can inhibit the desired selectivity route and can damage the catalyst as well. Furthermore, the fast temperature rise can lead to reaction runaway. In order to contribute to the development of the GTL technology, it is an important task, to contribute in the modeling and simulation of the FTS in low aspect-ratio packed bed reactors, called slender packed bed reactors.

Using a slender packed bed reactor, the excess amount of heat can be rapidly evacuated from the reactor, via the wall. A slender packed bed reactor is a way of process intensification, because it allows operating at the optimum temperature, to obtain the maximum conversion and yields.

In the context of small GTL applications, a multitubular packed bed reactor, which is composed of slender packed tubes, can be used to implement the Fischer-Tropsch reaction, using biomass-based syngas to produce liquid hydrocarbons.

CHAPTER II

MODELING AND SIMULATION OF FISCHER-TROPSCH PACKED BED REACTOR

2.1 Introduction

With recent increases in computational power, Computational Fluid Dynamics (CFD) has become a viable method to analyze the complex flows in packed beds. The flow could be cold or reactive, for which the computational cost is higher. The CFD analyses require Three-Dimensional (3D) models when incorporating the bed structure's complexities (Resolved-Particle) for assessing the local flow field. In addition to the 3D Resolved-Particle models, 2D representative models are used in order to reduce the computation costs. 2D models could not properly seize local hydrodynamic phenomena, such as local velocity field. Nevertheless, global macroscopic parameters (such as pressure drop) can be predicted, accurately.

This chapter is divided into two sections. Firstly, the hydrodynamics of a slender packed bed reactor with an aspect ratio of 2 will be modeled and simulated, using CFD. The slender PBR is crossed by an incompressible laminar flow. Two approaches will be considered, namely: the Resolved-Particle Method (RPM) and the Pseudo-homogeneous Method (PHM). The conservation equations of mass and momentum will be applied. Secondly, the FT reaction in packed bed reactors (FTPBR), with different aspect ratio values, will be modeled and simulated. The simulated packed beds are crossed by a concurrent gas-liquid downward flow. In this case, the conservation equations of heat and species will be applied, additionally, to the mass and momentum conservation equations. COMSOL Multiphysics 5.6 will be used to carry out all the simulations. For the two studies, the applied code CFD is composed of four steps, which are: (1) defining the system parameters and variables (2) generation (or build) of geometry, (3) setting the physics (4) meshing, (5) solver and (6) post processing [128]. While the first three steps will be treated in the current section, the last one will be developed in the third chapter.

2.2 Simulation methodology on COMSOL Multiphysics 5.6

COMSOL Multiphysics is a numerical simulation software based on the finite element method. This software allows simulating many physics and engineering

applications, mainly coupled phenomena or Multiphysics simulations. Its operating principle consists of solving a set of partial differential and algebraic equations of the set physics and all the system variables, such as: closure relationships of density, viscosity, specific heat capacity, etc. This can be done by discretizing the geometry into small parts called finite elements. The characteristics of each finite element are expressed through simple equations, which are derived from the system governing equations. The simple equations establish a connection between the nodal values of the finite elements and its physical behavior. The resulting equations set with adequate boundary conditions will be solved iteratively using numerical methods involving matrix algebra. These computations will be repeated until getting an acceptable solution, which has to satisfy a convergence condition (the convergence will be evaluated based on a well precise relative tolerance value).

Each set physics has its own partial differential equations. For instance, the laminar flow physics uses the mass conservation equation as well as the momentum conservation equation in vector forms. By setting the boundary conditions, the laminar flow interface will be used to compute the velocity and pressure fields.

The steps below will be followed for both the hydrodynamic and the FTPBR models.

- 1) Defining the system parameters and variables,
- 2) Creating geometries, using the geometry operation,
- 3) Adding the required physics: applying the conservation equations for mass, momentum, heat and concentrated species, as well as creating the reaction kinetics through the chemistry interface,
- 4) Meshing the domains (appropriate mesh sequence is required for accurate results) and
- 5) Solving the models by running the study

These steps will be developed for the two studies in the subsequent sections.

2.3 Hydrodynamic simulation: Pressure drop analysis in a slender packed bed reactor using CFD

In the hydrodynamic study, 2D and 3D simulations have been carried out. The 2D simulations use the classical porous media approach where the packed bed is represented by a continuous and homogeneous porous medium. The resistance source terms are applied as closure drag law models in the modified Navier-Stokes equation (for porous media).

The obtained sets of partial differential equations were solved for the macroscopic flow field in the PBR (i.e., 2D pseudo homogeneous models). The effect of the solid phase is incorporated in the model equations implicitly via the bed porosity and the implemented drag force sub-models. These closure relationships can influence considerably the computed values of pressure drop, especially for PBRs with low aspect ratio. A 2D porosity distribution function was considered and three drag force-sub models were tested, resulting in three axisymmetric pseudohomogeneous models (PHMs). The drawback of this conventional modeling approach is its dependency on closure sub-models, which were developed on the basis of parametric fitting. This involves finding coefficients (parameters) using a data set covering a limited range of operating conditions. Therefore, a new method was proposed, which is based on transforming the complex 3D structure into a conceptual 3D structure. This conceptual geometry preserves some geometrical information. Furthermore, it can be properly and easily transformed into a simple representative 2D structure, using cross section geometry operation, available in COMSOL Multiphysics software, as will be described, hereinafter. The main advantage of this new approach is that, it does not rely on any closure sub-models.

Concerning the 3D simulation, 3D Particle-Resolved Direct Numerical Simulations (PRDNS) have been carried out. The flow is supposed to be incompressible and laminar. The low Reynolds number flows are crucial for assessing the heat and mass transfer performances of PBRs. The Resolved-Particle Model (RPM) uses the original Navier-Stokes equations. In this case, no closures are required.

2.3.1 Generation of geometries

Three different geometries were created according to the space dimension (2D or 3D) and the type of the CFD model (Pseudo-homogeneous or Resolved-Particle). The created geometries are (A) a 3D real geometry of the packed bed, (B) a 2D geometry representing implicitly the bed domain and (C) a 2D geometry representing explicitly the bed domain.

A. Real 3D geometry: Cylindrical column packed with spherical particles

Identical-sized spheres are used and put one at a time into a cylindrical column with a diameter twice as large as the particle diameter. So that, one layer can accommodate only two tangential spheres. Then, the first two spheres stand on the column base, tangentially to its wall. The next two spheres are arranged in a such a way that, their centerlines make an

angle of 90° with that of the two spheres of the previous layer. This geometric arrangement is repeated for the subsequent layers up to the bed's top. This can be represented by repeating cells, having the same overall properties, particularly the void fraction. The void fraction within a single cell is equal to the overall porosity of the bed. The height of a unit cell, denoted by h^* , can be expressed in term of particle diameter as follows:

$$h^* = \frac{d_p}{\sqrt{2}} \quad (2.1)$$

The used total number of layers is 21 with a bed height to particle diameter ratio of about 15.14, which is sufficient to avoid column top and bottom effects on the porosity, although a desirable ratio should be greater than 20 [52]. To eliminate the entrance and the exit effects, the volume meshes was extended one cylinder diameter in the axial direction at the inlet and outlet [177] as shown in Figure (2.1a). The obtained results, which will be presented in the third chapter, confirm the fact that, considering 21 layers and extending the total reactor length (H) one cylinder diameter at the inlet and outlet, is sufficient for bulk unit cell pressure drop to reach a fully developed state. The spheres diameter was set to be equal 0.019 m, but it was reduced by 1% to avoid unsuitable thin cells near the contact points between particles as well as between particles and the cylinder wall, which may induce solution convergence problems. Due to symmetry of the system, simulations were run over one quarter of the geometrical domain to reduce the computational time.

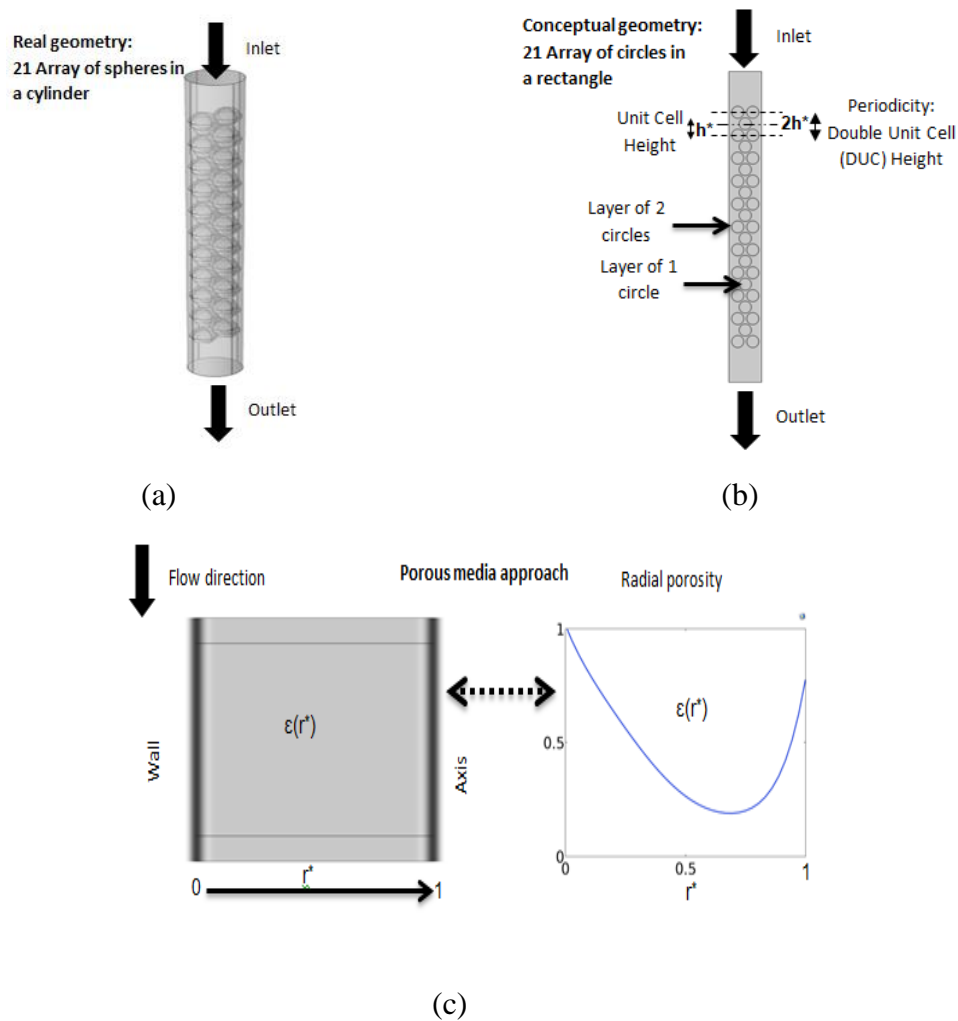


Figure 2.1: Geometries used in different modeling approaches: (a) Real geometry: Three-Dimensional Resolved-Particle Model (3D-RPM); (b) Conceptual geometry: Two-dimensional Resolved-Particle Model (2D-RPM); (c) Two-Dimensional axisymmetric: Pseudo-homogeneous Model (2D-PHM).

B. Axisymmetric rectangle: Flow in an empty tube

Concerning the 2D pseudo-homogeneous cases, there is no need to include any details of the bed structure, since the domain is considered continuous and homogeneous. In this case, the flow can be represented by a flow in an empty tube. Therefore, the geometry of the domain is an axisymmetric rectangular, as shown in Figure (2.1c). Based on the porous media approach, the effect of the bed textual properties on the flow is integrated into the transport equations via a porosity distribution function and drag force closure relationships.

C. Rectangle composed of an array of circles: Fictitious flow past an array of circular cylinders

Regarding the conceptual model, an imaginary 3D geometry was proposed. This alternative geometry, of the bed, has to satisfy two conditions. Firstly, it should capture to some extent the explicit description of the textual characteristics of the real bed geometry. Secondly, it can be easily transformed into a 2D geometry, by using the cross-section geometry operation available in COMSOL Multiphysics 5.6. Therefore, the proposed conceptual 3D geometry is a group of circular cylinders (hypothetical cylindrical particles), which will be positioned horizontally between two vertical parallel plates. This is as if the cylindrical reactor is bisected, vertically, into two identical stretched halves. This similarity can be put forward for two considerations. Firstly, the circular shape of the hypothetical cylindrical particles may capture the curvature of the real spherical particles. Secondly, the vertical plates surrounding the hypothetical cylindrical particles (in the conceptual geometry) could be in consistent with the column enclosing the spherical particles (in the real bed). The plate height is the same as that of the column and the distance between the plates is equivalent to the bed diameter. The number, position and diameter for the imaginary cylindrical particles determine the tortuous pattern and the void fraction distribution in the new 3D geometry. By using the cross-section geometry operation on the conceptual 3D domain, a fictitious 2D geometry was created. This latter is represented by a rectangle containing 32 mono-sized circles, as shown in Figure (2.1b), which are located as follows:

- The i -th Layer containing two circles ($i=1:11$):

$$x_{2i-1} = -x_{2i-1} = \frac{dp}{3} \quad (2.2)$$

$$y_{2i-1} = \frac{5dp}{2} + (2i - 2)h^* \quad (2.3)$$

- The j -th Layer containing one circle ($j=1:10$):

$$x_{2j} = 0 \quad (2.4)$$

$$y_{2j} = \frac{5dp}{2} + (2j - 1)h^* \quad (2.5)$$

Where x and y represent the coordinates of the circles centers.

The hypothetical circle diameter is determined assuming that, the hypothetical 2D unit cell porosity is equivalent to the real 3D unit cell porosity, as described in Appendix

A. This means that, the circles locations and the overall void fraction are the main geometrical information captured by the conceptual 2D geometry.

2.3.2 Meshing

Regarding the 3D modeling and due to the complex 3D geometry, the generated mesh consisted of free tetrahedral. Furthermore, to solve the viscous effects, the meshing is refined in a boundary layer at the fluid-particles and fluid-walls interfaces, which include two boundary layers to enhance the cells quality, without an excessive cell count [22–24]. Finally, a corner refinement procedure was also implemented to further refine the mesh and get a better resolution of the corners and edges in narrow regions.

Similarly, in order to attain a high-level accuracy of 2D simulations, the same meshing sequences were built, but free triangular shapes cells were used in the two-dimensional domains. In each of these studies, the mesh density was determined in a mesh independence study.

2.3.3 CFD modeling

A. Three and two-dimensional resolved particle models (3D-RPM and 2D-RPM)

The hydrodynamic model for both resolved-particle cases is described by Equations (2.6) and (2.7), which represent the continuity and the momentum balance equations, respectively.

$$\rho \nabla \cdot \vec{u} = 0 \quad (2.6)$$

$$\rho(\vec{u} \cdot \nabla) \vec{u} = \nabla \cdot [-p\bar{I} + \mu(\nabla \vec{u} + (\nabla \vec{u})^T)] + \rho \vec{g} \quad (2.7)$$

Where: ρ [kg.m⁻³], μ [kg.m⁻¹.s⁻¹] and \vec{g} [m.s⁻²] are the fluid density, fluid dynamic viscosity and gravity acceleration vector, respectively, \vec{u} [m.s⁻¹] and p [Pa] are the local velocity vector and pressure at any given position in the interstitial porous bed and in the extended inlet and outlet free volumes and \bar{I} is the unit matrix. Equation (2.7) is the standard Navier-Stokes equation for incompressible flow. Equations (2.6) and (2.7) were solved in the interstitial domain of the bed and the extended free domains, similarly to the model implementation carried out by Uribe and coworkers [118], [178]. An important aspect to highlight on the implemented model is that, there is no need to include any expressions for porosity distribution and fluid-solid drag, since the implemented model explicitly includes these parameters via the solid distribution and the solid walls boundary conditions. Hence, the solid phase distribution is required by implemented geometries

representation, as described in Figures (1a) and (1b). Additionally, the average fluid-solid interactions are assumed at the fluid-solid contact surface through setting the boundary conditions.

The boundary conditions set to the model were an inlet velocity (U_{in}), outlet pressure (P_{out}) and a non-slip condition at the column walls and at the fluid-solid interface (A_{fs}). Equations (2.8) to (2.10) describe the boundary conditions for equations (2.6) and (2.7).

$$\text{Inlet} \quad \vec{u}_{in} = -U_{in}\vec{n} \quad (2.8)$$

$$\text{Outlet} \quad [-p\bar{I} + \mu(\nabla\vec{u} + (\nabla\vec{u})^T)]\vec{n} = -P_{out}\vec{n} \quad (2.9)$$

$$\text{Walls and } A_{fs} \quad \vec{u} = \vec{0} \quad (2.10)$$

Where: \vec{n} is the normal vector. The boundary condition described by Equation (2.9) specifies that, the normal stress at the reactor outlet is equal to the outlet pressure, which was set to be 1 atm. It can be seen from Equation (2.10) that, the solids are considered as impermeable, and therefore a no-slip boundary condition was set at their surface.

In both resolved particle cases (I and II), which are illustrated in Table (2.1), the governing equations are the same, with the same physical properties, inlet, outlet and operating conditions. Thus, the possible differences in the macroscopic average behaviors, such as pressure drop, may result from differences between the real and the conceptual geometries.

Table 2.1: Simulated hydrodynamic cases

Case N°	Model type	Features
I	Resolved-particle (Real geometry): 3D- RPM	Three-Dimensional
		No closure sub-models
II	Resolved-Particle (Conceptual geometry): 2D-RPM	Two-Dimensional
		No closure sub-models
III	Pseudo-homogeneous: 2D-PHM_Ergun	Two-Dimensional
		Semi-empirical drag law by (Ergun, 1952)
		Porosity distribution function by (Mueller, 2010)
IV	Pseudo-homogeneous: 2D-PHM_Tang	Two-Dimensional
		First principle-based drag law by (Tang et al., 2015)
		Porosity distribution function by (Mueller, 2010)
V	Pseudo-homogeneous: 2D-PHM_ES	Two-Dimensional
		Semi-empirical drag law by (Eisfeld and Schnitzlein, 2001)
		Taking into account the wall effects
		Porosity distribution function by (Mueller, 2010)

B. Pseudo-homogeneous models (PHMs)

The hydrodynamic model of the pseudo-homogeneous cases is described by Equations (2.11) and (2.12), which represent the continuity and the momentum balance equations under the steady state operation conditions, respectively.

$$\rho \nabla \cdot \vec{U} = \vec{0} \quad (2.11)$$

$$\frac{1}{\varepsilon} \rho (\vec{U} \cdot \nabla) \vec{U} \frac{1}{\varepsilon} = \nabla \cdot \left[-P \vec{I} + \mu \frac{1}{\varepsilon} (\nabla \vec{U} + (\nabla \vec{U})^T) \right] + \left(\frac{\mu}{k_1} + \frac{\rho}{k_2} |\vec{U}| \right) \vec{U} + \rho \vec{g} \quad (2.12)$$

In these \vec{U} [m.s⁻¹], is the superficial average velocity vector, which is a hypothetical velocity of the flowing fluid in a free channel, and P [Pa] is the intrinsic average pressure.

Actually, Equation (2.12) is the Navier-Stokes-Darcy-Forchheimer equation which is the modification of the original Navier-Stokes equation (Equation (2.7)) [56], [179]. This modified transport equation includes additional terms, capturing the porous media information, which are the bed porosity, the Darcian ($k_1[\text{m}^2]$) and the non-Darcian ($k_2[\text{m}^2]$) permeabilities.

The boundary conditions set to the pseudo-homogeneous models are described by Equations (2.13) to (2.15)

$$\text{Inlet} \quad \vec{U}_{\text{in}} = -U_{\text{in}}\vec{n} \quad (2.13)$$

$$\text{Outlet} \quad \left[-P\vec{I} + \mu(\nabla\vec{U} + (\nabla\vec{U})^T) \right] \vec{n} = -P_{\text{out}}\vec{n} \quad (2.14)$$

$$\text{Walls} \quad \vec{U} = \vec{0} \quad (2.15)$$

Regarding the bed porosity, the analytical expression by [180] and the semi-analytical expression by [181] for the radial porosity distribution in packed bed with aspect ratio of 2 are benchmarks, with existing experimental data for mono-sized spheres. The void fraction in the bed with aspect ratio equal to 2 begins at unity at the wall, decreases to a minimum of 0.19 at a distance of around $0.68 \times d_p$ from the wall, and then increases to reach unity at the bed's axis, as illustrated in Figure (2.1c). In fact, this geometrical parameter is an average property, so that, the expressions that forecast radial variations are actually forecasting the average profile of an average property.

The second important variable is permeability, which measures the capacity and the ability of a porous medium to transmit a fluid [182]. In another way, it measures the resistance to flow caused by the porous medium structure [56]. Actually, there exist two permeabilities, as appearing in the right-hand side of Equation (2.12), which are well described as follows:

$$k_1 = \frac{\varepsilon^3}{\alpha S_V^2 (1 - \varepsilon)^2} \quad (2.16)$$

$$k_2 = \frac{\varepsilon^3}{\beta S_V (1 - \varepsilon)} \quad (2.17)$$

In these, $S_V = 6/d_p$ (1/m) is the solid particles specific area and $\alpha (-)$ and $\beta (-)$ are viscous and inertial parameters, respectively, which depend on the single-phase flow tortuosity factor [58].

In fact, the second term in the right side of Equation (2.12) may represent the pressure drop per unit length of the PBR, called also momentum transfer or drag force. Three drag force models were applied, which are illustrated in Table (2.2). While Ergun

and Einfeld and Schnitzlein correlations are semi-empirical, Tang model was developed, using the Immersed Boundary Method (IBM) [183]. This first principle-based model is considered as the best possible expression of the drag force, in static mono disperse arrays of spheres for $Re_p \leq 1000$ [184]. It is noteworthy that, the drawback of the Ergun and Tang models is that, they do not consider the column wall effect.

COMSOL Multiphysics uses the Forchheimer equation, to account for the momentum transfer term, written as:

$$\frac{\Delta P}{L} = \frac{\mu}{k_1} U + \frac{c_f \rho}{\sqrt{k_1}} U^2 \quad (2.18)$$

Where $c_f (-)$ is the Forchheimer coefficient that accounts for inertia drag.

The first and the second terms in the right side in Equation (2.18) represent the viscous and the kinetic energy losses, respectively. Confronting this Equation with the momentum transfer term in Equation (2.12), leads to the following equality:

$$k_2 = \sqrt{k_1}/c_f \quad (2.19)$$

User defined functions, in COMSOL Multiphysics, was used to define the Darcian permeability, and the Forchheimer coefficient of the three drag laws tested in the 2D pseudo-homogeneous models, which are summarized in Table (2.2).

Table 2.2: Drag force sub-models

Drag law	Darcian permeability (k_1)	Forchheimer coefficient (c_f)	Model parameters
Ergun (1952)	$\frac{\varepsilon^3 d_p^2}{A_{Ergun}(1-\varepsilon)^2}$	$\frac{B_{Ergun}(1-\varepsilon)}{\varepsilon^3 d_p} \sqrt{k_1}$	$A_{Ergun} = 150$ $B_{Ergun} = 1.75$
Einfeld and Schnitzlein (2001)	$\frac{\varepsilon^3 d_p^2}{eE^2(1-\varepsilon)^2}$	$\frac{E(1-\varepsilon)}{\hat{E} \varepsilon^3 d_p} \sqrt{k_1}$	$e = 154, \acute{e} = 1.15, e'' = 0.87$ $E = 1 + \frac{2}{3\gamma(1-\varepsilon)},$ $\acute{E} = (\acute{e}\gamma^{-2} + e'')^2$ $\gamma = 2$
Tang et al., 2015	$1/A_{Tang}^{(1)}$	$B_{Tang}^{(2)}$	-

$$^{(1)}A_{Tang} = 180 \frac{(1-\varepsilon)^2}{\varepsilon^3 d_p^2} + 18(1-\varepsilon) \frac{\varepsilon}{d_p^2} (1 + 1.5\sqrt{1-\varepsilon})$$

$$^{(2)}B_{Tang} = 18(1-\varepsilon)(0.11(2-\varepsilon)(1-\varepsilon) - \frac{0.00456}{\varepsilon^4} + \left(0.169\varepsilon + \frac{0.0644}{\varepsilon^4}\right) Re_p^{-0.343}) \left(\frac{1}{\varepsilon d_p}\right)$$

2.3.4 Numerical setup

Simulations were conducted using the steady-state incompressible solver for the laminar flow available in COMSOL Multiphysics 5.6. All models were tested at low particle Reynolds numbers (Re_p), ranging from $Re_p = 27$ to $Re_p = 111$, which correspond to laminar steady flow conditions [33], [69], [185]. The convergence was evaluated based on relative tolerance of 0.001. A consistent mesh independence study was performed for the 3D simulations (Case I), to ensure the accuracy of the results as well as to determine the asymptotic pressure drop values (See Appendix B). Besides, 2D simulations were conducted on extremely-finer meshes, where the grid is refined in stages until no significant differences in results occur between two successive grid refinement stages. The simulations were performed on an Intel(R) Core (TM) i5-7200U CPU@ 2.50 GHz 2.71 GHz, 8 Go RAM. Figure (2.2) shows a flow chart of the basic steps of the 2D and 3D programs developed using COMSOL Multiphysics 5.6.

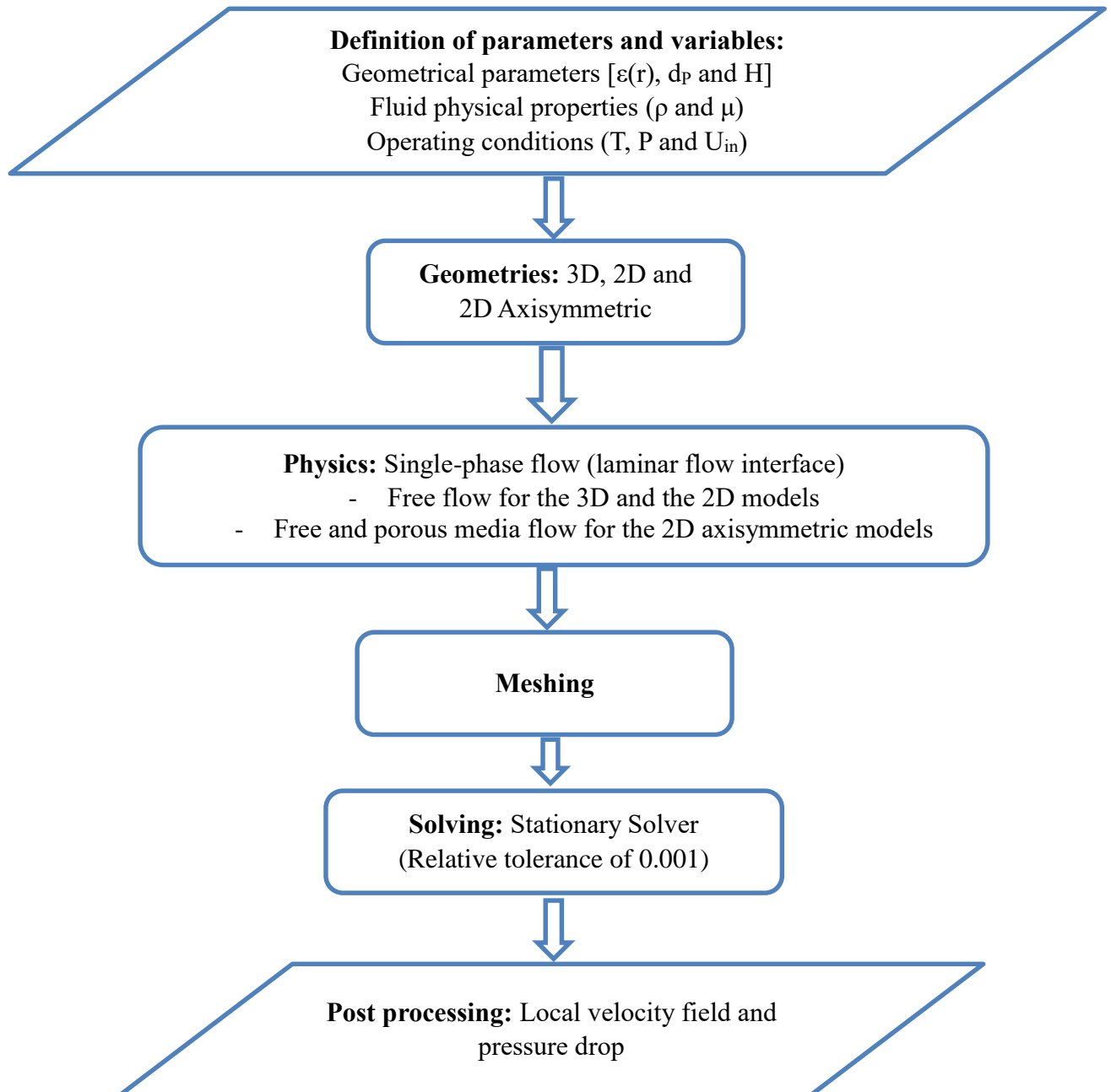


Figure 2.2: Flow chart of the hydrodynamic simulations

2.4 Case study of Fischer-Tropsch Synthesis in packed bed reactors

Generally, a sophisticated model that describes the FT reaction in a packed bed reactor includes mass and momentum conservation coupled with heat and mass transfer equations as well as reaction kinetics model. The model's objective was to determine the reactor temperature, carbon monoxide conversion and products yields. The model validity will be studied by comparing the predicted results by the current model and models from literature. Based on the reactor model, the influence of syngas content, tube diameter, feed flow rate and inlet/cooling temperature on the behavior of the reactor will be investigated.

2.4.1 The Fischer-Tropsch MultiTubular Packed Bed Reactor (FT-MTPBR)

A multitubular packed bed reactor for Fischer-Tropsch reaction has been modeled in this work, as illustrated in Figure (2.3). The characteristics of the multitubular packed bed reactor of the baseline case and the operating conditions are listed in Table (2.3). These data are relevant to the Arbeitsgemeinschaft (AGRE) packed bed process. It has been adopted in this study for comparison and validation reasons by the model of Jess and Kern (2009) [174] and the model of Lee and Cheng (2012) [108]. Because the tubes are parallel, identical and there is no interaction between the tubes, the work will be focusing on single tube, as depicted in the right hand of Figure (2.3). Therefore, a Fischer-Tropsch Packed Bed Reactor (FTPBR) model will be developed, on a single tube process.

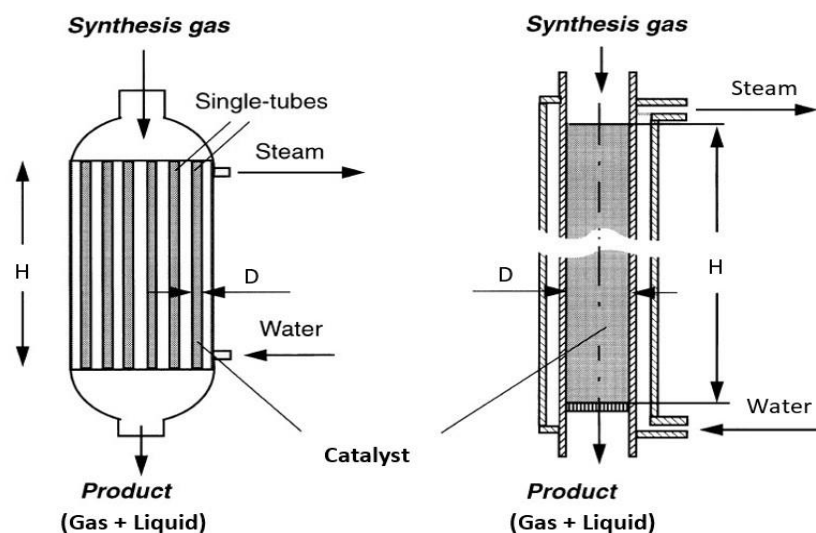


Figure 2.3: MTPBR and single tube demonstration for FTS: reproduced from Jess et al.

[186]

Table 2.3: Characteristics of the baseline case FT-MTPBR and the operating conditions [108], [174]

Feed superficial velocity	0.55 m s ⁻¹ (of the baseline case)
Total pressure	24 bars
Operating temperature	198-260 °C
Reactor type	Tubes-and-shell
Catalyst shape	Spherical
Catalyst	Cobalt based
Diameter of single tube (D)	46 mm
Tube thickness	5 mm
Solid particles diameter	3 mm
Packed bed mean porosity	0.3415
Total number of tubes	2000
Height of tubes (H)	1200 mm
Bulk density of catalyst bed	700 kg m ⁻³
Inlet concentration of Hydrogen	66.66 (vol.-%)
Inlet concentration of Carbon monoxide	33.33 (vol.-%)
Feed kinematic viscosity, ν_{feed}	4.10 m ² s ⁻¹
Feed thermal conductivity, λ_{feed}	0.16 W m ⁻¹ K ⁻¹
Effective radial thermal conductivity, λ_{rad}	6.3 W m ⁻¹ K ⁻¹
Feed specific heat capacity, C_p	30 J mol ⁻¹ K ⁻¹
Wall internal heat transfer coefficient, $\alpha_{w,\text{int}}$ (tube to wall)	900 W m ⁻² K ⁻¹
Wall thermal conductivity (steel), λ_{wall}	50 W m ⁻¹ K ⁻¹
Wall external heat transfer coefficient, $\alpha_{w,\text{ent}}$ (wall to boiling water)	1600 W m ⁻² K ⁻¹
Wall thermal transmittance, U_{wall}	1380 W m ⁻² K ⁻¹
Overall thermal transmittance, U_{overall}	364 W m ⁻² K ⁻¹

2.4.2 Simplifying assumptions

The assumptions below will be considered in order to develop the current FTPBR model:

1. No changes over time (Steady state operation)

2. No shear at the gas-liquid interface, therefore, both gas and liquid phases flow at the same velocity [108]
3. The mixture-averaged diffusion model is considered, and the diffusion due to thermal gradients is neglected [159]
4. Heavier hydrocarbons, starting from C7, forms the liquid phase [108]
5. The liquid phase is supposed to be represented by C₁₆H₃₄ [29]
6. The cooling boiling water is assumed to flow fast enough, to maintain its temperature at a constant value [16], [159]
7. The product distribution follows the ASF model and only alkanes are considered
8. The value of the chain growth probability is 0.9 (to maximize diesel yield).

2.4.3 Geometry generation

Figure (2.4) represents the generation of the simulated geometry in COMSOL Multiphysics 5.6. Zooming in from the left to the right of the figure, a 2D axisymmetric plane (or rectangle) was generated. Considering this simplified geometry, rather than simulating the 3D tube or the 2D plane is an effective way to save the computation cost in terms of processing memory and computing time. The width of the 2D axisymmetric plane is equal to the half of the tube diameter ($D/2$), and its length is equal to the tube height (H)

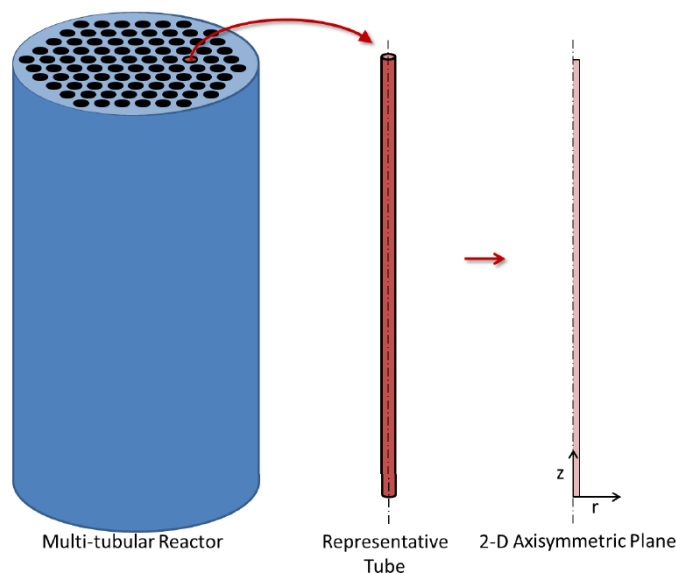


Figure 2.4: Generated geometry of the FTPBR model: J. W. Pratt [159]

2.4.4 Mesh generation

COMSOL Multiphysics has significant meshing capabilities to discretize complex computing domains, which can be tweaked and optimized by the user, as required. The mesh utilized has a crucial impact on the capacity to solve the problem numerically, rapidly and accurately. Applying a coarser mesh will accelerate convergence. Nevertheless, a too-coarse mesh can generate instabilities inside the model, perhaps making it worse. Unstructured quadrilateral mesh on boundaries and on the 2D domain was generated, by adding the Free Quad node. This mesh type has a higher aspect ratio than that of triangular mesh, which has an aspect ratio of unity (ratio between the longest and the shortest edges). Therefore, a better resolution near the wall boundary will be obtained, when applying the Free Quad node. In order to determine the suitable mesh density, a consistent mesh independence study was carried out.

2.4.5 Governing equations

In this section, the governing equations, in differential forms, used to model the FT reactor will be presented. An axisymmetric 2D multiphase pseudo-homogeneous model has been developed, to simulate the FTPBR. The flow across a single tube packed with catalyst particles will be modeled as two-phase downward flow. The Eulerian-Eulerian approach is recommended to model macroscale flow processes occurring in packed bed reactors crossed by a single or Two-phase flow [2]. The Eulerian mixture method, which is one of the Eulerian-Eulerian approaches, has been used in this study. In this method, each phase is considered as interpenetrating continuum, without looking for the precise location of the interfaces between the gas, the liquid and the solid phases [187]. In every point within the bed, the mixture properties, such as fluid density and dynamic viscosity, will be calculated. Hereinafter, all the transport equations will be written under steady state conditions, relying on assumption N° 1.

❖ The continuity equation

The continuity equation, also called the mass conservation equation, can be written as follows:

$$\nabla \cdot (\rho_m \vec{U}_m) = 0 \quad (2.20)$$

The mixture density, ρ_m [$\text{kg} \cdot \text{m}^{-3}$] and the mixture velocity, \vec{U}_m [$\text{m} \cdot \text{s}^{-1}$] are given by:

$$\rho_m = S_g \rho_g + S_l \rho_l \quad (2.21)$$

$$\vec{U}_m = \frac{(S_g \rho_g \vec{U}_g + S_l \rho_l \vec{U}_l)}{\rho_m} = \vec{U}_g = \vec{U}_l = \vec{U} \quad (2.22)$$

Where ρ_g [kg. m⁻³] and ρ_l [kg. m⁻³] are the gas and liquid densities, respectively. S_g [-] and S_l [-] are the gas and liquid saturations. \vec{U}_g [m. s⁻¹] and \vec{U}_l [m. s⁻¹] are the mass-averaged velocity vectors of the gas and the liquid phases, respectively. Equation (2.20) is used for compressible flows, in steady state operations. Equalities (2.22) hold true, relying on assumption N° 2.

❖ The momentum conservation equation

The conservation of momentum equation, also called a force balance equation, is mathematically, described by the modified Navier-Stokes equation, for flows in porous media. Its physical interpretation is based on Newton's second law, which is averaged over a Representative Elementary Volume (REV). The REV must satisfy two conditions. From the one hand, its length scale must be far smaller than the tube size. On the other hand, the REV must be large enough to generate representative averaged values [188], [189]. For higher values of the modified Reynolds number, under the turbulent flow regime conditions, the brinkman equation can be deduced, written as [190]:

$$\frac{1}{\varepsilon} \rho_m (\vec{U} \cdot \nabla) \vec{U} \frac{1}{\varepsilon} = \nabla \cdot \left[-P \vec{I} + \mu_m \frac{1}{\varepsilon} (\nabla \vec{U} + (\nabla \vec{U})^T) - \frac{2}{3} \mu_m \frac{1}{\varepsilon} (\nabla \cdot \vec{U}) \vec{I} \right] + \left(\frac{\mu_m}{k_1} + \frac{\rho_m}{k_2} |\vec{U}| \right) \vec{U} + \rho_m \vec{g} \quad (2.23)$$

Where: μ_m [Pa. s] is the mixture dynamic viscosity, given as follows:

$$\mu_m = \rho_m \sum \omega_i \frac{\mu_i}{\rho_i} \quad (2.24)$$

Where: μ_i [Pa. s] is the dynamic viscosity of species (i)

Equation (2.23) is applied to compute the mixture fluid velocity and pressure fields, within a single tube packed with catalyst particles. The Einfeld and Schnitzlein and the Ergun correlations, to account for the momentum transfer term in porous media, will be applied in the current model. While the first will be used for slender packed beds, the second will be applied for the large packed bed. This has been demonstrated by the results of hydrodynamic simulations, which will be presented in the third chapter.

❖ The species conservation equation

The transport of concentrated species equation is used to study gaseous and liquid mixtures where the species concentrations are the same order of magnitude and no one of the species can be identified as solvent. The driving force of each species depends on the

mixture composition, temperature and pressure. The transport equation solves for the mass fractions of all the participating species. The basic equation for the conservation of mass of a species 'i', under steady state conditions, is as follows:

$$\rho_m(\vec{U} \cdot \nabla)\omega_i = -\nabla \cdot \vec{j}_i + r_i \quad (2.25)$$

Where ω_i [-]: the mass fraction of species (i), r_i [$\text{kg} \cdot \text{m}^{-3} \cdot \text{s}^{-1}$]: the consumption or production rate of species (i) and \vec{j}_i [$\text{kg} \cdot \text{m}^{-2} \cdot \text{s}^{-1}$] is the mass flux vector of species (i). Relying on assumption N° 3, the equation that describes the diffusion of species (i) can be written as follows:

$$\vec{j}_i = -\rho_m D_i^m \nabla \omega_i - \rho_m \omega_i D_i^m \frac{\nabla M_m}{M_m} + \rho_m \omega_i \sum_k \frac{M_i}{M_m} D_i^m \nabla X_k \quad (2.26)$$

In Equation (2.26), D_i^m [$\text{m}^2 \cdot \text{s}^{-1}$] represents the mixture-averaged diffusion coefficient of species (i), given as:

$$D_i^m = \frac{1 - \omega_i}{\sum_{k \neq i} \frac{X_k}{D_{\text{eff},i,k}}} \quad (2.27)$$

Where X_k [-] is the molar fraction of species 'k' and $D_{\text{eff},i,k}$ [$\text{m}^2 \cdot \text{s}^{-1}$] is the effective binary diffusion coefficient, given as [191]:

$$D_{\text{eff},i,k} = \frac{\varepsilon}{\tau_b} D_{i,k} \quad (2.28)$$

Actually, the effective binary diffusion coefficient can be considered as a correction of the binary diffusion coefficient $D_{i,k}$ [$\text{m}^2 \cdot \text{s}^{-1}$], called also the molecular diffusion coefficient [174], to take into account the porous medium domain properties, in terms of bed porosity, ε [-], and bed tortuosity, τ_b [-].

In Equation (2.28) the ratio bed porosity to tortuosity, can be calculated using different models available in COMSOL Multiphysics 5.6, such as the tortuosity model. For temperatures ranging between 200 and 260 °C, which is the temperature condition of the current study, this ratio can be taken as [174]:

$$\frac{\varepsilon}{\tau_b} = 0.3 \quad (2.29)$$

Besides, in Equation (2.26) M_m [$\text{kg} \cdot \text{mol}^{-1}$] represents the mixture molecular weight, given as:

$$M_m = \left(\sum \frac{\omega_i}{M_i} \right)^{-1} \quad (2.30)$$

Where: M_i [$\text{kg} \cdot \text{mol}^{-1}$] is the molecular weight of species (i).

❖ Heat conservation equation

The equation of conservation of heat in porous medium, also called temperature equation in porous medium domain, corresponds to the convection-diffusion equation with thermodynamic properties averaging models, to account for both solid matrix and fluid properties. It can be written, for steady state operations, as follows:

$$\rho_f C_{P,m} \vec{U} \cdot \nabla T + \nabla \cdot \vec{q} = Q \quad (2.31)$$

Where: T [K] is the medium temperature, $C_{P,m}$ [$J \cdot kg^{-1} \cdot K^{-1}$] is the mixture specific heat capacity, which can be expressed in terms of individual species' specific heat capacity $C_{P,i}$ [$J \cdot kg^{-1} \cdot K^{-1}$] as follows:

$$C_{P,m} = \sum \omega_i C_{P,i} \quad (2.32)$$

Where: Q [$W \cdot m^{-3}$] is the heat source, given by Equation (2.33)

$$Q = -\Delta H_{FT} \Gamma_{FT} \quad (2.33)$$

And \vec{q} [$W \cdot m^{-2}$] is the conduction heat flux vector, given by:

$$\vec{q} = -\lambda_{eff} \nabla T \quad (2.34)$$

In Equation (2.34), λ_{eff} [$W \cdot m^{-1} \cdot K^{-1}$] is the effective thermal conductivity, defined by an averaging model to take into account both solid matrix and fluid properties. Using the volume averaging method, it can be calculated as follows:

$$\lambda_{eff} = (1 - \varepsilon) \lambda_s + \varepsilon \lambda_{f,m} \quad (2.35)$$

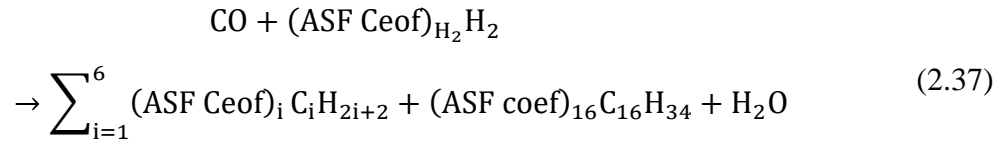
Where: λ_s [$W \cdot m^{-1} \cdot K^{-1}$] is the solid catalyst thermal conductivity and $\lambda_{f,m}$ [$W \cdot m^{-1} \cdot K^{-1}$] is the fluid mixture thermal conductivity, given as

$$\lambda_{f,m} = \rho_m \sum \frac{\omega_i}{\rho_i} \lambda_i \quad (2.36)$$

Where: ρ_i [$kg \cdot m^{-3}$] and λ_i [$W \cdot m^{-1} \cdot K^{-1}$] are the mass density and the thermal conductivity of the i -th species, respectively.

❖ Chemistry

This section provides the mathematics applied for modeling chemical species and reaction systems. The generated variables, in terms of reaction rate and thermodynamic properties will be communicated to the other interfaces (physics). Based on assumption N^o 7, the full FT reaction implemented in COMSOL Multiphysics is as follows:



Where: $(\text{ASF Ceof})_{\text{H}_2}$ and $(\text{ASF Ceof})_i$ are the stoichiometric coefficients of hydrogen and the i^{th} species, which can be calculated using the following expressions [16], [192]:

$$(\text{ASF Ceof})_{\text{H}_2} = 3 - \alpha \quad (2.38)$$

$$(\text{ASF Ceof})_i = (1 - \alpha)^2 \alpha^{(i-1)} \quad 1 \leq i \leq 6 \quad (2.39)$$

$$(\text{ASF Ceof})_i = (1 - \alpha) \alpha^6 \quad i \geq 7 \quad (2.40)$$

Based on hypothesis N°: 8, the calculated values are summarized in Table (2.4)

Table 2.4: Stoichiometric coefficients of the FT reaction

Species	Stoichiometric coefficient (v_i)
CO	-1
H ₂	-2.1
CH ₄	0.01
C ₂ H ₆	0.009
C ₃ H ₈	0.008
C ₄ H ₁₀	0.007
C ₅ H ₁₂	0.007
C ₆ H ₁₄	0.006
C ₁₆ H ₃₄	0.053
H ₂ O	1

The sum of all stoichiometric coefficients of Equation (2.37), expressed as a function of chain growth probability is [193]:

$$\sum_{i=1}^{\infty} (\text{ASF Ceof})_i = 1 - \alpha \quad (2.41)$$

For $\alpha=0.9$ (using assumption N° 8):

$$\sum_{i=1}^{\infty} (\text{ASF Ceof})_i = 0.1 \quad (2.42)$$

This means that, for each consumed molecule of CO, the total number of molecules of hydrocarbon produced is 0.1 molecules.

The FT reaction enthalpy was taken from [194], [195]. The authors considered the following value:

$$\Delta_{\text{FT}}H = -165 \text{ [kJ. mol}^{-1}\text{]} \quad (2.43)$$

The FT reaction kinetics rate model, applied in this study, is the one used by Jess et al. (2009), given as follows [108], [174]:

$$r_{m,H_2,eff} = \eta_{pore} k_{m,H_2} C_{H_2,g} \quad (2.44)$$

Where: $r_{m,H_2,eff}$ [mol. kg_{cat}⁻¹. s⁻¹] is the effective consumption rate of hydrogen, η_{pore} [-] is the effectiveness factor, given by Equation (2.45), $C_{H_2,g}$ [mol. m⁻³] is the concentration of hydrogen in the gas phase and k_{m,H_2} [m³. kg_{cat}⁻¹. s⁻¹] is the pseudo first-order reaction rate constant, given by Equation (2.47).

$$\eta_{pore} = \frac{\tanh \phi}{\phi} \quad (2.45)$$

In Equation (2.45), ϕ [-] is the Thiele modulus, given as by Equation (2.46).

$$\phi = \frac{V_P}{A_P} \sqrt{\frac{k_{m,H_2} \rho_P}{D_{eff,H_2,l} \frac{RT}{H_{H_2}}}} \quad (2.46)$$

Where V_P [m³], A_P [m²], and ρ_P [kg. m⁻³] are the volume, external surface area and density of catalyst particles, R [J. mol⁻¹. K⁻¹] is the universal ideal gas constant, H_{H_2} [Pa. m³. mol⁻¹] is the Henry coefficient for hydrogen, which has a value of around 20000 under the current conditions of pressure and temperature [174] and $D_{eff,H_2,l}$ [m² s⁻¹] is the effective diffusion coefficient of hydrogen in the FT liquid products, calculated using Equation (2.28).

$$k_{m,H_2} = k_{m,H_2,LH} \frac{C_{CO,g}}{(1 + K_{CO} C_{CO,g})^2} \quad (2.47)$$

In Equation (2.47), $k_{m,H_2,LH}$ [m⁶. mol⁻¹. kg⁻¹. s⁻¹] is the rate constant of the Langmuir-Hinshelwood equation for FT on Cobalt and K_{CO} [m³. mol⁻¹] is the adsorption coefficient of CO. The values of these two constants are given as follows [174]:

$$k_{m,H_2,LH} = 0.8 e^{-\frac{37400}{RT}} \text{ [m}^6 \cdot \text{mol}^{-1} \cdot \text{kg}^{-1} \cdot \text{s}^{-1}\text{]} \quad (2.48)$$

$$K_{CO} = 5 \cdot 10^{-9} e^{\frac{68500}{RT}} \text{ [m}^3 \cdot \text{mol}^{-1}\text{]} \quad (2.49)$$

The FT reaction kinetics model written in Equation (2.44), which represents the amount of hydrogen consumed per unit time per unit catalyst mass, can be expressed in term of CO-moles consumed per unit time per unit bed volume, as follows:

$$r_{CO,eff} = \left(\frac{1}{2.1}\right) r_{m,H_2,eff} \rho_P (1 - \epsilon) \quad (2.50)$$

2.4.6 Boundary conditions

In this section, the boundary conditions of the three transport-physics will be set as follows:

❖ Brinkman equations (mass and momentum conservation)

The boundary conditions set to the model were an inlet velocity (U_{in}), outlet pressure (P_{out}) and a non-slip condition at the column wall. Equations (2.51) to (2.53) describe the boundary conditions for Equation (2.23).

$$\text{Inlet} \quad \vec{U}_{in} = -U_{in}\vec{n} \quad (2.51)$$

$$\text{Outlet} \quad \left[-P\vec{I} + \mu(\nabla\vec{U} + (\nabla\vec{U})^T) \right] \vec{n} = -P_{out}\vec{n} \quad (2.52)$$

$$\text{Column wall} \quad \vec{U} = \vec{0} \quad (2.53)$$

❖ Transport of concentrated species

The boundary conditions set to the model were inlet species mole fractions ($X_{i,in}$), an outlet condition and a no flux condition at the column wall. Since no recycle streams was considered, the mole fractions of the products at the bed inlet were set to be zero. Equations (2.54) to (2.56) describe the boundary conditions for Equation (2.25).

$$\text{Inlet} \quad X_{i,in} = X_{i,0} \quad (2.54)$$

$$\text{Outlet} \quad \vec{n} \cdot \rho_m D_i^m \nabla \omega_i = 0 \quad (2.55)$$

$$\text{Column wall} \quad -\vec{n} \cdot \vec{J}_i = 0 \quad (2.56)$$

❖ Transport of heat

At the inlet of the FT reactor, the temperature of the gaseous mixture is set to equal that of the cooling medium [16], [159], [195]. Based on assumption N° 6, Equalities (2.57) can be written.

$$\text{Inlet} \quad T_{in} = T_{cool} = \text{const} \quad (2.57)$$

At the reactor outlet, there is no heat flow across this boundary, thus the outlet condition can be written as:

$$\text{Outlet} \quad -\vec{n} \cdot \vec{q} = 0 \quad (2.58)$$

Furthermore, the heat removed from the system can be represented by the following boundary condition, at the tube wall:

$$\text{Column wall} \quad -\vec{n} \cdot \vec{q} = U_{\text{Overall}}(T_{\text{cool}} - T) \quad (2.59)$$

Where: U_{overall} [$\text{W} \cdot \text{m}^{-2} \cdot \text{K}^{-1}$] is the overall heat transfer coefficient.

Equations (2.57) to (2.59) describe the boundary conditions for Equation (2.31).

2.4.7 Numerical simulations

Simulations were conducted using the steady-state compressible solver for the fourth physics developed, hereinbefore. COMSOL Multiphysics 5.6 was used for solving the set of differential equations, based on the finite element method. The convergence was evaluated based on relative tolerance of 0.001. Different FTPBR models were simulated, under multiple operating conditions, which are illustrated in Table (2.5).

Table 2.5: Operating conditions of FT reactors simulations

Model Parameter	Unit	Value/range
Feed superficial velocity (% U_{base})	[$\text{m} \cdot \text{s}^{-1}$]	8.39-270
Total pressure	[bar]	24
Operating temperature	[$^{\circ}\text{C}$]	198-260
Catalyst shape		Spherical
Catalyst		Cobalt based
Bed Aspect Ratio (AR)	[-]	2-15.33
Solid particles diameter	[mm]	3
Packed bed mean porosity	[-]	0.3415-0.5286
Height of tube (H)	[m]	2-12
Density of catalyst	[$\text{kg} \cdot \text{m}^{-3}$]	1063
H ₂ to CO ratio	[-]	1.5 to 3
Wall thermal conductivity (steel), λ_{wall}	[$\text{W} \cdot \text{m}^{-1} \cdot \text{K}^{-1}$]	50
Solid particle thermal conductivity, λ_{s}	[$\text{W} \cdot \text{m}^{-1} \cdot \text{K}^{-1}$]	10 [196], [197]
Solid particles specific heat capacity, $C_{\text{p,s}}$	[$\text{J} \cdot \text{mol}^{-1} \cdot \text{K}^{-1}$]	600 [195]

The wall thickness for each packed bed model was calculated using Barlow's formula [198].

The simulations will provide information about the effects of packed bed characteristics (particle diameter and bed porosity), the feed composition and velocity as well as the inlet/cooling temperature, on the reactor performance. Similarly, to the

hydrodynamic simulations, the simulations were performed on an Intel(R) Core (TM) i5-7200U CPU@ 2.50 GHz 2.71 GHz, 8 Go RAM.

Figure (2.5) shows a flow chart of the basic steps of the bi-dimensional FTPBR program developed using COMSOL Multiphysics 5.6.

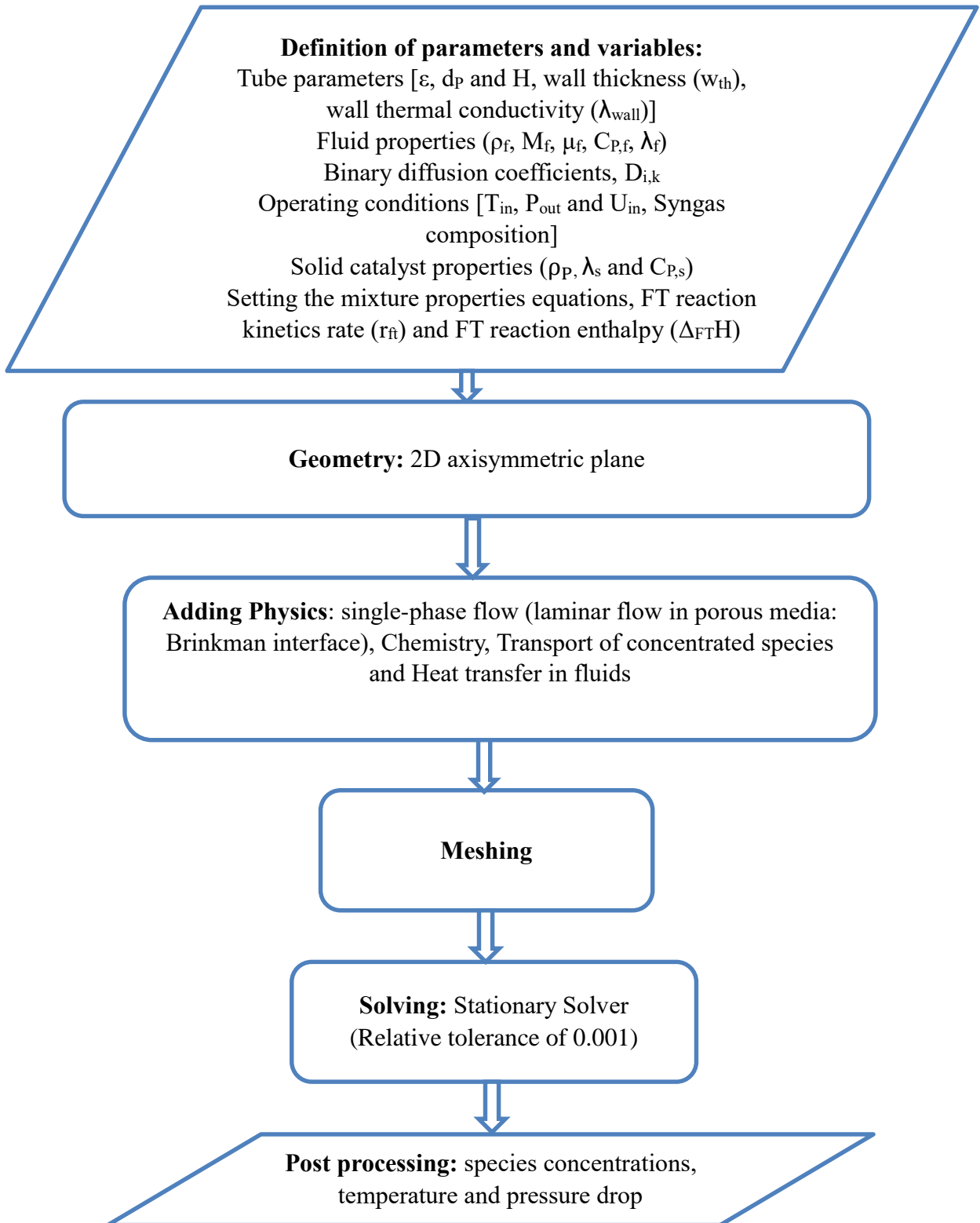


Figure 2.5: Flow chart of the FTPBR reactor simulation

2.5 Conclusion

In this chapter, two studies were done.

Firstly, cold flow models of a slender packed bed reactor were developed and simulated. Two CFD approaches were applied, which are the pseudo-homogeneous and resolved particle methods. While the former requires a closure relationships of porosity distribution and drag force sub-models, the later uses the direct numerical simulation, without any closures. The simulations were run for incompressible laminar flow conditions, using COMSOL Multiphysics 5.6.

Secondly, a Fischer-Tropsch Packed Bed Reactor (FTPBR) model crossed by two-phase reacting flow was developed. The mixture-Eulerian modeling approach was adopted. Therefore, the mixture properties in terms of density, molecular weight, dynamic viscosity, specific heat capacity, effective thermal conductivity and effective species diffusivity were developed. Then, four physics were applied, which are the Brinkman equation interface under laminar flow physics, chemistry, the transport of concentrated species and the transport of heat in porous media. The resulting set of differential equations was solved using the finite element method. COMSOL Multihysics 5.6 was used for computations. For each of the two studies, a flow chart describing the modeling and the simulations methodology was presented.

CHAPTER III

RESULTS AND DISCUSSION

3.1 Introduction

In this chapter, the results and their discussion will be presented. The main objectives are as follows:

1. Validate the 3D hydrodynamic model,
2. Confronting the results of the 3D simulation against those of the 2D simulations in order to investigate the appropriate drag force sub-model as well as to examine the proposed 2D new modeling approach,
3. Investigate the Fischer-Tropsch synthesis at the large scale, when processing associated natural gas of a small oil field, in Algeria, within the framework of developing new small and remote gas-associated oil fields, and
4. Design an FT reactor for small-scale applications, which can transform syngas delivered from biomass into liquid fuels, within the limits of data and equipment availability.

We will start by presenting the results of hydrodynamic study. The results of the 3D simulations, in term of local velocity field, will be presented and discussed. Once the 3D model is validated by experimental values from literature and a consistent error discretization uncertainty analysis, it will be used to validate the 2D simulations. Pressure drop was used as the hydrodynamic key parameter for validating the 2D simulations against the accurate 3D model. The comparison results will be presented and the new 2D modeling approach will be discussed.

After that, in order to have an overall insight about the FT kinetics, under the ideal conditions, the FT kinetics was investigated in the 0th dimension (0D). Next, the hydrodynamic results were implemented in the momentum balance equation to simulate the FT reaction in a packed bed reactor, crossed by a concurrent gas-liquid down-ward flow. The model equations already set in the second chapter, including the momentum equation, will be used to simulate the whole FT process occurring in the packed bed reactor.

Firstly, a consistent mesh independence study will be conducted. It is a way of validating when the experimental data are scarce or not available. Later, the developed model will be confronted against models from literature.

Secondly, the large-scale FT reactor will be optimized, regarding the optimum packed bed aspect ratio.

Finally, a small-scale FT reactor will be designed and optimized, regarding the amount of biomass to be processed as well as the packed bed aspect ratio.

3.2 Hydrodynamic study

In the hydrodynamic study, the 3D and 2D simulations were conducted. The obtained results will be presented and discussed.

3.2.1 Validation of the Three Dimension Resolved Particle Model (3D-RPM)

The developed 3D hydrodynamic model will be validated in terms of local velocity field by two ways, which are: (i) comparison with the model of Robbins et al. (2012) [185] and (ii) conducting a consistent error discretization uncertainty study

❖ **Local flow validation: Comparison between the 3D-RPM model and Robbins' CFD model with respect to experimental data of literature.**

The simulated results in terms of axial particle Reynolds (Re_p) number by the 3D-RPM model, using COMSOL Multiphysics 5.6, were compared to those by Robbins et al [185], with respect to its flow-field data obtained using magnetic resonance imaging (MRI) applied on a 2D slice in the middle of the packed bed, as shown in Figure (3.1a). In the experiments of Robbins et al., Water was forced into the packed bed, firstly, through a preconditioning zone, where the full parabolic velocity profile was established, secondly, through the bed and thirdly, through an exit zone to avoid reversed flow induced by recirculation at the boundary. The simulation parameters of our hydrodynamic study presented in the previous chapter, in terms of packed bed characteristics and operating conditions, are the same applied by Robbins et al, who used a 3-D unstructured finite-volume method code, developed in-house at Cambridge University, called 'NEWT' and written in FORTRAN.

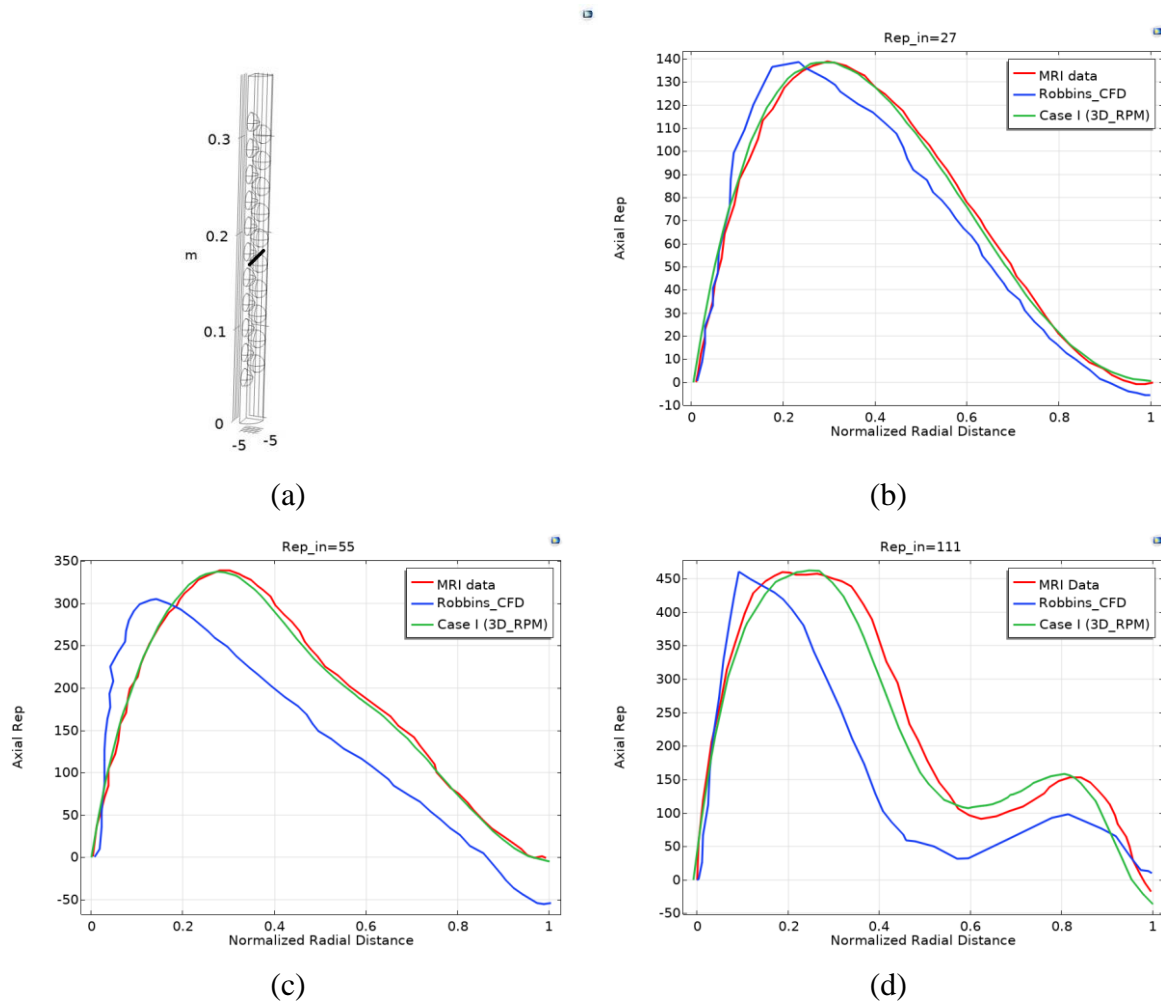


Figure 3.1: Comparison between the 3D-RPM and Robbins' CFD models, with respect to MRI data in term of axial Reynolds particle number as a function of normalized radial distance for different inlet Re_{P_in} values: (a) line graph position, (b) $Re_{P_in}=27$, (c) $Re_{P_in}=55$ and (d) $Re_{P_in}=111$

Readers who are interested in the experimental details may refer to the work by Robbins [185]. The authors scaled up the local axial particle Reynolds number for the MRI by $2.19/2$ to take into account the oversizing of their CFD model geometry with a factor of 5%. Since our 3D model geometry is undersized, the calculated local axial particle Reynolds number was scaled up by $(2.19/2 * (1 - 0.01))$.

Figures (3.1b), (3.1c) and (3.1d) show the variation of the axial particle Reynolds number predicted by the two CFD models and the MRI-derived data through the arc length of the line graph highlighting the velocity maxima of the computed flow field, which is shown in Figure (3.1a).

It is clearly observed that, the peaks in all the graphs are translated toward the wall of the geometry, demonstrating a higher velocity gradient. Besides, the green and the red

lines are almost superimposed namely for inlet $Rep=27$ and $Rep=55$, indicating that, the current model showed the best fits to the MRI data. To have a quantitative assessment, the Mean Relative Deviation (MRD) of the averaged axial Rep , over the arc length of the line graph, predicted by the two CFD models in reference to MRI data were calculated and presented in Table (3.1).

Table 3.1: Mean Relative Deviation of the predicted axial Rep : Comparison between the current 3D model and Robbin's CFD model, with respect to MRI data

Inlet Rep	Robbins_CFD	3D-RPM (current model)
27	7.3%	2.2%
55	25.3%	0.5%
111	30.2%	3.7%

While the MRD of the 3D-RPM model varies slightly between 2.2% and 3.7%, the MRD of Robbins' model changes significantly between 7.3% and 30.2%, demonstrating an excellent agreement between the 3D-RPM model and the MRI data, in comparison with the model by Robbins. This might be, because the reactor used in the CFD simulations by Robbins was relatively short (5 layers, as opposed to 21 layers in our CFD model and 69 layers in the MRI experiments) which prevents the velocity components to approach a fully developed state solution.

The great discrepancy observed for the $Rep=111$, could be due to the grid size not being able to resolve all the transitioning elements of the flow field. The case of $Rep=111$ is close to the observed onset of flow instability (transition to unsteady flow), as has been verified by the MRI experiments.

❖ Estimation of discretization errors of the 3D simulations

In the following, the discretization error estimates in the 3D simulations, in term of pressure drop, were calculated and reported. It is a way of validation when experimental data are scarce or not available for comparison [199]. Assessing the accuracy of code and calculations requires that the grid is sufficiently refined to the extent that the solution is within the asymptotic range of convergence. This can be checked by observing two grid convergence index (GCI) values as computed over three grids, as described in Appendix B. The GCI is a measure of the percentage the computed value is away from the asymptotic

value. A small value of GCI indicates that the solution is within the asymptotic range. This can be further checked by fulfilling the solution accuracy condition written as follows [37]:

$$\frac{GCI_{32}}{r_{21}^m GCI_{21}} = 1 \quad (3.1)$$

Where: $r_{21}^m [-]$ is a grid refinement factor.

Then the reason to trust the accuracy of a numerical simulation is validated and the solution is independent of the mesh size.

Table (3.2) displays results of asymptotic pressure drop, grid convergence index and the solution accuracy check for the tree inlet Rep values. Here, the pressure drop values were calculated in the bulk region of the bed where the flow is fully developed, as it will be demonstrated in the following section.

Table 3.2: Mesh independence study: Error estimates in 3D simulations, in term of pressure drop, at different inlet Rep values

Results	Rep_in=27	Rep_in=55	Rep_in=111
Asymptotic pressure drop value, $\Delta P_{\text{asyp}} [\text{Pa}]$	2.71	6.91	20.48
$GCI_{21} [\%]$	0.23	0.84	4.44
Solution accuracy condition, $\frac{GCI_{32}}{r_{21}^m GCI_{21}} [-]$	1.000	1.003	1.007

Overall, the solution accuracy condition ratio is almost equal to one for all the inlet Rep values, thus the solutions are within the asymptotic ranges of convergence. In term of grid convergence index, for all cases, GCI_{21} is lower than 4.5%, having the smallest value for Rep_in=27. The observed higher values of GCI_{21} for Rep_in=111, comparing to the other cases, could be attributed to the grid size not being able to capture all the information of the flow field. Using the asymptotic pressure drop values as well as their respective GCIs, the exact solution of pressure drop through the packed bed can be written as:

$$\Delta P_{\text{exact}} = \Delta P_{\text{asyp}} \frac{(100 \pm GCI_{21})}{100} \quad (3.2)$$

3.2.2 Comparison of pressure drop simulated results

The predicted results of pressure drop by the 3D simulations (Case I) and the 2D simulations (Cases II-V) could be obtained by calculating the difference in the radially-

averaged pressure between the inlet and outlet bed boundaries. However, to eliminate any entrance and exit effects on the results, pressure drop should be calculated between two stages in the bed within a region where the flow becomes fully developed.

The geometrical domains were divided into a number of cut planes (for the 3D domain) or cut lines (for the 2D domains) with distances between two successive planes or lines of $z_{i+1} - z_i = h^*/10$ or $y_{i+1} - y_i = h^*/10$, respectively. Next, the pressures were measured by computing the average pressure on each cross section or line graph, at a level z or y , respectively. The elementary pressure drop results were then calculated by subtracting two sequential averaged pressure values.

Figures (3.2a), (3.2b) and (3.2c) show the change in frictional pressure drop, simulated for all cases, as a function of the normalized axial distance, at inlet Re_p values of 27, 55 and 111, respectively. It can be seen that, for the three inlet Re_p values tested, the observed behaviors of the five models are different.

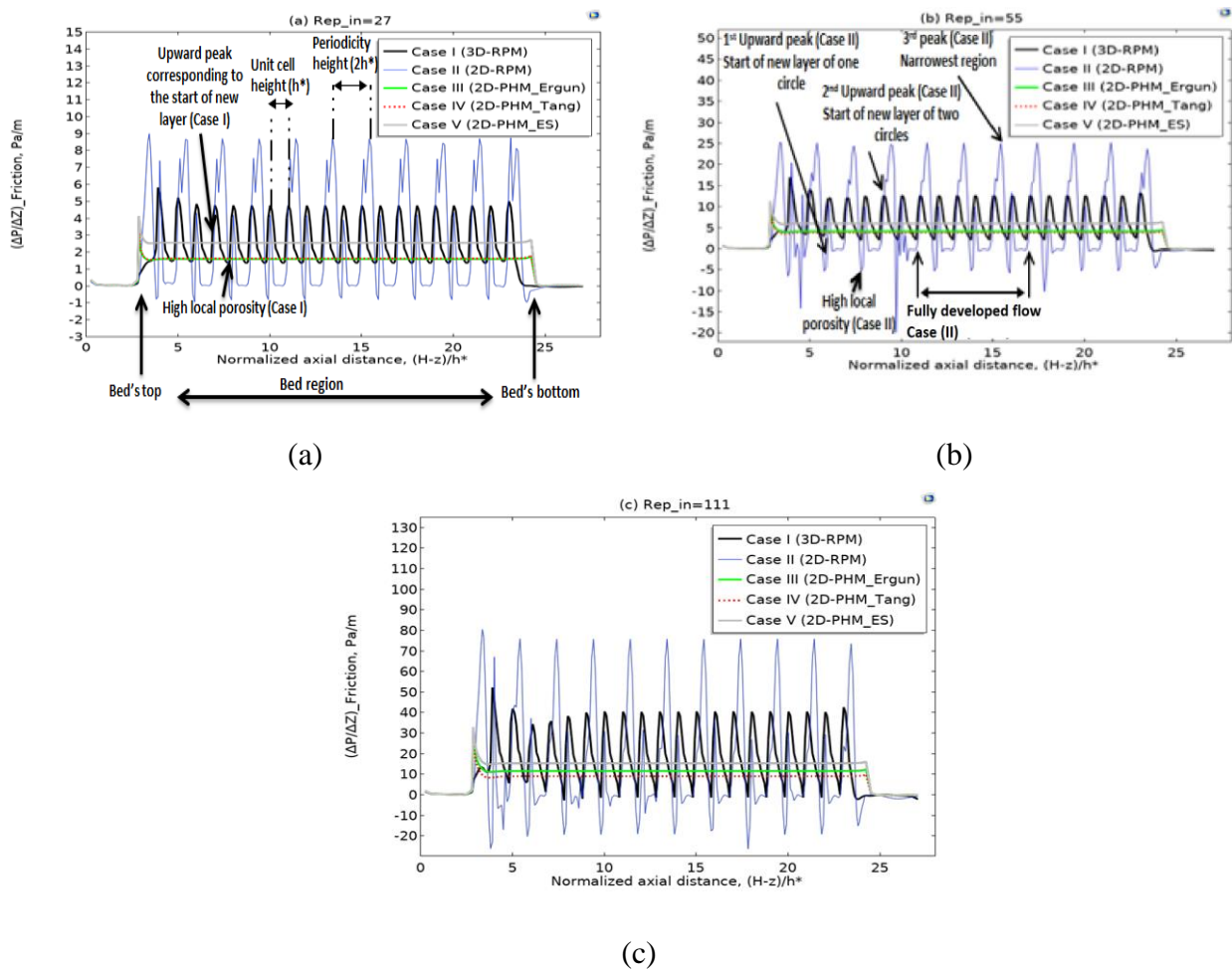


Figure 3.2: Comparison of frictional pressure drop simulated results as a function of normalized axial distance, for all cases at different inlet Re_p values: (a) 27, (b) 55 and (c)

111.

Concerning the pseudo homogeneous models, Cases (III, IV and V) show a smoother variation of the frictional pressure drop profile along the bed length. The observed peaks at the bed boundaries are due the transition between the free and the porous zones. Differently, both of the resolved-particle cases exhibit important fluctuations inside the bed region. These fluctuations are of a greater extent for Case II, which are generated by substantial variations in the textual characteristics of the fictitious 2D geometry comparing to the real domain in Case I. Each upward peak of Case I coincides with the start of a new layer. Similarly, each first and second upward peak in Case II coincides with the start of new layers containing one and two circles, respectively. Additionally, while the peaks in Case I and the third peaks in Case II correspond to the narrowest regions within the bed, the low points in both cases coincide with high local porosity regions. Moreover, it can be seen clearly that, while the black curves show a periodicity every regular interval of one unit cell height, the blue one exhibits it every regular interval of Double Unit Cell (DUC) height. Furthermore, the height of the repeating parts, of both curves, becomes stable toward the bulk region of the bed where the flow is becoming fully developed (see Figure (3.2b) and Figure (3.3b)). This means that the averaged pressure drops, for both cases, over a DUC height become constants within the bulk region of the bed, where any entrance and exit effects may be eliminated.

Figures (3.3a), (3.3b) and (3.3c) give information about the variation in frictional pressure drop every double unit cell height within the bed region, for all cases at inlet particle Reynolds number of 27, 55 and 111, respectively. As initial remark, the simulated frictional pressure drop has to some extent similar trends for all the models and for all the three inlet Rep values.

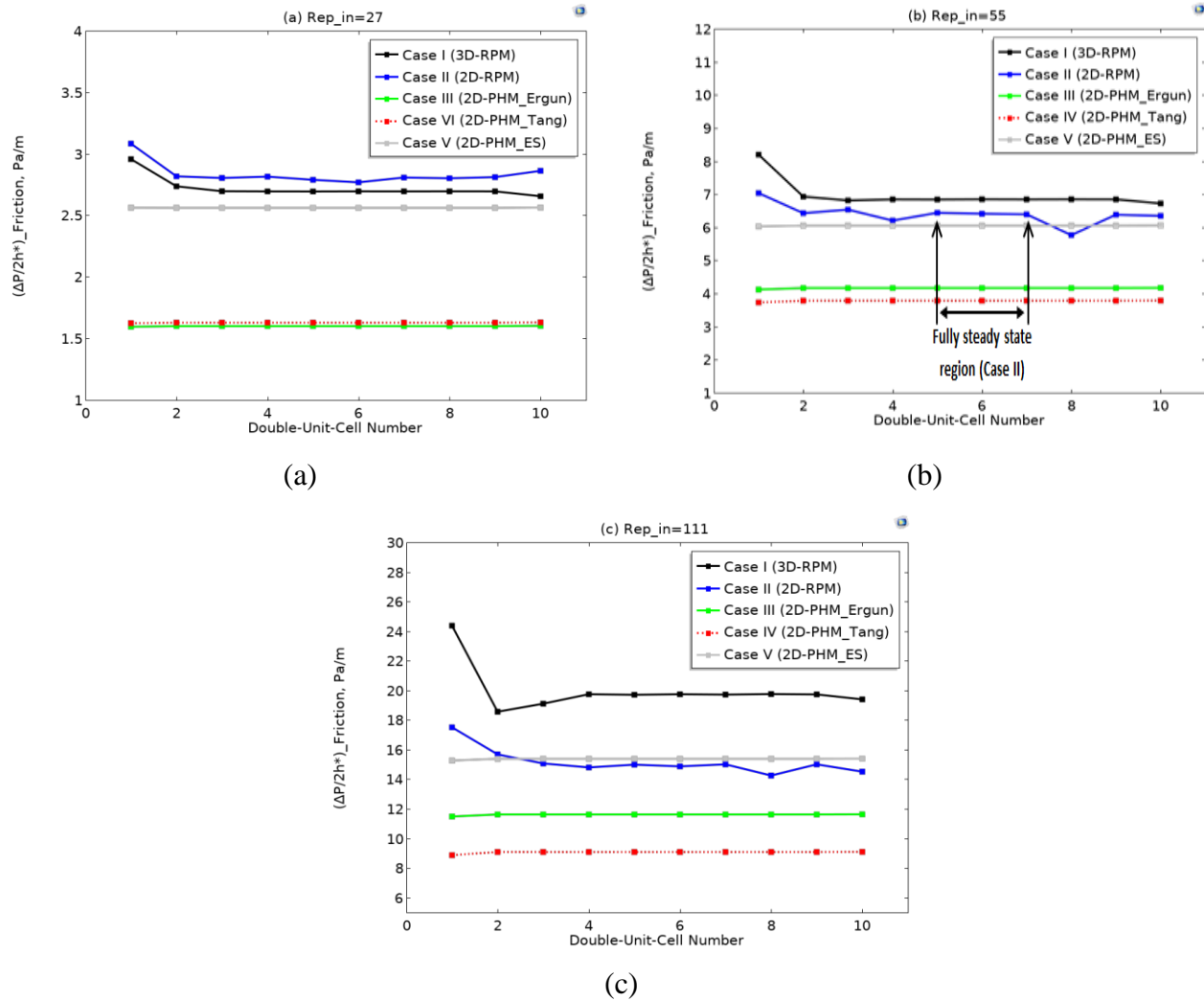


Figure 3.3: Comparison of frictional pressure drop simulated results as a function of Double-Unit-Cell number for all cases at different inlet Rep values: (a) 27, (b) 55 and (c) 111.

All the pseudo homogeneous cases showed constant Double-Unit-Cell (DUC) pressure drop profiles $(\Delta P/2h^*)$ between the second DUC and the last DUC, which are represented by straight lines. The lower values through the first DUC are attributed to the redistribution of flow toward the low local porosity regions, mainly near the column wall. These variations are of greater extent in the resolved-particle Cases (I and II), which exhibit more instability of the DUC pressure drop simulated results within the bed region compared to the pseudo homogeneous Cases (III, IV and V). This may be explained by the strong influence of the bed's textual characteristics in the Resolved-Particle cases. Nevertheless, for both cases, the simulated DUC pressure drop leveled out in the bulk region of the bed, where any impacts of the bed's entrance and exit can be eliminated, mainly for Case I. For instance, the simulated DUC pressure drop profile by Case II is

stable between the fifth and the seventh DUC, as shown in Figure (3.3b), which correspond to the eighth and the fourteenth layers, as shown in Figure (3.2b). Therefore, to make an effective comparison between all cases, the DUC pressure drop should be calculated in the middle of the bed, to eliminate any entrance and exit effects.

The bar chart, in Figure (3.4), illustrates the mean relative deviation (MRD) of the predicted pressure drop results by the 2D simulations (Cases II, III, IV and V) with respect to the 3D simulations (Case I), for inlet particle Reynolds numbers of 27, 55 and 111.

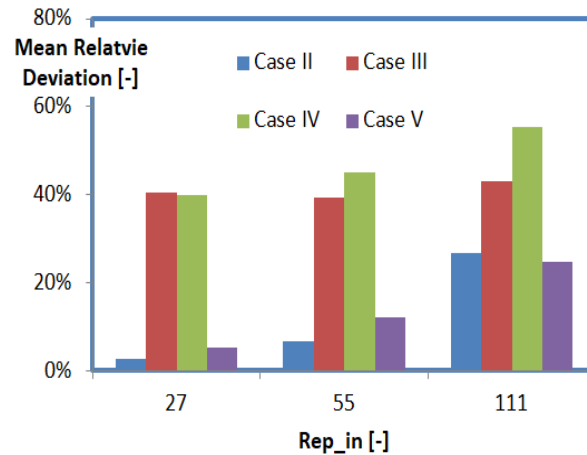


Figure 3.4: Mean Relative Deviation (MRD) of the simulated pressure drop results in Cases (II, III, IV and V) in reference to Case I at different inlet Rep values.

Overall, Case II and to a lower extent Case V showed the best fits to Case I, concerning the bulk pressure drop, for all the inlet Rep values. In Case II, the MRD was about 3% at inlet Rep of 27, then it increased to around 7% at inlet Rep of 55, being the lowest values, and continued to increase reaching almost 27% at inlet Rep of 111. Similarly, the MRD by Case V was about 5% at inlet Rep of 27, and then it rose to around 12% at inlet rep of 55, being the second lowest values, and increased further achieving nearly 25%, at inlet Rep of 111. While, the MRD of both Cases (II and V) did not exceed 27% for all the inlet Rep tested, the MRDs by Cases (III and IV) did not fall below 39%. These findings can be attributed to the wall effects, which is well taken into consideration by Case II, through the 2D imaginary geometry, and by Case V, using the ES semi-empirical correlation.

These results were the subject of an article published in « The International Journal of Multiphysics » under the title « Pressure Drop Analysis of Incompressible Laminar Flow in a Low Aspect-Ratio Packed Bed Using CFD Simulations »

3.3 Results of the case study: modeling and simulation of Fischer-Tropsch Packed Bed Reactor

Before simulating the FT reactor, one should investigate about the kinetics of the FT reaction on some ideal conditions.

3.3.1 Kinetics of the FT reaction: Effect of the temperature on the CO consumption rate

To evaluate the FT kinetic rate, independently of the reaction medium, the FT reaction (Equation (2.37)), was simulated in Zero Dimension space (0D), under isothermal and adiabatic conditions.

❖ Isothermal conditions

Figure (3.5) illustrates the predicted evolution, over time, of CO consumption rate, for different values of reaction temperature, under isothermal conditions. The temperature varies between 220 C° and 250 °C, covering almost all the temperature range of the current study. Generally, for all the temperature values, the molar fraction of CO decreases, inconsistently, from the same initial value (33.33%) to different final values. The final values are around 3.5%, 4%, 5.5% and 11% for reaction temperature values of 250, 240, 230 and 220, respectively. This can be attributed to the fact that; the FT reaction is highly exothermic which tends to be faster as the reaction temperature increases. Another important remark is that, for all the cases, the CO fraction drops sharply during the first stage of the FT reaction. For instance, at a temperature of 250 °C, the CO fraction falls from 33.33% to 6% in 50 seconds. Over the next same period, it falls from 6% to 3%.

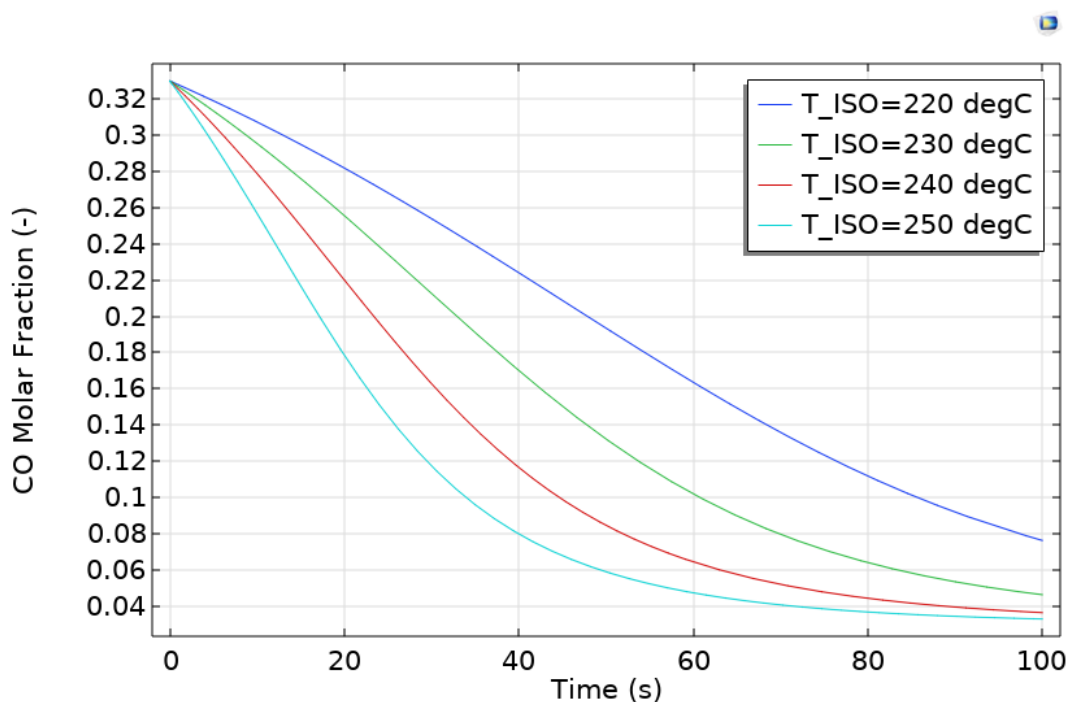


Figure 3.5: Predicted CO consumption rate versus time, under isothermal conditions:
Effect of reaction temperature ($H_2/CO=2$)

Taking this remark into consideration, it can be concluded that, almost all the CO is consumed during the first stage of the FT reaction. This finding may provide important information about the behavior of a cylindrical-shape FT reactor. It is expected that, almost all the CO will be consumed in the first few meters of a tubular Fischer-Tropsch packed bed reactor.

❖ Adiabatic conditions

To investigate the thermal behavior of the FT reaction, Equation (2.37) was simulated in 0D space, under adiabatic conditions. The results in term of adiabatic temperature profile over time are presented in Figure (3.6).

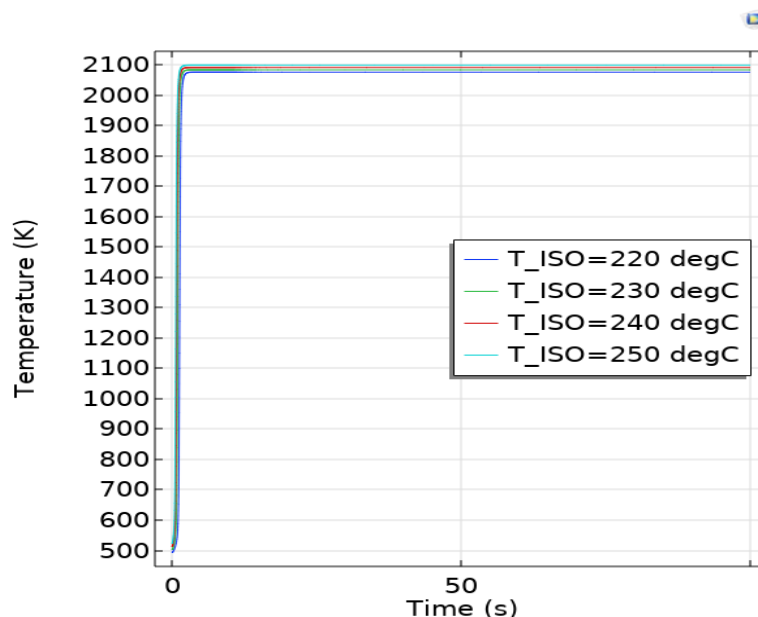


Figure 3.6: Evolution of adiabatic temperature over time, for different initial temperature values ($H_2/CO=2$)

Assuming that, the kinetic model defined by Equations (2.44) to (2.50) as well as the FT reaction enthalpy defined by Equation (2.43) are invariants regarding temperature, the evolution of adiabatic temperature over time was simulated and presented in Figure (3.6). As seen in Figure (3.6), for all the initial temperature values, the dramatic jump of the simulated temperature occurs during the initial stage of the FT reaction, reaching nearly 2100 K, which is higher than that reported by Zhu et al [200], which was 1750 K. The difference between these two values may be attributed, mainly, to the implemented mixture specific heat capacity. While in our model, using COMSOL Multiphysics 5.6, the thermodynamic system functionality was applied to calculate the temperature-dependent mixture specific heat capacity, Zhu et al considered a fixed mixture specific heat capacity of the reactants. This sudden and significant increase in temperature reflects the strong exothermicity of the FT reaction. Reaction runaway and catalyst damage are the unwanted effects of such adiabatic operation. To prevent this rise of temperature, excess produced heat must be removed. Using a multitubular packed bed reactor with a strong cooling system is an effective way to carry out an FT reaction. To further enhance the heat removal, a multitubular packed with slender tubes can be utilized. This allows optimum operation near the catalyst deactivation temperature, few degrees lesser than 260 °C, and results in high FT reactor performance.

3.3.2 Mesh independence study

The mesh independence study is essential for ensuring convergence, enhancing the accuracy of the solution, and establishing what can be considered an acceptable computational time for the numerical model. The initial convergence of the numerical model presents one of the most significant challenges in the solution process. Therefore, it was advantageous to begin with a relatively coarse mesh to facilitate rapid convergence, followed by refining the mesh in subsequent computational iterations.

To ensure the independence of the results from the mesh density during the optimization of both the solution and the solution time, it was essential to perform a mesh and convergence test utilizing the Grid Convergence Index (GCI) methodology, as explained in Appendix B. In contrast to conventional techniques employed in computational fluid mechanics, such as Richardson Extrapolation, which necessitates the mesh sizes to be doubled, meaning that each successive mesh size is altered by a factor of two [201], the Grid Convergence Index (GCI) offers an estimation of discretization error even when the refinements of the mesh are not integer multiples. In this section, the discretization error estimates in the 2D simulations, in terms of maximum temperature (T_{\max}) and CO conversion rate (X_{CO}), were calculated and reported. As previously mentioned, it is a way of validation when experimental data are not often available for comparison.

So that, three grid sizes were chosen, to discretize the domain and run the simulations, as presented in Table (3.3). In order to accomplish a representative mesh independence study for all the simulations in this work, the mesh independence study was performed using the baseline feed velocity as well as for H_2 to CO ratio of 1.5, which correspond to the highest particle Reynolds number. At these conditions, the errors of computations are the highest, as proved by the hydrodynamic simulations. Therefore, all the results of simulations of this study, in terms of maximum reactor temperature and CO conversion rate, will be within the asymptotic ranges of convergence. It is worthy to note that, the turbulent flow regime within the bed bulk region is taken into account through the turbulent terms, in the drag expressions by Ergun or Einfeld and Schnitzlein.

Figures (3.7a) and (3.7b) present the simulated axial reactor temperature profile along the bed length as well as the radial CO conversion rate along the bed's exit, for the three different meshing sizes.

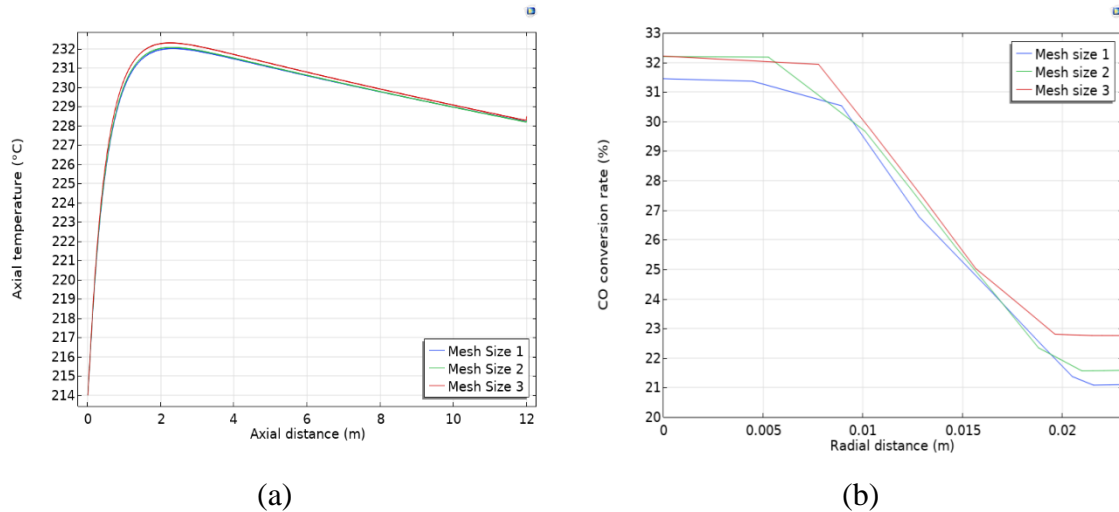


Figure 3.7: Effect of grid size on results (a) axial reactor temperature profile and (b) CO conversion rate profile at the bed's exit: $U=0.55$ m/s, $H_2/CO=1.5$ and $T=214$ °C

As it can be seen from the above figures, there are slight differences between the axial temperature and exit CO conversion rate profiles, for the three grid sizes. This is a qualitative comparison between the simulated results, with respect to the grid size. The question that can be asked now is: to what extent these results may change, when varying the mesh density? For this reason, we had to make a quantitative comparison using the GCI methodology. The statistics about the three generated meshing sequences are presented in Table (3.3).

Table 3.3: Data used for the GCI methodology

Grid size (mm)	h_1 (fine)	h_2 (medium)	h_3 (coarse)
	2.836	4.164	6.251
Number of cells (Quads)	N_1	N_2	N_3
	34300	15911	7060
Computation time (s)	3503	564	176
	Results		
T_{Max} (°C)	232.009	232.069	232.303
X_{CO} (%)	25.27	25.54	26.12

Following the GCI methodology, described in Appendix B, the three values of the grid size with their associated number of cells as well as the simulated results in terms of maximum reactor temperatures and CO conversion rates were used to compute the asymptotic values.

Table (3.4) presents the asymptotic values of the maximum reactor temperature and the CO conversion rates, with their associated Grid Convergence Index on the fine grid $(GCI)_{\text{Fine}}$ and on the medium grid $(GCI)_{\text{Medium}}$.

Table 3.4: Mesh independence study: Asymptotic values of maximum reactor temperature and CO conversion rate with their associated GCIs

	$T_{\text{Max}} (^{\circ}\text{C})$	$X_{\text{CO}} (\%)$
Asymptotic value	231.98	24.98
$GCI_{\text{Fine}} [\%]$	0.013	0.12
$GCI_{\text{Medium}} [\%]$	0.045	0.24

Actually, the asymptotic values are the expected solution values when using zero grid size, as shown in Figures (3.8a) and (3.8b).

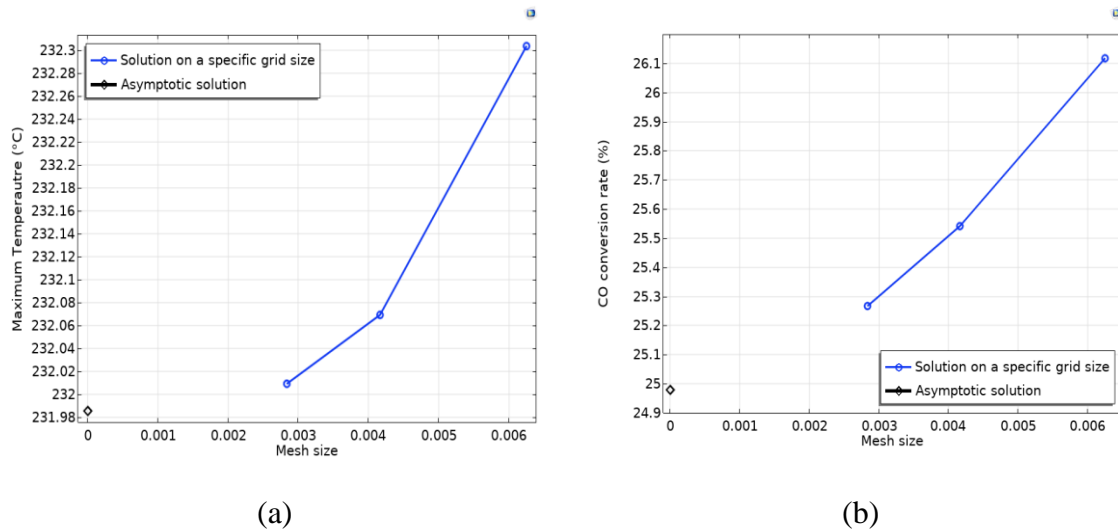


Figure 3.8: Mesh independence tests for (a) maximum reactor temperature and (b) CO conversion rate

From Table (3.4), the expected solution values of the maximum reactor temperature and CO conversion rate were 231.98 °C and 24.98 %, respectively. Furthermore, the information provided by the GCIs values indicates how the computed values are far from the expected exact solution values, which can be explained as follows:

- If we use the finer grid, the computed values of maximum reactor temperature and CO conversion rate can be considered with maximum relative errors of 0.013% and 0.12%, respectively.
- If we use the medium grid, the computed values of averaged reactor temperature and CO conversion rate can be considered with maximum relative errors of 0.045% and 0.24%, respectively.

The second important factor when deciding which grid size may be adopted for running simulations is the computed time. It can be seen clearly from Table (3.3) that, using a medium grid size may reduce the simulations time about three-fold when using the finer grid size. Taking these findings into consideration, the medium grid size was selected for running the simulations.

3.3.3 Comparison between the current model and models from literature

This section is addressed to present and discuss the simulation results of the developed mathematical model set out in chapter II. Our simulated results were compared against those obtained by the comprehensive model of Lee and Cheng (2012) as well as the benchmark model of Jess and Kern (2009). The parameters of comparison were the axial temperature, CO conversion rate and products yield. It is noteworthy that, the model of Lee and Cheng was validated, with regard to the model by Jess and Kern (2009), which is considered as a benchmark model in the literature. It was found that, the model of Lee and Cheng generally predicts slightly lower temperatures and CO conversion rates, compared to the simulated results by Jess and Kern. The major difference between our model and the model of Lee and Cheng is that, the former considered the ASF distribution of products, whereas the later used its specific product distribution model. The effects of H₂ to CO ratio, feed velocity and coolant temperature were investigated.

❖ Effects of cooling/inlet temperature on the axial temperature profile and CO conversion

The effects of inlet/cooling temperature on the predicted axial temperature profile and CO conversion rate, using our model and the two models of literature, along the bed axis was studied at three different temperatures, which are 200, 210 and 214 °C. The results are presented in Figures (3.9) and (3.10). Overall, the predicted results of axial temperature and CO conversion rate, by all models, increase with the increase of the cooling/inlet temperature. This is expected as the kinetic rate is proportional to the reacting medium temperature. As the FT reaction progresses along the FT reactor, the temperature increases, which by turn leads to further increase of the reaction kinetics rate and so on. This can be manifested by the sharp increase near the bed inlet, to a maximum value. Additionally, the peaks recorded at the highest temperature (214) °C, are shifted to a more downstream position compared to those observed at 210 and 200 °C.

Furthermore, it can be seen clearly that for all the inlet/cooler temperature values, the trends predicted by the three models are similar, mainly for the lower temperature (200 °C). Under this operating temperature, the line graphs by the current model and that by Jess and Kern are almost identical. Whereas, the predicted results by Lee and Cheng are slightly lesser. For the higher inlet/cooling temperature, the three graphs reach maximum values of about 260, 251 and 245 °C, at distances of about 4, 4.5 and 2.7 meters far from the bed inlet. Then the predicted axial temperatures, by the three models, decrease because of the increasing of the averaged specific heat capacity of the mixture due to the production of heavier products. This is can be confirmed by the findings presented in Figure (3.11), which shows the fraction of the products with different carbon numbers, as will be explained hereinafter. Furthermore, because of the progressing of the FT reaction along the bed length, the reactants concentrations as well as the heat released rate decrease.

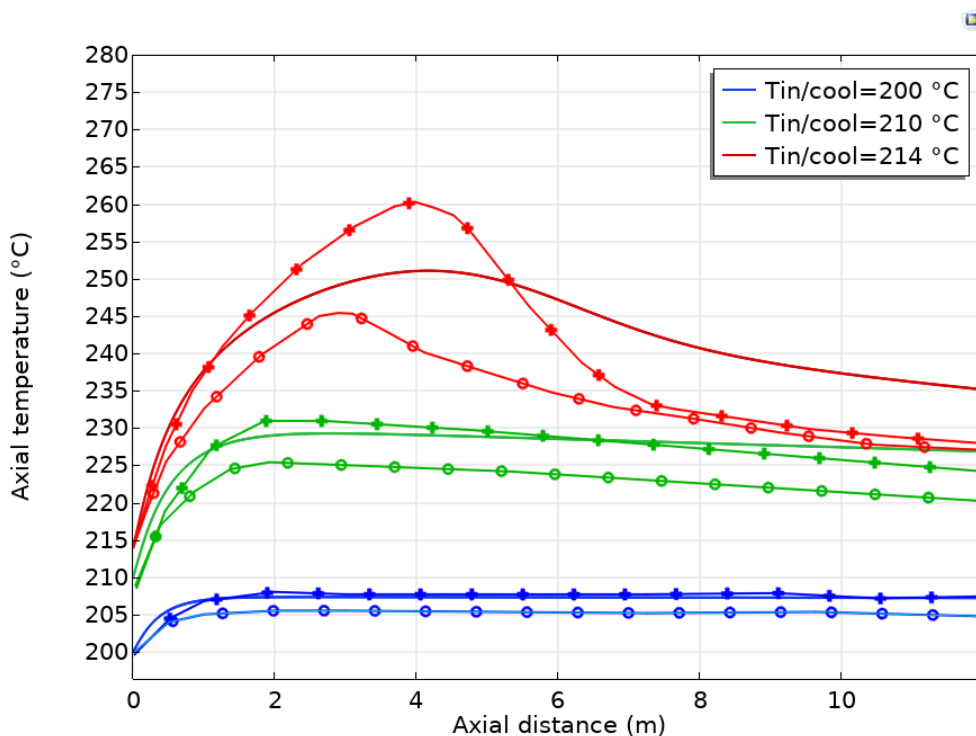


Figure 3.9: Comparison between the current model (continuous curves), Lee and Cheng (marked curves: o) and Jess and Kern (marked curves: +): Effect of inlet/cooling temperature on the axial temperature profiles ($U=0.55$ m/s and $H_2/CO=2$)

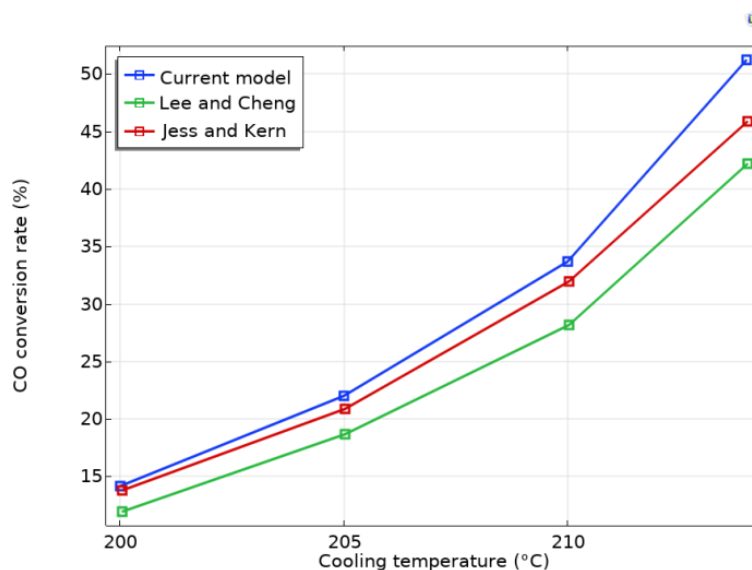


Figure 3.10: Comparison between the current model and model of literature: Effect of inlet/cooling temperature on CO conversion rates ($U=0.55$ m/s and $H_2/CO=2$)

Concerning the rate of consumption of carbon monoxide, the three models show similar increasing trends. As expected, the increase in the inlet temperature leads to the increase of the reaction kinetics rate within the FT reactor, and thus leads to the rise in the amount of CO consumed throughout the reactor. This is evident from the higher CO conversion rate recorded at the reactor exit. The predicted CO consumption rate by the current model is higher than that by the models of literature, despite using the same kinetic reaction rate model. This is attributed to the higher average reacting temperature predicted by our model compared to the models of literature.

❖ Comparison in term of products distribution

The logarithmic value of normalized hydrocarbon product weight fraction versus carbon number is presented in Figure (3.11). While the products distribution predicted by the current model follows the ASF distribution model, the one predicted by the model of Lee and Cheng follows a specific distribution, which was proposed by the authors.

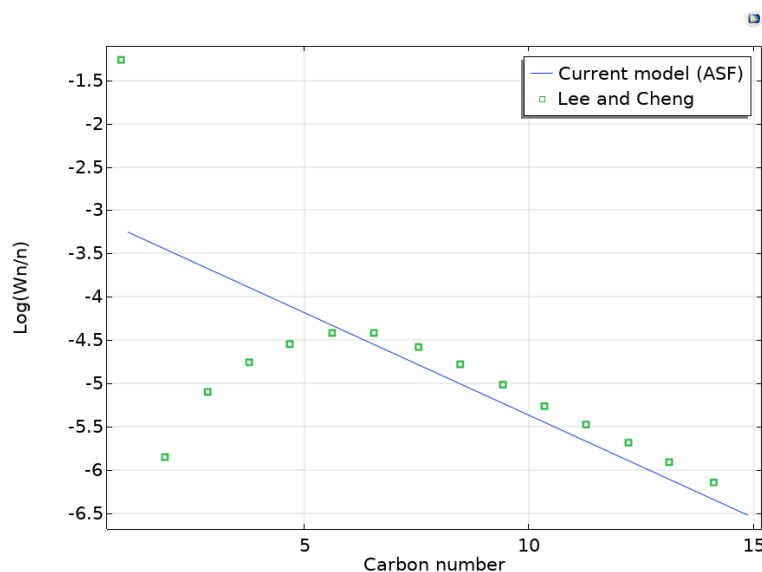


Figure 3.11: Logarithmic values of normalized hydrocarbon product weight fraction versus carbon number: Comparison between the current and Lee and Cheng models

According to the graphs of the figure above, except of methane, the fractions of products, which have a carbon number lesser or equal to six, predicted by the model of Lee and Cheng are lesser than those predicted by the current model. However, by increasing the carbon number, the fraction of products predicted by the model of Lee and Cheng are higher, compared to those predicted by our model. Since the specific heat capacity is proportional to the hydrocarbon compound chain length, the absorbed heat rate by the reacting system increases as the FT reaction progresses. This can explain the rapid decrease of the axial temperature predicted by the model of Lee and Cheng, compared to the current model and the model of Jess and Kern, as shown in Figure (3.9). It is worth nothing that, the model of Jess and kern did not consider any product distribution, and it used the feed properties to run the simulations (the mixture properties remain unchanged within the bed, during the FT reaction progress).

In Figures (3.12a) and (3.12b), the predicted axial mass fraction profiles in the gaseous phase, by the current model and that of Lee and Cheng, are illustrated. Two different scales were applied, which are linear and logarithmic scales for Figures (3.12a) and (3.12b), respectively. While the trends of hydrocarbon products (C_1 , C_2 and C_6), which are dispersed in the gas phase, are presented in the first figure, the reactant gaseous and water trends are presented in the second figure. As expected, for both models, the mass fractions of CO and H_2 decrease almost linearly along the bed axis, until reaching final values at the reactor exit. Different exit values predicted by the developed model and the

model of Lee and Cheng are observed. The mass fractions of CO and H₂ predicted by our model is lesser than those predicted by the model of Lee and Cheng, which confirms the findings about the simulated CO conversion rate by the two models, already presented in Figure (3.10). The mass fraction profile of water is also nearly linear, but it shows an increasing trend.

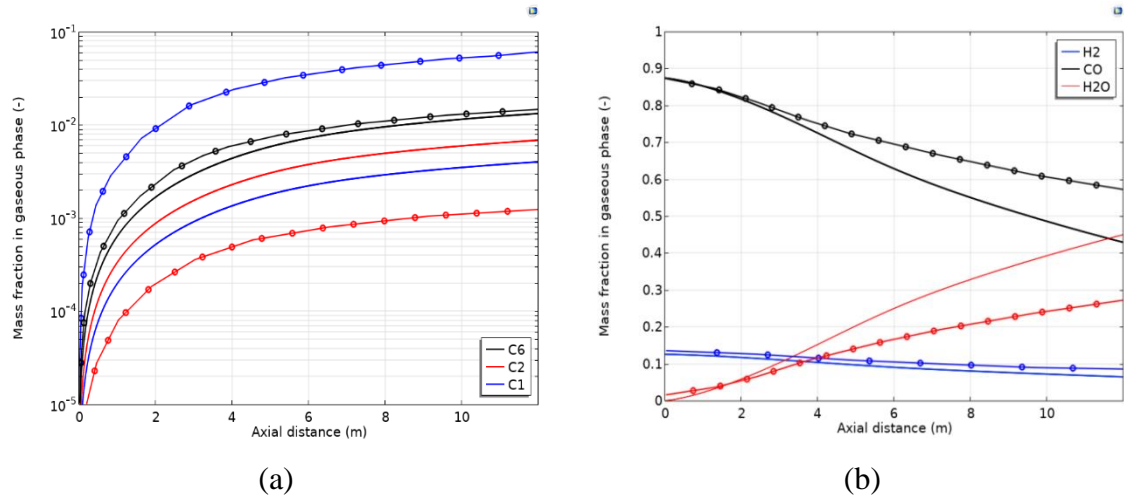


Figure 3.12: Mass fraction profiles in the gaseous phase, along the bed axis, for the baseline case conditions: Comparison between the current model (Continuous curves) and the model of Lee and Cheng (marked curves) (a) C1, C2 and C6 (b) H₂, CO and H₂O.

Concerning the light hydrocarbon products in the gas phase, their mass fractions exhibit almost linear profiles along the bed axis. Besides, the curves drawn by our model are much closer each other than the ones obtained by the model of Lee and Cheng, mainly for hexane. Moreover, except for methane, the mass fractions of the light hydrocarbons predicted by our model are almost equal (for hexane) or higher than those predicted by the model of Lee and Cheng. This finding matches well with the finding presented in Figure (3.11).

❖ Comparison in term of pressure drop

The predicted results of normalized pressure drop by our model and the model of Lee and Cheng are illustrated in Figure (3.13). The normalized pressure drop is defined as the ratio between the absolute pressure drop to the outlet pressure.

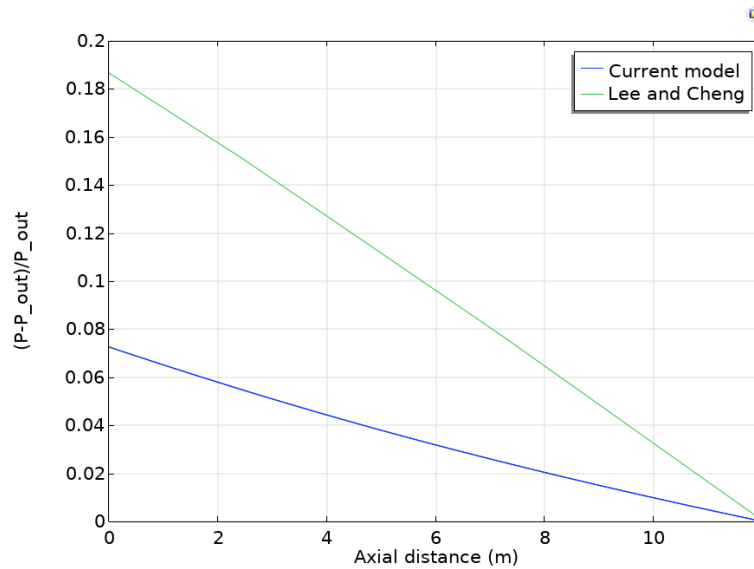


Figure 3.13: Normalized pressure profile: Comparison of the current model against that of Lee and Cheng for the baseline case conditions

As seen in the above figure, the predicted normalized pressure by the model of Lee and Cheng is about 2.5 times greater than that predicted by our model. The predicted value of the total pressure drop by our model is lesser than 8%, which justifies the use of packed bed reactor for Fischer-Tropsch synthesis [195]. The discrepancy observed between our model and the model of Lee and Cheng may be attributed to the fact that, the latter predicts higher fractions of heavier products compared to the former, resulting in higher mixture density, which by turn influences positively the computed pressure drop.

❖ Effects of H₂ to CO ratio

To study the effects of syngas composition, the simulated results of axial temperature profiles, by the current model and the one by and Lee and Cheng were plotted for different H₂ to CO ratio values, as shown in Figure (3.14). Furthermore, the CO conversion rates, at the reactor outlet were computed by the two models for different syngas composition values, as presented in Table (3.5).

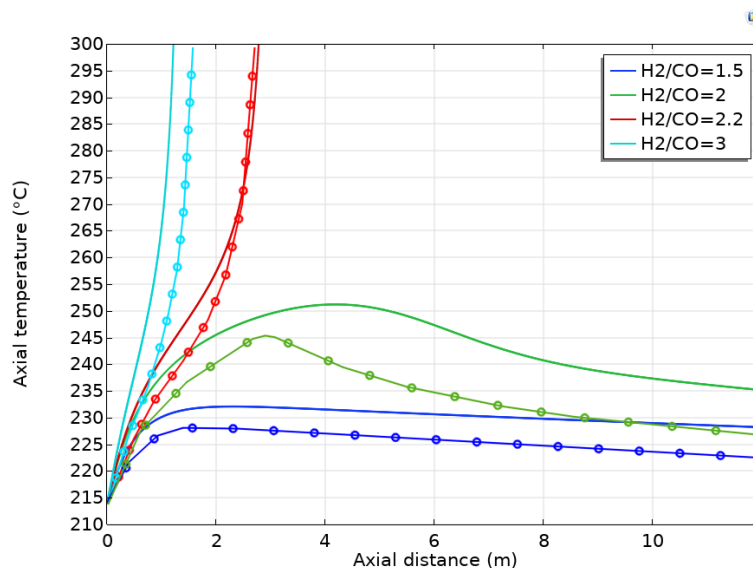


Figure 3.14: Comparison between the current model (Continuous curves) and that by Lee and Cheng (marked curves) at $T=214$ °C and $U=0.55$ m/s: Effect of H_2 to CO ratio on the axial temperature

While the blue and the green curves represent the axial temperature profiles for the thermally viable cases, the other two curves represent the thermally unviable cases. The former cases correspond to the lower H_2 to CO ratio values, which are 1.5 and 2. The later cases correspond to the higher ratio values, which are 2.2 and 3.

Table 3.5: Simulated results of CO conversion rates: Comparison between our model and that of Lee and Cheng

Operating conditions			Results: X_{CO} (%)	
Inlet/Cooling temperature, $T_{in/cool}$ (°C)	Normalized velocity, U/U_{base}	H_2/CO	Our model	Lee and Cheng's model
214	1	1.5	42.26	37.88
		2	74.19	58.58
	0.75	2	-	47.16
	1.25	2	38.69	-
210	1	2	33.69	28.39
205	1	2	22	18.74

Overall, for the two models and for all cases, the increase of the H_2 to CO ratio speeds up the temperature rise. Besides, the analysis of the impact of H_2 to CO ratio on the

axial temperature profiles within the tubular packed bed reactor reveals that, the trends forecasted by both models exhibit considerable similarity. However, it is noteworthy that, the developed model tends to predict marginally elevated temperatures compared to those indicated by the comprehensive model, of Lee and Cheng. The percentage differences in peak temperatures observed between the two models are 1.50% and 2.77% for H₂ to CO ratio of 1.5 and 2, respectively. These values are within the range of deviation recorded between the benchmark model by Jess and kern and the one by Lee and Cheng. The relationship between the temperature and the H₂/CO ratio can be elucidated through the inherent kinetic behavior associated with the concentrations of hydrogen and carbon monoxide. The intrinsic kinetics of Fischer-Tropsch synthesis, as described by Equations (2.44) to (2.50), exhibits a direct proportionality to the molar fraction of hydrogen. In contrast, the relationship with carbon monoxide is more intricate. At elevated concentrations, carbon monoxide behaves as an inhibitor. When the adsorption term for carbon monoxide in the denominator exceeds one, specifically when $K_{CO}C_{CO,g} \gg 1$, the denominator can be simplified to $(K_{CO}C_{CO,g})^2$. The intrinsic kinetics of FT reaction in this scenario exhibits an inverse relationship with the concentration of carbon monoxide, a hallmark of Langmuir–Hinshelwood kinetics. Increasing the molar ratio of hydrogen to carbon monoxide at the inlet leads to an enhanced consumption rate of syngas. This is attributed to the elevated concentration of hydrogen, which results in greater heat release. Consequently, the reactor temperature rises ultimately, resulting in higher CO conversion rates at the outlet, as illustrated in Table (3.5).

Another important finding can be deduced when comparing the viable and the unviable cases. It is clear that using a syngas with lower H₂ to CO ratio will permit to operate under temperature control. However, increasing this ratio up to 2.2 will make temperature runaway to happen. It can be clearly observed from Figure (3.14) that, using a syngas with H₂ to CO ratio of 2, at 214 °C, yields a better performance than when the ratio equal to 1.5. Actually, using a feed with an H₂ to CO ratio of 2.1, or even lower (a ratio of 2.03) will cause the reactor runaway, according to our simulations, which is not shown here because of the lack of data for comparison.

❖ **Effect of feed velocity**

The effect of feed (inlet) velocity on the bed axial temperature was studied by varying the inlet velocity, meanwhile keeping the other parameters constants and equal to

those of the baseline case. Three values of the inlet velocity were used, which are 75%, 100% and 125% of the baseline feed velocity. The simulated results by our model and the model of Lee and Cheng are presented in Figure (3.15). As seen, both models exhibit similar trends when using the baseline feed velocity, which has already been shown in Figures (3.9) and (3.14). If the feed velocity decreases below the baseline feed velocity ($U=0.75*U_{base}$), the heat transfer coefficient of the internal wall side decreases, so that, the overall heat coefficient decreases which reduces the heat transfer across the tube wall. On the other hand, the residence time increases, so that, almost all the reactants will be consumed in the first few meters, which generates a huge amount of heat. The combined effects of increasing the wall resistance heat transfer rate and releasing huge amount of heat add up, which further accelerates the reaction and causes the temperature runaway, just few meters far from the tube inlet. This logical explanation is evident through the results obtained by our simulations, which is illustrated by the continuous blue curve. This result is opposite to that obtained by Lee and Cheng, as shown by the marked blue curve. This is can be attributed to the fact that, the authors considered a constant overall heat transfer coefficient, equal to that of the baseline case (it remains unchanged while the FT reaction progress).

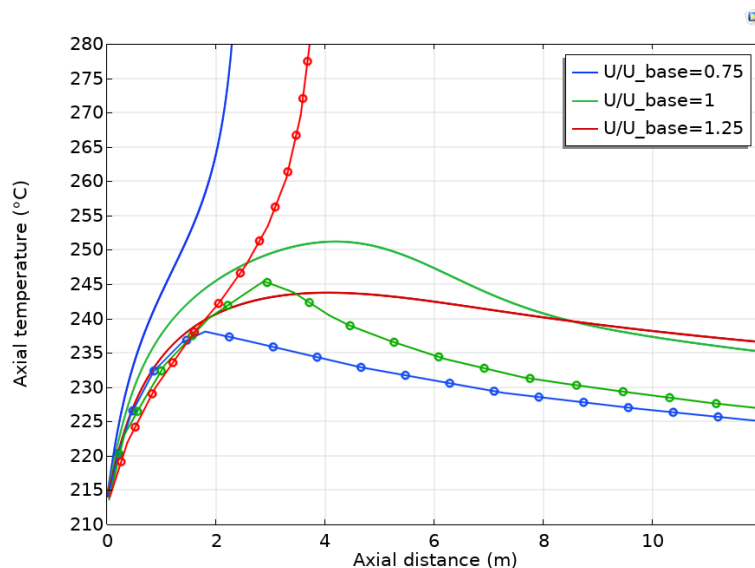


Figure 3.15: Comparison between the current model (continuous curves) and that of Lee and Cheng (marked curves) at $T=214$ °C and $H_2/CO=2$: Effect of feed velocity on the axial temperature

If the feed velocity increases over the baseline feed velocity ($U=1.25*U_{base}$), the heat transfer near the wall enhances, and the heat generation rate along the bed length

decreases. These two combined effects further slow-down the reaction rate, so that, the temperature runaway will not occur. The results derived from our simulations clearly confirm this logical explanation, as shown by the continuous red line graph. Oppositely, Lee and Cheng found that, increasing the feed velocity 1.25 times the baseline feed velocity causes thermal runaway, as shown by the marked red line. This is because, in this case the FT reaction becomes more intense, while the evacuated heat rate throughout the wall remains unchanged, as the overall heat transfer coefficient was considered constant by the authors.

3.3.4 Effects of the bed aspect ratio (AR)

To study the effects of tube-to-particle diameter ratio, four cases were studied. In each case, four PBRs with different aspect ratios were simulated and compared, under an operating pressure of 24 bars. The characteristics of the simulated PBRs are presented in Table (3.6).

Table 3.6: Characteristics of PBRs: Effect of aspect ratio

PBR model	PBR1	PBR2	PBR3	PBR4
AR (-)	2	4	8	15.33
Porosity (-)	0.5286	0.438	0.413	0.3415
Wall thickness (mm)	0.65	1.3	2.6	5
Tube section (mm ²)	56.52	226.08	904.32	3322.12
Number of tubes (N_{tubes}), feed velocity (U_{feed}) and bed length (H)				
Large-scale FT reactors				
Case 1 (H=12 m)				
$U_{\text{feed}}/U_{\text{base}}$ (%)	100			
N_{tubes}	117556	29389	7347	2000
Case 2 (H=12 m)				
$U_{\text{feed}}/U_{\text{base}}$ (%)	270	200	180	100
N_{tubes}	43539	14694	4082	2000
Small-scale FT reactors				
Case 3 (H=2 m)				
$U_{\text{feed}}/U_{\text{base}}$ (%)	8.39	8.49	8.69	9.08
N_{tubes}	27104	6698	1636	426
Case 4 (H=2 m)				
$U_{\text{feed}}/U_{\text{base}}$ (%)	16.79	16.98	17.38	18.17
N_{tubes}	27104	6698	1636	426

In Table (3.6), the number of tubes of the large-scale FT reactor was calculated in such a way the total flow rate equals the number of tubes, within the reactor bundle, multiplied by the flow rate of single tube. Concerning the small-scale FT reactors, the triangular pattern was considered, since it is widely common in practice. The tube pitch selected was medium, which is equal to 1.5 times the tube outer diameter, in order to maximize the tubes number in the reactor bundle, from one hand, and to ensure efficient and easy cleaning of the shell side of the reactor, on the other hand. The variation in the diameter of the reactor tube influences the quantity of tubes that can be accommodated within the reactor shell in the design, as detailed in Appendix C.

Four cases were studied. While Cases 1 and 2 concern the large-scale FT reactors, Cases 3 and 4 concern the small-scale FT reactors. The specifications of each case are illustrated in Table (3.7).

Table 3.7: Specifications of the studied cases

	Constraint	Feed composition
Case 1	<ul style="list-style-type: none"> Total feed flux=3.3 kg/s at the baseline conditions 	H ₂ : 66.66%, CO: 33.33% (Source of syngas is natural gas)
Case 2	<ul style="list-style-type: none"> Normalized pressure drop <8% 	
Case 3	<ul style="list-style-type: none"> Internal diameter of the FT reactors=1916 mm, Tubes length=2 m and Daily processed biomass 6 Ton of wood chips or 6.6 Ton of municipal solid waste (These figures were estimated based on the data from reference [10]) 	H ₂ : 49.90%, CO: 22.68% CO ₂ : 18.36%, N ₂ :9.06% (Source of syngas is biomass)
Case 4	<ul style="list-style-type: none"> Internal diameter of the FT reactors=1916 mm, Tubes length=2 m and Daily processed biomass: double of that of Case 3 	

Firstly, in Case 1, the baseline feed velocity (0.55 m/s) was considered for all the PBR models. This superficial velocity corresponds to a feed mass flow rate of 3.3 kg/s. Using Aspen HYSYS V12, a syngas production unit was simulated (See Appendix D). The

natural gas composition of a medium oil and gas field, in Algeria, was implemented as input in the simulation environment of Aspen HYSYS V12, as presented in Appendix D. The results indicate that, reforming 170000 STDCM/d of natural gas produces about 3.3 kg/s of syngas with a $H_2/CO=2$.

Secondly, in Case 2, a maximum pressure drop (8%) through each PBR was set as constraint. Also, in this case the source of syngas is the natural gas. Thirdly, in Cases 3 and 4, small scales PBRs, for Fischer-Tropsch synthesis, were studied. The difference between Cases 3 and 4 is that, the latter can process a double biomass quantity, compared to the former, as shown in Table (3.7). In each of the four cases, the number of tubes and the optimal operating parameters will be calculated using the constraints as appears in the second column of Table (3.7). The calculated number of tubes and the optimum feed velocities for each PBR model and for each case are presented in Table (3.6). In order to determine the optimum inlet/cooling temperature (T_{op}) for each PBR as well as for each case, one should look for the temperature limit for thermally viable PBRs.

3.3.5 Limit temperature of thermally viable PBRs of large-scale FT reactors: Cases 1 and 2

The limit temperature of thermally viable catalytic reactor, considered also as the optimum operating temperature, is the temperature value above it, the reactor runaway occurs. In this study, it is considered also as the maximum inlet or cooler temperature above it, the catalyst deactivation happens. For each of the packed beds of Case 1, the current model calculated three reactor bed temperature profiles, corresponding to the baseline feed velocity and H_2 to CO ratio, utilizing more precise coolant temperatures, as illustrated in Figures (3.16) and (3.17). The analysis revealed that, the thermally viable and unviable cases, of the large PBR model, are separated by a narrow range of coolant temperatures, specifically between 214.3 and 214.4 °C, as seen in Figure (3.16d). Concerning the slender PBRs, the coolant temperature should not exceed certain limits to avoid the catalyst deactivation. These limits are almost 1 °C higher of Case 2 than those of Case 1. For Case 1, they vary between 256 and 256.5 °C, 250 and 251 °C and 237 and 238 °C for the slender PBRs with aspect ratios of 2, 4 and 8, respectively. For Case 2, they vary between 256.5 and 257 °C, 251 and 252 °C and 239 and 239.5 °C for the slender PBRs with aspect ratios of 2, 4 and 8, respectively. It is worthy to note that, a 0.3 °C was considered as the maximum value of the cooler temperature fluctuations around its set point, in order to operate at the maximum possible temperature and avoid reactor runaway

or catalyst deactivation. The results of optimum temperatures for each PBR model of Cases 1 and 2 are presented in Table (3.8). It was found that, for both cases, decreasing the bed aspect ratio leads to the increase of the optimum operating cooler temperature. This proportionality is attributed to the enhanced heat removal process through the reactor wall along the radial direction, when using slender packed beds. The simulated optimum working temperatures of Case 1 were 256.2, 250.4, 237.6 and 214 °C for the PBRs with aspect ratios of 2, 4, 8 and 15.33, respectively. Whereas, the simulated optimum working temperatures of Case 2 were slightly higher, which were 256.7, 251.5, 239 and 214 °C for the PBRs with aspect ratios of 2, 4, 8 and 15.33, respectively.

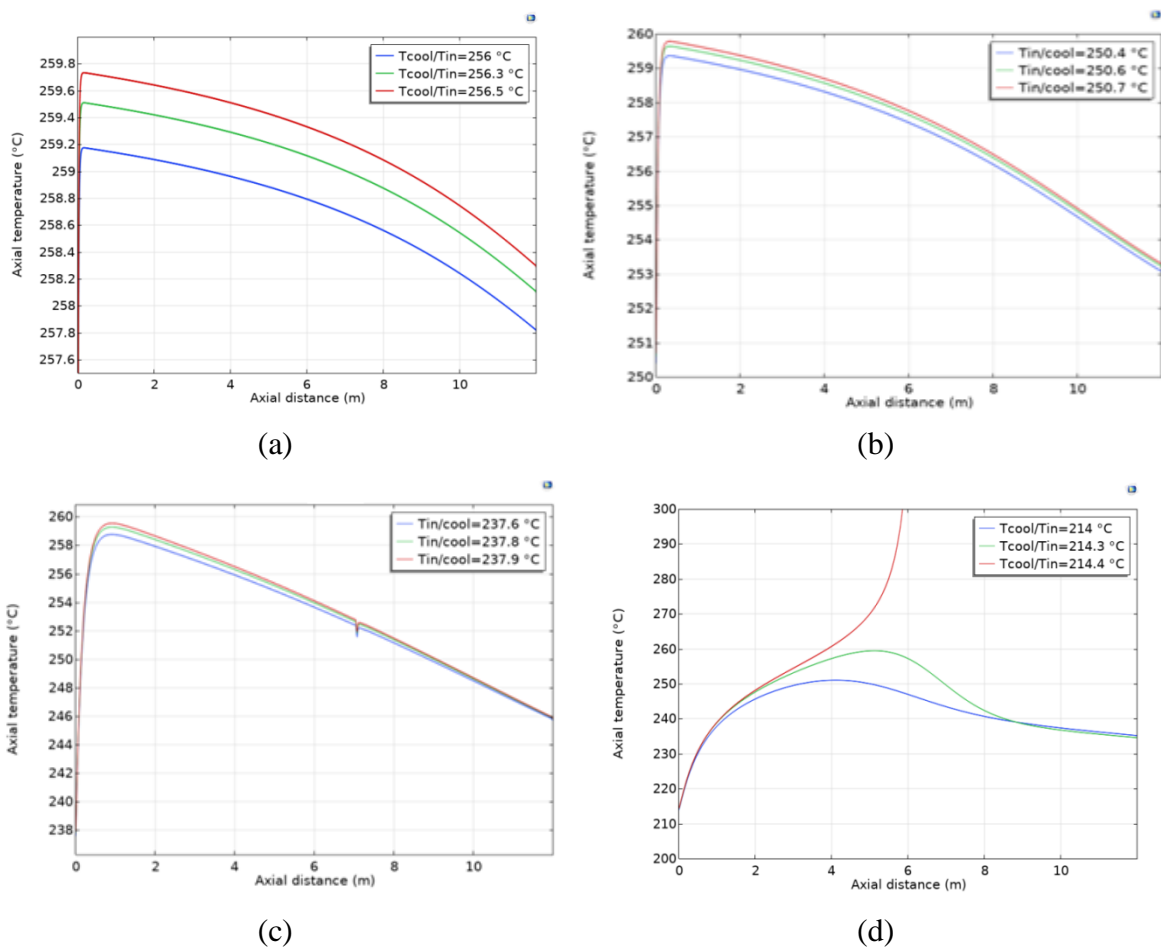


Figure 3.16: Limit temperature for thermally viable reactors of Case 1 (a) AR=2, (b) AR=4, (c) AR=8 and (d) AR=15.33

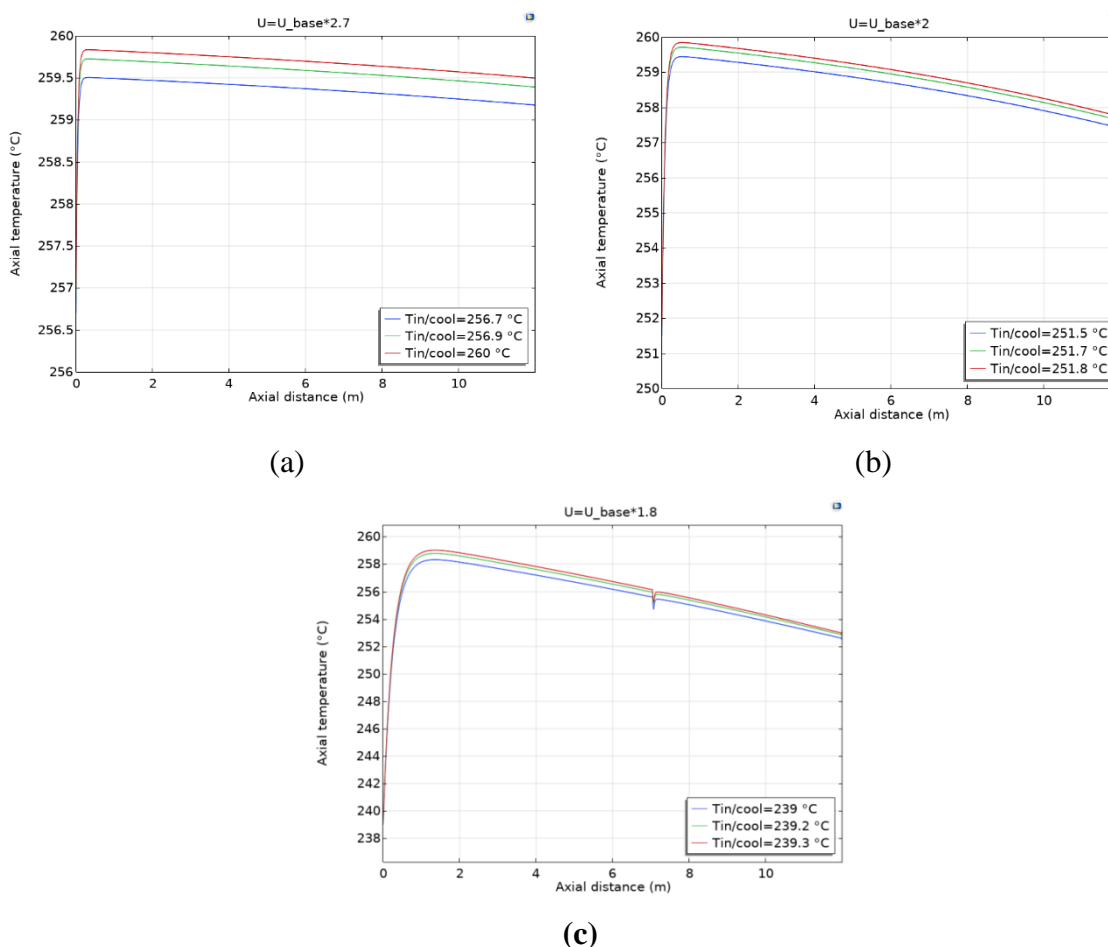


Figure 3.17: Limit temperature for thermally viable reactors of Case 2 (a) AR=2, (b) AR=4 and (c) AR=8

3.3.6 Performance comparison of packed beds with different aspect ratios for large-scale FT reactors: Cases 1 and 2

The simulated results of Cases 1 and 2, in terms of axial temperature profile, axial CO conversion rate, C_{5+} yields and normalized pressure drop are presented in Figures (3.18) and (3.19). All the figures show the center-line axial profiles. Overall, the variations of the studied parameters exhibit similar trends for all the PBRs and for both cases. Figures (3.18a) and (3.19a) illustrate the axial temperature profiles along the bed axis. For all PBRs and for both cases, the axial temperature increases rapidly just at the bed's inlet, reach a peak and then fall smoothly along the remaining axial distance. The peaks shift toward the bed's entrance as the bed aspect ratio decreases.

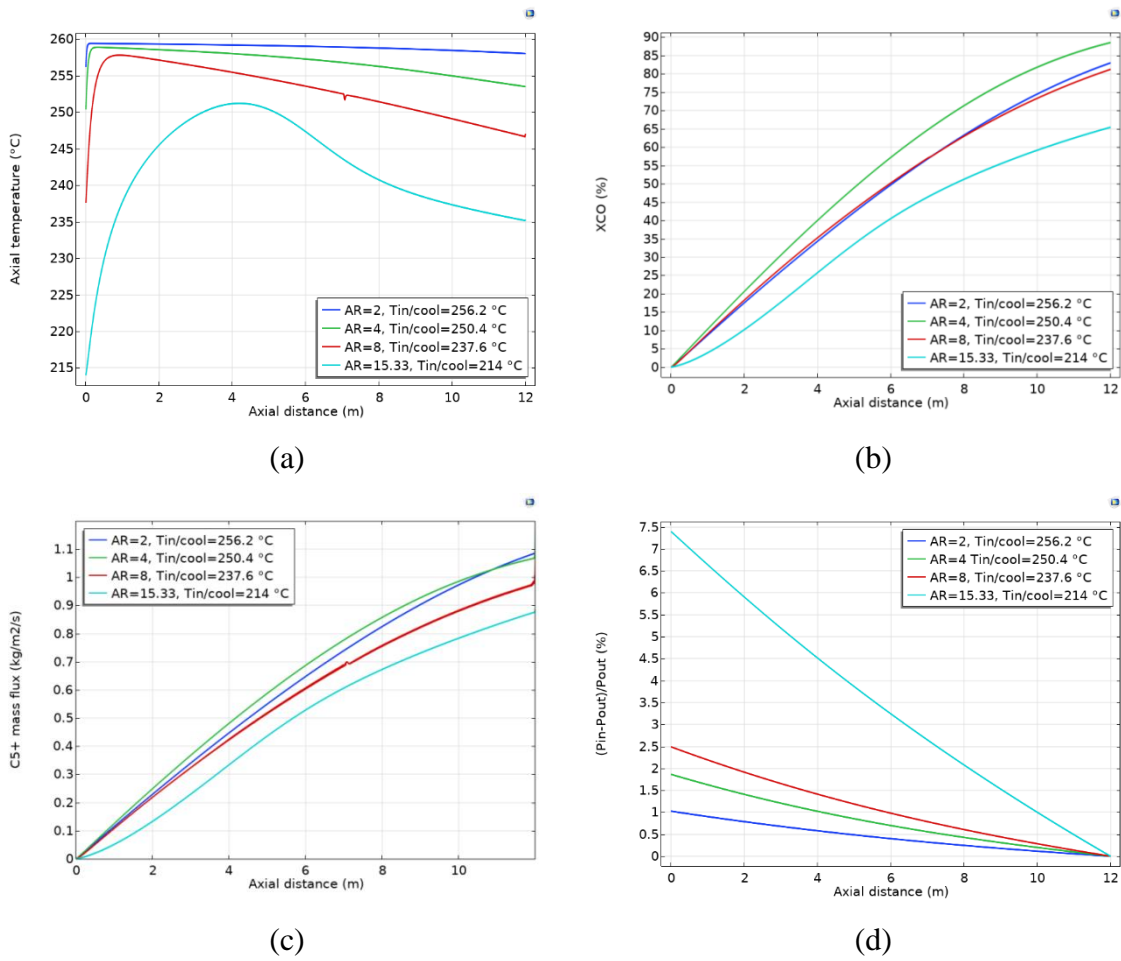


Figure 3.18: Simulated results of Case 1 in terms of (a) axial temperature and (b) CO conversion rates, (c) C₅₊ radial exit flux and (d) axial normalized pressure drop: Comparison between packed beds with different aspect ratios

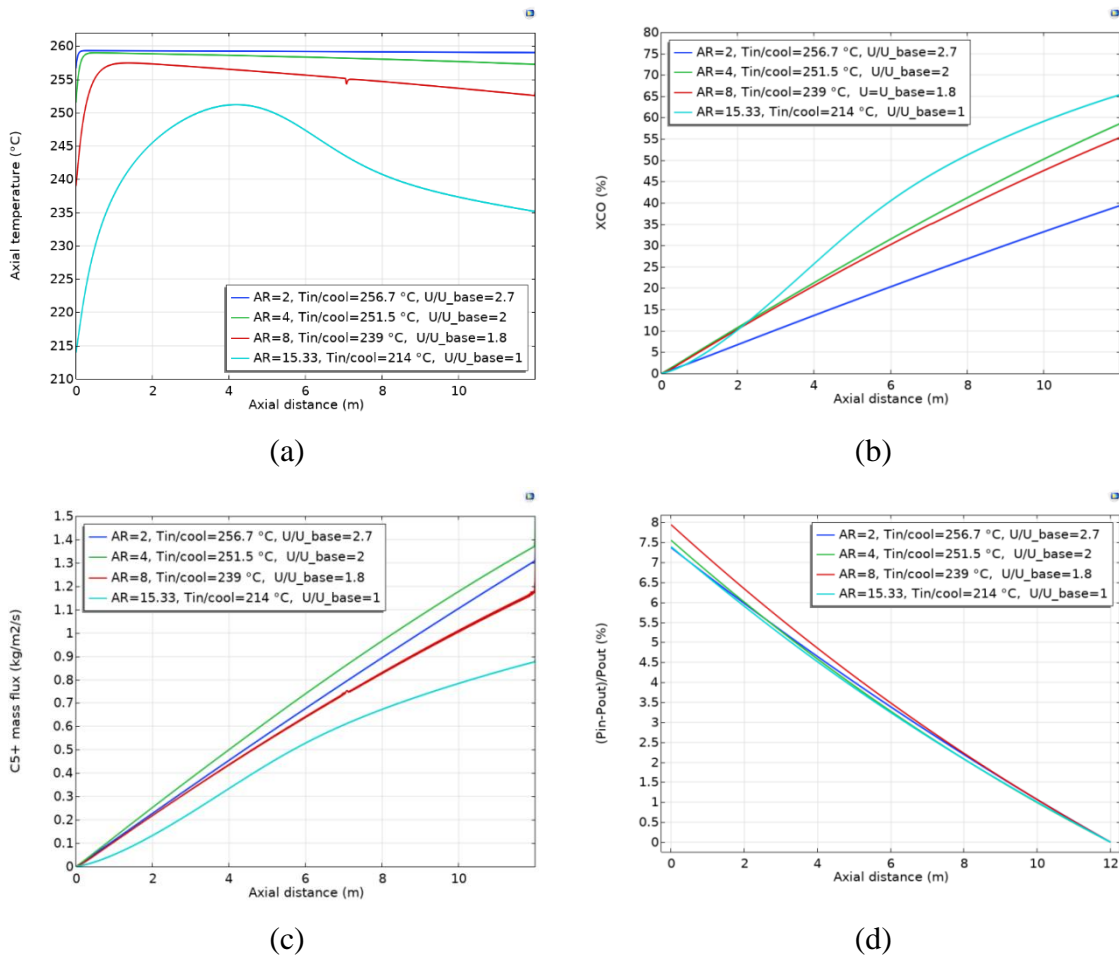


Figure 3.19: Simulated results of Case 2 in terms of (a) axial temperature and (b) CO conversion rates, (c) C₅₊ mass flux and (d) axial normalized pressure drop: Comparison between packed beds with different aspect ratios

Concerning CO conversion rate profiles, shown in Figures (3.18b) and (3.19b), in both cases and for all the PBR models, CO is consumed rapidly during the first few meters of the beds and then at lower rates through the rest of the axial distance. It is clearly observed that, for Case 1 the line graph of CO conversion rate of the large PBR has the highest slope, whereas for Case 2 it has the lowest slope. These results may trick us about the total CO conversion rates, at the reactor exit. Therefore, one should calculate the averaged values of CO conversion rate at the bed's exit using the line average operation, applied on the bed's exit cut line. The results are presented in Table (3.8). From this table, it is clearly shown that the PBR2 of Case 2 gave the highest CO conversion rate (88.52%).

Table 3.8: Simulated results of the large-scale FT reactors (Cases 1 and 2): Comparison between packed beds with different aspect ratios

Case	PBR model	X _{CO} (%)	C ₅₊ yields (t/d)	T _{OP} (°C)	Axial normalized pressure drop (%)
Case 1	PBR1	82.97	626.93	256.2	1.02
	PBR2	88.52	669.75	250.4	1.86
	PBR3	81.25	614.67	237.6	2.49
	PBR4	51.30	402.58	214	7.39
Case 2	PBR1	39.52	298.80	256.7	7.37
	PBR2	58.83	445.33	251.5	7.55
	PBR3	55.26	418.40	239	7.94
	PBR4	51.30	402.58	214	7.39

Regarding the daily production rate of C₅₊, illustrated in Figures (3.18c) and (3.19c), for both cases and for all the PBRs, the hydrocarbon liquids (HCLs) produced gradually along the bed length until reach the maximum at the bed's exit. In the actual multitubular reactor configuration, it was assumed that, each reactor tube operates under identical conditions. Consequently, the total C₅₊ yields of the multitubular reactor were calculated by multiplying the production rate of single tube by the tubes number. Therefore, the single tube C₅₊ production was calculated by applying the line average operation on the bed's exit. Then the total C₅₊ daily production rates, for each PBR and for both cases, were calculated and presented in Table (3.8).

As expected, similarly to CO conversion rate, the PBR2 of Case 1 gave the highest C₅₊ yields with a daily production of 669.75 tons. The higher values of CO conversion rates and C₅₊ yields for PBR2 with respect to PBR1, despite the fact that, the inlet temperature for the former is higher than that of the latter, is attributed to the catalyst density. The reaction kinetics is expressed in consumed moles per unit bed volume. This rate is proportional to (1-ε), so that, the amounts of CO consumed or C₅₊ produced are expected to be higher for PBR2 than those for PBR1.

With regard to pressure drop, the normalized pressure drop was calculated for all PBRs and both cases. Not surprisingly, it can be clearly revealed that, the normalized pressure drop increases as the bed aspect ratio increases. This is attributed to the fact that; the bed porosity is inversely proportional to its aspect ratio. Thus, the available space for flow decreases when increasing the bed aspect ratio. Therefore, the flow resistance

increases as the aspect ratio increases, which is taken into account via the Ergun or Einfeld and Schnitzlein correlations, which were already presented in Table (2.2).

Another important finding is that, the CO conversion rates and C₅₊ yields were much higher in Case 1 than in Case 2, for all the slender PBR models, although the operating temperatures were higher for Case 2. This can be explained by the fact that, operating under lower feed velocities, offers more residence time for the FT reaction. The effect of the residence time, on the reactor performance, is stronger than the effect of the slight rise of the operating temperature.

Using the remarks outlined from Figures (3.18) and (3.19), as well as from Table (3.8), the PBR2 of Case 1 is the first candidate large-scale FT reactor to be selected. To have a final decision, one should conduct an economic efficiency analysis, in terms of the Internal Rate of Return (IRR), the Net Present Value (NPV) and the payout time (POT), for each scenario. In this study, we did not make a detailed economical evaluation study, but we have touched on the economic key indicators that may give us an overview of the decision-making methodology. Actually, the PBR2 of Case 1 exhibited the high performance in term of C₅₊ productivity, but using a higher number of tubes, which is 29389, regarding the number of tubes of PBR3 and PBR4, which are 7347 and 2000, respectively. From one hand, the capital cost (CAPEX) is proportional to the tubes number, but it spent in a full at once before the plant start-up phase. On the other hand, the revenues are proportional to products yields, mainly C₅₊ and inversely proportional to the operating cost (OPEX). Assuming excess energy is available (taking into account the total energy balance of the whole GTL plant), the only variable costs are the syngas reactants (CO and H₂) supply cost. This later by turn it depends on the upstream process costs, which are supposed to be the same for all the PBR models and for both cases. This assumption holds true, since the feed composition is the same for all the simulated scenarios. Generally, in the gas and oil sector, the POT is very short due to the relatively high price of the final products. Therefore, for long period producing plants the economic indicator for investment decision is the variable income function (INCOM [DZD.Day⁻¹]), which is defined as the sales revenues minus the variable cost, written as:

$$\text{INCOM} = \text{REVENUES} - \text{OPEX} \quad (3.3)$$

Actually, this objective function has to be maximized. Since the variable costs (OPEX) are assumed to be the same for all the scenarios, the objective function to be maximized is the sales revenues. These latter, are directly proportional to the quantities produced of LPG (C₃ and C₄) and C₅₊, during the life time period of the project.

Taking this into consideration, the PBR2 of Case 1 is the best choice.

Nevertheless, a technical route would be considered, which consists of recycling some fraction of the unconverted gaseous to the reactor entrance, after separation of water and hydrocarbon. Here, we introduced a recycle ratio, $Recy [-]$, representing the recycled volume flow rate, $Q_{Recy} [m^3 \cdot s^{-1}]$ to the inlet volume flow rate $Q_{in} [m^3 \cdot s^{-1}]$ ratio, written as:

$$Recy = \frac{Q_{Recy}}{Q_{in}} \quad (3.4)$$

By assuming, plug flow regime and constant volume fraction, the total conversion of CO may be given by:

$$X_{CO_{tot}} = X_{CO_{pass}}(1 + Recy) \quad (3.5)$$

Where $X_{CO_{tot}}[\%]$ and $X_{CO_{pass}}[\%]$ are the CO conversion rates with and without recycling, respectively. By varying the value of the recycle ratio, a complete conversion can be obtained for all the scenarios, however, the number of tubes in each bundle will be proportional the recycle ratio, which is by turn contributes in the total initial investments value (CAPEX) of each scenario. To achieve a complete conversion and a maximum products yield, the recycle ratio values and their corresponding numbers of tubes for all the PBRs and for both cases were calculated and presented in Table (3.9).

Table 3.9: Comparison between the tubes number with unconverted gas recycling and without recycling, for all scenarios of large-scale reactors

	Case 1				Case 2			
	PBR1	PBR2	PBR3	PBR4	PBR1	PBR2	PBR3	PBR4
Recy	1,21	1,13	1,23	1,95	2,53	1,70	1,81	1,95
N_{tubes}	117556	29389	7347	2000	43539	14694	4082	2000
N_{tubes_Recy}	141685	33200	9042	3899	110170	24977	7387	3899

From Table (3.9), it is clearly observed, that the numbers of tubes with recycling are higher than those without recycling. Although the number of tubes of the large PBR has almost doubled, it is still the least compared to the slender PBRs. By supposing that the CAPEX is proportional to the tubes number, the CAPEX relative to PBR4 will be the least. Furthermore, at a complete CO conversion the product yields will reach the maximum value, which will be the same for all scenarios. Thus, the sales revenues will be equal for

all scenarios. Taking all of the above remarks into consideration, the large PBR model (PBR4) will be selected.

3.3.7 Limit temperature of thermally viable PBRs of small-scale FT reactors: Cases 3 and 4

In this study, the small-scale FT reactors were used to transform synthesis gaseous issued from biomass to produce hydrocarbons with small quantities. The whole FTS plant is compacted to fit a portable container. The feed flow rate is much smaller compared to the large-scale reactors. Furthermore, the process is limited by the space constraints in terms of tubes length and number. For each tube, the active bed length is 1.6 m. Besides, it is limited at its ends (top and bottom) by inactive two beds each 0.2 m long. The feed crosses the packed tubes, with low velocities, under optimum inlet/cooling temperature, in order to allow the syngas to react as much as possible. Therefore, for a given inlet feed velocity, we looked for the optimum temperature to maximize the conversion without reaching the catalyst deactivation temperature ($<260\text{ }^{\circ}\text{C}$). Similarly, to Cases 1 and 2 of the large-scale FT reactors, the cooler temperature can fluctuate $0.3\text{ }^{\circ}\text{C}$ around its set point.

The sets of Figures (3.20) and (2.21) show the simulated axial temperature profiles for packed beds with different aspect ratios, of Cases 3 and 4. For each packed bed model and case, three values of the inlet/cooling temperature were used, in order to determine the optimum working temperatures. These values are the intersection of the blue curves with the vertical axis, which are presented in Table (3.10). The green curves represent the axial temperature profiles for inlet/cooling temperatures $0.3\text{ }^{\circ}\text{C}$ above the optimum temperature values. The red curves correspond to the thermally unviable cases ($T_{\text{max}} > 260\text{ }^{\circ}\text{C}$).

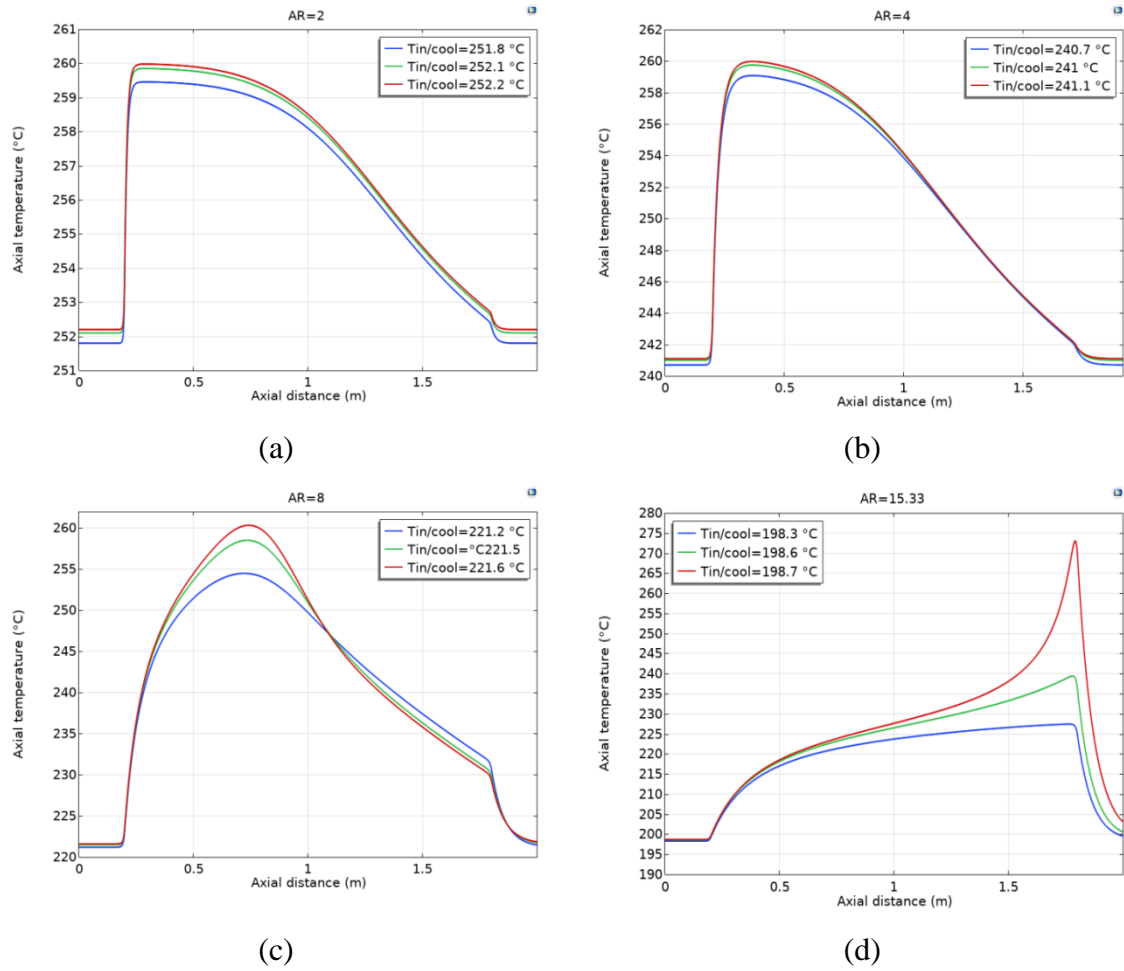


Figure 3.20: Limit temperatures of Case 3 (a) AR=2, (b) AR=4, (c) AR=8 and (d) AR=15.33

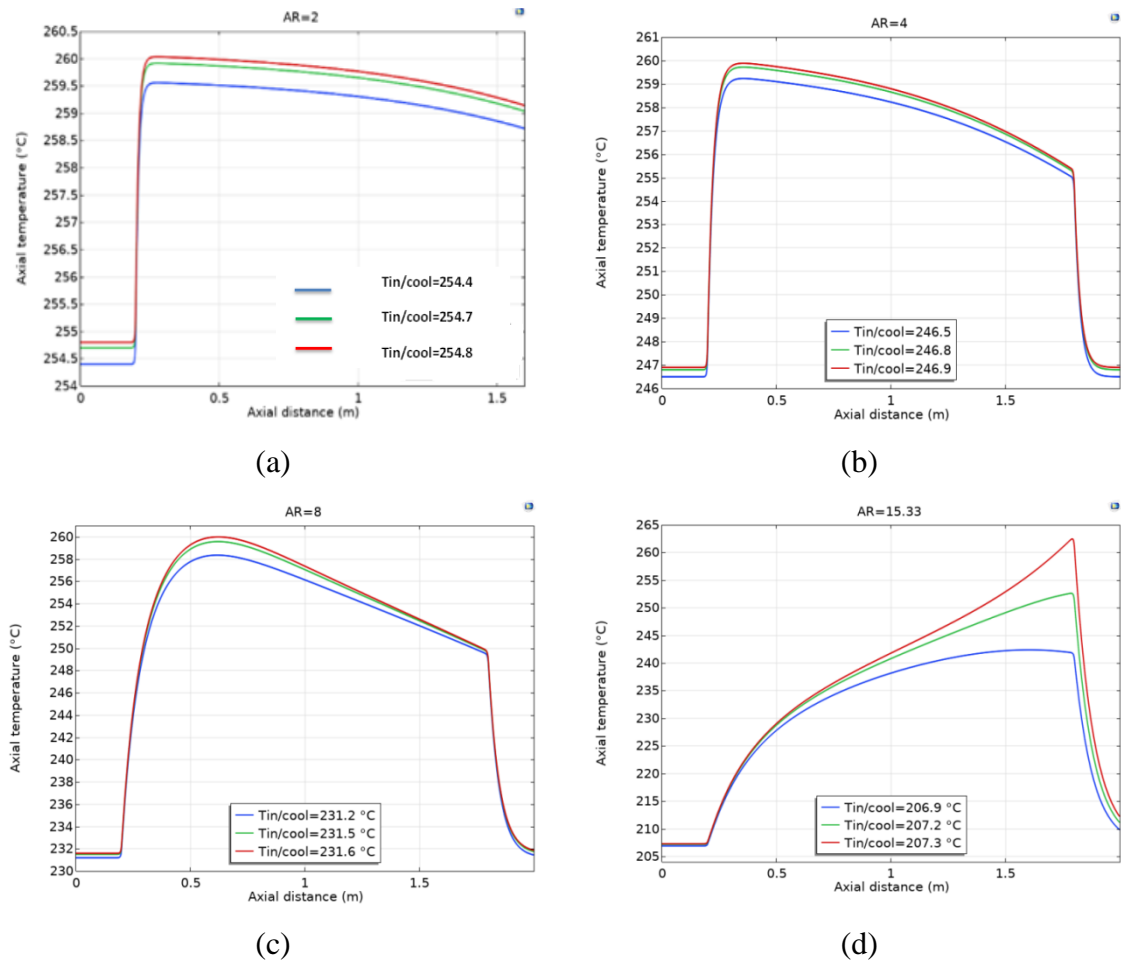


Figure 3.21: Limit temperatures of Case 4 (a) AR=2, (b) AR=4, (c) AR=8 and (d) AR=15.33

3.3.8 Performance comparison of packed beds with different aspect ratios for small scale FT reactors: Cases 3 and 4

Table (3.10) summarizes the key performance simulated results of the small-scale FT reactor scenarios, in terms of CO conversion rate, C_{5+} and LPG productivities, optimum inlet/cooler temperature and pressure drop along the FT reactor.

Table 3.10: Simulated results of the small-scale FT reactors (Cases 3, 4): Comparison between packed beds with different aspect ratios

Case	PBR model	X _{CO} (%)	C5+ yield (kg/d)	GPL yield (kg/d)	T _{OP} (°C)	Pressure drop (Pa)
Case 3	PBR1	99.85	4802.84	285.87	251.8	6.29
	PBR2	99.90	4827.16	281.55	240.7	9.99
	PBR3	96.54	4693.03	273.72	221.2	12.23
	PBR4	51.23	2556.42	149.09	198.3	31.30
Case 4	PBR1	79.39	7793.06	454,55	254.4	433.12
	PBR2	83.82	8360.16	487,63	246.5	777.21
	PBR3	75.55	7595.27	443.02	231.2	940.59
	PBR4	42.27	4279.45	249.63	206.9	2405.17

The optimum inlet/cooling temperature values for each scenario are also presented in Figure (3.22). As seen in Figure (3.22), the calculated optimum temperatures of Case 3 are lower than those obtained of Case 4. This can be explained by our findings in section 3.3.4, where we have found that, the maximum reactor temperature is inversely proportional to the feed velocity. Since in Case 3, the feed velocities are lower than those of Case 4, the inlet/cooling temperature should be further reduced, for the low feed velocity cases, to avoid reaching the catalyst deactivation temperature. Moreover, it can be seen clearly from Figure (3.22) that, the calculated optimum temperature of both cases decreases as the bed aspect ratio increases. This is to avoid reaching the deactivation temperature or the reactor thermal runaway behavior.

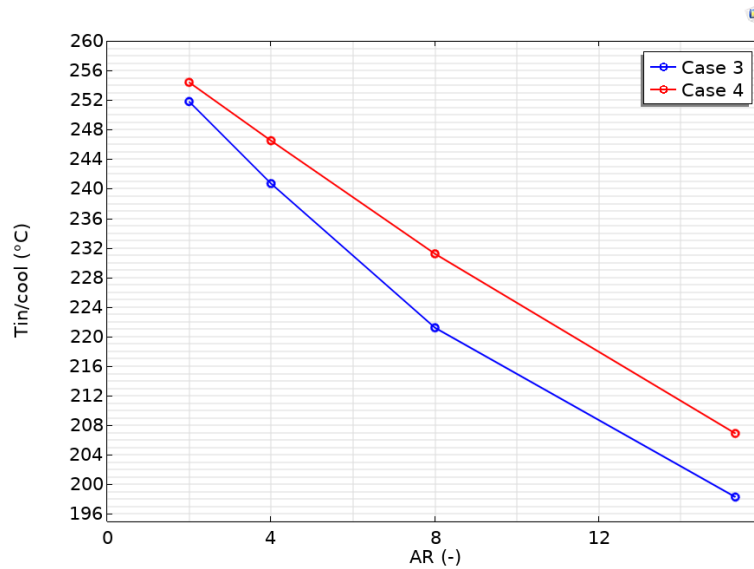


Figure 3.22: Inlet/cooling temperature versus bed aspect ratio: Comparison between Cases 3 and 4

The pressure drop values shown in the last column of Table (3.10) are plotted in Figure (3.23). As expected, the pressure drop along the bed length increases as the feed velocity or the bed aspect ratio increases. This is because the mean bed porosity decreases as the bed aspect ratio increases. Moreover, the flow resistance term in the momentum balance equation (Equation (2.23)), which is described by the Ergun equation for the large PBR or the Einfeld and Schnitzlein for the slender PBRs, is inversely proportional to the mean bed porosity, and directly proportional to the flow velocity.

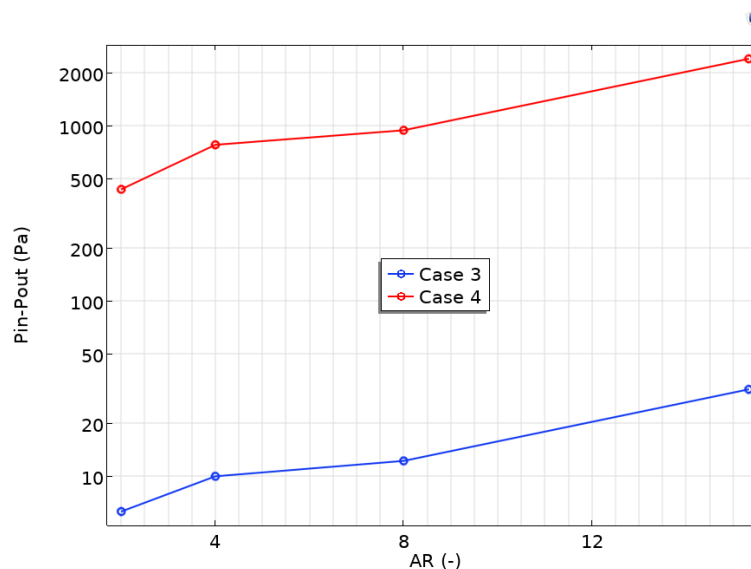


Figure 3.23: Pressure drop versus bed aspect ratio: Comparison between Cases 3 and 4

The simulated CO conversion rates are presented in the third column of Table (3.10) as well as in the bar chart of Figure (3.24).

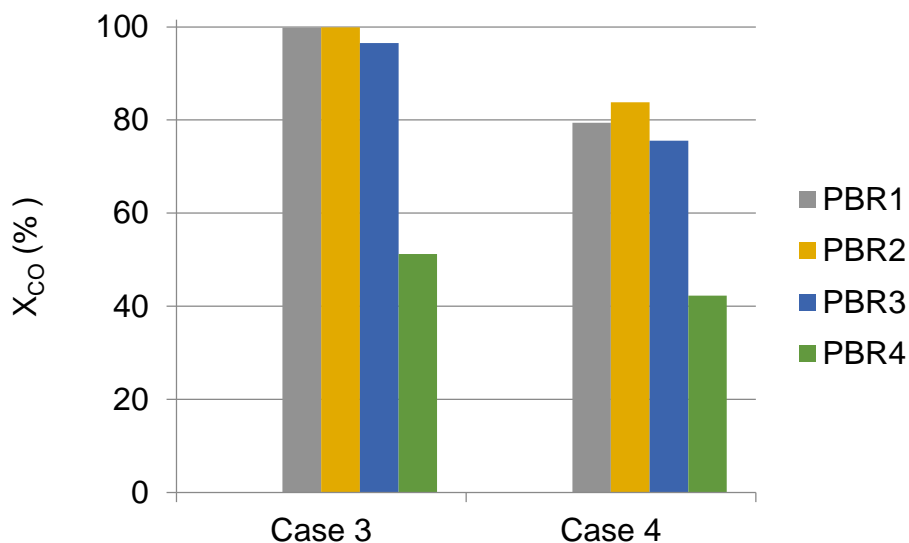


Figure 3.24 : CO conversion rate of different PBRs: Comparison between Cases 3 and 4

Overall, the CO conversion rate results predicted in Case 3 are higher than those predicted in Case 4. This was expected, because the residence times in the former case are higher than those in the latter case. Besides, for both cases the slender PBRs exhibited higher CO conversion rates compared to the large PBR. Additionally, in Case 3, almost a complete CO conversion occurred when using PBRs with aspect ratios of 2 and 4. Their respective values were 99.90% and 99.85%. The 99.90% conversion rate in PBR2 was obtained a distance only 1.52 m from the bed inlet, which is lower than the actual bed length (<1.6 m). By lowering the feed velocity, the required length of PBR1, for full CO conversion, might be reduced further, or their tubes number might be increased further. Therefore, if the amount of the processed biomass is lesser than that used in Case 3, the actual FT reactor will not be economically feasible, and a smaller reactor will be necessary.

Concerning Case 4, only PBR2 provided a satisfactory value of CO conversion rate above 80%, which was 83.82%. The other PBRs gave values, which are still lower than 80%. This means that operating with these PBR models is not economically feasible for the operation of single pass FTS. Initially, the thinnest PBR (PBR1) seems to be the most preferable due to its low aspect ratio, for which the heat removed across the wall is the fastest among the other beds. However, after doing simulations, the optimized packed bed was PBR2 with aspect ratio twice that of the thinnest bed (PBR1). We believe that this finding is attributed to the catalyst effective mass density, which is proportional to the term

(1- ϵ). The FT reaction kinetics rate is directly proportional to the catalyst affective mass density, as proven by Equation (2.50).

Actually, in Case 4, the amount of biomass processed by the compacted FTS plant was twice that processed in Case 3. According to the results, the CO conversion rate throughout PBR2, decreased from 99.90% in Case 3 to 83.82% in Case 4. By extrapolating the results, and if we aim to increase further the amount of biomass to be processed, the CO conversion rate will be lower than 83.82% and it could drop below 80%, becoming not economically profitable.

To sum up, the current small FT plant can use the packed bed with aspect ratio of 4 (PBR2) to process approximately 6 tons/d of wood chips or 6.6 tons/d of municipal solid wastes with a CO conversion rate of 99.90 %. It can also process twice the above-mentioned amounts, but with only 83.82% of CO conversion rate. Furthermore, the following limitations of the use of the optimized FT reactor (PBR2) can be considered:

- A quantity lesser than 6 tons of wood chips or 6.6 tons of municipal solid waste per day should be processed in a smaller packed bed reactor than PBR2 with aspect ratio of 4, for the economic efficiency;
- A quantity higher than 12 tons of wood chips or 13.2 tons of municipal solid waste per day could not be processed in the current compacted FTS plant due to the space limitation as well as the economic efficiency.

Therefore, the minimum and the maximum daily amount of biomass, which can be processed efficiently in the current compacted FTS plant, using PBR2, are 6 tons of wood chips or 6.6 tons of municipal solid waste and 12 tons of wood chips or 13.2 tons of municipal solid waste, respectively.

Figures (3.25) and (3.26) show the productivity of C_{5+} , LPG and C_{3+} for all scenarios of small-scale FT reactors. While Figure (3.25) concerns Case 3, Figure (3.26) concerns Case 4. For both Cases, PBR2 is considered as the reference packed bed, so all the figures are normalized with respect to the simulated results of PBR2. As expected, in Case 3, PBR1 and PBR2 gave the highest productivities of about 4827 kg/d of C_{5+} and a little more than 280 kg/d of LPG, as shown in Table (3.10). The share of LPG in C_{3+} was around 5.5%.

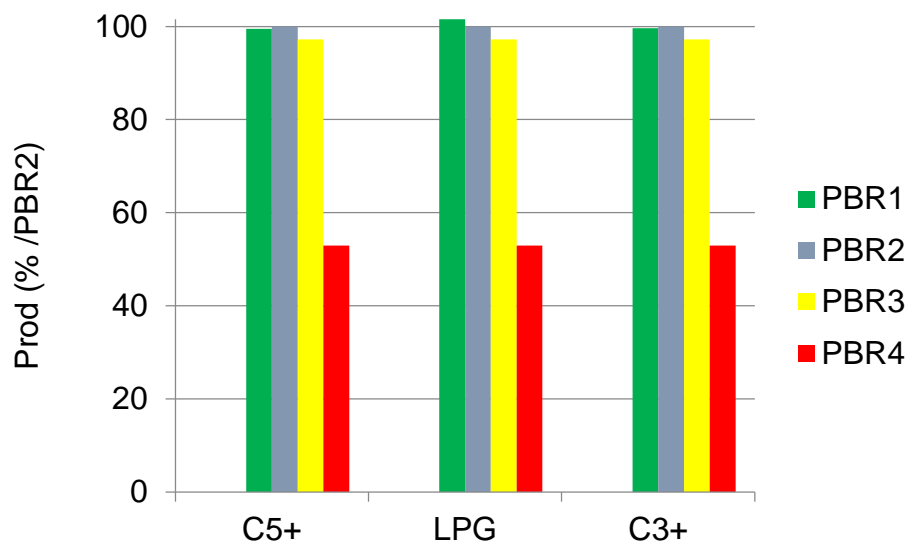


Figure 3.25: Simulation results of the productivity of C₅₊, LPG and C₃₊, with respect to the productivity of PBR2: Comparison between packed beds with different aspect ratios (Case 3)

Regarding Case 4, shown in Figure (3.26), only PBR2 gave the highest productivities of C₃₊, C₅₊ and LPG.

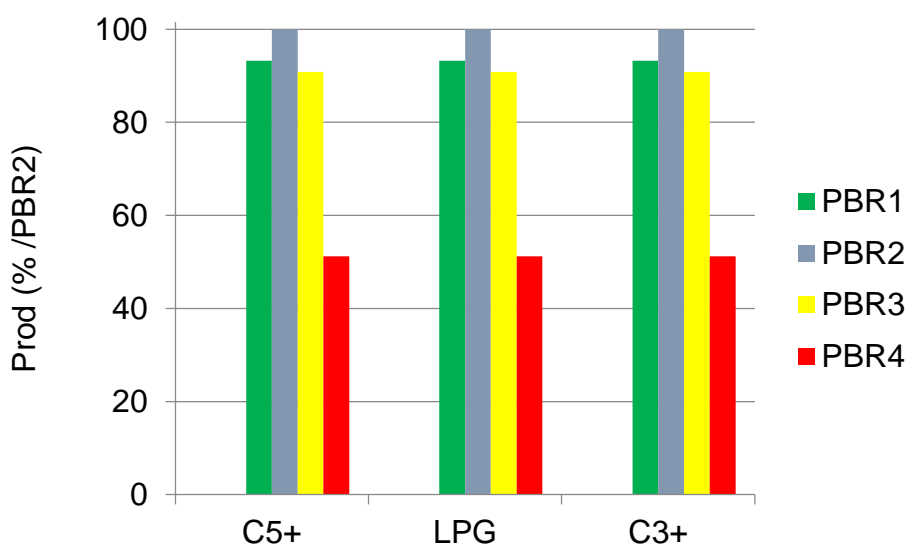


Figure 3.26: Simulation results of the productivity of C₅₊, LPG and C₃₊, with respect to the productivity of PBR2: Comparison between packed beds with different aspect ratios of Case 4

The simulated values of Case 4/PBR2 are around 8360 kg/d and 487 kg/d of C₅₊ and LPG, respectively, as shown in Table (3.10).

Based on the productivity results of both cases, it can be concluded that the packed bed with aspect ratio of 4 (PBR2) is the optimized FT reactor, for the small-scale FTS, of this study, but which case is more efficient?

While the processed amount of Case 4, using PBR2, represents twice that processed in Case 3, the productivity of C_{3+} of Case 4, using PBR2, represents only 1.73 times that of Case 3, as shown in Table (3.10). This is evident, because almost a full CO conversion occurred in Case 3, compared to only about 83% of CO conversion rate obtained in Case 4. In other way, for each 1 ton of wood chips, the productivity of C_{3+} , using PBR2, was as follows:

- In case 3: 851.45 kg of C_{3+} per day per 1 ton of wood chips
- In Case 4: 737.31 kg of C_{3+} per day per 1 ton of wood chips

Here we are in front of two scenarios, as presented in Table (3.11). Either we maximize the daily rate of biomass processed (Case 4/PBR2), or process a smaller quantity, but with greater efficiency (Case3/PBR2). A third scenario can be proposed, which is the use of two modular FTS plants, each operates under the conditions of Case 3/PBR2. In this case, the amount of biomass to be processed is as the same as that of Case 4/PBR2, with the efficiency of Case 3/PBR2. Regarding economics, the CAPEX will be doubled, but also the revenues will increase. This can be explained below.

For long time operating period, the difference in sales between scenarios 3 and 2 will cover the difference in CAPEX between the two scenarios. This is because in the oil and gas sector the POT is generally short. Therefore, the objective function defined by Equation (3.3) has to be maximized. Since the OPEX are supposed to be the same for both scenarios, the objective function to be maximized is the sales revenues. As seen in Table (3.11), using two modular FTS units, on the basis of Case 3/PBR2 gave the highest revenues, being the most profitable scenario.

Table 3.11: Economical comparison between the three scenarios of small-scale FTS

Scenario	CAPEX [Unit Money]	OPEX [Unit Money.Day ⁻¹]	Prod (C ₃₊) [kg.Day ⁻¹]	Sales revenues [Unit Money.Day ⁻¹]
1 st scenario: 1 modular unit of FTS Plant (under conditions of Case 3)	CAPEX_FT	6 Ton * Price (biomass)	5108.71	Price (C ₃₊)*5108.71
2 nd scenario: 1 modular unit of FTS Plant (under conditions of Case 4)	CAPEX_FT	12 Ton * Price (biomass)	8847.79	Price (C ₃₊)*8847.79
3 rd scenario: 2 modular units of FTS Plant (under conditions of Case 3)	2*CAPEX_FT	12 Ton * Price (biomass)	10217.42	Price (C ₃₊)*10217.42

In Table (3.11), Price (C₃₊) and Price (biomass) are the prices of 1 kg of C₃₊ and Biomass respectively, in [Unit Money.kg⁻¹].

3.4 Conclusion

The results obtained in this chapter can be summarized as follows:

- The hydrodynamic study confirmed the accuracy of the Einfeld and Schnitzlein correlation compared to Ergun correlation to account for pressure drop in low aspect ratio packed bed reactors. Therefore, the Einfeld and Schnitzlein correlation will be used in the momentum balance equation when modeling slender packed reactors.
- An error discretization uncertainty study was conducted on the 3D model to ensure the accuracy of the 3D simulations.
- Besides the 3D model was validated, in term of local field velocity, against model from literature
- The validity of the conceptual 2D model proposed in this study was proven for packed bed with aspect ratio of 2 and for incompressible laminar flow conditions, mainly for $Re_p < 111$.
- The correlations of Einfeld and Schnitzlein and Ergun were applied in the momentum balance equations of the FTPBR models. While, the former was applied for the slender packed bed reactors the latter was applied for the large packed bed reactor.
- The FT reaction was simulated in 0th dimension, in order to study its kinetics and thermal behavior under ideal conditions. It was revealed that, under the FT conditions,

almost all the CO is consumed during the first stage of the reaction. Moreover, the temperature rises sharply during the initial stage of the FT reaction, reaching dramatic values during just few seconds, under adiabatic operation mode. This runaway behavior can be prevented by external cooling when using multitubular packed bed reactor.

- A mesh independence study was conducted to ensure the accuracy of the developed FTPBR model.

- The results of the developed FTPBR model, in terms of CO conversion rate, axial temperature profile, products selectivity, were confronted to some results of literature. The comparison results were presented and discussed.

- The results showed that the packed bed aspect ratio has a considerable impact on the performance of the FT packed bed reactor. This is attributed to the heat transfer intensification when using a packed bed reactor with a low bed to particle diameter ratio.

- The developed FTPBR model was used to conduct a parametric study, regarding the bed aspect ratio, for large scale FT process. The daily NG flow rate was 170000 STDCM to produce 3.3 kg/s of syngas, using a gas sample from an associated gas oil field, in Algeria. It has been confirmed that, the large packed bed with aspect ratio of 15.33 is the optimum FT reactor for large-scale FT operations. This optimum FT packed bed reactor can be used to transform associated gas of undeveloped and remote oil fields in Algeria, into hydrocarbon liquids instead of flaring.

- A similar parametric study on FT packed bed reactor was conducted, in order to design the optimum packed bed reactor for small-scale FT synthesis. It was found that, the slender packed bed with aspect ratio of 4 is the optimum packed bed. The designed packed bed reactor represents a tubes bundle, which consists of 6698 tubes arranged in triangular pattern. This FT reactor was designed to process 6 tons of wood chips or 6.6 tons of municipal solid waste per day.

GENERAL CONCLUSION AND PERSPECTIVES

The Fischer-Tropsch synthesis technology, which has been in existence for nearly a century, occupies a distinctive role in the energy worldwide supply, addressing the increasing global energy needs. This process is versatile in its ability to utilize a diverse range of sources for syngas production, including biomass, stranded natural gas and coal. Furthermore, the resulting liquid fuels are characterized by their ultra-clean properties, being free from aromatics, particulates, sulfur, and nitrogen compounds. These make the Fischer-Tropsch process as a viable solution to adapt to evolving energy preferences, more stringent environmental regulations and the rising demands for energy worldwide. The recent resurgence of interest in catalytic processes has led to the application of Fischer-Tropsch synthesis in both conventional methods, such as large-scale packed bed reactors, and innovative approaches, such as mobile FTS plants utilizing micro-reactors or small-scale packed bed reactors. The packed bed reactor type, which is prevalent among commercially available reactors, poses the most considerable challenges in heat transfer and has been chosen as the focus of this investigation. The minimization of tube diameters may facilitate the reduction of thermal transport resistance, thereby aiding in the regulation of temperature within a fixed bed reactor. The utilization of a packed bed reactor configuration with a low aspect ratio in order to enhance heat transfer in multi-tubular packed bed Fischer-Tropsch reactors has not been widely studied in the existing open literature. It was essential to create a model that effectively forecasts the influence of the bed aspect ratio on the performance of the FTPBR. To achieve this objective, simulations were conducted utilizing the commercial Finite Element based-software, COMSOL Multiphysics 5.6.

Two modeling studies were carried out; a hydrodynamic model of low aspect ratio packed bed reactor and an overall model of the Fischer-Tropsch reaction in a Packed Bed Reactor (FTPBR model). Firstly, the hydrodynamic model uses the mass and the momentum balance equations to simulate single incompressible laminar flow in a slender packed bed with aspect ratio of 2. The resulting 3D model was validated against experimental results of literature. Furthermore, due to the scarcity of the experimental results, a consistent error discretization uncertainty study, which is based on the Grid Convergence Index (GCI), was conducted. Once the 3D model validated; it was used to validate the resulting 2D hydrodynamic models. It was confirmed that the Einfeld and Schnitzlein correlation gives accurate results of pressure drop, through a slender packed

bed, compared to Ergun correlation, when implemented in a 2D pseudo-homogeneous model. Moreover, a new modeling approach was proposed and validated. It consists of transforming the real 3D geometry of the reactor into conceptual 2D geometry, using the cross-section geometry operation, available in COMSOL Multiphysics. The limit of this approach is that, it is only valid for a slender packed bed with aspect ratio of 2, operating under laminar flow regime conditions, mainly for particle Reynolds number lower than 111. Secondly, the FTPBR model, which is a 2D pseudo-homogeneous model, was developed. It uses the mass, momentum, heat transfer and species transport conservation equations coupled with a kinetic model of the FTS on cobalt catalyst. Similarly, to the hydrodynamic study and by setting out the limit conditions, the FTPBR model was solved using COMSOL multiphysics 5.6. The model outputs are the axial temperature, CO conversion rate and products yields, mainly (C₅₊, LPG and C₃₊). The FTPBR model was validated with respect of benchmark models of literature. Additionally, because of the limited availability of experimental results, a thorough investigation on the uncertainties associated with error discretization was performed, using the Grid Convergence Index (GCI) methodology.

Once the FTPBR model was validated, it was used to conduct a parametric study on the FTS applied for large and small scales. The influence of the bed to catalyst particle diameter ratio (aspect ratio) was investigated. Four cases were studied. While, Cases 1 and 2 were related to the large-scale FT reactors, Cases 3 and 4 concerned the small-scale FT reactors. For each case, four packed beds with different aspect ratios were simulated and compared. It has been concluded that, for the large-scale FTS, the optimum packed bed is the large packed bed with aspect ratio of 15.33. This reactor can be used in a GTL plant to process 170000 m³ of natural gas for producing more than 626 tons of C₅₊ per day. Otherwise, the slender packed bed with aspect ratio of 4 is the best choice for the small-scale FTS. Then, the multitubular packed bed reactor, which consists of slender tubes packed with cobalt catalyst, was designed. All the tubes are similar with aspect ratio of 4. The obtained number of the tubes is 6698 tubes arranged in triangular pattern. The resulting FT reactor is 2 m long and 1916 mm in diameter. This FT reactor was designed to process 6 tons of wood chips or 6.6 tons of municipal solid waste per day, to daily produce 4827.16 kg/d and 281.55 kg/d of C₅₊ and LPG, respectively.

The research outlined in this thesis could be enhanced through additional investigation in four main areas. Firstly, conducting a detailed techno-economic study could help decision makers to decide whether it is time to implement the GTL technology

for gas recovery from the stranded oil and gas fields not still developed, in Algeria, or other more beneficial options are still persist including gas reinjection, or gas selling via pipelines of Liquefied Natural Gas (LNG). Secondly, carrying out the simulation of the whole FTS process, in a mobile container, which includes all the units; the biomass gasifier, the FT reactor and the products separation unit, could serve further information such as real reactor outputs, which can be compared and integrated back into the model to refine its predictive accuracy, regarding the reactor performance. This can be accomplished by using a process simulator, such as Aspen HYSYS. Thirdly, the results of the simulations could be a basis for manufacturing at the laboratory scale a pilot FTS plant, including all the process steps, within the limits of equipment availability. Finally, one of the reasons to study the packed bed reactor configuration for FTS in this thesis is to conduct an investigation study about its thermal management, via reducing the bed aspect ratio. Other reactor types may be also explored such as those utilize proprietary catalysts called GreyCat to transform the mixture of H_2 and CO directly into synthetic diesel. This eliminate the products upgrading step, which make the FTS plant to be modular and appropriate for recovering small flare gas volume.

As the industry that depends on this configuration of packed bed reactors with low aspect ratio is becoming more concerned all over the world, any additional contribution to its design and/or modeling of various parameters will not only lead to technology progress, resulting in significant savings, but also help to preserve our precious environment.

REFERENCES

- [1] A. Azarpour, N. Rezaei, and S. Zendehboudi, 'Performance analysis and modeling of catalytic trickle-bed reactors: a comprehensive review', *Journal of Industrial and Engineering Chemistry*, vol. 103, pp. 1–41, Nov. 2021, doi: 10.1016/j.jiec.2021.04.020.
- [2] V. V. Ranade, R. V. Chaudhari, and P. R. Gunjal, *Trickle bed reactors: reactor engineering & applications*. Amsterdam: Elsevier, 2011.
- [3] 'Croissance et analyse du marché des gaz liquides Gtl 2032'. Accessed: Mar. 03, 2025. [Online]. Available: <https://www.wiseguyreports.com/fr/reports/gas-liquids-gtl-market>
- [4] C. Trevisanut *et al.*, 'Micro-syngas technology options for GtL', *Can J Chem Eng*, vol. 94, no. 4, pp. 613–622, Apr. 2016, doi: 10.1002/cjce.22433.
- [5] V. Ribun, S. Boichenko, and U. Kale, 'Advances in gas-to-liquid technology for environmentally friendly fuel synthesis: Analytical review of world achievements', *Energy Reports*, vol. 9, pp. 5500–5508, Dec. 2023, doi: 10.1016/j.egyr.2023.04.372.
- [6] K. T. Knutsen, 'Modelling and optimization of a Gas-to-Liquid plant', Institutt for kjemisk prosessteknologi, 2013.
- [7] H. Mahmoudi, 'Performance of cobalt-based eggshell catalyst in low-temperature Fischer-Tropsch synthesis process to produce long-chain hydrocarbons from synthesis gas utilizing fixed-bed reactor technology', PhD Thesis, University of Birmingham, 2015.
- [8] J. Haydary, *Chemical process design and simulation: Aspen Plus and Aspen Hysys applications*. John Wiley & Sons, 2019.
- [9] D. Braide, C. Panaritis, G. Patience, and D. C. Boffito, 'Gas to liquids (GTL) microrefinery technologies: A review and perspective on socio-economic implications', *Fuel*, vol. 375, p. 132385, 2024.
- [10] J. Shen *et al.*, 'Design of a Fischer-Tropsch multi-tube reactor fitted in a container: A novel design approach for small scale applications', *Journal of Cleaner Production*, vol. 362, p. 132477, Aug. 2022, doi: 10.1016/j.jclepro.2022.132477.
- [11] A. Holwell, 'Small-scale gas to liquids', *Petroleum technology quarterly*, vol. 16, no. 3, pp. 97–101, 2011.
- [12] M. Loewert, J. Hoffmann, P. Piermartini, M. Selinsek, R. Dittmeyer, and P. Pfeifer, 'Microstructured Fischer-Tropsch reactor scale-up and opportunities for decentralized application', *Chemical Engineering & Technology*, vol. 42, no. 10, pp. 2202–2214, 2019.
- [13] K. Zayer Kabeh and R. Haghighi Khoshkhou, 'Economic feasibility of small-scale gas to liquid technology in reducing flaring in Iran and case study of implementing the technology at the third South Pars refinery', *Energy Equipment and Systems*, vol. 9, no. 4, pp. 317–330, 2021.
- [14] Z. He, G. Khatu, E. Tenenbaum, W. Li, and Z. Han, 'Flared Gas Monetization with Modular Gas-to-Liquid Units: Oilfield Conversion of Associated Gas into Petrol at Small-Scales', in *Abu Dhabi International Petroleum Exhibition & Conference*, Abu Dhabi, UAE: SPE, Nov. 2016, p. D021S029R001. doi: 10.2118/183510-MS.
- [15] S. Kanshio, H. O. Agogo, and T. J. Chior, 'Techno-Economic Assessment of Mini-GTL Technologies for Flare Gas Monetization in Nigeria', in *SPE Nigeria Annual International Conference and Exhibition*, Lagos, Nigeria: SPE, Jul. 2017, p. D023S026R003. doi: 10.2118/189120-MS.

- [16] V. Chandra, D. Vogels, E. Peters, and J. A. M. Kuipers, 'A multi-scale model for the Fischer-Tropsch synthesis in a wall-cooled packed bed reactor', *Chemical Engineering Journal*, vol. 410, p. 128245, 2021.
- [17] G. D. Wehinger and F. Scharf, 'Thermal radiation effects on heat transfer in slender packed-bed reactors: Particle-resolved CFD simulations and 2D modeling', *Chemical Engineering Research and Design*, vol. 184, pp. 24–38, Aug. 2022, doi: 10.1016/j.cherd.2022.05.034.
- [18] 75, 'Algeria - Oil and Gas - Hydrocarbons'. Accessed: Mar. 01, 2025. [Online]. Available: <https://www.trade.gov/country-commercial-guides/algeria-oil-and-gas-hydrocarbons>
- [19] R. L. d'Algérie, 'Speech by the Minister of Environment and Renewable Energy, Fatma Zahra Zerouati in 2018', L'Echo d'Algérie. Accessed: Mar. 01, 2025. [Online]. Available: <https://lechodalgerie.dz/environnement-lalgerie-produit-34-millions-de-tonnes-de-dechets-par-an/>
- [20] A. Suneja and S. Roy, 'Liquid flow distribution in trickle bed reactors containing trilobed extrusions packed using different techniques', *Results in Engineering*, vol. 17, p. 100704, 2023.
- [21] J. Tan, Y.-N. Ji, W.-S. Deng, and Y.-F. Su, 'Process intensification in gas/liquid/solid reaction in trickle bed reactors: A review', *Petroleum Science*, vol. 18, no. 4, pp. 1203–1218, 2021.
- [22] A. T. P. Neto, T. C. R. L. Fernandes, H. B. da Silva Junior, A. C. B. de Araújo, and J. J. N. Alves, 'Three-phase trickle-bed reactor model for industrial hydrotreating processes: CFD and experimental verification', *Fuel Processing Technology*, vol. 208, p. 106496, 2020.
- [23] M. S. Parandin, H. A. Ebrahim, and H. R. Norouzi, 'Flue gas desulfurization by natural recyclable manganese ore in packed bed reactor and its performance prediction by random pore model', *Journal of Industrial and Engineering Chemistry*, vol. 141, pp. 243–259, 2025.
- [24] C. E. Ramírez-Castelán, A. Hidalgo-Vivas, J. Brix, A. D. Jensen, and J. K. Huusom, 'Mathematical Modelling and Simulation of a Trickle-Bed Reactor for Hydrotreating of Petroleum Feedstock', *International Journal of Chemical Reactor Engineering*, vol. 17, no. 7, Jul. 2019, doi: 10.1515/ijcre-2018-0176.
- [25] O. N. Manjrekar and P. L. Mills, 'Trickle Bed Reactors', in *Multiphase Flows for Process Industries*, 1st ed., V. V. Ranade and R. P. Utikar, Eds., Wiley, 2022, pp. 533–588. doi: 10.1002/9783527812066.ch9.
- [26] F. S. Mederos, J. Ancheyta, and J. Chen, 'Review on criteria to ensure ideal behaviors in trickle-bed reactors', *Applied Catalysis A: General*, vol. 355, no. 1–2, pp. 1–19, 2009.
- [27] M. J. Al-Ani, 'Hydrodynamics of trickle bed reactors (TBRS) packed with industrial catalyst using advanced measurement techniques', PhD Thesis, Missouri University of Science and Technology, 2019.
- [28] N. Jurtz, M. Kraume, and G. D. Wehinger, 'Advances in fixed-bed reactor modeling using particle-resolved computational fluid dynamics (CFD)', *Reviews in Chemical Engineering*, vol. 35, no. 2, pp. 139–190, Feb. 2019, doi: 10.1515/revce-2017-0059.
- [29] I. Iliuta and F. Larachi, 'Fischer-Tropsch synthesis in vertical, inclined and oscillating trickle-bed reactors for offshore floating applications', *Chemical Engineering Science*, vol. 177, pp. 509–522, 2018.
- [30] A. Hernandez-Aguirre, E. Hernandez-Martinez, F. López-Isunza, and C. O. Castillo, 'Framing a novel approach for pseudo continuous modeling using Direct Numerical

- Simulations (DNS): Fluid dynamics in a packed bed reactor', *Chemical Engineering Journal*, vol. 429, p. 132061, 2022.
- [31] Y. Li, G. He, B. Yu, S. Yan, and L. Xie, 'DEM-CFD modeling and simulations of hydrodynamic characteristics and flow resistance coefficient in fixed-bed reactors', *Chemical Engineering Journal Advances*, vol. 8, p. 100167, Nov. 2021, doi: 10.1016/j.cejadv.2021.100167.
- [32] J. Peng, B. Yu, S. Yan, and L. Xie, 'CFD Modeling and Simulation of the Axial Dispersion Characteristics of a Fixed-Bed Reactor', *ACS Omega*, vol. 7, no. 30, pp. 26455–26464, Aug. 2022, doi: 10.1021/acsomega.2c02417.
- [33] A. G. Dixon and B. Partopour, 'Computational fluid dynamics for fixed bed reactor design', *Annual review of chemical and biomolecular engineering*, vol. 11, no. 1, pp. 109–130, 2020.
- [34] T. Claes, T. Van Gerven, and M. E. Leblebici, 'Design considerations for photocatalytic structured packed bed reactors', *Chemical Engineering Journal*, vol. 403, p. 126355, 2021.
- [35] M. Ibáñez Borde *et al.*, 'Performance comparison between washcoated and packed-bed monolithic reactors for the low-temperature Fischer-Tropsch synthesis', *Chemical Engineering Journal*, 425 (2021) 130424, 2021.
- [36] X. Duan, X. Wang, X. Chen, and J. Zhang, 'Continuous and selective hydrogenation of heterocyclic nitroaromatics in a micropacked bed reactor', *Organic Process Research & Development*, vol. 25, no. 9, pp. 2100–2109, 2021.
- [37] W. Liu, B. Xie, C. Zhang, X. Duan, and J. Zhang, 'Nature and characteristics of gas–liquid flow regimes in a micro-packed bed reactor', *AIChE Journal*, vol. 69, no. 7, p. e18004, 2023.
- [38] A. Fathiganjehlou, K. A. Buist, E. Peters, L. A. de Graaf, and J. A. M. Kuipers, 'Magnetic resonance imaging of trickle flow', *AIChE Journal*, vol. 70, no. 5, p. e18352, 2024.
- [39] N. Jurtz, M. Kraume, and G. D. Wehinger, 'Advances in fixed-bed reactor modeling using particle-resolved computational fluid dynamics (CFD)', *Reviews in Chemical Engineering*, vol. 35, no. 2, pp. 139–190, Feb. 2019, doi: 10.1515/revce-2017-0059.
- [40] V. Dieterich, A. Buttler, A. Hanel, H. Spliethoff, and S. Fendt, 'Power-to-liquid via synthesis of methanol, DME or Fischer–Tropsch-fuels: a review', *Energy & Environmental Science*, vol. 13, no. 10, pp. 3207–3252, 2020.
- [41] Z. Guo, Z. Sun, N. Zhang, and M. Ding, 'Influence of confining wall on pressure drop and particle-to-fluid heat transfer in packed beds with small D/d ratios under high Reynolds number', *Chemical Engineering Science*, vol. 209, p. 115200, 2019.
- [42] A. Džiugys, A. H. Mahmoudi, E. Misiulis, R. Navakas, and G. Skarbalius, 'Fractal dependence of the packed bed porosity on the particles size distribution', *Chaos, Solitons & Fractals*, vol. 159, p. 112144, 2022.
- [43] K. Ravindran* and Dr. G. Madhu, 'Impact of Shape and Size of Catalysts on the Physical Properties and Pressure Drop in Fixed Bed Catalytic Systems', *IJITEE*, vol. 9, no. 6, pp. 1103–1109, Apr. 2020, doi: 10.35940/ijitee.F4214.049620.
- [44] J. von Seckendorff and O. Hinrichsen, 'Review on the structure of random packed-beds', *The Canadian Journal of Chemical Engineering*, vol. 99, no. S1, pp. S703–S733, 2021, doi: 10.1002/cjce.23959.
- [45] B. Eisfeld and K. Schnitzlein, 'The influence of confining walls on the pressure drop in packed beds', *Chemical Engineering Science*, vol. 56, no. 14, pp. 4321–4329, Jul. 2001, doi: 10.1016/S0009-2509(00)00533-9.
- [46] L. Mei and Y. J. Dai, 'A technical review on use of liquid-desiccant dehumidification for air-conditioning application', *Renewable and Sustainable*

- Energy Reviews*, vol. 12, no. 3, pp. 662–689, Apr. 2008, doi: 10.1016/j.rser.2006.10.006.
- [47] F. Scala, *Fluidized bed technologies for near-zero emission combustion and gasification*. Elsevier, 2013.
- [48] P. M. Bester, C. G. Du Toit, and M. C. Potgieter, ‘A numerical analysis of the porosity of the HTR-10 packed pebble bed’, *Nuclear Engineering and Design*, vol. 383, p. 111438, 2021.
- [49] S. Sabet, M. Mobedi, and T. Ozgumus, ‘A pore scale study on fluid flow through two dimensional dual scale porous media with small number of intraparticle pores’, *Polish Journal of Chemical Technology*, vol. 18, no. 1, pp. 80–92, Mar. 2016, doi: 10.1515/pjct-2016-0013.
- [50] M. Matsushita, I. Tajima, M. Abe, and H. Tokuyama, ‘Experimental study of porosity and effective thermal conductivity in packed bed of nano-structured FeTi for usage in hydrogen storage tanks’, *International Journal of Hydrogen Energy*, vol. 44, no. 41, pp. 23239–23248, 2019.
- [51] C. G. Du Toit, ‘Analysing the porous structure of packed beds of spheres using a semi-analytical approach’, *Powder Technology*, vol. 342, pp. 475–485, 2019.
- [52] J. von Seckendorff, K. Achterhold, F. Pfeiffer, R. Fischer, and O. Hinrichsen, ‘Experimental and numerical analysis of void structure in random packed beds of spheres’, *Powder Technology*, vol. 380, pp. 613–628, Mar. 2021, doi: 10.1016/j.powtec.2020.11.026.
- [53] P. Lovreglio, S. Das, K. A. Buist, E. Peters, L. Pel, and J. A. M. Kuipers, ‘Experimental and numerical investigation of structure and hydrodynamics in packed beds of spherical particles’, *AIChE Journal*, vol. 64, no. 5, pp. 1896–1907, 2018.
- [54] Z. Guo, Z. Sun, N. Zhang, X. Cao, and M. Ding, ‘Mean porosity variations in packed bed of monosized spheres with small tube-to-particle diameter ratios’, *Powder Technology*, vol. 354, pp. 842–853, Sep. 2019, doi: 10.1016/j.powtec.2019.07.001.
- [55] G. E. Mueller, ‘A modified packed bed radial porosity correlation’, *Powder Technology*, vol. 342, pp. 607–612, 2019.
- [56] S. Uribe, B. Qi, M. E. Cordero, and M. Al-Dahhan, ‘Comparison between pseudo-homogeneous and resolved-particle models for liquid hydrodynamics in packed-bed reactors’, *Chemical Engineering Research and Design*, vol. 166, pp. 158–171, Feb. 2021, doi: 10.1016/j.cherd.2020.12.001.
- [57] P. R. Gunjal, M. N. Kashid, V. V. Ranade, and R. V. Chaudhari, ‘Hydrodynamics of Trickle-Bed Reactors: Experiments and CFD Modeling’, *Ind. Eng. Chem. Res.*, vol. 44, no. 16, pp. 6278–6294, Aug. 2005, doi: 10.1021/ie0491037.
- [58] A. Pavlišič, R. Ceglar, A. Pohar, and B. Likozar, ‘Comparison of computational fluid dynamics (CFD) and pressure drop correlations in laminar flow regime for packed bed reactors and columns’, *Powder Technology*, vol. 328, pp. 130–139, Apr. 2018, doi: 10.1016/j.powtec.2018.01.029.
- [59] S. Flaischlen and G. D. Wehinger, ‘Synthetic packed-bed generation for CFD simulations: Blender vs. STAR-CCM+’, *ChemEngineering*, vol. 3, no. 2, p. 52, 2019.
- [60] M. Marek, ‘Numerical modeling of random packed beds of various packing densities with a sequential deposition algorithm’, in *AIP Conference Proceedings*, AIP Publishing, 2019.
- [61] A. B. Hamzah, S. Ookawara, S. Yoshikawa, and H. Matsumoto, ‘Numerical study on porosity distribution and hydrodynamics of packed bed in narrow square

- channels', *Chemical Engineering and Processing - Process Intensification*, vol. 151, p. 107905, May 2020, doi: 10.1016/j.cep.2020.107905.
- [62] M. L. Ali, S. Mehlhose, Q. Fradet, and U. Riedel, 'Particle-resolved computational modeling of hydrogen-based direct reduction of iron ore pellets in a fixed bed. Part II: Influence of the pellet sizes and shapes', *International Journal of Hydrogen Energy*, vol. 86, pp. 1401–1413, Oct. 2024, doi: 10.1016/j.ijhydene.2024.08.384.
- [63] S. A. Al-Naimi, F. T. J. Al-Sudani, and E. K. Halabia, 'Hydrodynamics and flow regime transition study of trickle bed reactor at elevated temperature and pressure', *Chemical Engineering Research and Design*, vol. 89, no. 7, pp. 930–939, 2011.
- [64] M. Ochowiak, S. Woziwodzki, M. Doligalski, and P. T. Mitkowski, *Practical Aspects of Chemical Engineering*. Poland: Springer, 2018.
- [65] M. Al-Ani and M. Al-Dahhan, 'Effect of catalyst shape on pressure drop and liquid holdup in a pilot plant trickle bed reactor', *Fuel*, vol. 284, p. 118860, 2021.
- [66] G. Bartelmus, D. Janecki, and A. Burghardt, 'Parametric sensitivity of a CFD model concerning the hydrodynamics of trickle-bed reactor (TBR)', *Chemical and Process Engineering*, pp. 97–107, 2016.
- [67] A. Atta, S. Roy, and K. D. P. Nigam, 'A two-phase Eulerian approach using relative permeability concept for modeling of hydrodynamics in trickle-bed reactors at elevated pressure', *Chemical Engineering Research and Design*, vol. 88, no. 3, pp. 369–378, 2010.
- [68] M. E. Cordero *et al.*, 'CFD analysis of BED textural characteristics on TBR behavior: hydrodynamics and scaling-up', *International Journal of Chemical Reactor Engineering*, vol. 15, no. 6, 2017, doi: 10.1515/ijcre-2017-0095.
- [69] D. Nemeč and J. Levec, 'Flow through packed bed reactors: 1. Single-phase flow', *Chemical Engineering Science*, vol. 60, no. 24, pp. 6947–6957, 2005.
- [70] H. Bouras, Y. Haroun, F. F. Bodziony, R. Philippe, P. Fongarland, and F. Augier, 'Use of CFD for pressure drop, liquid saturation and wetting predictions in trickle bed reactors for different catalyst particle shapes', *Chemical Engineering Science*, vol. 249, p. 117315, 2022.
- [71] S. Ahmadi and F. Sefidvash, 'Study of pressure drop in fixed bed reactor using a computational fluid dynamics (CFD) code', *ChemEngineering*, vol. 2, no. 2, p. 14, 2018.
- [72] J. Feder, E. G. Flekkøy, and A. Hansen, *Physics of flow in porous media*. Cambridge University Press, 2022.
- [73] R. Schulz, N. Ray, S. Zech, A. Rupp, and P. Knabner, 'Beyond Kozeny–Carman: predicting the permeability in porous media', *Transport in Porous Media*, vol. 130, pp. 487–512, 2019.
- [74] S. Ergun, 'Fluid flow through packed columns', *Chem. Eng. Prog.*, vol. 48, no. 2, pp. 89–94, 1952, doi: 10.1021/ie50474a011.
- [75] P. R. Gunjal, V. V. Ranade, and R. V. Chaudhari, 'Computational study of a single-phase flow in packed beds of spheres', *AIChE Journal*, vol. 51, no. 2, pp. 365–378, Feb. 2005, doi: 10.1002/aic.10314.
- [76] R. S. Almusafir, A. A. Jasim, and M. H. Al-Dahhan, 'Review of the fluid dynamics and heat transport phenomena in packed pebble bed nuclear reactors', *Nuclear Science and Engineering*, vol. 197, no. 6, pp. 1001–1037, 2023.
- [77] P. R. Duchowicz, J. F. Aranda, D. E. Babelo, and S. E. Fioressi, 'QSPR study of the Henry's law constant for heterogeneous compounds', *Chemical Engineering Research and Design*, vol. 154, pp. 115–121, 2020.

- [78] A. H. Beni and M. R. Khosravi-Nikou, 'Modeling hydrodynamics of trickle-bed reactors at high and low pressure using CFD method', *Petroleum Science and Technology*, vol. 33, no. 20, pp. 1770–1779, 2015.
- [79] C. S. L. Narasimhan, R. P. Verma, A. Kundu, and K. D. P. Nigam, 'Modeling hydrodynamics of trickle-bed reactors at high pressure', *AIChE journal*, vol. 48, no. 11, pp. 2459–2474, 2002.
- [80] I. Calderón-Vásquez *et al.*, 'Review on modeling approaches for packed-bed thermal storage systems', *Renewable and Sustainable Energy Reviews*, vol. 143, p. 110902, 2021.
- [81] E. B. Hassan and J. Hoffmann, 'Review on pressure drop through a randomly packed bed of crushed rocks', *Discover Applied Sciences*, vol. 6, no. 3, p. 126, 2024.
- [82] D. Reger, E. Merzari, P. Balestra, S. Schunert, Y. Hassan, and H. Yuan, 'An improved pressure drop correlation for modeling localized effects in a pebble bed reactor', *Nuclear Engineering and Design*, vol. 403, p. 112123, 2023, doi: 0.1016/j.nucengdes.2022.112123.
- [83] L. Lin, C. I. Contescu, and N. C. Gallego, 'Initial Assessment of Erosion/Abrasion Issues Related to Gas-Cooled Reactors', Oak Ridge National Laboratory (ORNL), Oak Ridge, TN (United States), 2023.
- [84] B. Qi, S. Uribe, O. Farid, and M. Al-Dahhan, 'Random trilobe packing using rigid body approach and local Gas-Liquid hydrodynamics simulation through CFD with experimental validation', *Chemical Engineering Journal*, vol. 435, p. 134481, 2022.
- [85] A. E. Saez and R. G. Carbonell, 'hydrodynamic parameters for gas-liquid cocurrent flow in packed beds', *AIChE Journal*, vol. 31, no. 1, pp. 52–62, 1985.
- [86] V. V. Ranade and R. P. Utikar, *Multiphase Flows and Process Industries*, vol. 1. Wiley Online Library, 2022.
- [87] P. Kawatra, S. Panyaram, and B. A. Wilhite, 'Hydrodynamics in a pilot-scale cocurrent trickle-bed reactor at low gas velocities', *AIChE Journal*, vol. 64, no. 7, pp. 2560–2569, 2018.
- [88] M. Lakkaichi, N. Outili, and A. H. Meniai, 'Pressure Drop Analysis of Incompressible Laminar Flow in a Low Aspect-Ratio Packed Bed Using CFD Simulations.', *International Journal of Multiphysics*, vol. 18, no. 2, 2024.
- [89] M. Winterberg and E. Tsotsas, 'Impact of tube-to-particle-diameter ratio on pressure drop in packed beds', *American Institute of Chemical Engineers. AIChE Journal*, vol. 46, no. 5, p. 1084, 2000.
- [90] A. K. Saroha and I. Nandi, 'Pressure drop hysteresis in trickle bed reactors', *Chemical engineering science*, vol. 63, no. 12, pp. 3114–3119, 2008.
- [91] R. Maiti, R. Khanna, and K. D. P. Nigam, 'Hysteresis in trickle-bed reactors: a review', *Industrial & engineering chemistry research*, vol. 45, no. 15, pp. 5185–5198, 2006.
- [92] D. Loudon, W. van der Merwe, and W. Nicol, 'Multiple hydrodynamic states in trickle flow: quantifying the extent of pressure drop, liquid holdup and gas-liquid mass transfer variation', *Chemical engineering science*, vol. 61, no. 22, pp. 7551–7562, 2006.
- [93] S. Li *et al.*, 'Investigation of pressure drop in a cocurrent downflow three-phase moving bed', *AIChE Journal*, vol. 66, no. 7, p. e16227, 2020.
- [94] Y. Chen, G. Chinello, P. Tait, and J. Jia, 'A New Correlation to Determine the Lockhart-Martinelli Parameter from Differential Pressure Measurement in a Vertical Pipe', *Available at SSRN 4161384*.
- [95] M. J. Ellman, N. Midoux, A. Laurent, and J. C. Charpentier, 'A new, improved pressure drop correlation for trickle-bed reactors', *Chemical Engineering Science*,

- vol. 43, no. 8, pp. 2201–2206, 1988, doi: [https://doi.org/10.1016/0009-2509\(88\)87104-5](https://doi.org/10.1016/0009-2509(88)87104-5).
- [96] S. Dasgupta and A. Atta, ‘Computational insights on intensification of hydrodenitrogenation in a trickle bed reactor using periodic flow modulation’, *Chemical Engineering and Processing-Process Intensification*, vol. 157, p. 108135, 2020.
- [97] A. Lakota, J. Levec, and R. G. Carbonell, ‘Hydrodynamics of trickling flow in packed beds: relative permeability concept’, *AIChE journal*, vol. 48, no. 4, pp. 731–738, 2002.
- [98] D. Nemeč and J. Levec, ‘Flow through packed bed reactors: 2. Two-phase concurrent downflow’, *Chemical Engineering Science*, vol. 60, no. 24, pp. 6958–6970, 2005.
- [99] R. A. Holub, M. P. Duduković, and P. A. Ramachandran, ‘A phenomenological model for pressure drop, liquid holdup, and flow regime transition in gas-liquid trickle flow’, *Chemical Engineering Science*, vol. 47, no. 9–11, pp. 2343–2348, 1992.
- [100] R. A. Holub, M. P. Duduković, and P. A. Ramachandran, ‘Pressure drop, liquid holdup, and flow regime transition in trickle flow’, *AIChE Journal*, vol. 39, no. 2, pp. 302–321, 1993.
- [101] I. Iliuta, F. Larachi, and B. P. Grandjean, ‘Pressure drop and liquid holdup in trickle flow reactors: improved Ergun constants and slip correlations for the slit model’, *Industrial & engineering chemistry research*, vol. 37, no. 12, pp. 4542–4550, 1998.
- [102] M. H. Al-Dahhan, M. R. Khadilkar, Y. Wu, and M. P. Duduković, ‘Prediction of pressure drop and liquid holdup in high-pressure trickle-bed reactors’, *Industrial & engineering chemistry research*, vol. 37, no. 3, pp. 793–798, 1998.
- [103] I. Iliuta, F. Larachi, and M. H. Al-Dahhan, ‘Double-slit model for partially wetted trickle flow hydrodynamics’, *AIChE journal*, vol. 46, no. 3, pp. 597–609, 2000.
- [104] I. Iliuta and F. Larachi, ‘The generalized slit model: pressure gradient, liquid holdup & wetting efficiency in gas-liquid trickle flow’, *Chemical engineering science*, vol. 54, no. 21, pp. 5039–5045, 1999.
- [105] I. Iliuta, B. P. A. Grandjean, and F. Larachi, ‘Hydrodynamics of trickle-flow reactors: updated slip functions for the slit models’, *Chemical Engineering Research and Design*, vol. 80, no. 2, pp. 195–200, 2002.
- [106] A. Attou, C. Boyer, and G. Ferschneider, ‘Modelling of the hydrodynamics of the cocurrent gas-liquid trickle flow through a trickle-bed reactor’, *Chemical Engineering Science*, vol. 54, no. 6, pp. 785–802, 1999.
- [107] C. Boyer, C. Volpi, and G. Ferschneider, ‘Hydrodynamics of trickle bed reactors at high pressure: Two-phase flow model for pressure drop and liquid holdup, formulation and experimental validation’, *Chemical Engineering Science*, vol. 62, no. 24, pp. 7026–7032, Dec. 2007, doi: 10.1016/j.ces.2007.08.036.
- [108] T. S. Lee and J. N. Chung, ‘Mathematical modeling and numerical simulation of a Fischer–Tropsch packed bed reactor and its thermal management for liquid hydrocarbon fuel production using biomass syngas’, *Energy & Fuels*, vol. 26, no. 2, pp. 1363–1379, 2012.
- [109] H. Deng, B. Guo, H. Dong, C. Liu, and Z. Geng, ‘Computational investigation of liquid holdup and wetting efficiency inside trickle bed reactors with different catalyst particle shapes’, *Applied Sciences*, vol. 10, no. 4, p. 1436, 2020.
- [110] B. Qi, O. Farid, S. Uribe, and M. Al-Dahhan, ‘Maldistribution and dynamic liquid holdup quantification of quadrilobe catalyst in a trickle bed reactor using gamma-ray computed tomography: Pseudo-3D modelling and empirical modelling using deep

- neural network', *Chemical Engineering Research and Design*, vol. 164, pp. 195–208, 2020.
- [111] R. Lange, M. Schubert, and T. Bauer, 'Liquid holdup in trickle-bed reactors at very low liquid Reynolds numbers', *Industrial & engineering chemistry research*, vol. 44, no. 16, pp. 6504–6508, 2005.
- [112] M. Bazmi, S. H. Hashemabadi, and M. Bayat, 'Extrudate trilobe catalysts and loading effects on pressure drop and dynamic liquid holdup in porous media of trickle bed reactors', *Transport in porous media*, vol. 99, pp. 535–553, 2013.
- [113] B. Qi, S. Uribe, O. Farid, and M. Al-Dahhan, 'Development of a hybrid pressure drop and liquid holdup phenomenological model for trickle bed reactors based on two-phase volume averaged equations', *The Canadian Journal of Chemical Engineering*, 2020.
- [114] Z. Cheng *et al.*, 'External Wetting Efficiency in a Three-Phase Fixed Bed Loaded with Porous and Non-Porous Packings', *Processes*, vol. 10, no. 1, p. 135, 2022.
- [115] Q. Wu, X. Hu, P.-L. Yue, and D. Wang, 'Measurement of Wetting Efficiency in Trickle-Bed Reactor', in *17th International Symposium of Chemical Reaction Engineering, Hong Kong*, 2002.
- [116] Y. Wang, J. Chen, and F. Larachi, 'Modelling and simulation of trickle-bed reactors using computational fluid dynamics: A state-of-the-art review', *The Canadian Journal of Chemical Engineering*, vol. 91, no. 1, pp. 136–180, 2013.
- [117] A. Tavanaei, 'Unravelling Wetting Phenomena in Trickle Bed Reactors: A Direct Numerical Simulation Approach', PhD Thesis, Eindhoven University of Technology, 2024.
- [118] S. Uribe, M. Al-Ani, M. E. Cordero, and M. Al-Dahhan, 'Modelling and validation of TBR Hydrodynamics: Local comparison between CFD and experiments', *Fuel*, vol. 277, p. 118244, 2020, doi: 10.1016/j.fuel.2020.118244.
- [119] A. R. Ahmadi, F. Samimi, and M. R. Rahimpour, 'Three-phase reactor model for simulation of methylacetylene and propadiene selective hydrogenation process', *Chemical Product and Process Modeling*, vol. 14, no. 2, p. 20180047, 2019.
- [120] S. Limtrakul, P. Bannatham, S. Teeraboonchaikul, T. Vatanatham, and P. A. Ramachandran, 'Modeling and evaluation of hydrodesulfurization and deactivation rates for partially wetted Trilobe catalyst using finite element method', *Powder Technology*, vol. 354, pp. 779–791, 2019.
- [121] A. Azarpour, N. Rezaei, and S. Zندهboudi, 'Product quality control in hydropurification process by monitoring reactor feed impurities: Dynamic mathematical modeling', *Journal of Industrial and Engineering Chemistry*, vol. 92, pp. 62–76, 2020.
- [122] J. S. Al-Huwaidi, M. A. Al-Obaidi, A. T. Jarullah, C. Kara-Zaitri, and I. M. Mujtaba, 'Modeling and simulation of a hybrid system of trickle bed reactor and multistage reverse osmosis process for the removal of phenol from wastewater', *Computers & Chemical Engineering*, vol. 153, p. 107452, 2021.
- [123] N. Aryal, M. Odde, C. B. Petersen, L. D. M. Ottosen, and M. V. W. Kofoed, 'Methane production from syngas using a trickle-bed reactor setup', *Bioresource Technology*, vol. 333, p. 125183, 2021.
- [124] F. Ebrahimian *et al.*, 'Effect of pressure on biomethanation process and spatial stratification of microbial communities in trickle bed reactors under decreasing gas retention time', *Bioresource technology*, vol. 361, p. 127701, 2022.
- [125] M. Hachhach, V. Russo, D. Y. Murzin, and T. Salmi, 'Dynamic modelling of trickle bed reactor: Case study of arabinose oxidation', *Powder Technology*, vol. 425, p. 118608, 2023.

- [126] C. F. Fenske, F. Kirzeder, D. Strübing, and K. Koch, 'Biogas upgrading in a pilot-scale trickle bed reactor–Long-term biological methanation under real application conditions', *Bioresource Technology*, vol. 376, p. 128868, 2023.
- [127] C. F. Fenske, D. Strübing, and K. Koch, 'Biological methanation in trickle bed reactors–a critical review', *Bioresource Technology*, vol. 385, p. 129383, 2023.
- [128] Z. Teimouri, V. B. Borugadda, A. K. Dalai, and N. Abatzoglou, 'Application of computational fluid dynamics for modeling of Fischer-Tropsch synthesis as a sustainable energy resource in different reactor configurations: A review', *Renewable and Sustainable Energy Reviews*, vol. 160, p. 112287, 2022.
- [129] A. A. Al-Yaeshi, A. AlNouss, G. McKay, and T. Al-Ansari, 'A Model based analysis in applying Anderson–Schulz–Flory (ASF) equation with CO₂ Utilisation on the Fischer Tropsch Gas-to-liquid Process', in *Computer Aided Chemical Engineering*, vol. 46, Elsevier, 2019, pp. 397–402.
- [130] O. Richard-Koko, J. O. Owolabi, I. I. Olateju, and A. Giwa, 'Modelling and Simulation of a Gas-to-Liquid Technology Using Fischer-Tropsch Process.', *Turkish Online Journal of Qualitative Inquiry*, vol. 12, no. 8, pp. 2890–2907, 2021.
- [131] V. Eyberg, V. Dieterich, S. Bastek, M. Dossow, H. Spliethoff, and S. Fendt, 'Techno-economic assessment and comparison of Fischer–Tropsch and Methanol-to-Jet processes to produce sustainable aviation fuel via Power-to-Liquid', *Energy Conversion and Management*, vol. 315, p. 118728, 2024.
- [132] E. S. Toochukwu *et al.*, 'Economics of gas-to-liquids (GTL) plants', *Petroleum Science and Engineering*, vol. 3, no. 2, pp. 85–93, 2019.
- [133] M. A. Ismael, M. A. Rosli, A. R. A. Aziz, S. E. Mohammed, R. A. Opatola, and M. El-Adawy, 'Gas to liquid (GTL) role in diesel engine: Fuel characteristics and emission: A review', *Cleaner Engineering and Technology*, p. 100706, 2023.
- [134] F. T. Alsudani *et al.*, 'Fischer–Tropsch Synthesis for Conversion of Methane into Liquid Hydrocarbons through Gas-to-Liquids (GTL) Process: A Review', *Methane*, vol. 2, no. 1, pp. 24–43, 2023.
- [135] X. Lu, 'Fischer-Tropsch synthesis: towards understanding', PhD Thesis, University of the Witwatersrand, 2011.
- [136] Z. Gholami, Z. Tišler, and V. Rubáš, 'Recent advances in Fischer-Tropsch synthesis using cobalt-based catalysts: A review on supports, promoters, and reactors', *Catalysis Reviews*, vol. 63, no. 3, pp. 512–595, 2021.
- [137] N. I. Loseva, I. I. Niyazbakiev, and A. V. Silman, 'Fischer–Tropsch synthesis technology evolution', in *IOP Conference Series: Materials Science and Engineering*, IOP Publishing, 2019, p. 012067.
- [138] 'Oryx GTL', *Wikipedia*. Oct. 01, 2024. Accessed: Mar. 07, 2025. [Online]. Available: https://en.wikipedia.org/w/index.php?title=Oryx_GTL&oldid=1248746407
- [139] 'Synfuels China demonstrates First Fischer-Tropsch products from the new Shenhua Ningxia Coal-to-Liquids plant – Syngaschem BV'. Accessed: Mar. 19, 2025. [Online]. Available: <https://www.syngaschem.com/2016/12/12/synfuels-china-demonstrates-first-fischer-tropsch-products-from-the-new-shenhua-ningxia-coal-to-liquids-plant/>
- [140] R. Brelsford, 'Cerilon lets contract for proposed North Dakota GTL complex', *Oil & Gas Journal*. Accessed: Mar. 19, 2025. [Online]. Available: <https://www.ogj.com/refining-processing/gas-processing/article/14310348/cerilon-lets-contract-for-proposed-north-dakota-gtl-complex>
- [141] E. Brancaccio, 'GTL: Small scale and modular technologies for gas to liquid industry', *Serintel Srl, Rome (Italy)*, 2018.

- [142] Y. H. Kim, K.-W. Jun, H. Joo, C. Han, and I. K. Song, 'A simulation study on gas-to-liquid (natural gas to Fischer-Tropsch synthetic fuel) process optimization', *Chemical Engineering Journal*, vol. 155, no. 1–2, pp. 427–432, Dec. 2009, doi: 10.1016/j.cej.2009.08.018.
- [143] B. Bao, M. M. El-Halwagi, and N. O. Elbashir, 'Simulation, integration, and economic analysis of gas-to-liquid processes', *Fuel Processing Technology*, vol. 91, no. 7, pp. 703–713, 2010.
- [144] H.-J. Lee, 'Optimization of Fischer-Tropsch plant', The University of Manchester (United Kingdom), 2011.
- [145] I. J. Otaraku and O. A. Vincent, 'Technical Analysis of the Natural Gas to Hydrocarbon Liquid Process', *American Journal of Chemical Engineering*, vol. 10, no. 1, pp. 25–40, 2015.
- [146] A. Rafiee and M. Panahi, 'Optimal Design of a Gas-to-Liquids Process with a Staged Fischer-Tropsch Reactor', *Chem Eng & Technol*, vol. 39, no. 10, pp. 1778–1784, Oct. 2016, doi: 10.1002/ceat.201600040.
- [147] I. Nkemakolam Chinedu *et al.*, 'Gas-to-Liquids (GTL) Plant Optimization Using Enhanced Synthesis Gas Reforming Technology', *PSE*, vol. 3, no. 2, p. 94, 2019, doi: 10.11648/j.pse.20190302.18.
- [148] S. Greyling, H. Marais, G. Van Schoor, and K. R. Uren, 'Application of exergy-based fault detection in a gas-to-liquids process plant', *Entropy*, vol. 21, no. 6, p. 565, 2019.
- [149] V. Khezri, M. Panahi, E. Yasari, and S. Skogestad, 'Application of surrogate models as an alternative to process simulation for implementation of the self-optimizing control procedure on large-scale process plants—A natural gas-to-liquids (GTL) case study', *Industrial & Engineering Chemistry Research*, vol. 60, no. 13, pp. 4919–4929, 2021.
- [150] Z. Ataya, M. Challiwala, G. Ibrahim, H. A. Choudhury, M. M. El-Halwagi, and N. O. Elbashir, 'Decarbonizing the Gas-to-Liquid (GTL) Process Using an Advanced Reforming of Methane Process', *ACS Engineering Au*, vol. 4, no. 1, pp. 99–111, 2023.
- [151] M. Jafari, V. Spallina, and K. Ghasemzadeh, 'Techno-economic assessment of flare gas valorisation during membrane-based GTL process by net-zero strategy', *Energy Conversion and Management*, vol. 315, p. 118796, Sep. 2024, doi: 10.1016/j.enconman.2024.118796.
- [152] Z. Qi, L. Chen, S. Zhang, J. Su, and G. A. Somorjai, 'A mini review of cobalt-based nanocatalyst in Fischer-Tropsch synthesis', *Applied Catalysis A: General*, vol. 602, p. 117701, 2020.
- [153] M. Amin, M. Usman, T. Kella, W. U. Khan, I. A. Khan, and K. Hoon Lee, 'Issues and challenges of Fischer-Tropsch synthesis catalysts', *Frontiers in Chemistry*, vol. 12, p. 1462503, 2024.
- [154] P. Hazemann, D. Decottignies, S. Maury, S. Humbert, F. C. Meunier, and Y. Schuurman, 'Selectivity loss in Fischer-Tropsch synthesis: The effect of cobalt carbide formation', *Journal of Catalysis*, vol. 397, pp. 1–12, 2021.
- [155] A. De Klerk, *Fischer-tropsch refining*. John Wiley & Sons, 2012.
- [156] M. Martinelli, M. K. Gnanamani, S. LeViness, G. Jacobs, and W. D. Shafer, 'An overview of Fischer-Tropsch Synthesis: XtL processes, catalysts and reactors', *Applied Catalysis A: General*, vol. 608, p. 117740, 2020.
- [157] Z. Teimouri, N. Abatzoglou, and A. K. Dalai, 'Kinetics and selectivity study of Fischer-Tropsch synthesis to C5+ hydrocarbons: a review', *Catalysts*, vol. 11, no. 3, p. 330, 2021.

- [158] C. I. Méndez and J. Ancheyta, 'Kinetic models for Fischer-Tropsch synthesis for the production of clean fuels', *Catalysis Today*, vol. 353, pp. 3–16, 2020.
- [159] J. W. Pratt, 'A Fischer-Tropsch synthesis reactor model framework for liquid biofuels production.', Sandia National Laboratories (SNL), Albuquerque, NM, and Livermore, CA (United States), 2012.
- [160] N. Moazami, M. L. Wyszynski, K. Rahbar, A. Tsolakis, and H. Mahmoudi, 'A comprehensive study of kinetics mechanism of Fischer-Tropsch synthesis over cobalt-based catalyst', *Chemical Engineering Science*, vol. 171, pp. 32–60, 2017.
- [161] R. Zennaro, M. Tagliabue, and C. H. Bartholomew, 'Kinetics of Fischer-Tropsch synthesis on titania-supported cobalt', *Catalysis Today*, vol. 58, no. 4, pp. 309–319, 2000.
- [162] A. Irankhah, A. Haghtalab, E. V. Farahani, and K. Sadaghianizadeh, 'Fischer-Tropsch reaction kinetics of cobalt catalyst in supercritical phase', *Journal of natural gas chemistry*, vol. 16, no. 2, pp. 115–120, 2007.
- [163] C. G. Visconti, E. Tronconi, L. Lietti, P. Forzatti, S. Rossini, and R. Zennaro, 'Detailed kinetics of the Fischer-Tropsch synthesis on cobalt catalysts based on H-assisted CO activation', *Topics in Catalysis*, vol. 54, pp. 786–800, 2011.
- [164] M. Mansouri, H. Atashi, A. A. Mirzaei, and R. Jangi, 'Kinetics of the Fischer-Tropsch synthesis on silica-supported cobalt-cerium catalyst', *International Journal of Industrial Chemistry*, vol. 4, pp. 1–10, 2013.
- [165] P. Kaiser, F. Pöhlmann, and A. Jess, 'Intrinsic and effective kinetics of cobalt-catalyzed fischer-tropsch synthesis in view of a power-to-liquid process based on renewable energy', *Chemical Engineering & Technology*, vol. 37, no. 6, pp. 964–972, 2014.
- [166] J. H. Yang *et al.*, 'Mass transfer limitations on fixed-bed reactor for Fischer-Tropsch synthesis', *Fuel Processing Technology*, vol. 91, no. 3, pp. 285–289, 2010.
- [167] H. S. Fogler, *Elements of chemical reaction engineering, 3rd*. Prentice Hall International, Inc, New Jersey, 1999.
- [168] D. Weber *et al.*, 'Recent Advances in the Mitigation of the Catalyst Deactivation of CO₂ Hydrogenation to Light Olefins', *Catalysts*, vol. 11, no. 12, p. 1447, Nov. 2021, doi: 10.3390/catal11121447.
- [169] C. Niu *et al.*, 'Effect of process conditions on the product distribution of Fischer-Tropsch synthesis over an industrial cobalt-based catalyst using a fixed-bed reactor', *Applied Catalysis A: General*, vol. 601, p. 117630, 2020.
- [170] A. P. Savost'yanov *et al.*, 'Unexpected increase in C₅₊ selectivity at temperature rise in high pressure Fischer-Tropsch synthesis over Co-Al₂O₃/SiO₂ catalyst', *Catalysis Communications*, vol. 99, pp. 25–29, 2017.
- [171] J.-S. Park, D.-E. Kim, Y.-J. Lee, G. Kwak, K.-W. Jun, and M.-J. Park, 'CFD modeling of a thermally efficient modular reactor for Fischer-Tropsch synthesis: determination of the optimal size for each module', *Industrial & Engineering Chemistry Research*, vol. 55, no. 35, pp. 9416–9425, 2016.
- [172] A. Shaikh, M. M. Taha, and M. H. Al-Dahhan, 'Phase distribution in Fischer-Tropsch mimicked slurry bubble column via computed tomography', *Chemical Engineering Science*, vol. 231, p. 116278, 2021.
- [173] C. I. Méndez and J. Ancheyta, 'Modeling and control of a Fischer-Tropsch synthesis fixed-bed reactor with a novel mechanistic kinetic approach', *Chemical Engineering Journal*, vol. 390, p. 124489, 2020.
- [174] A. Jess and C. Kern, 'Modeling of Multi-Tubular Reactors for Fischer-Tropsch Synthesis', *Chemical Engineering & Technology: Industrial Chemistry-Plant*

- Equipment-Process Engineering-Biotechnology*, vol. 32, no. 8, pp. 1164–1175, 2009.
- [175] I. Iliuta and F. Larachi, ‘Fischer-Tropsch synthesis in vertical, inclined and oscillating trickle-bed reactors for offshore floating applications’, *Chemical Engineering Science*, vol. 177, pp. 509–522, 2018.
- [176] C. I. Méndez and J. Ancheyta, ‘Dynamic one-dimensional pseudo-homogeneous model for Fischer-Tropsch fixed-bed reactors’, *Fuel*, vol. 252, pp. 371–392, 2019.
- [177] W. J. S. Van der Merwe, ‘Analysis of flow through cylindrical packed beds with small cylinder diameter to particle diameter ratios’, Master dissertation, North-West University, Potchefstroom Campus, 2014.
- [178] S. Uribe, L. G. Zárate, E. Peralta-Reyes, A. Regalado-Méndez, and M. E. Cordero, ‘Multiscale CFD modelling and analysis of a Trickle Bed Reactor for a hydrodesulfurization process.’, doi: 10.1016/j.fuel.2018.11.104.
- [179] L. Amiri, S. A. Ghoreishi-Madiseh, F. P. Hassani, and A. P. Sasmito, ‘Estimating pressure drop and Ergun/Forchheimer parameters of flow through packed bed of spheres with large particle diameters’, *Powder Technology*, vol. 356, pp. 310–324, 2019, doi: 10.1016/j.powtec.2019.08.029.
- [180] V. M. Govindarao, K. V. Ramrao, and A. V. Rao, ‘Structural characteristics of packed beds of low aspect ratio’, *Chemical engineering science*, vol. 47, no. 8, pp. 2105–2109, 1992, doi: 10.1016/0009-2509(92)80330-F.
- [181] G. E. Mueller, ‘Radial porosity in packed beds of spheres’, *Powder Technology*, vol. 203, no. 3, pp. 626–633, 2010, doi: 10.1016/j.powtec.2010.07.007.
- [182] S. Taheri, S. Ghomeshi, and A. Kantzas, ‘Permeability calculations in unconsolidated homogeneous sands’, *Powder Technology*, vol. 321, pp. 380–389, 2017, doi: 10.1016/j.powtec.2017.08.014.
- [183] B. Hardy, O. Simonin, J. De Wilde, and G. Winckelmans, ‘Simulation of the flow past random arrays of spherical particles: Microstructure-based tensor quantities as a tool to predict fluid–particle forces’, *International Journal of Multiphase Flow*, vol. 149, p. 103970, 2022, doi: 10.1016/j.ijmultiphaseflow.2021.103970.
- [184] Y. Y. Tang, E. (Frank) Peters, J. A. M. (Hans) Kuipers, S. H. L. (Sebastian) Kriebitzsch, and M. A. (Martin) van der Hoef, ‘A new drag correlation from fully resolved simulations of flow past monodisperse static arrays of spheres’, *AIChE journal*, vol. 61, no. 2, pp. 688–698, 2015, doi: 10.1002/aic.14645.
- [185] D. J. Robbins, M. S. El-Bachir, L. F. Gladden, R. S. Cant, and E. von Harbou, ‘CFD modeling of single-phase flow in a packed bed with MRI validation’, *AIChE journal*, vol. 58, no. 12, pp. 3904–3915, 2012, doi: 10.1002/aic.13767.
- [186] A. Jess, R. Popp, and K. Hedden, ‘Fischer–Tropsch-synthesis with nitrogen-rich syngas: fundamentals and reactor design aspects’, *Applied Catalysis A: General*, vol. 186, no. 1–2, pp. 321–342, 1999.
- [187] S. Markthaler, T. Plankenbühler, T. Weidlich, M. Neubert, and J. Karl, ‘Numerical simulation of trickle bed reactors for biological methanation’, *Chemical Engineering Science*, p. 115847, 2020.
- [188] S. Whitaker, *The method of volume averaging*, vol. 13. Springer Science & Business Media, 2013.
- [189] M. Fourati, V. Roig, and L. Raynal, ‘Liquid dispersion in packed columns: experiments and numerical modeling’, *Chemical Engineering Science*, vol. 100, pp. 266–278, 2013.
- [190] L. de Paulo Ferreira, T. D. S. de Oliveira, R. Surmas, M. A. P. da Silva, and R. P. Peçanha, ‘Brinkman equation in reactive flow: Contribution of each term in

- carbonate acidification simulations’, *Advances in Water Resources*, vol. 144, p. 103696, 2020.
- [191] D. B. Bukur, M. Mandić, B. Todić, and N. Nikačević, ‘Pore diffusion effects on catalyst effectiveness and selectivity of cobalt based Fischer-Tropsch catalyst’, *Catalysis Today*, vol. 343, pp. 146–155, 2020.
- [192] M. F. I. Bin Abdul Rashid, ‘Optimization study of Fischer-Tropsch gas-to-liquid (GTL) process using Aspen HYSYS’, Bachelor Thesis, Universitat Politècnica de Catalunya, 2019.
- [193] M. Hillestad, ‘Modeling the Fischer–Tropsch Product Distribution and Model Implementation’, *Chemical Product and Process Modeling*, vol. 10, no. 3, pp. 147–159, Sep. 2015, doi: 10.1515/cppm-2014-0031.
- [194] G. P. van der Laan, ‘Kinetics, selectivity and scale up of the Fischer-Tropsch synthesis’, Doctoral dissertation, University of Groningen, 1999.
- [195] A. O. Odunsi, ‘Temperature control in a multi-tubular fixed bed Fischer-Tropsch reactor using encapsulated phase change materials’, PhD Thesis, Heriot-Watt University, 2017.
- [196] R. A. Sehr, ‘The thermal conductivity of catalyst particles’, *Chemical Engineering Science*, vol. 9, no. 2–3, pp. 145–152, Nov. 1958, doi: 10.1016/0009-2509(58)80006-8.
- [197] M. Soomro and R. Hughes, ‘The thermal conductivity of porous catalyst pellets’, *The Canadian Journal of Chemical Engineering*, vol. 57, no. 1, pp. 24–28, 1979.
- [198] ‘Barlow’s Formula | American Piping Products’. Accessed: Mar. 14, 2025. [Online]. Available: <https://amerpipe.com/reference/charts-calculators/barlows-formula/>
- [199] I. B. Celik, U. Ghia, P. J. Roache, and C. J. Freitas, ‘Procedure for estimation and reporting of uncertainty due to discretization in CFD applications’, *Journal of fluids Engineering-Transactions of the ASME*, vol. 130, no. 7, 2008, doi: 10.1115/1.2960953.
- [200] X. Zhu, X. Lu, X. Liu, D. Hildebrandt, and D. Glasser, ‘Heat transfer study with and without Fischer-Tropsch reaction in a fixed bed reactor with TiO₂, SiO₂, and SiC supported cobalt catalysts’, *Chemical Engineering Journal*, vol. 247, pp. 75–84, Jul. 2014, doi: 10.1016/j.cej.2014.02.089.
- [201] P. J. Roache, ‘Perspective: A Method for Uniform Reporting of Grid Refinement Studies’, *Journal of Fluids Engineering*, vol. 116, no. 3, pp. 405–413, Sep. 1994, doi: 10.1115/1.2910291.
- [202] ‘Chapter_4_Design_Fundamentals.pdf’. Accessed: Mar. 19, 2025. [Online]. Available: https://cheguide.com/doc/Chapter_4_Design_Fundamentals.pdf
- [203] SONATRACH, Exploration & Production Activity, Production Division, Hassi R'mel Regional Division, Oued Noumer Division, 2024.

APPENDICES

Appendix A: Deriving the circle diameter of the hypothetical 2D geometry

The hypothetical 2D unit cell porosity can be defined according to Equation (A.1)

$$\varepsilon_{2D} = \frac{\frac{3}{2}S_C}{S_{2D-UC}} \quad (A.1)$$

Where S_C and S_{2D-UC} are the surface areas of one circle and the hypothetical 2D unit cell (2D-UC) in the conceptual geometry, which may be given by:

$$S_C = \frac{\pi}{4}d_c^2 \quad (A.2)$$

$$S_{2D-UC} = 2dph^* \quad (A.3)$$

Where d_c is the diameter of a hypothetical circular particle.

Let the 3D unit cell porosity be given by

$$\varepsilon_{3D} = \frac{\frac{3}{2}V_p}{V_{3D-UC}} \quad (A.4)$$

Where V_p and V_{3D-UC} are the particle and the unit cell volumes (in the real bed), which may be given by:

$$V_p = \frac{\pi}{6}dp^3 \quad (A.5)$$

$$V_{3D-UC} = \pi dp^2h^* \quad (A.6)$$

Assuming that ε_{2D} and ε_{3D} are equals, the circle diameter can be derived according to Equation (A.7)

$$d_c = 2\sqrt{\frac{1}{3\pi}}dp \quad (A.7)$$

Appendix B: The GCI methodology

To ensure that the results are independent of mesh size, the numerical errors of the simulations were analyzed using the procedure provided by [199]. Let us first define the representative grid size h , for three-dimensional space, by

$$h = \left[\frac{1}{N} \sum_{k=1}^N (\Delta V_k) \right]^{1/3} \quad (B.1)$$

where ΔV_k is the volume of the k^{th} cell and N is the total number of cells used for computations. Three grid sizes were selected such that, the grid refinement factors, defined by Equation (B.2) and (B.3), should be greater than 3.

$$r_{21} = \frac{h_2}{h_1} \quad (\text{B.2})$$

And

$$r_{32} = \frac{h_3}{h_2} \quad (\text{B.3})$$

Then, the expression that defines the apparent order of the method is as follows:

$$p = \frac{1}{\ln r_{21}} \left| \ln \left| \frac{\theta_{32}}{\theta_{21}} \right| + q(p) \right| \quad (\text{B.4a})$$

$$q(p) = \ln \left(\frac{r_{21}^p - s}{r_{32}^p - s} \right) \quad (\text{B.4b})$$

$$s = 1. \operatorname{sgn} \left(\frac{\theta_{32}}{\theta_{21}} \right) \quad (\text{B.4c})$$

In these, $\theta_{32} = (\Delta P)_3 - (\Delta P)_2$ and $\theta_{21} = (\Delta P)_2 - (\Delta P)_1$ with $(\Delta P)_1$, $(\Delta P)_2$ and $(\Delta P)_3$ are the simulated pressure drop results using the three grid sizes h_1 , h_2 and h_3 , respectively.

Finally, the asymptotic pressure drop and its associated Grid Convergence Index on the finer grid (GCI_{21}), may be calculated as follows:

$$(\Delta P)_{\text{Asymp}} = \frac{r_{21}^p (\Delta P)_1 - (\Delta P)_2}{(r_{21}^p - 1)} \quad (\text{B.5})$$

$$GCI_{21} = \frac{1.25 \epsilon_{21}}{r_{21}^p - 1} \quad (\text{B.6})$$

Appendix C: Design of the FTBPR (Computing the tubes number)

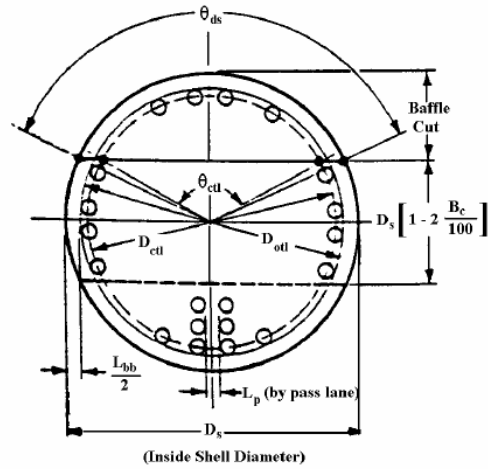


Figure C.1: Required Parameters to design a multitubular packed bed reactor [202].

The total number of tubes can be calculated using Equation (C.1) [202]

$$N_t = \frac{0.78 \cdot D_{ct}^2}{CL \cdot (P_T)^2} \tag{C.1}$$

Where D_{ct} is the diameter of the circle through the centers of the tube located within the outermost tubes, P_T is tube layout pitch, given by Equation (A.2), and CL is the tube layout constant having the value of 0.87 for 60° layouts.

$$P_T = 1.5 \cdot D_e \tag{C.2}$$

Where D_e is the external tube diameter.

Appendix D: Aspen HYSYS program: Simplified syngas production unit, using natural gas as feedstock

The syngas production unit is composed of:

- Pre-reforming unit (CONVERSION REACTOR 1 and EQUILIBRIUM REACTOR 1): To transform C2, C3, iC4, nC4, iC5 and nC5 into (Methane) C1
- Reforming unit (CONVERSION REACTOR 2 and EQUILIBRIUM REACTOR 2): To transform C1 into syngas (H₂ and CO)
- It includes also heaters, two-phase separator and compressor



Figure D.1: Program on Aspen HYSYS V12

The composition of Natural Gas (NG) feedstock, introduced in Aspen HYSYS V12 program, is presented in Table (D.1)

Table D.1: Composition of the natural gas feed to the syngas production unit (Source SONATRACH, 2024 [203])

Component	Molar fraction (%)
N ₂	3.69
CO ₂	0.22
C1	84.89
C2	9.47
C3	1.44
IC4	0.12
NC4	0.15
IC5	0.01
NC5	0.01

Appendix E: List of Publications

- M. Lakkaichi, N. Outili, and A. H. Meniai, 'Pressure Drop Analysis of Incompressible Laminar Flow in a Low Aspect-Ratio Packed Bed Using CFD Simulations.', *International Journal of Multiphysics*, vol. 18, no. 2, 2024.
- M. Lakkaichi, N. OUTILI & S. Nacef 'A mechanistic hydrodynamic model for pressure drop prediction in trickle-bed reactors' *Algerian Journal of Engineering Research*, vol. 1, no. 2, 2017

Conferences:

- **'Hydrodynamic modeling and simulation of trickle-bed reactor'** Les 4^{èmes} Journée du Jeune Chercheur, 15-16/05/ 2017, Faculté du génie des procédés, Université Salah boubnider Constantine 3.
- **'Design of small-scale Fischer-Tropsch Multitubular Packed Bed Reactor to transform biomass into synthetic liquid fuels'** ICGS2025, 14-15 May 2025, Meridian Hotel, Oran, Algeria.
- **'Mathematical Modelling and Numerical Simulation of Fischer-Tropsch Multitubular Packed Bed reactor using COMSOL Multiphysics'** JST 12 of SONATRACH, 24-26 June 2025, Oran, Algeria.

Published article

Pressure drop analysis of incompressible laminar flow in a low aspect-ratio packed bed using CFD simulations

Maher Lakkaichi*, Nawel Outili and Abdeslam Meniai

University of Constantine 3, Algeria

*Corresponding author maher.lakkaichi@univ-constantine3.dz

Abstract

Computational Fluid Dynamics (CFD) is a worthwhile method for studying complex flows in packed bed reactors. The paper debates different CFD modeling approaches of incompressible laminar flow through packed beds with a particle to column diameter ratio of 2. Using COMSOL Multiphysics 5.6, Five different cases have been simulated and compared in term of pressure drop. Excellent agreement was found between the proposed hypothetical and the resolved-particle (3D) models, mainly for the lower Inlet particle Reynolds numbers, with relative deviation of 3% and 7% at inlet Reynolds numbers of 27 and 55, respectively. Concerning the pseudo homogeneous cases, three different drag laws have been exercised and it has been found that applying the semi-empirical correlation, which takes into account the wall effects, in the flow equations showed the best agreement to the 3D model, with relative deviation being in the range 5%-25%. Considering these, one can recommend to use the proposed less computationally intensive approach or to apply the chosen drag law model in the momentum balance when designing a packed bed with aspect ratio of 2.

1. INTRODUCTION

Numerous industrial processes use packed bed reactors (PBRs) with low aspect ratio (AR), due to its straightforward configuration, low pressure drop, large interstitial velocities and high surface-to-volume ratios inducing enhanced heat and mass transfer phenomenon [1–3]. These low AR packed beds have been shown to be effective for various applications such as steam reforming, oxidative dehydrogenation, nuclear reactors, separators and compact heat exchangers [1,2,4,5]. Despite these important applications, the number of studies to understand the hydrodynamics in low AR packed bed systems is unfortunately very low, particularly for AR less than 3 [1,3]. Only few publications considering the hydrodynamics of these types of reactors are reported in the literature.

One of the most crucial elements that must be precisely predicted when designing a packed bed, crossed by a fluid, is pressure drop, since it affects the flow distribution, pumping power and operating expenditures [6,7]. Additionally, the reliability of the applied pressure drop correlation determines the validity of pseudo-homogeneous models for complex flow in packed beds and the accurate prediction of the average behavior of the entire bed [8,9].

With recent increases in computational power, computational fluid dynamics (CFD) has become a viable method to analyze the complex flows in packed beds. Such CFD analyses require Three-Dimensional (3D) models when incorporating the bed structure's complexities (Resolved-Particle) for assessing the local flow field [10,11]. In addition to the 3D Resolved-Particle models, 2D representative models are used in order to reduce the computational cost. Although local hydrodynamic phenomena required by 3D Resolved-Particle models could not be properly seized by 2D models [12], global macroscopic parameters (such as pressure drop) may be predicted accurately by 2D models [10].

Actually, 2D simulations use the classical porous media approach where the packed bed is represented by a continuous and homogeneous porous medium [13–15]. The resistance

source terms are applied as closure drag law models in the averaged Navier-Stokes equations [16]. The obtained sets of partial differential equations were solved for the macroscopic flow field in the PBR (i.e. 2D pseudo homogeneous models). The effect of the solid phase is incorporated in the model equations implicitly via the bed porosity and the implemented drag force sub-models. These closure relationships can influence considerably the computed values of pressure drop especially for PBRs with low aspect ratio.

In the present study, a 2D porosity distribution function was considered and three drag force-sub models were tested and implemented in the modified Navier-Stokes equations to account for the momentum transfer at the fluid-solid interfaces leading to three axisymmetric pseudohomogeneous models. The drawback of this conventional modeling approach was its dependency on closure sub-models which were developed on the basis of parametric fitting which involves finding coefficients (parameters) using a data set covering a limited range of operating conditions. Also a new method was proposed and based on transforming the complex 3D structure into a conceptual 3D structure which preserved some geometrical information and could be properly and easily simplified and transformed into a representative 2D structure by cross section geometry operation as will be described, hereinafter. The main advantage of this new approach is that it did not rely on any closure sub-models.

The main objectives of the present paper are to (1) assess different drag laws using a 2D CFD pseudo homogeneous model and (2) study the efficiency of the new modeling approach, using a conceptual geometry, versus 3D modeling of laminar liquid flow in a packed bed with an aspect ratio of 2.

The remainder of the paper is organized as follows: (1) Writing the mathematical model equations and carrying out the simulations on COMSOL Multiphysics 5.6; (2) Conduct a

mesh independence study of the 3D simulations, following the procedure established by [17], to determine the asymptotic pressure drop values and (3) Investigate the effectiveness of 2D against 3D simulations by comparison of the simulated results, in term of pressure drop, for different inlet particle Reynolds numbers.

2. Materials and Methods

2.1. Geometries and meshing

Creating geometry and meshing process are prior steps in performing a reliable CFD simulation [18]. One of the promising CFD software is COMSOL Multiphysics which has the capability of creating and dividing geometries into elements that can be used for the discretization of a computing domain.

2.1.1. Geometries

Three different geometries were created according to the space dimension (2D or 3D) and the type of the CFD model (Pseudo-homogeneous or Resolved-Particle). The created geometries are (1) a 3D real geometry of the packed bed, (2) a 2D geometry representing implicitly the bed domain and (3) a 2D geometry representing explicitly the bed domain.

2.1.1.1. Real 3D Geometry: Cylindrical column packed with spherical particles

Identical-sized spheres are used and put one at a time into a cylindrical column with a diameter twice as large as the particle diameter (d_p), so that one layer can accommodate only two tangent spheres. Then the first two spheres stand on the column base tangentially to its wall and their centerline passes through the center of the circular base of the column and is in a plane perpendicular to the column vertical axis. The next two spheres are

arranged so that their centerline makes an angle of 90° with that of the two spheres of the previous layer [19]. This geometric arrangement is repeated for the subsequent layers up to the top of the bed [10] and can be represented by a number of repeating unit cells having the same overall properties, particularly an overall void fraction equal to that of the entire bed [19]. The height of a unit cell, denoted by h^* , is related to the particle diameter, as follows:

$$h^* = \frac{dp}{\sqrt{2}} \quad (1)$$

The used total number of layers is 21 with a bed height to particle diameter ratio of about 15.14, which is sufficient to avoid column top and bottom effects on the porosity, although a desirable ratio should be greater than 20 [20,21].

To eliminate the entrance and the exit effects, the volume meshes was extended one cylinder diameter in the axial direction at the inlet and outlet [20] as shown in Figure 1a. The obtained results presented below confirm the fact that considering 21 layers and extending the total reactor length one cylinder diameter at the inlet and outlet, is sufficient for bulk unit cell pressure drop to reach a fully developed state. The spheres diameter was set to be equal 0.019 mm, but it was reduced by 1% to avoid unsuitable thin cells near the contact points between particles as well as between particles and the cylinder wall, which may induce solution convergence problems. Exploiting the symmetry of the system, simulations were run over one quarter of the geometrical domain to reduce the computational time.

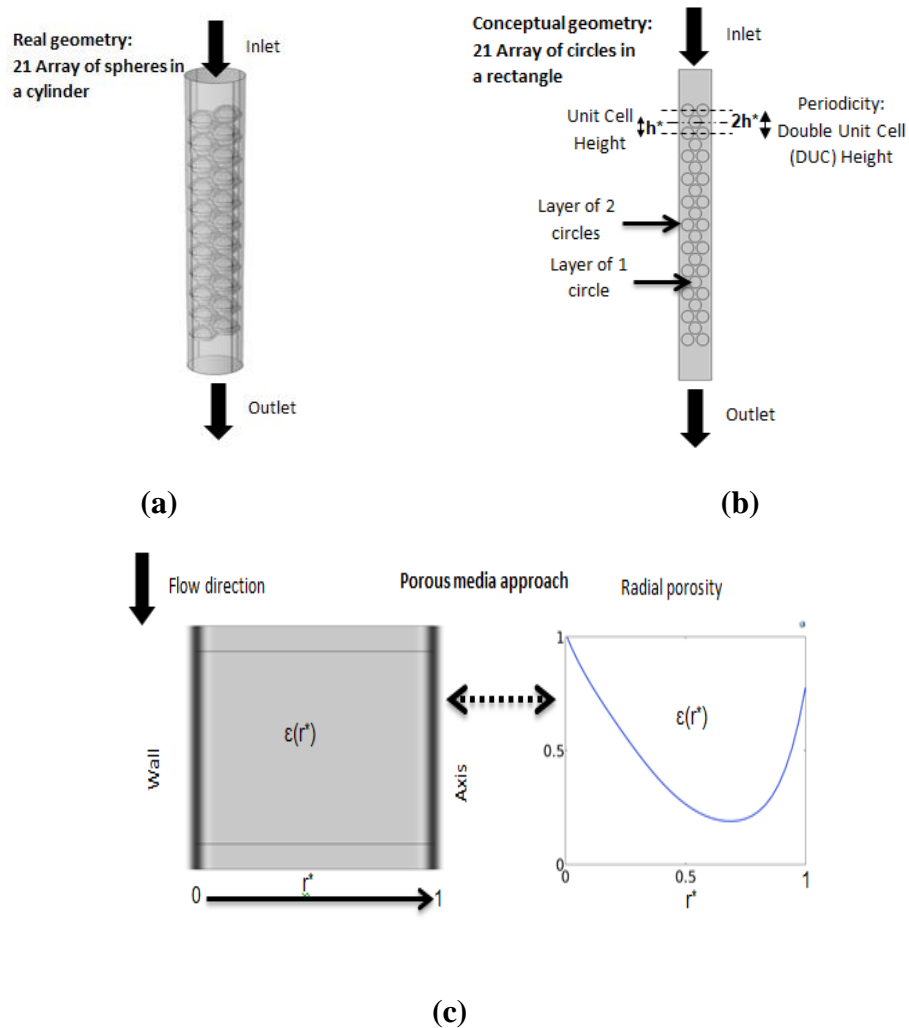


Figure 27: Geometries used in different modelling approaches: (a) Real geometry: Three-Dimensional Resolved-Particle Model (3D-RPM); (b) Conceptual geometry: Two-dimensional Resolved-Particle Model (2D-RPM); (c) Two-Dimensional axisymmetric: Pseudo-homogeneous Model (2D-PHM).

2.1.1.2. 2D Axisymmetric rectangle: Flow in an empty tube

Concerning the 2D pseudo homogeneous cases, there is no need to include any details of the bed structure, since the domain is considered continuous and homogeneous. In this case, the liquid is assumed to be flowing in an empty tube. Therefore, the geometry of the domain is rectangular as shown in Figure 1c. Based on the porous media approach, the

effect of the bed textual properties on the flow is integrated into the transport equations via a porosity distribution function and drag force closure relationships.

2.1.1.3. 2D Rectangle containing a group of circles: Fictitious flow past an array of circular cylinders

Regarding the conceptual model, an imaginary 3D geometry was proposed, which is able to capture to some extent the explicit description of the textual characteristics of the real bed geometry and which can be easily simplified and transformed into a 2D geometry by using cross section geometry operation available in COMSOL Multiphysics 5.6 software. The proposed conceptual 3D geometry is a group of circular cylinders (hypothetical particles) positioned horizontally between two vertical and parallel plates, as if the cylindrical column (real bed) is bisected into two stretched halves. This similarity can be put forward for two considerations. Firstly, the circular shape of the hypothetical particles, in the conceptual geometry, may capture the circular curvature of the spherical particle in the real bed. Secondly, the vertical plates containing the cylindrical particles (in the conceptual geometry) could be consistent with the real column surrounding the spherical particles (in the real geometry). The height of the plates is the same as that of the cylindrical column and the distance between the two plates is equivalent to the bed diameter. The number, the position and the diameter of the circular cylinders determine the tortuous pattern and the void fraction in the new 3D geometry.

By using the cross section geometry operation on the conceptual 3D domain, a fictitious 2D geometry was created. This latter is represented by a rectangle containing 32 mono-sized circles, as shown in Figure 1b, which are located as follows:

- The i -th Layer containing two circles ($i=1:11$):

$$x_{2i-1} = -x_{2i-1} = \frac{dp}{3} \text{ and } y_{2i-1} = \frac{5dp}{2} + (2i - 2)h^* \quad (2)$$

- The j -th Layer containing one circle ($j=1:10$):

$$x_{2j} = 0 \text{ and } y_{2j} = \frac{5dp}{2} + (2j - 1)h^* \quad (3)$$

Where x and y are the coordinates of the circles center.

The hypothetical circle diameter is determined assuming that the hypothetical 2D unit cell porosity is equivalent to the real 3D unit cell porosity, as described in Appendix A. These mean that the circles locations and the overall void fraction are the main geometrical information required by the conceptual 2D geometry.

2.1.2. Meshing

Regarding the 3D modeling and due to the complex 3D geometry, the generated mesh consisted of free tetrahedral. Furthermore, to solve viscous effects, the meshing is refined in a boundary layer at the fluid-particles and fluid-walls interfaces, which include two boundary layers to enhance the cells quality, without an excessive cell count [22–24].

Finally, a corner refinement procedure was also implemented to further refine the mesh and get a better resolution of the corners and edges in narrow regions.

Similarly, in order to attain a high level accuracy of 2D simulations, the same meshing sequences were built, but free triangular shapes cells were used in the two dimensional domains.

In each of these studies, the mesh density was determined in a mesh independence study.

2.2. CFD modeling

2.2.1. Three and two-dimensional resolved particle models (3D-RPM and 2D-RPM)

The hydrodynamic model for both resolved-particle cases is described by Equations (4) and (5), which represent the continuity and the momentum balance equations, respectively.

$$\rho \nabla \cdot \mathbf{u} = 0 \quad (4)$$

$$\rho(\mathbf{u} \cdot \nabla)\mathbf{u} = \nabla \cdot [-p\mathbf{I} + \mu(\nabla\mathbf{u} + (\nabla\mathbf{u})^T)] + \rho\mathbf{g} \quad (5)$$

Where ρ , μ and \mathbf{g} are the fluid density, dynamic viscosity and gravity acceleration, respectively, \mathbf{u} and p are the local velocity and pressure at any given position in the interstitial porous bed and in the extended inlet and outlet free volumes. Equation (5) is the standard Navier-Stokes equation for incompressible flow. Equations (4) and (5) were solved in the interstitial domain of the bed and the extended free domains, similarly to the model implementation carried out by Uribe and coworkers [24,25]. An important aspect to highlight on the implemented model is that there is no need to include any expressions for porosity distribution and fluid-solid drag [12,24,26,27], which is a common practice when implementing pseudo homogeneous models, since the implemented model explicitly includes these parameters via the solids distribution and the solid walls boundary conditions. Hence, the solid phase distribution is required by implemented geometries representation as described in Figures 1a and 1b, while the average fluid-solid interactions are assumed at the fluid-solid contact surface through setting the boundary conditions. The boundary conditions set to the model were an inlet velocity (u_{in}), outlet pressure (p_{out}) and a non-slip condition at the column walls and at the fluid-solid interface (A_{fw}). Equations (6) to (8) describe the boundary conditions for equations (4) and (5).

$$\mathbf{u}_{in} = -U_{in}\mathbf{n} \quad (\text{inlet}) \quad (6)$$

$$[-p\mathbf{I} + \mu(\nabla\mathbf{u} + (\nabla\mathbf{u})^T)]\mathbf{n} = -p_{out}\mathbf{n} \quad (\text{outlet}) \quad (7)$$

$$\mathbf{u} = 0 \quad (\text{walls and } A_{fw}) \quad (8)$$

where U_{in} is the superficial inlet velocity. The boundary condition described by Equation (7) specifies that the normal stress at the reactor outlet is equal to the outlet pressure, which was set to be 1 atm. It can be seen from Equation (8) that the solids are considered as impermeable, and therefore a no-slip boundary condition is set at their surface.

In both resolved particle cases (I and II), which are illustrated in Table 1, the governing equations are the same, with the same physical properties, inlet, outlet and operating conditions. Thus, the possible differences in the macroscopic average behaviors, such as pressure drop, may result from differences between the real and the conceptual geometries.

Table 12: Simulated cases

Case N°	Model type	Features
I	Resolved-particle (Real geometry): 3D-RPM	Three-Dimensional No closure sub-models
II	Resolved-Particle (Conceptual geometry): 2D-RPM	Two-Dimensional No closure sub-models
III	Pseudo-homogeneous: 2D-PHM_Ergun	Two-Dimensional Semi-empirical drag law by (Ergun, 1952) Porosity distribution function by (Mueller, 2010)
IV	Pseudo-homogeneous: 2D-PHM_Tang	Two-Dimensional First principle-based drag law by (Tang et al., 2015) Porosity distribution function by (Mueller, 2010)
V	Pseudo-homogeneous: 2D-PHM_ES	Two-Dimensional Semi-empirical drag law by (Eisfeld and Schnitzlein, 2001) Taking into account the wall effects Porosity distribution function by (Mueller, 2010)

2.2.2. Pseudo homogeneous models (PHMs)

The hydrodynamic model for both pseudo homogeneous cases is described by Equations (9) and (10), which represent the continuity and the momentum balance equations, respectively.

$$\rho \nabla \cdot \mathbf{U} = 0 \quad (9)$$

$$\frac{1}{\varepsilon} \rho (\mathbf{U} \cdot \nabla) \mathbf{U} \frac{1}{\varepsilon} = \nabla \cdot \left[-P \mathbf{I} + \mu \frac{1}{\varepsilon} (\nabla \mathbf{U} + (\nabla \mathbf{U})^T) \right] + \left(\frac{\mu}{k_1} + \frac{\rho}{k_2} |\mathbf{U}| \right) \mathbf{U} + \rho \mathbf{g} \quad (10)$$

In these, \mathbf{U} is the superficial average velocity, which is a hypothetical velocity of the flowing fluid in a free channel and P is an intrinsic average pressure. Actually, Equation (10) is the Navier-Stokes-Darcy-Forchheimer equation which is the modification of the original Navier-Stokes equation (Equation (5)) [12,28]. This modified transport equation includes additional terms, capturing the porous media information, which are the porosity (ε), the Darcian (k_1) and the non-Darcian (k_2) permeabilities.

Regarding the bed porosity, the analytical expression by [19] and the semi-analytical expression by [29] for the radial porosity distribution in packed bed with aspect ratio of 2 are benchmarks with existing experimental data for mono-sized spheres. The void fraction in the bed with aspect ratio equal to 2 begins at unity at the wall, decreases to a minimum of 0.19 at a distance of around $0.68d_p$ from the wall, and then increases to reach unity at the bed's axis (see Figure 1c). In fact, this geometrical parameter is an average property, so that the expressions that forecast radial variations are actually forecasting the average profile of an average property. This suggests that the predicted profiles might not actually have any physical significance, but they do allow for some partial capture of the influence of the bed structure on the averaged macroscopic parameter profiles [12].

The second important variable is permeability, which measures the capacity and the ability of a porous medium to transmit a fluid [30]. In another way, it measures the resistance to

flow caused by the porous medium structure [12]. Actually, there exist two permeabilities as appearing in the right-hand side of Equation (10) which were well described as follows [18,31]:

$$k_1 = \frac{\varepsilon^3}{\alpha S_V^2 (1-\varepsilon)^2} \quad (11)$$

$$k_2 = \frac{\varepsilon^3}{\beta S_V (1-\varepsilon)} \quad (12)$$

In these, $S_V = 6/d_p$ is the solid particles specific area, where α and β are the viscous and inertial parameters, respectively, defined by Equations (14) and (15).

Actually, the second term in the right side of Equation (10) may represent the pressure drop per unit length of the PBR and is a function of: (1) the flow rate, (2) the fluid viscosity and density (3) closeness and orientation of the packing and (4) size, shape and surface roughness of the particles. Hence, this term is very sensitive to the geometrical properties of the bed [20]. A number of methods exist to describe and predict the pressure drop over PBRs such as empirical relationships, capillary models, statistical models and hydraulic radius principles [30]. The most common method uses hydraulic radius concept to calculate the resistance to flow inside the bed. In this context, the well know drag force correlation by [32], states that the pressure drop per unit length of porous medium is the sum of viscous and inertial terms, which can be written as:

$$\frac{\Delta p}{L} = A_{Ergun} \frac{(1-\varepsilon)^2}{\varepsilon^3} \frac{\mu U_s}{d_p^2} + B_{Ergun} \frac{(1-\varepsilon)}{\varepsilon^3} \frac{\rho U_s^2}{d_p} \quad (13)$$

In Equation (13), A_{Ergun} and B_{Ergun} are the viscous and inertial Ergun constants, which are related to the viscous and inertial parameters in expressions (11) and (12), through the following equalities [18]:

$$A_{Ergun} = \alpha 36 = (2\alpha^*) 36 = 150 \quad (14)$$

$$B_{Ergun} = \beta 6 = (\beta^*/8) 6 = 1.75 \quad (15)$$

In these, α^* and β^* are parameters which include the tortuosity factor and which could be determined theoretically or experimentally [18].

In recent years, advances of Particle Resolved-Direct Numerical Simulations (PR-DNS) have led to new correlations based on first principles [33]. Through PR-DNS the fluid-solid momentum transfer is modeled depending on the boundary conditions at the particles surface rather than on empirical hypotheses. What distinguishes PR-DNS is that, unlike experiments, arbitrary material and flow characteristics may be established and fully controlled in simulations.[33–36]. Based on the Immersed Boundary condition Method (IBM), Tang (2015) developed an accurate drag law which is considered as the best possible expression of the drag force in static mono disperse arrays of spheres for $Rep \leq 1000$ [36].

The disadvantage of both the semi empirical correlation by [32] and the first principle-based correlation by [36] is that they do not take the wall effects into account and present inaccurate predictions at aspect ratios lesser than 10 [4,7]. It is noteworthy to mention that for low particle to column diameter ratios the column wall may affect the flow within the packed bed considerably through two opposite effects, notably a local increase in porosity near the wall and additional resistance due to the wall friction [4,7,8]. Therefore, many authors have attempted to improve these correlations to include the wall effect, by fitting semi-empirical correlations to their experimental data. One of the most promising correlations is the Einfeld and Schnitzlein (ES) correlation which is an Ergun-type equation and which was derived from more than 2300 experimental data points [8]. This correlation is relevant to the current investigation since it takes the wall effect into consideration, and predicts accurate values of the friction factor at low aspect ratios [20].

COMSOL Multiphysics uses the Forchheimer equation, to account for the momentum transfer term in Equation (10), which is written as follows [18,28]:

$$\frac{\Delta p}{L} = \frac{\mu}{k_1} U + \frac{c_F \rho}{\sqrt{k_1}} U^2 \quad (16)$$

Where c_F is the Forchheimer coefficient that account for inertia drag.

The first and the second terms in the right side in Equation (16) represent the viscous and the kinetic energy losses, respectively. Confronting this Equation with the momentum transfer term in equation (10), leads to the following equalities:

$$k_2 = \sqrt{k_1}/c_f \quad (17)$$

User defined function, in COMSOL Multiphysics, is used to define the Darcian permeability, k_1 , and the Forchheimer coefficient, c_F of the three drag laws exercised in the 2D CFD pseudo homogeneous model (Equations 9 and 10), which are summarized in Table 2.

Table 13: Drag force sub-models

Drag law	Darcian permeability (k_1)	Forchheimer coefficient (c_f)	Constants
Ergun (1952)	$\frac{\varepsilon^3 d_p^2}{A_{Ergun}(1-\varepsilon)^2}$	$\frac{B_{Ergun}(1-\varepsilon)}{\varepsilon^3 d_p} \sqrt{k_1}$	$A_{Ergun} = 150$ $B_{Ergun} = 1.75$
Eisfeld and Schnitzlein (2001)	$\frac{\varepsilon^3 d_p^2}{eE^2(1-\varepsilon)^2}$	$\frac{E(1-\varepsilon)}{\dot{E} \varepsilon^3 d_p} \sqrt{k_1}$	$e = 154, \acute{e} = 1.15, e'' = 0.87$ $E = 1 + \frac{2}{3\gamma(1-\varepsilon)},$ $\acute{E} = (\acute{e}\gamma^{-2} + e'')^2$
Tang et al. 2015	$1/A_{Tang}^{(1)}$	$B_{Tang}^{(2)}$	-

$$^{(1)}A_{Tang} = 180 \frac{(1-\varepsilon)^2}{\varepsilon^3 d_p^2} + 18(1-\varepsilon) \frac{\varepsilon}{d_p^2} (1 + 1.5\sqrt{1-\varepsilon})$$

$$^{(2)}B_{Tang} = 18(1-\varepsilon)(0.11(2-\varepsilon)(1-\varepsilon) - \frac{0.00456}{\varepsilon^4} + \left(0.169\varepsilon + \frac{0.0644}{\varepsilon^4}\right) Re_p^{-0.343}) \left(\frac{1}{\varepsilon d_p}\right)$$

2.3. Numerical setup

Simulations were conducted using the steady-state incompressible solver for the laminar flow available in COMSOL Multiphysics 5.6. All models were tested at low particle Reynolds numbers (Re_p), ranging from $Re_p = 27$ to $Re_p = 111$, which correspond to laminar steady flow conditions [10]. The convergence was evaluated based on relative tolerance of 0.001. A consistent mesh independence study was performed for the 3D simulations (Case I) to ensure the accuracy of the results and to determine the asymptotic pressure drop values. Besides, 2D simulations were conducted on extremely-finer meshes, where the grid is refined in stages until no significant differences in results occur between successive grid refinement stages.

3. Results and discussion

3.1. Estimation of discretization errors of the 3D simulations

In the following, the discretization error estimates in the 3D simulations, in term of pressure drop, are calculated and reported. It is a way of validation when experimental data are scarce or not available for comparison [17]. Assessing the accuracy of code and calculations requires that the grid is sufficiently refined to the extent that the solution is within the asymptotic range of convergence. This can be checked by observing two grid convergence index (GCI) values as computed over three grids as described in Appendix B. The GCI is a measure of the percentage the computed value is away from the asymptotic value. A small value of GCI indicates that the solution is within the asymptotic range. This can be further verified by fulfilling the solution accuracy condition written as follows [37]:

$$\frac{GCI_{32}}{r_{21}^m GCI_{21}} = 1 \quad (18)$$

Then the reason to trust the accuracy of a numerical simulation is validated and the solution is independent of the mesh size.

Table 14: Mesh independence study: Error estimates in 3D simulations, in term of pressure drop, at different inlet Re_p values

Results	Rep_in=27	Rep_in=55	Rep_in=111
Asymptotic pressure drop value (Pa/m)	2.71	6.91	20.48
GCI_{21} (%)	0.23	0.84	4.44
$\frac{GCI_{32}}{r_{21}^m GCI_{21}}$ (Solution accuracy condition)	1.000	1.003	1.007

Table III displays results of asymptotic pressure drop, grid convergence index and a solution accuracy check for the tree inlet Re_p values. Here, the pressure drop values were calculated in the bulk region of the bed where the flow is fully developed, as it will be demonstrated in the following section.

Overall, the solution accuracy ratio is almost equal to one for all the inlet Re_p values, thus the solutions are within the asymptotic ranges of convergence. In term of grid convergence index, for all cases, GCI_{21} is lower than 4.5%, having the smallest value for $Re_{p_in}=27$.

The observed higher values of GCI_{21} for $Re_{p_in}=111$, comparing to the other cases, could be attributed to the grid size not being able to capture all the information of the flow field.

Using the asymptotic pressure drop values as well as their respective GCIs, the exact solutions of pressure drop through the packed bed may be written as:

$$\Delta P_{exact} = \Delta P_{asympt} \frac{(100 \pm GCI_{21})}{100} \quad (19)$$

3.2. Comparison of pressure drop simulated results

Predicted results of pressure drop by the 3D simulations (Case I) and the 2D simulations (Cases II-V) could be obtained by calculating the difference in the radially-averaged pressure between the inlet and outlet bed boundaries. However, to eliminate any entrance and exit effects on the results, pressure drop should be calculated between two stages in the bed within a region where the flow becomes fully developed.

The geometrical domains were divided into a number of cut planes (for the 3D domain) or cut lines (for the 2D domains) with distances between two successive planes or lines of $z_{i+1} - z_i = h^*/10$ or $y_{i+1} - y_i = h^*/10$, respectively. Next, the pressures were measured by computing the average pressure on each cross section, at a level z or y . The elementary

pressure drop results were then calculated by subtracting two sequential averaged pressure values.

Figures 2a, 2b and 2c show the change in frictional pressure drop, simulated by all cases, as a function of the normalized axial distance at inlet Re_p values of 27, 55 and 111, respectively. It can be seen that for the three inlet Re_p values tested, the observed behaviors of the five models are different.

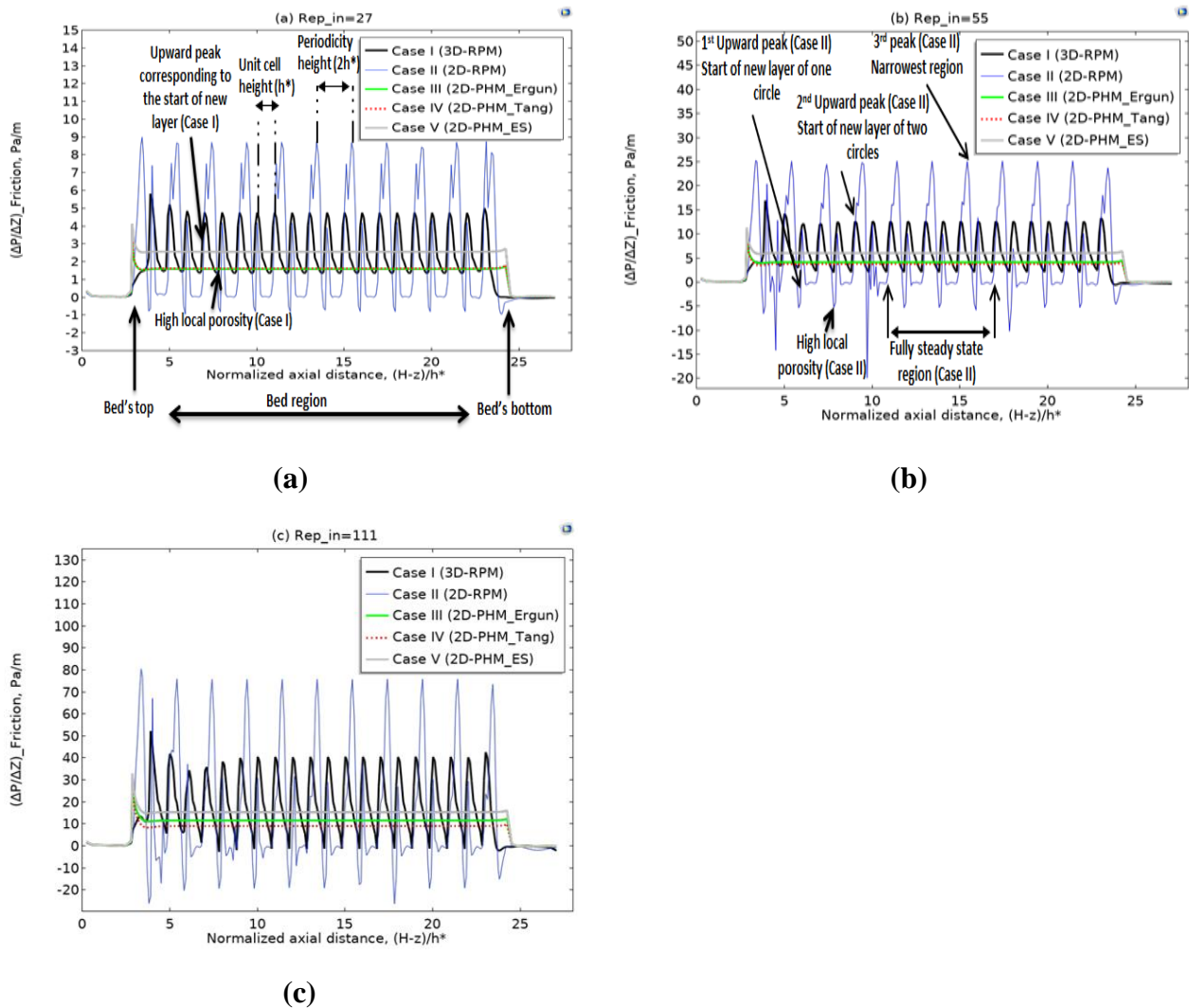


Figure 28: Comparison of frictional pressure drop simulated results as a function of normalized axial distance for all cases at different inlet Re_p values: (a) 27; (b) 55; (c) 111.

Concerning the pseudo homogeneous models, Cases (III, IV and V) show a smoother variation of the frictional pressure drop profile along the bed length. The observed peaks at the bed boundaries are due the transition between the free and the porous zones.

Differently, both of the resolved-particle cases exhibit important fluctuations inside the bed region. These fluctuations are of a greater extent for Case II, which are generated by substantial variations in the textual characteristics of the fictitious 2D geometry comparing to the real domain in Case I. Each upward peak of Case I coincides with the start of a new layer. Similarly, each first and second upward peak in Case II coincides with the start of new layers containing one and two circles, respectively. Additionally, while the peaks in Case I and the third peaks in Case II correspond to the narrowest regions within the bed, the low points in both cases coincide with high local porosity regions. Moreover, it can be seen clearly that while the black curves show a periodicity every regular interval of one unit cell height, the blue one exhibits it every regular interval of Double Unit Cell (DUC) height. Furthermore, the height of the repeating parts, of both curves, becomes stable toward the bulk region of the bed where the flow is becoming fully developed (see Figure 2b and Figure 3b), which means that the averaged pressure drops, for both cases, over a DUC height become constants within the bulk region of the bed, where any entrance and exit effects may be eliminated.

Figures 3a, 3b and 3c give information about the variation in frictional pressure drop every double unit cell height within the bed region, for all cases at inlet particle Reynolds number of 27, 55 and 111, respectively. As initial remark, simulated frictional pressure drop has to some extent similar trends for all the models and for all the three inlet Rep values.

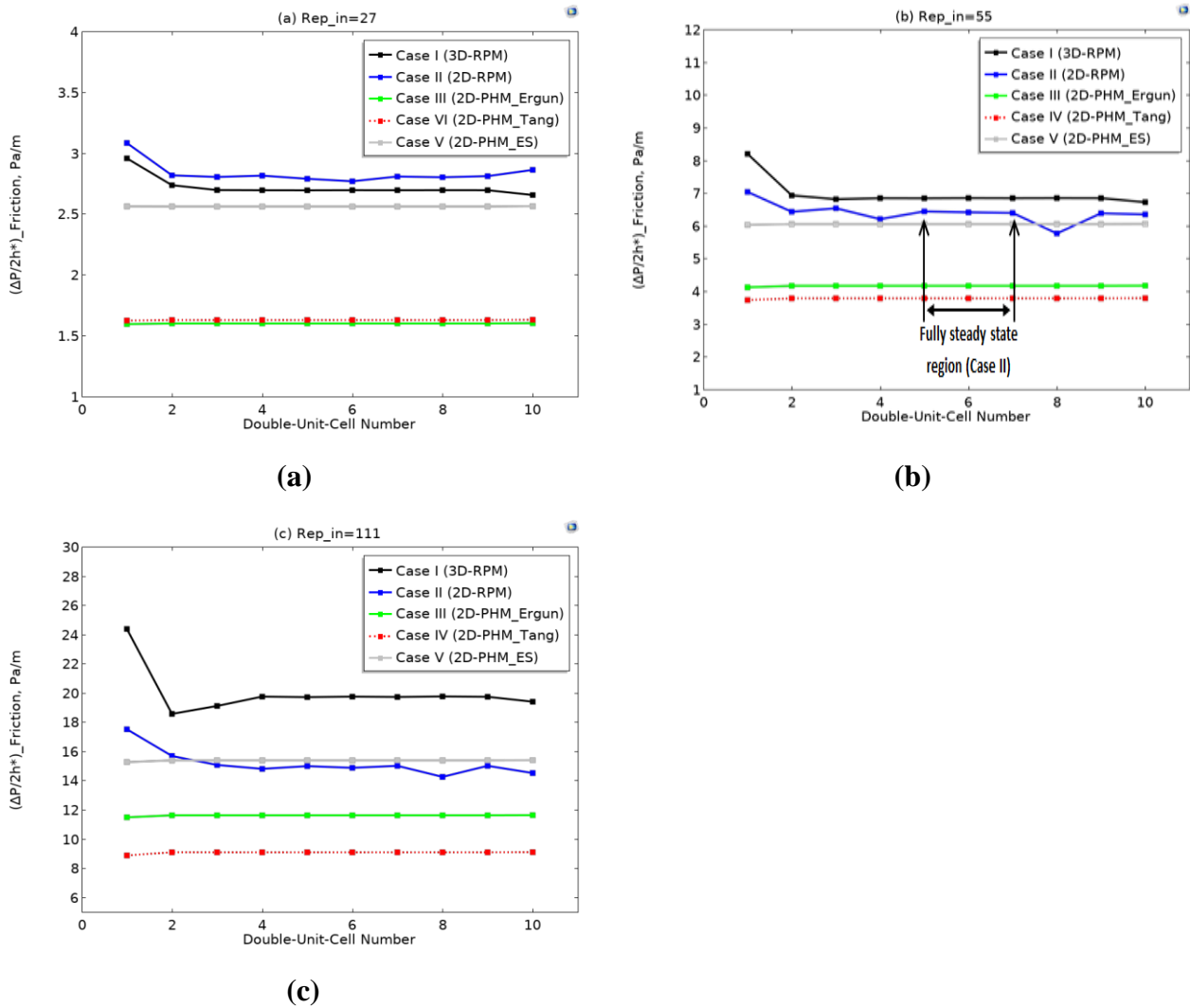


Figure 29: Comparison of frictional pressure drop simulated results as a function of Double-Unit-Cell number for all cases at different inlet Rep values: (a) 27; (b) 55; (c) 111.

All the pseudo homogeneous cases show constant Double-Unit-Cell (DUC) pressure drop profiles $(\Delta P/2h^*)$ between the second DUC and the last DUC, which are represented by straight lines. The lower values through the first DUC are attributed to the redistribution of flow toward the low local porosity regions, mainly near the column wall. These variations are of greater extent in the resolved-particle Cases (I and II), which exhibit more instability of the DUC pressure drop simulated results within the bed region compared to the pseudo homogeneous Cases (III, IV and V). This may be explained by the strong influence of the

bed's textual characteristics in the Resolved-Particle cases. Although, for both cases, the simulated DUC pressure drop level out in the bulk region of the bed, where any impacts of the bed's entrance and exit can be eliminated, mainly for Case I. For instance, simulated DUC pressure drop profile by Case II is stable between the fifth and the seventh DUC, as shown in Figure 3b, which correspond to the eighth and the fourteenth layers, as shown in Figure 2b. Therefore, to make an effective comparison between all cases, the DUC pressure drop should be calculated in the middle of the bed, to eliminate any entrance and exit effects.

The bar chart, in figure 4, illustrates the mean relative deviation (MRD) of the predicted pressure drop results by the 2D simulations (Cases II, III, IV and V) with respect to the 3D simulations (Case I) for inlet particle Reynolds numbers of 27, 55 and 111.

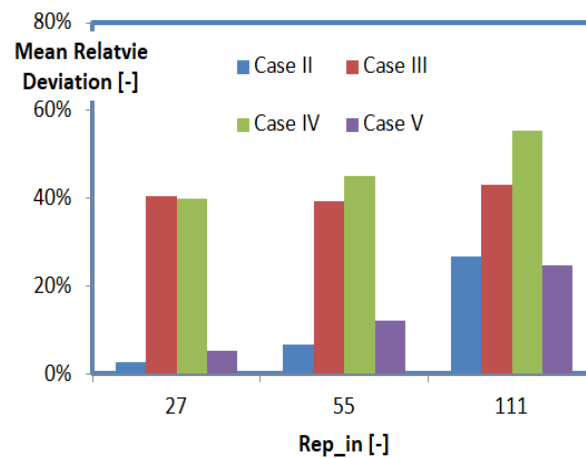


Figure 30 Mean Relative Deviation (MRD) of the simulated pressure drop results in Cases (II, III, IV and V) in reference to Case I at different inlet Rep values.

Overall, Case II and to a lower extent Case V showed the best fits to Case I, concerning the bulk pressure drop, for all the inlet Rep values. In Case II, the MRD was about 3% at inlet Rep of 27, then it increased to around 7% at inlet Rep of 55, being the lowest values, and continued to increase reaching almost 27% at inlet Rep of 111. Similarly, the MRD by

Case V was about 5% at inlet Rep of 27, and then it rose to around 12% at inlet rep of 55, being the second lowest values, and increased further achieving nearly 25% at inlet Rep of 111. While, the MRD for both Cases (II and V) did not exceed 27% for all the inlet Rep tested, the MRDs by Cases (III and IV) did not fall below 39%. These findings can be explained by the wall effects, which is well taken into consideration by Case II, through the 2D imaginary geometry, and by Case V, using the ES semi-empirical correlation.

4. CONCLUSION

The simulation of the considered five different cases (a Three-Dimensional Resolved-Particle, a Two-Dimensional Resolved-Particle (conceptual) and three Pseudo-homogeneous and incompressible flow) in a packed bed with aspect ratio of 2, for three inlet particle Reynolds numbers of 27, 55 and 111, corresponding to the laminar flow regime, was a good contribution to the study of the efficiency of different drag laws when implemented in a 2D CFD pseudo homogeneous model and to the investigation of the efficacy of a new CFD modeling approach.

Clearly the comparison of the obtained results, in term of pressure drop, indicated that the proposed approach in Case II, using a conceptual geometry, and to a smaller extent in Case V, using the ES correlation, showed the best fit to the 3D model where the maximum MRD did not Exceed 27% at inlet Rep of 111. An excellent agreement was found at lower inlet Rep values, where the MRDs of Cases II and V varied between 3 and 5% at $Rep_{in} = 27$ to 7% and 12% at $Rep_{in}=55$, respectively. Summing up the results, it can be concluded that considering the conceptual 2D geometry or applying the ES correlation in the flow equations when designing a packed bed with aspect ratio of 2, may give accurate results with lesser computing time comparing with 3D simulations.

Clearly, future work will be needed to validate our new approach when coupling

hydrodynamics with chemical reactions.

As the industry that depends on these type of packed bed reactors with low aspect ratio is becoming more concerned all over the world, any additional contribution to its design and/or modeling of various parameters will not only lead to technology progress, resulting in significant savings, but will also help to protect the environment.

Appendices

Appendix A

The hypothetical 2D unit cell porosity can be defined according to Equation A1

$$\varepsilon_{2D} = \frac{\frac{3}{2}S_C}{S_{2D-UC}} \quad (\text{A1})$$

Where S_C and S_{2D-UC} are the surface areas of one circle and the hypothetical 2D unit cell (2D-UC) in the conceptual geometry, which may be given by:

$$S_C = \frac{\pi}{4}d_c^2 \quad (\text{A2})$$

$$S_{2D-UC} = 2dph^* \quad (\text{A3})$$

Where d_c is the diameter of a hypothetical circular particle.

Let the 3D unit cell porosity be given by

$$\varepsilon_{3D} = \frac{\frac{3}{2}V_p}{V_{3D-UC}} \quad (\text{A4})$$

Where V_p and V_{3D-UC} are the particle and the unit cell volumes (in the real bed), which may be given by:

$$V_p = \frac{\pi}{6}dp^3 \quad (\text{A5})$$

$$V_{3D-UC} = \pi dp^2 h^* \quad (\text{A6})$$

Assuming that ε_{2D} and ε_{3D} are equals, the circle diameter can be derived according to

Equation (A7)

$$d_c = 2 \sqrt{\frac{1}{3\pi}} dp \quad (\text{A7})$$

Appendix B

To ensure that the results are independent of mesh size, the numerical errors of the simulations were analyzed using the procedure provided by (17). Let us first define the representative grid size h , for three-dimensional space, by

$$h = \left[\frac{1}{N} \sum_{k=1}^N (\Delta V_k) \right]^{1/3} \quad (\text{B1})$$

where ΔV_k is the volume of the k th cell and N is the total number of cells used for computations. Three grid sizes were selected such that, the grid refinement factors, defined by Equation (B2) and (B3), should be greater than 3.

$$r_{21} = \frac{h_2}{h_1} \quad (\text{B2})$$

And

$$r_{32} = \frac{h_3}{h_2} \quad (\text{B3})$$

Then, the expression that defines the apparent order of the method is as follows:

$$p = \frac{1}{\ln r_{21}} \left| \ln \left| \frac{\theta_{32}}{\theta_{21}} \right| + q(p) \right| \quad (\text{B4a})$$

$$q(p) = \ln \left(\frac{r_{21}^p - s}{r_{32}^p - s} \right) \quad (\text{B4b})$$

$$s = 1. \operatorname{sgn} \left(\frac{\theta_{32}}{\theta_{21}} \right) \quad (\text{B4c})$$

In these, $\theta_{32} = (\Delta P)_3 - (\Delta P)_2$ and $\theta_{21} = (\Delta P)_2 - (\Delta P)_1$ with $(\Delta P)_1$, $(\Delta P)_2$ and $(\Delta P)_3$ are the simulated pressure drop results using the three grid sizes h_1 , h_2 and h_3 , respectively.

Finally, the asymptotic pressure drop and its associated Grid Convergence Index on the finer grid (GCI_{21}), may be calculated as follows:

$$(\Delta P)_{Asymp} = \frac{(r_{21}^P(\Delta P)_1 - (\Delta P)_2)}{(r_{21}^P - 1)} \quad (B5)$$

$$GCI_{21} = \frac{1.25e_{21}}{r_{21}^P - 1} \quad (B6)$$

REFERENCES

- [1] Alzahrani F, Aldehani M, Rusi H, McMaster M, Abreu Fernandes DL, Assabumrungrat S, et al. Gas flow visualization in low aspect ratio packed beds by three-dimensional modeling and near-infrared tomography. *Industrial & Engineering Chemistry Research* 2015;54:12714–29. <https://doi.org/10.1021/acs.iecr.5b02635.s002>.
- [2] Romero-Limonos A, Poissonnier J, Thybaut JW, Castillo-Araiza CO. A pseudo-local heat transfer approach in a low tube to particle diameter ratio packed bed catalytic reactor: Oxidative dehydrogenation of ethane as a case study. *Chemical Engineering Journal* 2023;454:140392. <https://doi.org/10.2139/ssrn.4173893>.
- [3] Guo Z, Sun Z, Zhang N, Ding M, Wen J. Experimental characterization of pressure drop in slender packed bed ($1 < D/d < 3$). *Chemical Engineering Science* 2017;173:578–87. <https://doi.org/10.1016/j.ces.2017.08.022>.
- [4] Freund H, Zeiser T, Huber F, Klemm E, Brenner G, Durst F, et al. Numerical simulations of single phase reacting flows in randomly packed fixed-bed reactors and experimental validation. *Chemical Engineering Science* 2003;58:903–10. [https://doi.org/10.1016/S0009-2509\(02\)00622-x](https://doi.org/10.1016/S0009-2509(02)00622-x).
- [5] Pistocchini L, Garone S, Motta M. Fluid dynamics optimization of a novel isothermal adsorption dehumidification system for solar driven applications. *Energy Procedia* 2014;48:1689–98. <https://doi.org/10.1016/j.egypro.2014.02.073>.
- [6] Das S, Deen NG, Kuipers JAM. A DNS study of flow and heat transfer through slender fixed-bed reactors randomly packed with spherical particles. *Chemical Engineering Science* 2017;160:1–19. <https://doi.org/10.1016/j.ces.2016.11.008>.
- [7] Hassan YA, Kang C. Pressure drop in a pebble bed reactor under high Reynolds number. *Nuclear Technology* 2012;180:159–73. <https://doi.org/10.13182/nt12-a14631>.
- [8] Einfeld B, Schnitzlein K. The influence of confining walls on the pressure drop in packed beds. *Chemical Engineering Science* 2001;56:4321–9. [https://doi.org/10.1016/S0009-2509\(00\)00533-9](https://doi.org/10.1016/S0009-2509(00)00533-9).
- [9] Reger D, Merzari E, Balestra P, Schunert S, Hassan Y, Yuan H. An improved pressure drop correlation for modeling localized effects in a pebble bed reactor. *Nuclear*

Engineering and Design 2023;403:112123.

<https://doi.org/0.1016/j.nucengdes.2022.112123>.

[10] Robbins DJ, El-Bachir MS, Gladden LF, Cant RS, von Harbou E. CFD modeling of single-phase flow in a packed bed with MRI validation. *AIChE Journal* 2012;58:3904–15. <https://doi.org/10.1002/aic.13767>.

[11] Micale D, Ferroni C, Uglietti R, Bracconi M, Maestri M. Computational fluid dynamics of reacting flows at surfaces: Methodologies and applications. *Chemie Ingenieur Technik* 2022;94:634–51. <https://doi.org/0.1002/cite.202100196>.

[12] Uribe S, Qi B, Cordero ME, Al-Dahhan M. Comparison between pseudo-homogeneous and resolved-particle models for liquid hydrodynamics in packed-bed reactors. *Chemical Engineering Research and Design* 2021;166:158–71.

<https://doi.org/0.1016/j.cherd.2020.12.001>.

[13] Ranade VV, Chaudhari R, Gunjal PR. *Trickle bed reactors: Reactor engineering and applications*. Elsevier; 2011.

[14] George GR, Bockelmann M, Schmalhorst L, Beton D, Gerstle A, Torkuhl L, et al. Workflow for computational fluid dynamics modeling of fixed-bed reactors packed with metal foam pellets: Hydrodynamics. *AIChE Journal* 2023;69:e17284.

[15] Bded AS. Performance simulation for gas flow through a porous media in packed bed columns using CFD. *IOP Conference Series: Materials Science and Engineering*, vol. 579, Baghdad, Republic of Iraq: IOP Publishing; 2019, p. 012001.

[16] Crolet J-M. *Computational methods for flow and transport in porous media* 2013. <https://doi.org/10.1016/j.cej.2010.10.053>.

[17] Celik IB, Ghia U, Roache PJ, Freitas CJ. Procedure for estimation and reporting of uncertainty due to discretization in CFD applications. *Journal of Fluids Engineering-Transactions of the ASME* 2008;130. <https://doi.org/10.1115/1.2960953>.

[18] Pavlišič A, Pohar A, Likozar B. Comparison of computational fluid dynamics (CFD) and pressure drop correlations in laminar flow regime for packed bed reactors and columns. *Powder Technology* 2018;328:130–9.

<https://doi.org/0.1016/j.powtec.2018.01.029>.

[19] Govindarao VM, Ramrao KV, Rao AV. Structural characteristics of packed beds of low aspect ratio. *Chemical Engineering Science* 1992;47:2105–9.

[https://doi.org/10.1016/0009-2509\(92\)80330-F](https://doi.org/10.1016/0009-2509(92)80330-F).

[20] Van der Merwe WJS. Analysis of flow through cylindrical packed beds with small cylinder diameter to particle diameter ratios. North-West University, Potchefstroom Campus, 2014.

[21] von Seckendorff J, Achterhold K, Pfeiffer F, Fischer R, Hinrichsen O. Experimental and numerical analysis of void structure in random packed beds of spheres. *Powder Technology* 2021;380:613–28. <https://doi.org/10.1016/j.powtec.2020.11.026>.

[22] Eppinger T, Seidler K, Kraume M. DEM-CFD simulations of fixed bed reactors with small tube to particle diameter ratios. *Chemical Engineering Journal* 2011;166:324–31.

[23] Preller ACN. Numerical modelling of flow through packed beds of uniform spheres. North-West University, Potchefstroom Campus, 2011.

[24] Uribe S, Al-Ani M, Cordero ME, Al-Dahhan M. Modelling and validation of TBR Hydrodynamics: Local comparison between CFD and experiments. *Fuel* 2020;277:118244.

<https://doi.org/10.1016/j.fuel.2020.118244>.

[25] Uribe S, Cordero ME, Reyes EP, Regalado-Méndez A, Zárate LG. Multiscale CFD modelling and analysis of TBR behavior for an HDS process: Deviations from ideal behaviors. *Fuel* 2019;239:1162–72. <https://doi.org/10.1016/j.fuel.2018.11.104>.

- [26] Du Toit CG. Radial variation in porosity in annular packed beds. *Nuclear Engineering and Design* 2008;238:3073–9. <https://doi.org/10.1016/j.nucengdes.2007.12.018>.
- [27] van Antwerpen W d, Du Toit CG, Rousseau PG. A review of correlations to model the packing structure and effective thermal conductivity in packed beds of mono-sized spherical particles. *Nuclear Engineering and Design* 2010;240:1803–18. <https://doi.org/10.1016/j.nucengdes.2010.03.009>.
- [28] Amiri L, Ghoreishi-Madiseh SA, Hassani FP, Sasmito AP. Estimating pressure drop and Ergun/Forchheimer parameters of flow through packed bed of spheres with large particle diameters. *Powder Technology* 2019;356:310–24. <https://doi.org/10.1016/j.powtec.2019.08.029>.
- [29] Mueller GE. Radial porosity in packed beds of spheres. *Powder Technology* 2010;203:626–33. <https://doi.org/10.1016/j.powtec.2010.07.007>.
- [30] Taheri S, Ghomeshi S, Kantzas A. Permeability calculations in unconsolidated homogeneous sands. *Powder Technology* 2017;321:380–9. <https://doi.org/10.1016/j.powtec.2017.08.014>.
- [31] Ergun S, Orning AA. Fluid flow through randomly packed columns and fluidized beds. *Industrial & Engineering Chemistry* 1949;41:1179–84. <https://doi.org/10.1021/ie50474a011>.
- [32] Ergun S. Fluid flow through packed columns. *Chem Eng Prog* 1952;48:89–94. <https://doi.org/10.1021/ie50474a011>.
- [33] Hardy B, Simonin O, De Wilde J, Winckelmans G. Simulation of the flow past random arrays of spherical particles: Microstructure-based tensor quantities as a tool to predict fluid–particle forces. *International Journal of Multiphase Flow* 2022;149:103970. <https://doi.org/10.1016/j.ijmultiphaseflow.2021.103970>.
- [34] Beetstra R, van der Hoef MA, Kuipers JAM. Drag force of intermediate Reynolds number flow past mono-and bidisperse arrays of spheres. *AIChE Journal* 2007;53:489–501. <https://doi.org/10.1002/aic.11065>.
- [35] Tenneti S, Garg R, Subramaniam S. Drag law for monodisperse gas–solid systems using particle-resolved direct numerical simulation of flow past fixed assemblies of spheres. *International Journal of Multiphase Flow* 2011;37:1072–92. <https://doi.org/10.1016/j.ijmultiphaseflow.2011.05.010>.
- [36] Y. Tang Y, (Frank) Peters E, (Hans) Kuipers JAM, (Sebastian) Kriebitzsch SHL, (Martin) van der Hoef MA. A new drag correlation from fully resolved simulations of flow past monodisperse static arrays of spheres. *AIChE Journal* 2015;61:688–98. <https://doi.org/10.1002/aic.14645>.
- [37] Examining Spatial (Grid) Convergence n.d. <https://www.grc.nasa.gov/www/wind/valid/tutorial/spatconv.html> (accessed July 19, 2023).

REPUBLIQUE ALGERIENNE DEMOCRATIQUE ET POPULAIRE
MINISTRE DE L'ENSEIGNEMENT SUPERIEUR ET DE LA RECHERCHE
SCIENTIFIQUE

UNIVERSITE SALAH BOUBNIDER CONSTANTINE 3

DECLARATION SUR L'HONNEUR

RELATIVE A L'ENGAGEMENT AUX REGLES D'INTEGRITE SCIENTIFIQUE EN
VUE D'ELABORATION D'UNE RECHERCHE

Je, soussigné(e),

Mme, Melle, Mr Maher LAKKACHI

Qualité : étudiant, enseignant, chercheur, Doctorant ès sciences...

Portant carte d'identité n° 118687354 Délivrée le ...11/10/2020.....

Inscrit à la faculté/Institut : Génie des procédés Département : Génie chimique

Chargé(e) d'élaborer des travaux de recherche (mémoire, mémoire de Master, mémoire de Magister, thèse de **Doctorat**) dont le titre est :

“Modeling of Trickle bed catalytic reactors and industrial applications to GTL process”

Et après avoir pris connaissance des dispositions de l'Arrêté n°1082 du 27/12/2020 et notamment son article 3.

Je déclare sur mon honneur de m'engager à respecter les critères scientifiques et méthodologiques ainsi que les critères d'éthique de la profession et de l'intégrité académique requises dans l'élaboration de la recherche suscitée.

Par ailleurs, je déclare assumer l'entière responsabilité quant à d'éventuelles manquements à l'éthique et à la déontologie émanant de ma part à l'occasion de l'élaboration des travaux de recherche, et dégage la responsabilité de mon institution de tout acte préjudiciable et malveillant.

Fait à Constantine le 23/03/2025

Signature de l'intéressé(e)

M. LAKKAICHI





Name and Surname : Maher LAKKAICHI

Title : Modeling of Trickle Bed Catalytic Reactors and Industrial Applications to
GTL Process

Thesis Submitted for the Award of the Degree of Doctor of Science in Process
Engineering.

Option: Chemical Engineering

Abstract

Trickle-Bed Reactors (TBRs) are widely utilized in industrial applications. One of the main industrial applications of TBRs is transforming a gaseous mixture of hydrogen and carbon monoxide, called syngas, to environment-friendly synthetic liquid fuels, via Fischer-Tropsch Synthesis (FTS), which is a strongly exothermic reaction.

The aim of this work is to develop a pseudo-homogeneous two-dimensional (2D) Fischer-Tropsch Packed Bed Reactor (FTPBR) model in order to investigate the use of slender packed bed reactors for FTS. This will facilitate the excess heat removal from the bed as well as enhance the performance. To accomplish this objective; two main studies have been conducted, which are (i) hydrodynamic study and (ii) then using its results to develop a FTPBR model. The modeling was carried out using the Finite Element Analysis (FEA) software known as COMSOL Multiphysics 5.6.

Firstly, it was confirmed that the Einfeld and Schnitzlein drag force model should be applied in the momentum balance equation of a two-dimensional pseudo-homogeneous model for low aspect-ratio packed beds. Moreover, a novel 2D modeling approach was proposed for packed bed reactors with an aspect ratio of 2, under laminar flow conditions, mainly of particle Reynolds number lesser than 111.

Secondly, based on the Eulerian mixture approach, a mathematical 2D pseudo-homogeneous model of the FTPBR was developed and validated by confronting its simulated results against those of models of literature as well as by conducting a consistent error discretization uncertainty study. Then it was exploited for the optimization of large-scale FT reactor as well as to optimize and design a small-scale FT reactor. For each scale, two cases were investigated. While the feedstock of the large-scale cases was natural gas, the small-scale cases used biomass as feedstock. For each case, four PBRs with different aspect ratios ranges from 2 to 15.33 were simulated.

It has been found that, the large PBR is the optimized reactor for the large scale, which can be used in a GTL plant to process 170000 m³ of natural gas - at standard conditions - for producing more than 626 tons of C₅₊ per day. Otherwise, the slender PBR with aspect ratio of 4 is the most efficient for the small scale. This reactor is 2 m long and 1916 mm in diameter, which is composed of 6698 tubes arranged in triangular pattern. Besides, it was designed to be fitted into a mobile micro-refinery to process 6 tons of wood chips or 6.6 tons of municipal solid waste per day, to daily produce 4827.16 kg/d and 281.55 kg/d of C₅₊ and LPG, respectively.

Keywords: Packed Bed Reactor, Pressure Drop, Gas-To-Liquid, Fischer-Tropsch, Thermal Runaway, Aspect Ratio, Modeling and Simulation, COMSOL Multiphysics.

Thesis Supervisor : Pr. Nawel OUTILI – University of Constantine 3 Salah Boubnider

Academic Year : 2024-2025